frontiers | Research Topics

Hydrodynamic characteristics and pollutant transport in rivers and nearshore environments

Edited by
Biyun Guo, XiuWen Cheng, Li Zhang, Xiaoning Zhao, Zengxin Zhang and Matteo Rubinato

Published in
Frontiers in Environmental Science

ISSN 1664-8714
ISBN 978-2-8325-4553-9
DOI 10.3389/978-2-8325-4553-9

About Frontiers

Frontiers is more than just an open access publisher of scholarly articles: it is a pioneering approach to the world of academia, radically improving the way scholarly research is managed. The grand vision of Frontiers is a world where all people have an equal opportunity to seek, share and generate knowledge. Frontiers provides immediate and permanent online open access to all its publications, but this alone is not enough to realize our grand goals.

Frontiers journal series

The Frontiers journal series is a multi-tier and interdisciplinary set of open-access, online journals, promising a paradigm shift from the current review, selection and dissemination processes in academic publishing. All Frontiers journals are driven by researchers for researchers; therefore, they constitute a service to the scholarly community. At the same time, the *Frontiers journal series* operates on a revolutionary invention, the tiered publishing system, initially addressing specific communities of scholars, and gradually climbing up to broader public understanding, thus serving the interests of the lay society, too.

Dedication to quality

Each Frontiers article is a landmark of the highest quality, thanks to genuinely collaborative interactions between authors and review editors, who include some of the world's best academicians. Research must be certified by peers before entering a stream of knowledge that may eventually reach the public - and shape society; therefore, Frontiers only applies the most rigorous and unbiased reviews. Frontiers revolutionizes research publishing by freely delivering the most outstanding research, evaluated with no bias from both the academic and social point of view. By applying the most advanced information technologies, Frontiers is catapulting scholarly publishing into a new generation.

What are Frontiers Research Topics?

Frontiers Research Topics are very popular trademarks of the *Frontiers journals series*: they are collections of at least ten articles, all centered on a particular subject. With their unique mix of varied contributions from Original Research to Review Articles, Frontiers Research Topics unify the most influential researchers, the latest key findings and historical advances in a hot research area.

Find out more on how to host your own Frontiers Research Topic or contribute to one as an author by contacting the Frontiers editorial office: frontiersin.org/about/contact

Hydrodynamic characteristics and pollutant transport in rivers and nearshore environments

Topic editors

Biyun Guo — Zhejiang Ocean University, China
XiuWen Cheng — Lanzhou University, China
Li Zhang — Tsinghua University, China
Xiaoning Zhao — Nanjing University of Information Science and Technology, China
Zengxin Zhang — Hohai University, China
Matteo Rubinato — Coventry University, United Kingdom

Citation

Guo, B., Cheng, X., Zhang, L., Zhao, X., Zhang, Z., Rubinato, M., eds. (2024). *Hydrodynamic characteristics and pollutant transport in rivers and nearshore environments*. Lausanne: Frontiers Media SA. doi: 10.3389/978-2-8325-4553-9

Table of contents

frontiers | Frontiers in Environmental Science

TYPE Editorial
PUBLISHED 23 February 2024
DOI 10.3389/fenvs.2024.1379032

OPEN ACCESS

EDITED AND REVIEWED BY
Angela Helen Arthington,
Griffith University, Australia

*CORRESPONDENCE
Biyun Guo,
biyunguo@163.com

RECEIVED 30 January 2024
ACCEPTED 15 February 2024
PUBLISHED 23 February 2024

CITATION
Guo B, Subrahmanyam MV and Xue S (2024), Editorial: Hydrodynamic characteristics and pollutant transport in rivers and nearshore environments.
Front. Environ. Sci. 12:1379032.
doi: 10.3389/fenvs.2024.1379032

Editorial: Hydrodynamic characteristics and pollutant transport in rivers and nearshore environments

Biyun Guo[1]*, M. V. Subrahmanyam[2] and Shutian Xue[3]

[1]College of Marine Science and Technology, Zhejiang Ocean University, Zhoushan, Zhejiang, China, [2]School of Marine Science and Technology, Hainan Tropical Ocean University, Sanya, Hainan, China, [3]School of Artificial Intelligence, Guilin University of Electronic Technology, Guilin, Guangxi, China

KEYWORDS

rivers, estuaries and nearshore environments, hydrodynamics, contaminants, migration and diffusion, sediment transport

Editorial on the Research Topic
Hydrodynamic characteristics and pollutant transport in rivers and nearshore environments

Wang et al. simulated the structural deformation and failure problem in fluid-structure interaction (FSI) based on models. This field of study is helpful in many engineering operations such as material selection, the study of fatigue damages and the estimation of structural life. The problem was that the original TLSPH (total Lagrangian smoothed particle hydrodynamics) method could not simulate structural cracks and their propagation, and the fracture model based on TLSPH was established. The present coupled WC-TLSPH (weakly compressible - TLSPH) model can accurately simulate the FSI problem where the figurative fracture process is involved, indicating the compromised potential of the established model to simulate the elastoplastic structural failure in scientific and industrial applications.

Shi et al. used remote sensing techniques to estimate dissolved oxygen (DO) concentration by applying a crucial means of water quality monitoring. They propose a novel model for DO concentration estimation in water bodies, termed Dissolved Oxygen Multimodal Deep Neural Network (DO-MDNN), which utilizes synchronous satellite remote sensing data for real-time DO concentration inversion. Using Lake Taihu as a case study, they validate the DO-MDNN model using Himawari-8 (H8) satellite imagery as input data and actual DO concentration in Lake Taihu as output data. Results demonstrate that the DO-MDNN model exhibits high accuracy and stability in estimating DO concentration inversion. This method holds significant practical value in enhancing the efficiency and precision of water quality monitoring.

With the development of societies and economies, the process of industrialization and urban modernization is accelerating, urban populations are increasing, and more and more wastewater is generated and released. Large quantities of hazardous industrial and agricultural wastewater and domestic sewage are discharged directly into reservoirs, lakes, rivers and the sea, without adequate treatment. The wide range of pollutants discharged can degrade, interact, and transform in aquatic environments. Rivers are the main channels of pollution transport from land-based activities within watersheds. Various

types of pollutants produced on land are transported downstream to estuaries and coastal areas through river networks, forming land-sea pollution transport chains. A large amount of terrigenous material is confined to the nearshore area when runoff, river discharge, and other processes deposit these materials on the continental shelf. Terrestrial water is usually rich in nutrients, pollutants and sediment, and their offshore diffusion through water bodies has an important impact on marine primary productivity, biological diversity and geochemical processes. The transport and diffusion of pollutants and changes in their concentration are affected by hydrodynamic forces. Therefore, the exploration of solid matter and organic matter content, diffusion processes and controlling factors in water bodies is of great significance for understanding the ecological environments of river and coastal systems under variable hydrological conditions and climate change.

Nine papers constitute this Research Topic mainly involving watershed hydrology, pollution transport, surface and groundwater quality and water quality monitoring. Due to the complex and variable processes of watershed hydrology, pollutant transport and diffusion, this Research Topic will attract scholastic attention to the hydrological, water quality and ecological characteristics of estuarine and nearshore environments and the mechanisms and interactions of the water environment and biota. Water environment, pollutant transport and biota.

Wang et al. analyzed bacterial composition, diversity, community composition and geographical distribution in lake water of three adjacent regions on the Qinghai Tibet Plateau (QTP). Results from 16S rRNA gene sequencing illustrate that bacterial alpha-diversity indices are much lower in the Hoh Xil (HX) than in the Yellow River Headwater (YRH) and Qaidam (QD) regions. Redundancy analysis suggests that the most important factors driving bacterial community composition in the three regions are altitude (QD), total nitrogen (YRH), and pH (HX). The results of this study provide insight into differences in bacterial features of lakes at the regional scale and the main drivers of community composition, thereby offering guidance on the protection and management of these plateau lake ecosystems.

Wang et al. use high throughput sequencing to explore archaeal communities in seawater from the hypoxic and non-hypoxic zones of the Changjiang (Yangtze) Estuary, China. Thaumarchaeota dominated archaeal communities in the hypoxic zones (bottom water), and Euryarchaeota were mainly distributed in the non-hypoxic zones (surface water). Archaeal richness was significantly influenced by DO, while archaeal diversity was influenced by nutrient levels. This study elucidated the shift in community structure of archaea caused by hypoxia in the Changjiang Estuary, and laid a foundation for future studies on the ecological patterns and functions of archaea in estuary ecosystems.

Ruan et al. took a section of the Yellow River in China from the Xiaolangdi Dam to Gaocun as their research area and analyzed the spatial distribution of Yellow River carp (*Cyprinus carpio*) spawning before (1980-1990) and after (2006-2018) the construction of Xiaolangdi Dam. This study shed light on the response of the Yellow River carp to hydrological and physical habitat changes after the construction of this dam. Construction and operation of the Xiaolangdi Dam decreased the extent of spawning reaches by 16.23%, delayed the breeding time of the carp and greatly affected larval fish development. Thus, this study provides a reference for restoring the spawning habitat of the Yellow River carp and for the scheduling of discharges from the Xiaolangdi Dam to provide for the reproductive needs of the carp.

With fair precision, Li et al. collected a series of water samples from six different rivers in China whose sediment concentration and size distribution vary widely and analyzed their phosphorus (P) properties in the laboratory. From this analysis of field samples, a highly consistent comet-shaped pattern of sediment effects on P is revealed, i.e., generally, the range of concentration of total P has a diverge-converge trend as the sediment concentration increases. The regime of fluvial P constituted by sediment obtained in this study serves as a knowledge base for further investigation of this fundamental biogeochemical cycle.

Ren et al. analyzed the evolution of intercrystalline brine in the Kunteyi Basin, China, based on major ionic concentrations and isotopic ratios (δ^2H, $\delta^{18}O$, and $\delta^{11}B$). The results show that the intercrystalline brine has a much higher concentration of total dissolved solids compared with oil-field brine. Results indicate that thermal water recharged the Pleistocene layer, reacted with polyhalite, and formed Mg- and K-rich brine. This solution rose along the channel formed by the Shuangqiquan Fault and was supplied to the shallow intercrystalline brine. Research on the origin of brine informs understanding of the process of mineral formation and improves the efficiency of mineral exploitation.

With fair precision, Liu et al. researched the Bingham fluid flow on a slope using a corrected smooth particle hydrodynamics (CSPH) method based on periodic density re-initialization and artificial stress. Results show that the CSPH method can accurately simulate the rheological behavior of the Bingham fluid, such as shear thinning. Furthermore, the numerical results with a large range of incline angles are given to prove the effectiveness and stability of the improved SPH (smooth particle hydrodynamics) method, which can effectively capture the complex transient flow behavior of Bingham fluid and be applied to large-scale and real scene debris flow numerical simulation with parallel technology.

Liu et al. studied the movement characteristics of *Oncomelania* (the snail intermediate host of schistosomiasis along rivers and irrigation schemes) using image recognition and wavelet analysis. They developed a simple settling velocity model that can predict the terminal velocity of *Oncomelania* fairly with several easy-to-measure parameters. These findings provide a basis for the further improvement of the hydraulic schistosomiasis control project and also supply a reference model for the settling characteristics and drag coefficient of cone-shaped particles.

Author contributions

BG: Conceptualization, Data curation, Formal Analysis, Funding acquisition, Investigation, Methodology, Project administration, Resources, Software, Supervision, Validation, Visualization, Writing–original draft, Writing–review and editing. MV: Conceptualization, Data curation, Visualization, Writing–review and editing. SX: Data curation, Formal Analysis, Investigation, Resources, Validation, Writing–review and editing.

Funding

The author(s) declare that financial support was received for the research, authorship, and/or publication of this article. This work

was supported by Consultation and Evaluation Program of the Department of Chinese Academy of Science (2020-ZW11-A-023), the open research fund program of State Key Laboratory of Hydroscience and Engineering, Tsinghua University (sklhse-2021-B-01), Zhejiang Provincial Virtual Simulation Experiment Projects (virtual simulation experimental project for monitoring of suspended sediment in coastal waters using remote sensing), The China Scholarship Council (NO. 20230833027), National College Students Innovation and Entrepreneurship Training Program (NO. 202110340039), Zhejiang University Students Science and Technology Innovation Activity Plan (New Talent Program. NO. 2022R411A003), and the National Natural Science Foundation of China (No. 52109092) also supported this research and the publication of findings.

Conflict of interest

The authors declare that the research was conducted in the absence of any commercial or financial relationships that could be construed as a potential conflict of interest.

Publisher's note

frontiers | Frontiers in Environmental Science

TYPE Original Research
PUBLISHED 27 September 2022
DOI 10.3389/fenvs.2022.1024488

OPEN ACCESS

EDITED BY
Biyun Guo,
Zhejiang Ocean University, China

REVIEWED BY
Huabin Shi,
University of Macau, China
Ningbo Zhang,
City University of London,
United Kingdom

*CORRESPONDENCE
Shenglong Gu,
sl.gu@qhu.edu.cn
Jiaye Li,
lijiaye@dgut.edu.cn

SPECIALTY SECTION
This article was submitted to Freshwater Science, a section of the journal Frontiers in Environmental Science

RECEIVED 21 August 2022
ACCEPTED 05 September 2022
PUBLISHED 27 September 2022

CITATION
Wu H, Gu S, Tian L, Li J, Chen C and Zhang C (2022), Modeling structural deformation and failure in fluid-structure interaction with WC-TLSPH. *Front. Environ. Sci.* 10:1024488. doi: 10.3389/fenvs.2022.1024488

Modeling structural deformation and failure in fluid-structure interaction with WC-TLSPH

Haitao Wu[1,2,3], Shenglong Gu[1,2,3]*, Lirong Tian[1,2,3], Jiaye Li[4,5]*, Chen Chen[4,5] and Chi Zhang[6]

[1]School of Water Resources and Electric Power, Qinghai University, Xining, China, [2]Laboratory of Ecological Protection and High-Quality Development in the Upper Yellow River, Xining, China, [3]Key Laboratory of Water Ecology Remediation and Protection at Headwater Regions of Big Rivers, Ministry of Water Resources, Xining, China, [4]School of Environment and Civil Engineering, Dongguan University of Technology, Dongguan, China, [5]Center for Hydrosphere Science, Key Laboratory of Engineering Software, Dongguan University of Technology, Dongguan, China, [6]TUM School of Engineering and Design, Technical University of Munich, Garching, Germany

In this paper, the coupled weakly compressible (WC) and total Lagrangian (TL) smoothed particle hydrodynamics (SPH) model based on the open-source multi-physics and multi-resolution SPHinXsys library is used to simulate the structural deformation and failure problem in fluid-structure interaction (FSI). Aiming at the problem that the original TLSPH method could not simulate the cracks and their propagation, the fracture model based on TLSPH is established, and then verified by fast-loading and slow-loading cases respectively. With the fracture model in hand, the TLSPH method is coupled with the WCSPH method to simulate the breaking dam flow impacting on an elastic/elastoplastic baffle. The comparison with the literature data shows that the present coupled WC-TLSPH model can accurately simulate the FSI problem where figurative fracture process is involved, indicating the compromising potential of the established model to simulate the elastoplastic structural failure in scientific and industrial applications.

KEYWORDS

structural deformation, structural failure, fluid-structure interaction, WC-TLSPH, fracture model, SPHinXsys

Introduction

Fluid-structure interaction (FSI) is a common phenomenon in various engineering problems which characterized by dramatic change of the flow domain size and shape with the movement or deformation of the structure, leading to its numerical solution is relatively complicated, and of great significance to ensure the safe and stable operation of the structure. Therefore, one of the primary aims of solving FSI problem is to accurately simulate the changing state of structure, and even its failure accurately.

The computational mechanics is considered to be the main approach for solving FSI problems because of its flexibility, and it has made great progress in the past few decades. From a solution point of view, there are generally two main solutions, *i.e.*, a direct solution and an indirect solution (Salehizadeh and Shafiei, 2022). The direct solution refers to

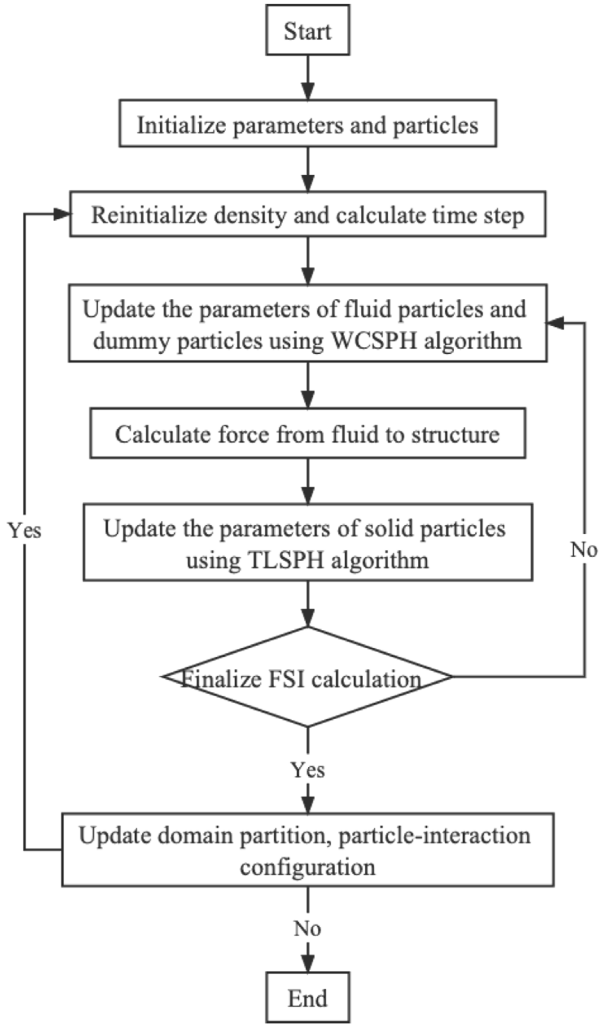

FIGURE 1
Flow chart for the WC-TLSPH model.

solving both fluid and structure dynamics synchronously, while the indirect solution refers to calculating the stress on the structure by solving the fluid dynamics firstly, and then imposing the stress as the boundary condition to solve the deformation of the structure. In terms of specific methods, several grid-based analytical/computational methods, *e.g.* finite difference method (FDM) (Sugiyama et al., 2011), finite element method (FEM) (Mitra andSinhamahapatra, 2008) and finite volume method (FVM) (Lv et al., 2007), have been applied and achieved certain degree of success. However, in violent FSI contact problems, the grid-based methods encounter serious mesh distortion and mesh redrawing problems. To address these issues, the Arbitrary Lagrangian Eulerian (ALE) (Sarrate et al., 2001) is proposed by modelling the structure with the fully Lagrangian formula, whereas a particular modification is required for the precision definition of interface and free surfaces (Salehizadeh and Shafiei, 2022).

With the development of meshless methods in the last decades, alternative solutions have been merged for solving FSI problems. Smoothed particle hydrodynamics (SPH) is a representative meshless method, originally proposed by Lucy, Gingold and Monaghan (Monaghan, 1992) and applied to astrophysics applications. It is a truly meshless, Lagrangian particle method in which the computational domain is discretized into a series of material points carry the field variables such as density, stress tensor and velocity, *etc.* Thanks to its pure Lagrangian property, it has unique advantages in dealing with large deformations, free surfaces and interfaces, and has been applied to in a wide range of fluid and solid computational problems (Bui et al., 2008; Shi et al., 2017; Shi et al., 2019; Gabreil et al., 2022; Gu et al., 2022; Zhang et al., 2022). Zheng et al. (2022) used the SPH method to model the FSI problem of icebreaker sailing in the ice river, where the updated Lagrangian SPH (ULSPH) formulation is used to solve the solid mechanics formulation. However, the using of ULSPH method in which the current configuration is used as the reference will lead to the problem of tensile instability hindering its application to a large extent because it leads to particle sticking and unphysical fracture. Although the application of kernel function reconstruction (Johnson and Beissel, 1996), artificial stress (Gray et al., 2001), generalized transport-velocity formulation (Zhang et al., 2017b) and other methods can solve the problem of tensile instability to a certain degree, these methods introduce additional model parameters, and the choice of these parameters has side effect on the simulation results. According to Belytschko et al. (2000), the use of Euler kernel in ULSPH is the main reason for tensile instability. To fundamentally solve the problem of tensile instability, it is necessary to avoid the use of Euler kernel, *viz.* the total Lagrangian SPH (TLSPH) which applies the Lagrangian kernel and being entirely free of tensile instability. The so-called Lagrangian kernel is to perform particle pairing and calculate the kernel function gradient according to the initial configuration only once before the calculation starts, which means that TLSPH is not suitable for the solution of fluid dynamics where the deformation of particles in the flow process is relatively large. Therefore, by the coupling of weakly compressible SPH (WCSPH) and TLSPH, respectively solving fluid dynamics and solid mechanics, the solution of FSI problems can be well realized.

In terms of the coupling of WCSPH and TLSPH, some scholars have carried out a series of research and achieved certain achievements (He et al., 2017; Zhan et al., 2019; Zhang et al., 2021a). However, in the research of FSI problems where the fracture and failure of materials are involved, the original TLSPH method cannot handle the cracking and fragmentation problems (Islam and Peng, 2019). In order to study the failure of structures in FSI and further expand the application of the TLSPH, the fracture model coupled with TLSPH is established based on the SPHinXsys (https://www.sphinxsys.org) in this paper. SPHinXsys is an open-source multi-physics and multi-resolution library acronym from Smoothed Particle Hydrodynamics for industrial complex systems. It provides open-source C++ APIs for physical accurate simulation and aims to model and to optimize coupled industrial dynamic

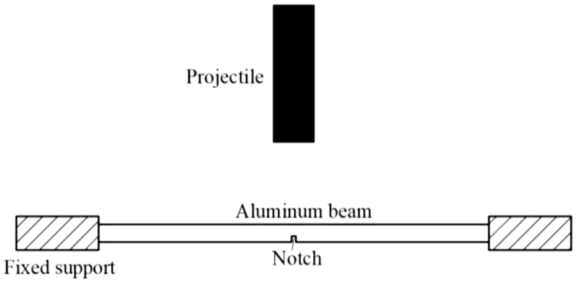

FIGURE 2
Schematic diagram of projectile impacting aluminum beam.

systems including fluid, solid, multi-body dynamics (Zhang et al., 2021b). In addition, SPHinXsys shows impressive computational performance thanks to implementing shared-memory parallel programming on multi-core processors by applying Threading Building Blocks (TBB) library developed by Intel (Zhang et al., 2021c).

This paper is structured as follows. The theory and fundamentals of WCSPH, TLSPH and WC-TLSPH are briefly summarized in Section 2. The fracture model for TLSPH is introduced in Section 3. The fast-loading fracture case of crack propagation in notched beam and the slow-loading fracture case of three-point bending of ice beam based on TLSPH, as well as the further model validations of breaking dam on elastic and elastoplastic baffles are investigated in Section 4 and finally the conclusions and future works are noted in Section 5.

Theory of WC-TLSPH

Scheme of WCSPH

The Navier-Stokes equations (N-S equations) for fluid dynamics in the Lagrangian framework can be written as

$$\begin{cases} \dfrac{\mathrm{d}\rho}{\mathrm{d}t} = -\rho\nabla\cdot\mathbf{v} \\ \dfrac{\mathrm{d}\mathbf{v}}{\mathrm{d}t} = -\dfrac{1}{\rho}\nabla P + \mathbf{g} \end{cases} \tag{1}$$

where ρ is the density, $\mathbf{v}$ the velocity, P the pressure, $\mathbf{g}$ the gravity, $\frac{\mathrm{d}}{\mathrm{d}t} = \frac{\partial}{\partial t} + \nabla\cdot\mathbf{v}$ stands for the material derivative. For the weakly compressible fluid, the governing equations above can be closed by an artificial equation of state (EoS) reads

$$P = c^2\left(\rho - \rho_0\right) \tag{2}$$

where ρ_0 is the reference density and the artificial sound speed $c = 10U_{\max}$ ($U_{\max}$ is the anticipated maximum flow speed) can ensure the density change is about 1% (Morris et al., 1997).

According to the discrete formula of the SPH method, the WCSPH method based on Riemann solver is applied in SPHinXsys to achieve stabilized simulations. Following Zhang et al. (2017a), one-dimensional Riemann problem is constructed along the interacting line of particle i and j, then discretization of the N-S equation can be rewritten as

$$\begin{cases} \dfrac{\mathrm{d}\rho_i}{\mathrm{d}t} = 2\rho_i\sum_j \dfrac{m_j}{\rho_j}\left(U^* - \mathbf{v}_i\mathbf{e}_{ij}\right)\dfrac{\partial W_{ij}}{\partial r_{ij}} \\ \dfrac{\mathrm{d}\mathbf{v}_i}{\mathrm{d}t} = -2\sum_j m_j\dfrac{P^*}{\rho_i\rho_j}\nabla_i W_{ij} + \mathbf{g} \end{cases} \tag{3}$$

where m is the particle mass, W the smooth kernel function, $\nabla_i W_{ij}$ the gradient of the kernel function from particle i to particle j, U^* and P^* represents the solutions of an inter-particle Riemann problem from a low-dissipation Riemann solver can be calculated by

$$\begin{cases} U^* = \bar{U} + \dfrac{1}{2}\dfrac{(P_L - P_R)}{\bar{\rho}c_0} \\ P^* = \bar{P} + \dfrac{1}{2}\bar{\rho}c_0\left(U_L - U_R\right) \end{cases} \tag{4}$$

where the subscprpts L and R represent the left and right states in Riemann problems and the initial L and R states are on particle i and j respectively, *i.e.*, $(\rho_L, U_L, P_L) = (\rho_i, \mathbf{v}_i\cdot\mathbf{e}_{ij}, P_i)$, $(\rho_R, U_R, P_R) = (\rho_j, \mathbf{v}_j\cdot\mathbf{e}_{ij}, P_j)$, $\mathbf{e}_{ij}$ is unit vector, $\bar{U} = (U_L + U_R)/2$ and $\bar{P} = (P_L + P_R)/2$ are inter-particle averages.

Scheme of TLSPH

For the solid mechanics, we follow the Lagrangian framework where all the conservation equations are expressed in terms of the initial coordinates $\mathbf{R}$, which are taken as the reference configuration. Then the displacement $\mathbf{s}$ of any material point can be defined as

$$\mathbf{s} = \mathbf{r} - \mathbf{R} \tag{5}$$

where $\mathbf{r}$ stands for the current, *viz.* deformed configuration. The conservation equations of mass and momentum read

$$\begin{cases} \rho = \rho^0\dfrac{1}{J} \\ \dfrac{\mathrm{d}\mathbf{v}}{\mathrm{d}t} = \dfrac{1}{\rho^0}\nabla^0\cdot\mathbf{P} + \rho^0\mathbf{g} \end{cases} \tag{6}$$

where the superscripts 0 indicates the values expressed in the initial configuration, J is the Jacobian given by $J = \det(\mathbf{F})$ with $\mathbf{F}$ denoting the deformation tensor, $\mathbf{P}$ stands for the first Piola-Kirchhoff stress tensor and the relation between $\mathbf{P}$ and Cauchy stress tensor $\boldsymbol{\sigma}$ can be written as:

$$\mathbf{P} = J\boldsymbol{\sigma}\mathbf{F}^{-T} \tag{7}$$

Another important stress tensor $\mathbf{S}$, *i.e.* the second Piola-Kirchhoff stress tensor, is given by

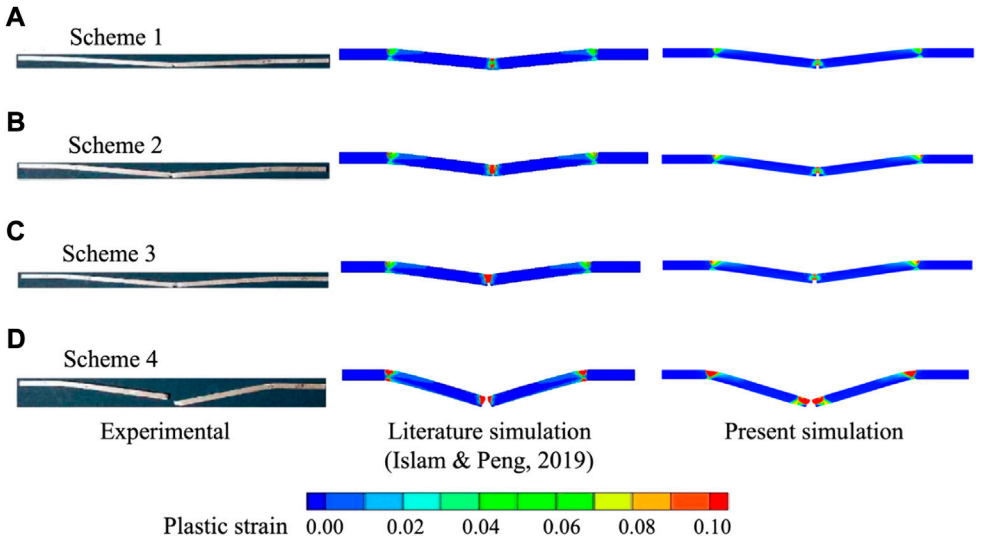

FIGURE 3
Comparison of present simulation (third column) with the experimental (first column) (Chen and Yu, 2004) and simulation (second column) (Islam and Peng, 2019) results of **(A)** Scheme 1, **(B)** Scheme 2, **(C)** Scheme 3 and **(D)** Scheme 4.

TABLE 1 The material properties of the aluminum beam.

Density (kg/m^3)	**Elastic modulus** (GPa)	**Poisson's ratio** (/)	**Yield stress** (MPa)	**Hardening modulus** (GPa)
2,680	68.95	0.33	277.8	0.466

TABLE 2 The details of simulation scheme.

Scheme number	**Scheme 1**	**Scheme 2**	**Scheme 3**	**Scheme 4**
Notch type	I	I	II	II
Initial velocity of projectile (m/s)	14.2	18.2	19.2	27.1

$$\mathbf{S} = J\mathbf{F}^{-1}\sigma\mathbf{F}^{-T} \tag{8}$$

Then, the first Piola-Kirchhoff stress tensor $\mathbf{P}$ can also be expressed as $\mathbf{P} = \mathbf{FS}$. Particularly, the second Piola-Kirchhoff stress tensor $\mathbf{S}$ can be calculated by the constitutive equation.

For the discretization of Eq. 6, a kernel correction matrix $\mathbf{B}^0$ is introduced to ensure the first-order consistency of the TLSPH methods as

$$\mathbf{B}_i^0 = \left(\sum_j V_j \left(\mathbf{r}_j^0 - \mathbf{r}_i^0 \right) \otimes \nabla_i^0 W_{ij} \right)^{-1} \tag{9}$$

where

$$\nabla_i^0 W_{ij} = \frac{\partial W\left(\left|\mathbf{r}_{ij}^0\right|, h\right)}{\partial \left|\mathbf{r}_{ij}^0\right|} \mathbf{e}_{ij}^0 \tag{10}$$

represents the gradient of the kernel function at the initial reference configuration. It is worth noting that the correction matrix is calculated in the initial configuration and therefore is calculated only once at the beginning of the simulation. Then, the mass and momentum conservation equations can be discretized as

$$\begin{cases} \rho_i = \rho^0 \dfrac{1}{\det(\mathbf{F})} \\ \dfrac{\mathrm{d}\mathbf{v}_i}{\mathrm{d}t} = \dfrac{2}{m_i} \sum_j V_i V_j \tilde{\mathbf{P}}_{ij} \nabla_i^0 W_{ij} + \mathbf{g} \end{cases} \tag{11}$$

where the average first Piola-Kirchhoff stress between particles is defined as

$$\tilde{\mathbf{P}}_{ij} = \frac{1}{2}\left(\mathbf{P}_i \mathbf{B}_i^0 + \mathbf{P}_j \mathbf{B}_j^0 \right) \tag{12}$$

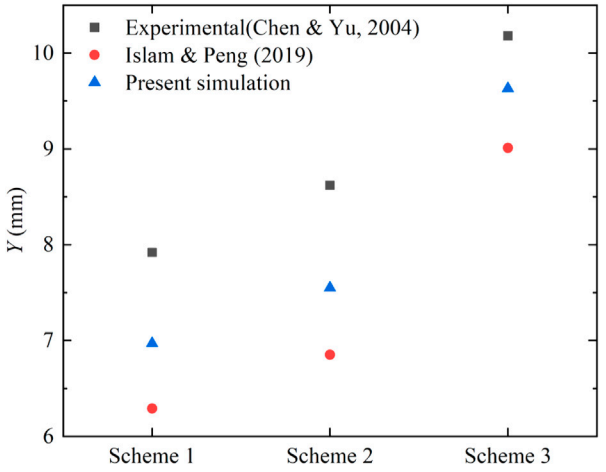

FIGURE 4
Comparison of deflection of present simulation with the experimental (Chen and Yu, 2004) and simulation (Islam and Peng, 2019) results.

and the first Piola-Kirchhoff stress tensor is calculated from the constitutive law with the deformation tensor $\mathbf{F}$, which links initial and current configuration is defined as

$$\mathbf{F} = \left(\sum_j V_j \left(\mathbf{s}_j - \mathbf{s}_i \right) \otimes \nabla_i^0 W_{ij} \right) \mathbf{B}_i^0 + \mathbf{I} \tag{13}$$

Coupling scheme of WC-TLSPH

In the FSI framework, the force of the solid structure on the fluid needs to be considered, so the governing equations of fluid dynamics are expressed as

$$\begin{cases} \dfrac{\mathrm{d}\rho_i}{\mathrm{d}t} = 2\rho_i \sum_j \dfrac{m_j}{\rho_j} \left(U^\star - \mathbf{v}_i \mathbf{e}_{ij} \right) \dfrac{\partial W_{ij}}{\partial r_{ij}} \\ \dfrac{\mathrm{d}\mathbf{v}_i}{\mathrm{d}t} = -2 \sum_j m_j \dfrac{P^\star}{\rho_i \rho_j} \nabla_i W_{ij} + \mathbf{g} + \mathbf{f}_i^{S:\,p} + \mathbf{f}_i^{S:\,v} \end{cases} \tag{14}$$

where $\mathbf{f}_i^{S:\,p}$ and $\mathbf{f}_i^{S:\,v}$ are the pressure and viscous forces exerted by solid structure on fluid particle, respectively. Similarly, the discretization of the solid dynamics equation is modified as

$$\begin{cases} \rho_a = \rho_0 \dfrac{1}{\det(\mathbf{F})} \\ \dfrac{\mathrm{d}\mathbf{v}_a}{\mathrm{d}t} = \dfrac{2}{m_a} \sum_b V_a V_b \tilde{\mathbf{P}}_{ab} \nabla_a^0 W_{ab} + \mathbf{g} + \mathbf{f}_a^{F:\,p} + \mathbf{f}_a^{F:\,v} \end{cases} \tag{15}$$

also $\mathbf{f}_a^{F:\,p}$ and $\mathbf{f}_a^{F:\,v}$ are the fluid pressure and viscous forces acting on the solid particle, respectively. Figure 1 specifies the details of the WC-TLSPH scheme.

In FSI, the surrounding solid structure is behaving as a moving boundary of the fluid, while no-slip boundary condition is imposed at the fluid-structure interface (Zhang et al., 2021a). The solid forces $\mathbf{f}_i^{S:\,p}$ and $\mathbf{f}_i^{S:\,v}$ acting on fluid of Eq. 14 can be calculated by

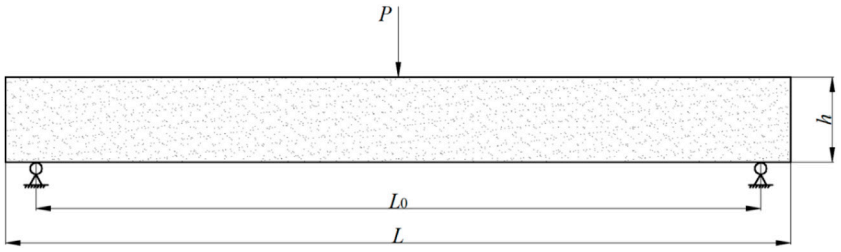

FIGURE 5
Schematic diagram of three-point bending test of ice beam.

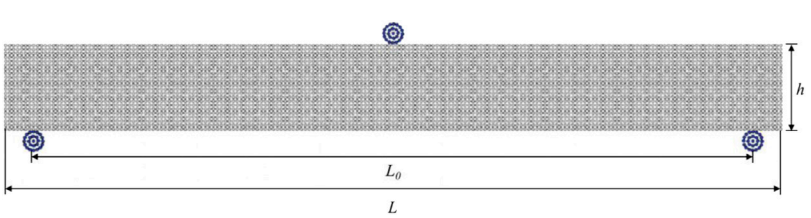

FIGURE 6
Particle model of three-point bending test of ice beam.

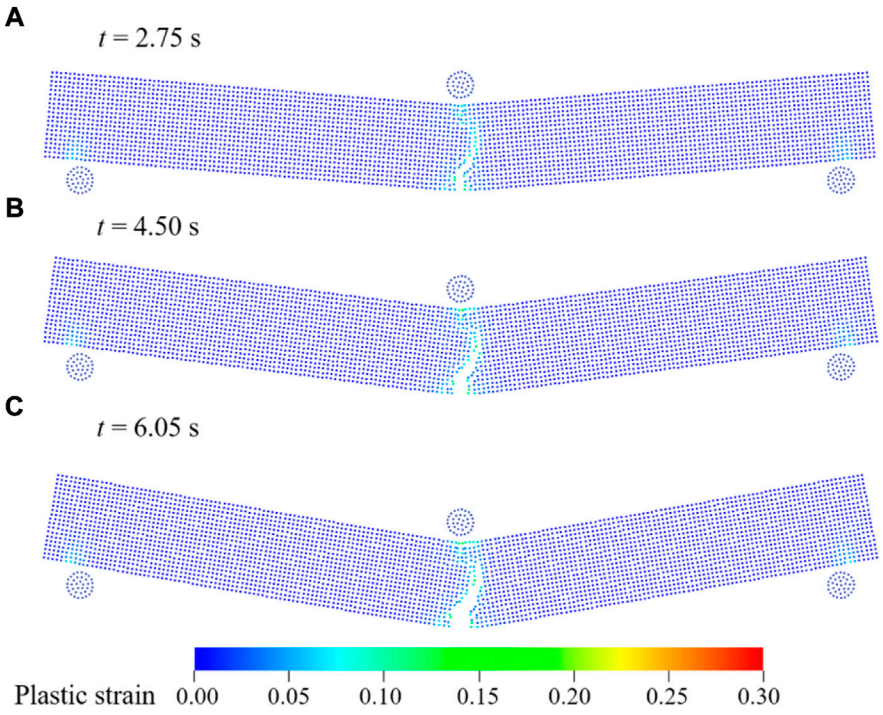

FIGURE 7
Snapshots of the ice beam in three-point bending experiment by SPH at **(A)** t = 2.75s, **(B)** t = 4.50s and **(C)** t = 6.05s.

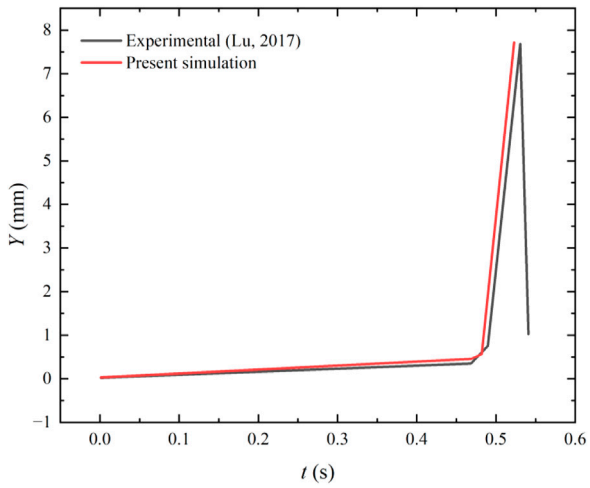

FIGURE 8
Comparison of deflection of present simulation with the experimental (Lu, 2017) results.

TABLE 3 The system and discretization parameters.

Parameters	Value (m)
Water length (L)	0.146
Water height ($2L$)	0.292
Baffle length (l)	0.012
Baffle height (h)	0.080
Box length	0.584
Box height	0.600
Particle spacing	0.0025

$$\mathbf{f}_i^{S:\,p} = -2\sum_a V_i V_a \frac{p_i \rho_a^d + p_a^d \rho_i}{\rho_i + \rho_a^d} \nabla_i W(\mathbf{r}_{ia}, h) \tag{16}$$

$$\mathbf{f}_i^{S:\,v} = 2\sum_a \eta V_i V_a \frac{\mathbf{v}_i - \mathbf{v}_a^d}{|\mathbf{r}_{ia}| + 0.01h} \frac{\partial W(\mathbf{r}_{ia}, h)}{\partial r_{ia}} \tag{17}$$

where the imaginary particle density ρ_a^d is calculated through the EoS presented in Eq. 2, the coefficient of η is relative with the fluid viscosity, the imaginary pressure p_a^d and velocity $\mathbf{v}_a^d$ are calculated by

$$p_a^d = p_i + \rho_i \max\left(0, \left(\mathbf{g} - \frac{\mathrm{d}\mathbf{v}_a}{\mathrm{d}t}\right) \cdot \mathbf{n}^S\right)(\mathbf{r}_{ia} \cdot \mathbf{n}^S) \tag{18}$$

$$\mathbf{v}_a^d = 2\mathbf{v}_i - \mathbf{v}_a \tag{19}$$

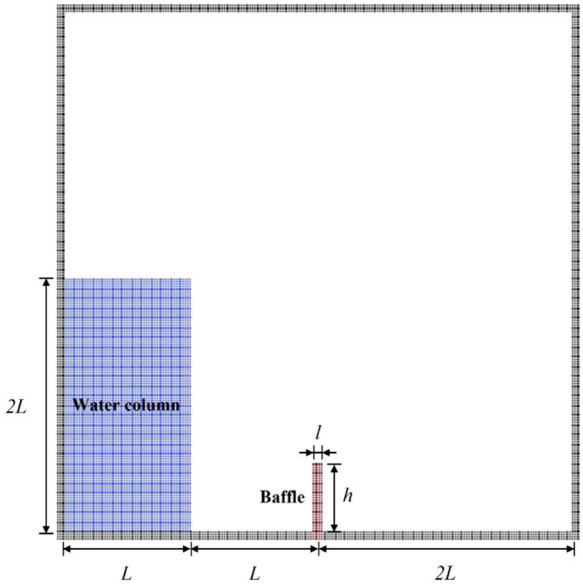

FIGURE 9
The initial configuration of the model: breaking dam on a baffle.

where $\mathbf{n}^S$ denotes the surface normal direction of the solid structure. Similarly, the interaction forces $\mathbf{f}_a^{F:\,p}$ and $\mathbf{f}_a^{F:\,v}$ acting on a solid particle a are given by

$$\mathbf{f}_a^{F:\,p} = -2\sum_i V_a V_i \frac{p_a^d \rho_i + p_i \rho_a^d}{\rho_i + \rho_a^d} \nabla_a W(\mathbf{r}_{ai}, h) \tag{20}$$

$$\mathbf{f}_a^{F:\,v} = 2\sum_i \eta V_a V_i \frac{\mathbf{v}_a^d - \mathbf{v}_i}{|\mathbf{r}_{ai}| + 0.01h} \frac{\partial W(\mathbf{r}_{ai}, h)}{\partial r_{ai}} \tag{21}$$

In order to ensure momentum conservation and force-calculation matching of FSI, a single time step

$$\Delta t = \min\left(0.25\min\left(\frac{h}{c^F + |\mathbf{v}|_{\max}}, \frac{h^2}{\eta}\right), 0.6\min\left(\frac{h}{c^S + |\mathbf{v}|_{\max}}, \sqrt{\frac{h}{\left|\frac{d\mathbf{v}}{dt}\right|_{\max}}}\right)\right) \tag{22}$$

is commonly used, where c^F and c^S are the sound speed of fluid and solid, respectively. However, this may lead to low computational efficiency since a very small time-step will be chosen when the sound speed of the solid structure is significantly larger than that of the fluid.

Fracture model for TLSPH

As discussed in the previous part, the TLSPH method applies the initial reference configuration for constructing particle configuration, including particle neighbor search and calculation of kernel function and its gradient, and keep it unaltered during the simulation. Therefore, additional treatment is necessary when applying TLSPH to resolve the fracture problem in solid mechanics.

Considering that the particle interaction in the SPH method is determined by the kernel function, the strength of the particle interaction can be adjusted by introducing a damage factor to the kernel function. Then, the material fracture can be resolved by adopting the damage factor according to fracture rule as pointed out by Islam and Peng (2019). The specific calculation process can be achieved through the following steps: firstly, establishing a virtual chain between the interacting particles. Here, the function of the virtual chain is to store the strength of particle interaction without providing any additional stiffness. Secondly, introducing the particle damage factor D to define the damage degree of material particles according to the plastic strain as

$$D = \begin{cases} 1, & \varepsilon_{pl} \geq (\varepsilon_{pl})_{\max} \\ 0, & \text{otherwise} \end{cases} \tag{23}$$

where $(\varepsilon_{pl})_{max}$ is the maximum plastic strain of the material and determined by its mechanical property. Finally, calculate the interparticle damage factor $f_{ij} = 1 - D_{ij}$ to modify the kernel function and its gradient of the particle at the fracture. According to the formula, when $f_{ij} = 1$ the virtual chain between particles is not destroyed, and when $0 < f_{ij} < 1$ the virtual chain is partially destroyed, while when $f_{ij} = 0$ the virtual chain is completely destroyed. Then the momentum conservation equation in the TLSPH formulation can be rewritten as

$$\frac{d\mathbf{v}_i}{dt} = \frac{2}{m_i}\sum_{j\in N_U^i} V_i V_j \tilde{\mathbf{P}}_{ij} \nabla_i^0 W_{ij} + \frac{2}{m_i}\sum_{j\in N_D^i} V_i V_j \tilde{\mathbf{P}}_{ij} f_{ij} \nabla_i^0 W_{ij} \tag{24}$$

where N_U^i and N_D^i are the sets of neighboring particles connected to the particle i through the undamaged and damaged virtual chains, respectively.

Model validation and application

In this section, the adopted fractural model for the TLSPH method is first validated by two benchmark tests, *viz.* crack propagation in notched beam and three-point bending of ice beam. Then, a test of dam break flow impacting on a structure with and without fractural model is investigated to study the accuracy, robustness and versatility of the proposed coupled WC-TLSPH method.

Fast-loading case crack propagation in notched beam

The fast-loading fracture case is firstly verified by considering a projectile impacting aluminum beam, as shown in Figure 2, where experimental data of Chen and Yu (2004) and numerical results of Islam and Peng (2019) are available for quantitative comparison.

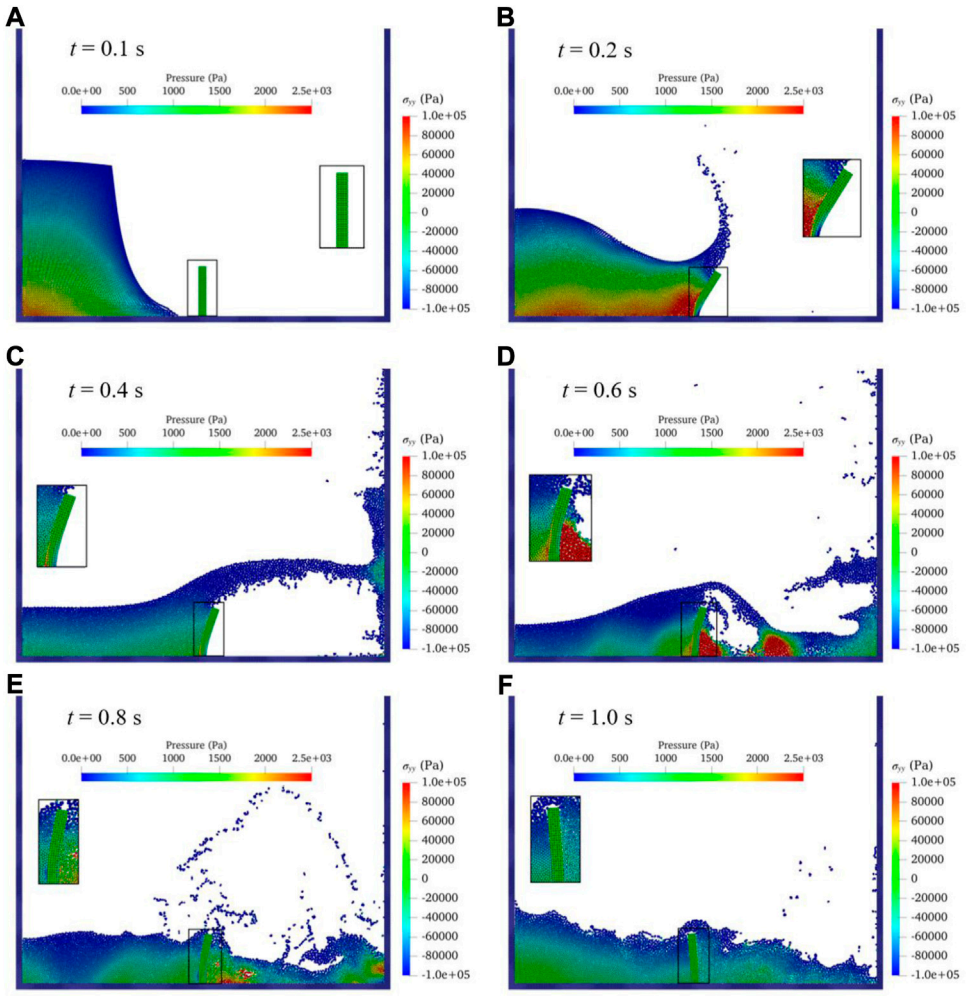

FIGURE 10
Contours of water pressure, surface profile and σ_{yy} of elastic baffle at **(A)** t = 0.1s, **(B)** t = 0.2s, **(C)** t = 0.4s, **(D)** t = 0.6s, **(E)** t = 0.8s and **(F)** t = 1.0s.

Following Chen and Yu (2004), the size of the aluminum beam is 142.24 × 6.35 mm and the I-type notch or II-type notch (the I-type notch is of 2.12 mm high and 0.8 mm wide, and the II-type notch is of 2.12 mm high and 1.5 mm wide) is preset in the middle and with fixed constraints being imposed on both ends.

The material properties of the aluminum beam are given in Table 1. The aluminum beam was impacted with a projectile to study the deformation and fracture phenomena of the aluminum beam. Note that the size of the projectile is of 50.00 × 14.74 mm.

Also, the simulation scheme sets four working conditions according to the literature and the detailed parameters are shown in Table 2.

To discretize the system, the particle spacing is set to 0.423 mm and the total number of particles is 12,906 including 8,894 particles for aluminum beam and 4,012 particles for projectile. The von Mises criterion is selected for the yield criterion, defined as $y_f = \sqrt{J_2} - \sigma_y/\sqrt{3}$, where σ_y is the yield stress of material and J_2 is the second invariant of the deviatoric stress tensor. According to the criterion, when $y_f \leq 0$ the material is in the elastic stage, and when $y_f > 0$ the material enters the plastic stage. And the plastic hardening model (Simo and Hughes, 2006) is applied to the constitutive model.

The simulation results are shown in Figure 3. The first column is the experimental results of Chen and Yu (2004), the second is the simulation results of Islam and Peng (2019) and the third is the present simulation. Under the four different initial impact velocities, the present model can better reflect the bending and fracture of the aluminum beam in comparison with those of Islam and Peng (2019). From the perspective of plastic strain distribution, the present results and those of Islam and Peng's (2019) show the same law. However, there are discrepancies can be noted, *e.g.* the present results show the plastic strain at middle part of the aluminum beam is slightly smaller than the results of Islam and Peng (2019) when the aluminum beam is not broken, but significantly larger than the results of Islam and Peng

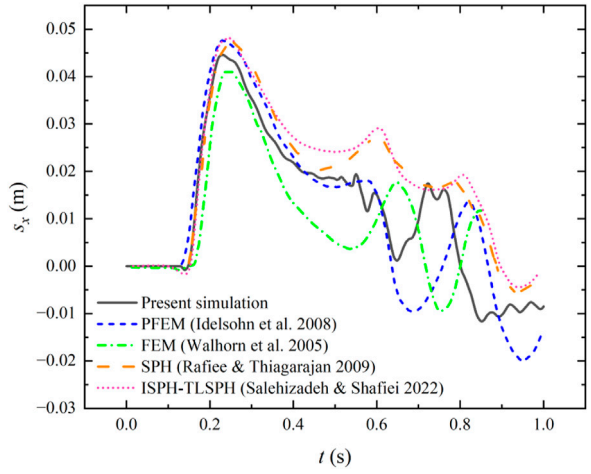

FIGURE 11
The time history of horizontal displacement of the upper left corner of the elastic baffle.

(2019) after the aluminum beam breaks. The reason for this phenomenon may be due to that the choice of different material constitutive model in the simulation.

In Figure 4, the present results are compared with the experimental observation of the deflection in *Y*-axis of the aluminum beam in Schemes 1-3. It can be seen from the results that the present results have a good agreement with the experimental results under different initial impact velocities. Quantitatively, the relative errors in the 3 schemes of present simulation are 11.99, 12.41 and 5.40%, respectively.

Slow-loading case three-point bending of ice beam

The slow-loading fracture case is verified by considering a three-point bending an ice beam, which is also studied by Lu (2017). The initial configuration is shown in Figure 5 where the size of the simply supported ice beam is 650 mm × 70 mm and the distance between the fixed ends on both sides 600 mm. Also, the loading speed of the point pressure is 0.763 mm/s.

To discretize the system as show in Figure 6, the particle spacing is set to Δx = 3.5 mm, resulting a total number of 3,720 particles. The plastic hardening constitutive model and the von Mises yield criterion are also applied herein. The mechanical properties of the ice material refer to Lu's work (Lu, 2017) where the density ρ = 896.977 kg/m^3, the elastic modulus E = 6.81 GPa and the Poisson's ratio υ = 0.33. The CPU time on an Intel(R) Xeon(R) Gold 6136 CPU @ 3.00 GHz computer are 7.06 h for 22,600,000 computational steps to simulate a physical process of 10 s.

Figure 7 shows the present results of the crack and its propagation during the loading process with the particles colored by the plastic strain contour. At t = 2.75 s, obvious cracks can be observed. At the same time, pronounced strain aera appear at the support of the beam and the compression and tension areas of the loader. As the loading process continues, the cracks gradually expand meanwhile the range of strain aera also increases slightly. When the time reaches t = 6.05 s, the crack expands to a certain extent and an obvious fracture surface appears, noting the increase of strain at the fracture. The present results herein show the same trend as those of Zhang et al. (2019), including the fracture degree and fracture location of the ice beam at each frame. However, detailed comparison is not conducted in this paper due to the slight differences in the model parameters.

In order to verify the accuracy of the present results under slow-loading, the deflection at the midpoint of the ice beam is compared with the experimental data in the literature (Lu, 2017) in Figure 8 where the deflection is represented by *Y*. The simulation results tend to be consistent with the experimental results. Before fracture, the deflection increases linearly with time. At t = 0.49 s, the ice beam breaks and the deflection increases significantly. However, the simulation results show a slightly larger deflection than the experimental data, and meanwhile fracture is also advanced probably because the maximum plastic strain $(\varepsilon_{pl})_{max}$ chosen in the simulation process is slightly different from the actual situation of the ice material.

FSI case breaking dam on an elastic/elastoplastic baffle

In this section, the case of breaking dam impacting on an elastic/elastoplastic baffle, in which a column of water collapses and influences on an elastic or elastoplastic baffle, is established to study the difference and response of elastic and elastoplastic materials under the impacting load of water flow. As shown in Figure 9, a column of water confined at the left end of the container is initially in hydrostatic equilibrium state and an elastic/elastoplastic baffle is attached to the bottom of the tank with one end free. The parameters of this test case are listed in Table 3.

The initial density of water and the baffle are set to 1,000 kg/m^3 and 2,500 kg/m^3, respectively. Other parameters for the baffle are Young's modulus E = 1.0 MPa and Poisson ratio υ = 0. The elastic baffle is modeled using the linear elastic constitutive model and the elastoplastic baffle using the plastic hardening constitutive model. In addition, in simulating the deformation and failure process of elastoplastic baffle, the von Mises yield criterion is also applied and the fracture model established in this paper is coupled. The convergence analysis of the model is shown in

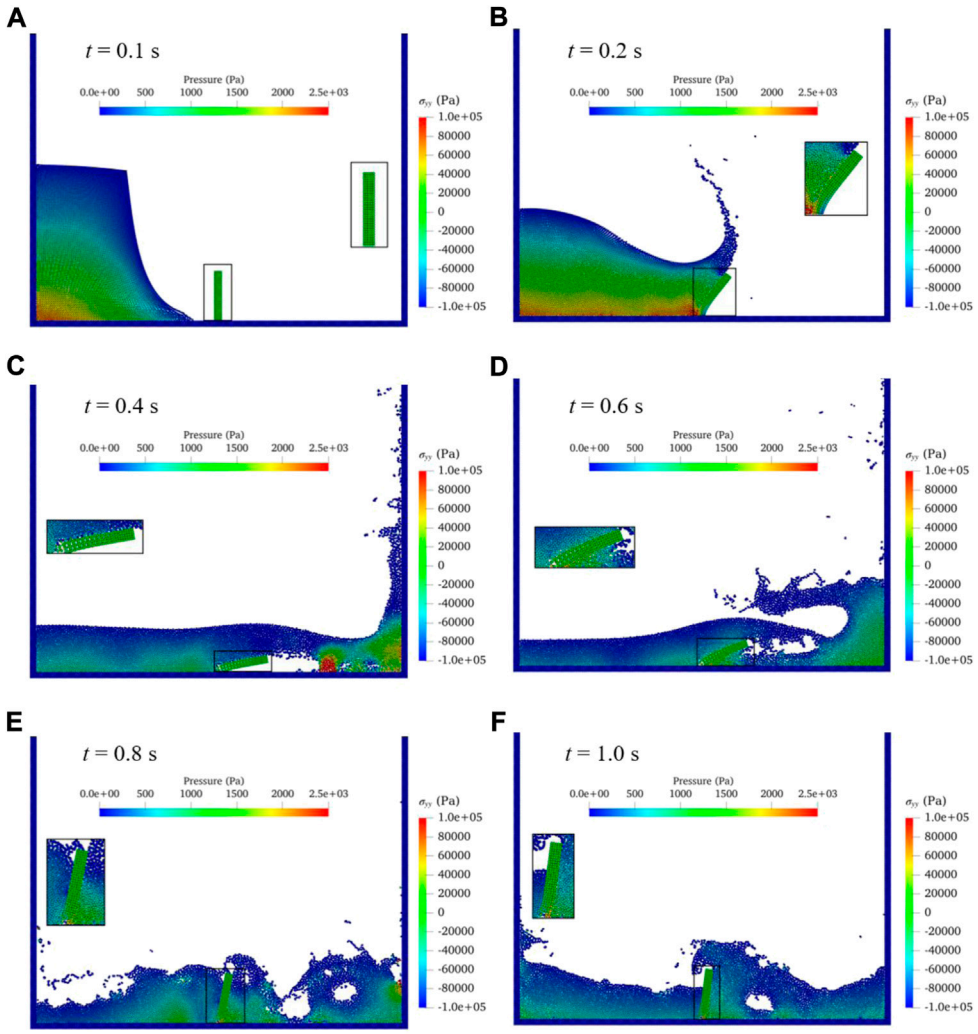

FIGURE 12
Contours of water pressure, surface profile and σ_{yy} of elastoplastic baffle at **(A)** t = 0.1s, **(B)** t = 0.2s, **(C)** t = 0.4s, **(D)** t = 0.6s, **(E)** t = 0.8s and **(F)** t = 1.0s.

the Appendix. The particle spacing is set to Δx = 2.5mm, resulting a total number of 10,820 particles are used in the simulation, including 6,785 fluid particles, 3,855 boundary particles and 180 solid particles. The CPU time on an 11th Gen Intel(R) Core (TM) i9-11900K @ 3.50 GHz computer are 2.78 min for 26,100 computational steps to simulate a physical process of 10.0 s.

The free-surface profile with pressure contour and the deformed configuration of the elastic baffle are shown in Figure 10A, corresponding to the flow state at t = 0.1s, t = 0.2s, t = 0.4s, t = 0.6s, t = 0.8s and t = 1.0s, respectively. Also, the figure shows a partial enlarged view of the distributions of stress component on the y-axis σ_{yy} in the elastic baffle. As the water column is released, the water naturally flows with gravity. Before reaching the elastic baffle, its pressure distribution conforms to the pressure distribution law of normal water flow, *viz.* the pressure is the largest at the lower left corner. When the water flow reaches the position of the elastic baffle and interacts with the elastic baffle at t = 0.2s, the falling water flow makes the elastic baffle tilt to the right and generates a large stress at the root of the elastic baffle, and the water pressure is also close to the maximum value at the position of the elastic baffle reaches. Then the water flow passes over the elastic baffle and the deformation of the elastic plate gradually recovers, imposing an ejection effect on the water flow. With the weakening of the energy of water flow and elastic baffle, the water pressure gradually tends to the distribution of the hydrostatic pressure, and the elastic baffle gradually returns to the initial state. The simulation results of the above part are in good agreement

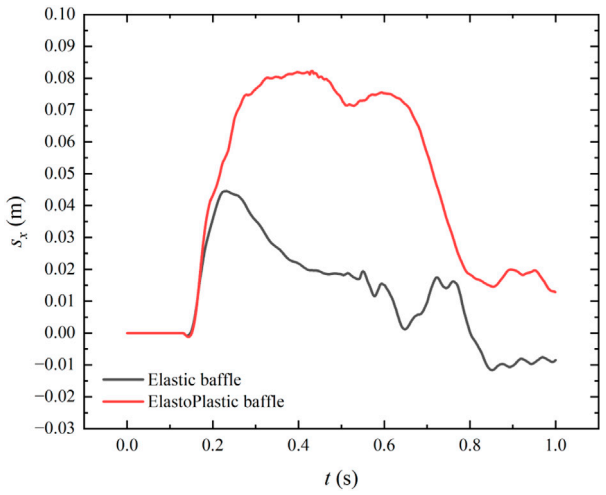

FIGURE 13
The time history of horizontal displacement of the upper left corner of the elastic/elastoplastic baffle.

with the simulation results of Zhan et al (2019) which presents the same study in three-dimensional using a stabilized TL–WCSPH approach with GPU acceleration.

Figure11 shows the time history of horizontal displacement of the upper left corner of the elastic baffle where horizontal displacement is represented by s_x. Several simulation results of PFEM (Idelsohn et al., 2008), FEM (Walhorn et al., 2005), SPH (Rafiee and Thiagarajan, 2009) and incompressible SPH (ISPH) -TLSPH (Salehizadeh and Shafiei, 2022) from literature are also given for comparison. It can be seen from the figure that the maximum displacement time of the elastic baffle in this paper is similar to the simulation results in the literatures, and the amplitude and frequency of the elastic baffle oscillation show basically the same trend as those in the literature and the present results is within the range of the above literature results. In addition, it can be seen that the simulation in this paper can better reflect the motion details of the elastic baffle.

Through the above analysis, the present WC-TLSPH has good accuracy in FSI simulation, and the fracture model based on TLSPH can simulate the fracture process of the material well. Therefore, it can also corroborate the WC-TLSPH model coupled with fracture model to simulate the failure process of the structure in the FSI.

Figure 12 shows the free-surface profile with water pressure contour and the deformation of the elastoplastic baffle, (a)-(f) corresponding to the flow state at t = 0.1s, t = 0.2s, t = 0.4s, t = 0.6s, t = 0.8s and t = 1.0s respectively. The figure also shows a partial enlarged view of the distributions of stress σ_{yy} in the elastoplastic baffle. As the water column is released, the water naturally flows with gravity. Before reaching the elastoplastic baffle, its pressure exhibits the same distribution as in the elastic baffle case. When the water flow reaches the position of the elastoplastic baffle, the baffle is tilted to the right significantly more than the elastic baffle, at t = 0.4s, the impact of the downward water flow causes obvious plastic damage to the root of the elastoplastic baffle. Compared with the elastic baffle, in this case, the baffle has lost the ability to rebound and eject the water, so the concentration point of the water pressure is mainly at the drop of the water flow. Then, with the backflow generated after the water flow reaches the right boundary, the displacement of the baffle gradually recovers. However, the connection between the baffle root and the boundary tends to be destroyed completely, leading to the lack of restraint at the root, the baffle basically does not have obvious deformation, which is closely related to the water flow. The interaction with the water flow is also mainly reflected in the buoyancy effect of the water flow on the baffle, and the pressure distribution of the water flow basically shows the distribution characteristics of the hydrostatic pressure.

Figure13 shows the time history of horizontal displacement of the upper left corner of the elastic baffle and elastoplastic baffle. It can be seen that before t = 0.18 s, *i.e.*, before the elastoplastic baffle reaches the plastic state, the displacement of the baffle in the two cases shows the same tendency, and then is significantly larger than that of the elastic baffle, although there is a lack of experimental data verification, from a qualitative point of view this is also in line with the common sense. In addition, compared with the displacement change of the elastic baffle, another significant difference in the displacement of the elastoplastic baffle is the lack of reciprocating motion in the displacement due to the lack of rebound effect.

Through the above comparative analysis, the method used in this paper can accurately simulate the deformation and failure process of the structure in FSI. Although the verification of experimental data is lacking in this process, combined with previous research experience, the simulation results of the flow process and pressure distribution of the water flow, as well as the stress distribution and movement trend of the baffle plate have good accuracy.

Conclusion

Based on the WC-TLSPH model in the SPHinXsys library, a fracture model is established to simulate the failure process of the structure in FSI. The fluid phase was simulated by the WCSPH method, the solid phase was simulated by the TLSPH method to reduce the influence of tensile instability, the fracture of the material was achieved by introducing a damage factor for kernel function correction. By comparing the numerical results of the fast-loading case of crack propagation in notched beam and the slow-loading case

of three-point bending of ice beam with the experimental data in the literature, the accuracy of the simulation results of the fracture model in different working conditions is verified respectively. The comparison with literature data demonstrates the accuracy and robustness of the WC-TLSPH model in FSI simulations. The above model verification can also corroborate the simulation results of the breaking dam on an elastoplastic baffle to a certain extent. The results show that the method of introducing the damage factor to modify kernel function can well realize the fracture model based on TLSPH, which solves the problem that TLSPH cannot simulate the fracture process naturally. The coupling of the WC-TLSPH model and the fracture model can simulate the fracture process of the structure in the case of FSI well and provide a certain reference for practical engineering applications.

This might be the first time that SPHinXsys is used for fracture of solid structures and there is no quantitative data of physical experiment for a comparison, so the depth of study is still relatively shallow. In the manuscript we tried to provide a few quantitative validations, but it seems quite insufficient. A series of more challenging benchmark tests are being carried out now and will be presented in future work.

Data availability statement

The raw data supporting the conclusions of this article will be made available by the authors, without undue reservation.

Author contributions

HW: methodology, simulation, visualization, validation, analysis, and writing—original draft. SG: supervision, conceptualization, management, and writing—review and editing. LT: investigation and writing—review and editing. JL: investigation and writing—review and editing. CC: investigation and writing—review and editing. CZ: supervision, conceptualization, management, and writing—review and editing. All authors contributed to the article and approved the submitted version.

Funding

This research work is supported by the National Natural Science Foundation of China (no. 51869025), Youth Scientific Research Fund Project of Qinghai University (no. 2022-QGY-9) and Guangdong Basic and Applied Basic Research Foundation (no. 2021A1515110768).

Acknowledgments

Author HW acknowledges the support of Professor Songdong Shao at Dongguan University of Technology and all the developers of SPHinXsys. We all acknowledge the Frontier Editorial Team for their professional handling of the manuscript and dedicated referees who provided very constructive and insightful comments to significantly improve the quality of the work.

Conflict of interest

The authors declare that the research was conducted in the absence of any commercial or financial relationships that could be construed as a potential conflict of interest.

Publisher's note

References

Belytschko, T., Guo, Y., Kam Liu, W., and Ping Xiao, S. (2000). A unified stability analysis of meshless particle methods. *Int. J. Numer. Methods Eng.* 48 (9), 1359–1400. doi:10.1002/1097-0207(20000730)48:9<1359::AID-NME829>3.0.CO;2-U

Bui, H. H., Fukagawa, R., Sako, K., and Ohno, S. (2008). Lagrangian meshfree particles method (SPH) for large deformation and failure flows of geomaterial using elastic–plastic soil constitutive model. *Int. J. Numer. Anal. Methods Geomech.* 32 (12), 1537–1570. doi:10.1002/nag.688

Chen, F., and Yu, T. (2004). An experimental study of pre-notched clamped beams under impact loading. *Int. J. solids Struct.* 41 (24-25), 6699–6724. doi:10.1016/j.ijsolstr.2004.05.036

Gabreil, E., Wu, H., Chen, C., Li, J., Rubinato, M., Zheng, X., et al. (2022). Three-dimensional smoothed particle hydrodynamics modeling of near-shore current flows over rough topographic surface. *Front. Mar. Sci.* 9, 935098. doi:10.3389/fmars.2022.935098

Gray, J. P., Monaghan, J. J., and Swift, R. P. (2001). SPH elastic dynamics. *Comput. Methods Appl. Mech. Eng.* 190 (49), 6641–6662. doi:10.1016/S0045-7825(01)00254-7

Gu, S., Zheng, W., Wu, H., Chen, C., and Shao, S. (2022). DualSPHysics simulations of spillway hydraulics: A comparison between single- and two-phase modelling approaches. *J. Hydraulic Res.* 60 (5), 835–852. doi:10.1080/00221686.2022.2064343

He, J., Tofighi, N., Yildiz, M., Lei, J., and Suleman, A. (2017). A coupled WC-TL SPH method for simulation of hydroelastic problems. *Int. J. Comput. Fluid Dyn.* 31 (3), 174–187. doi:10.1080/10618562.2017.1324149

Idelsohn, S. R., Marti, J., Limache, A., and Oñate, E. (2008). Unified Lagrangian formulation for elastic solids and incompressible fluids: Application to fluid–structure interaction problems via the PFEM. *Comput. Methods Appl. Mech. Eng.* 197 (19-20), 1762–1776. doi:10.1016/j.cma.2007.06.004

Islam, M. R. I., and Peng, C. (2019). A Total Lagrangian SPH method for modelling damage and failure in solids. *Int. J. Mech. Sci.* 157-158, 498–511. doi:10.1016/j.ijmecsci.2019.05.003

Johnson, G. R., and Beissel, S. R. (1996). Normalized smoothing functions for SPH impact computations. *Int. J. Numer. Methods Eng.* 39, 27252–27419. doi:10.1002/(SICI)1097-0207(19960830)39:16<2725::AID-NME973>3.0

Lu, W. (2017). The Study of the numerical simulation Method of peridynamic Based on the bending Fracture of sea ice master. China: Harbin Engineering University. Thesis.

Lv, X., Zhao, Y., Huang, X. Y., Xia, G. H., and Su, X. H. (2007). A matrix-free implicit unstructured multigrid finite volume method for simulating structural dynamics and fluid–structure interaction. *J. Comput. Phys.* 225 (1), 120–144. doi:10.1016/j.jcp.2006.11.023

Mitra, S., and Sinhamahapatra, K. P. (2008). 2D simulation of fluid-structure interaction using finite element method. *Finite Elem. Analysis Des.* 45 (1), 52–59. doi:10.1016/j.finel.2008.07.006

Monaghan, J. J. (1992). Smoothed particle hydrodynamics. *Annu. Rev. Astron. Astrophys.* 30, 543–574. doi:10.1146/annurev.aa.30.090192.002551

Morris, J. P., Fox, P. J., and Zhu, Y. (1997). Modeling low Reynolds number incompressible flows using SPH. *J. Comput. Phys.* 136 (1), 214–226. doi:10.1006/jcph.1997.5776

Rafiee, A., and Thiagarajan, K. P. (2009). An SPH projection method for simulating fluid-hypoelastic structure interaction. *Comput. Methods Appl. Mech. Eng.* 198 (33-36), 2785–2795. doi:10.1016/j.cma.2009.04.001

Salehizadeh, A. M., and Shafiei, A. R. (2022). A coupled ISPH-TLSPH method for simulating fluid-elastic structure interaction problems. *J. Mar. Sci. Appl.* 21 (1), 15–36. doi:10.1007/s11804-022-00260-3

Sarrate, J., Huerta, A., and Donea, J. (2001). Arbitrary Lagrangian–Eulerian formulation for fluid–rigid body interaction. *Comput. Methods Appl. Mech. Eng.* 190 (24), 3171–3188. doi:10.1016/S0045-7825(00)00387-X

Shi, H., Si, P., Dong, P., and Yu, X. (2019). A two-phase SPH model for massive sediment motion in free surface flows. *Adv. Water Resour.* 129, 80–98. doi:10.1016/j.advwatres.2019.05.006

Shi, H., Yu, X., and Dalrymple, R. A. (2017). Development of a two-phase SPH model for sediment laden flows. *Comput. Phys. Commun.* 221, 259–272. doi:10.1016/j.cpc.2017.08.024

Simo, J. C., and Hughes, T. J. (2006). *Computational inelasticity*, New York: Springer Science & Business Media.

Sugiyama, K., Ii, S., Takeuchi, S., Takagi, S., and Matsumoto, Y. (2011). A full Eulerian finite difference approach for solving fluid-structure coupling problems. *J. Comput. Phys.* 230 (3), 596–627. doi:10.1016/j.jcp.2010.09.032

Walhorn, E., Kölke, A., Hübner, B., and Dinkler, D. (2005). Fluid–structure coupling within a monolithic model involving free surface flows. *Comput. Struct.* 83 (25-26), 2100–2111. doi:10.1016/j.compstruc.2005.03.010

Zhan, L., Peng, C., Zhang, B., and Wu, W. (2019). A stabilized TL–WC SPH approach with GPU acceleration for three-dimensional fluid–structure interaction. *J. Fluids Struct.* 86, 329–353. doi:10.1016/j.jfluidstructs.2019.02.002

Zhang, C., Hu, X., and Adams, N. A. (2017a). A weakly compressible SPH method based on a low-dissipation Riemann solver. *J. Comput. Phys.* 335, 605–620. doi:10.1016/j.jcp.2017.01.027

Zhang, C., Hu, X. Y., and Adams, N. A. (2017b). A generalized transport-velocity formulation for smoothed particle hydrodynamics. *J. Comput. Phys.* 337, 216–232. doi:10.1016/j.jcp.2017.02.016

Zhang, C., Rezavand, M., and Hu, X. (2021a). A multi-resolution SPH method for fluid-structure interactions. *J. Comput. Phys.* 429, 110028. doi:10.1016/j.jcp.2020.110028

Zhang, C., Rezavand, M., Zhu, Y., Yu, Y., Wu, D., Zhang, W., et al. (2021b). SPHinXsys: An open-source multi-physics and multi-resolution library based on smoothed particle hydrodynamics. *Comput. Phys. Commun.* 267, 108066. doi:10.1016/j.cpc.2021.108066

Zhang, C., Wei, Y., Dias, F., and Hu, X. (2021c). An efficient fully Lagrangian solver for modeling wave interaction with oscillating wave surge converter. *Ocean. Eng.* 236, 109540. doi:10.1016/j.oceaneng.2021.109540

Zhang, C., Zhu, Y., Wu, D., and Hu, X. (2022). Review on smoothed particle hydrodynamics: Methodology development and recent achievement. arXiv preprint arXiv:2205.03074.

Zhang, N., Zheng, X., Ma, Q., and Hu, Z. (2019). A numerical study on ice failure process and ice-ship interactions by Smoothed Particle Hydrodynamics. *Int. J. Nav. Archit. Ocean Eng.* 11 (2), 796–808. doi:10.1016/j.ijnaoe.2019.02.008

Zheng, X., Tian, Z., Xie, Z., and Zhang, N. (2022). Numerical study of the ice breaking resistance of the icebreaker in the yellow river through smoothed-particle hydrodynamics. *J. Mar. Sci. Appl.* 21 (1), 1–14. doi:10.1007/s11804-022-00259-w

Appendix: Convergence analysis

This appendix checks the convergence of WC-TLSPH computation in spatial domain using three different particle sizes, *i.e.*, Δx = 1.5, 2.5, and 3.5 mm, for breaking dam on an elastoplastic baffle. The rest of the model parameters are set the same as the case in the main text. Figure A1 shows that the flow state of the water, the distribution of water pressure, the pouring degree and distributions of stress component on the y-axis σ_{yy} of the elastoplastic baffle are basically the same under three different particle spacings at t = 0.4 s.

Figure A2 reveal a good overlapping behavior of horizontal displacement of the upper left corner of the elastoplastic baffle for the three different particle spacings, indicating the convergence of numerical results.

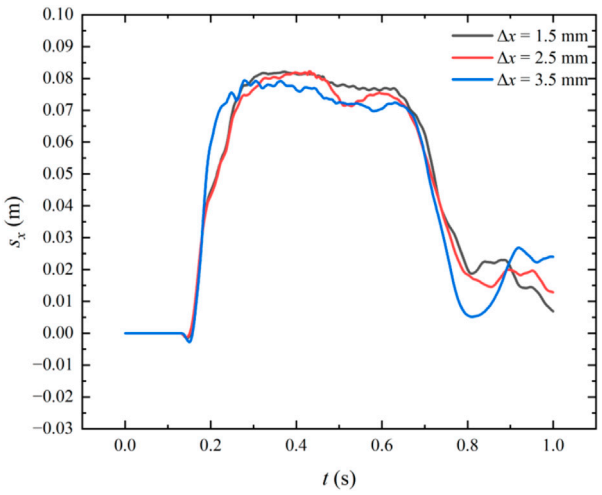

FIGURE A2
The time history of horizontal displacement of the upper left corner of the elastoplastic baffle.

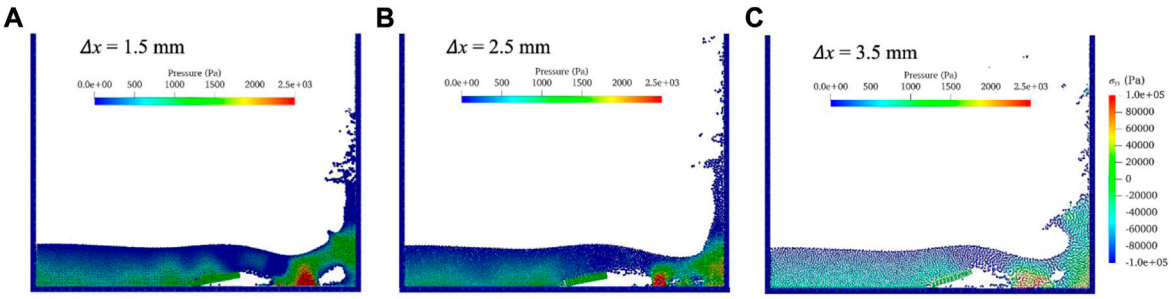

FIGURE A1
Contours of water pressure, surface profile and σ_{yy} of elastoplastic baffle of **(A)** Δx = 1.5 mm, **(B)** Δx = 2.5 mm, **(C)** Δx = 3.5 mm.

frontiers | Frontiers in Environmental Science

TYPE Original Research
PUBLISHED 02 November 2022
DOI 10.3389/fenvs.2022.1051392

OPEN ACCESS

EDITED BY
Biyun Guo,
Zhejiang Ocean University, China

REVIEWED BY
Feng Chen,
Jiangsu Hydraulic Research Institute, China
Jie Wang,
Nanjing University of Information Science and Technology, China

*CORRESPONDENCE
Jiasheng Wang,
wangjs@mail.crsri.cn

SPECIALTY SECTION
This article was submitted to Freshwater Science, a section of the journal Frontiers in Environmental Science

RECEIVED 22 September 2022
ACCEPTED 20 October 2022
PUBLISHED 02 November 2022

CITATION
Liu X, Wang J, Chai Z, Min F, Jiang X, Zhu K and Dai J (2022), New model for predicting terminal settling velocity and drag coefficient of the Oncomelania. *Front. Environ. Sci.* 10:1051392. doi: 10.3389/fenvs.2022.1051392

New model for predicting terminal settling velocity and drag coefficient of the *Oncomelania*

Xiaoguang Liu[1,2], Jiasheng Wang[1,2]*, Zhaohui Chai[1,2], Fengyang Min[1,2], Xi Jiang[3], Kongxian Zhu[1,2] and Juan Dai[1,2]

[1]River Department, Changjiang River Scientific Research Institute, Wuhan, China, [2]Key Laboratory of River and Lake Regulation and Flood Control in the Middle and Lower Reaches of the Yangtze River of Ministry of Water Resources, Changjiang River Scientific Research Institute, Wuhan, China, [3]Institute of Soil and Water Conservation, Northwest A&F University, Xianyang, Shaanxi, China

This paper presents a study of the terminal settling velocity and drag coefficient of the *Oncomelanias* with highly irregular shape in the range of particle Reynolds number ($10 < R_{ep} < 600$). The movement characteristics of the *Oncomelanias* with horizontal and slant postures are revealed using image analysis and wavelet analysis. The shape features of *Oncomelanias* with different dimensions are quantified and formulated. The authors propose a new model for predicting the drag coefficient of the dormant and active *Oncomelanias*, which is proven to be better than several widely-used formulas. Further, a simple settling velocity model that can predict the terminal velocity of the *Oncomelanias* fairly with several easy-to-measure parameters is developed. These findings provide a basis for the further improvement for the hydraulic schistosomiasis control project and supply reference for the settling characteristics and drag coefficient of cone-shaped particles.

KEYWORDS

prediction model, settling velocity, drag coefficient, the *Oncomelania*, settling trajectories

Introduction

Schistosomiasis is a parasitic infectious disease that is harmful to human health and restricts the development of the economy and society. It is prevalent mainly in 73 countries of Asia, Africa, and Latin America, and the number of patients affected is approximately 200 million (Mcmanus et al., 2011). The *Oncomelania* is the only intermediate host of Schistosoma japonicum, and its distribution is consistent with that of S. japonicum. One of the most key issues for schistosomiasis control is the dispersal of the snail intermediate host along rivers and irrigation schemes (Cheng et al., 2016). Thus, the hydraulic schistosomiasis control project can be considered an effective measure to control the epidemic spreading of S. japonicum, one of the keys of which is the physical traits and settling characteristics of the *Oncomelania*.

The settling process of solid particle occurs in many natural and industrial processes, such as the deposition of hydrochorous seeds and fish eggs (Jia et al., 2020; Liu et al., 2018; Zhu et al., 2017), transportation of drilling cuttings and fracturing proppants (Chien, 1994), chemical and powder processing (Chhabra and Richardson, 2011), alluvial channel (Hvitved-Jacobsen et al., 1998), and pipeline transportation of mining and coal particles (Delleur, 2001).

Although the settlement of the sphere is the basis of all settlement issues in practical applications, the most commonly encountered particles are non-spherical and the knowledge of drag coefficient and settling velocity for non-spherical particles is of fundamental significance (Song et al., 2017).

The settling mechanism of spherical particle has been deeply investigated. Stokes (1851) presented the standard drag coefficient curves from the experimental data. Meanwhile, Chhabra et al. (1999) developed a terminal velocity prediction model, which was suitable for different particle sizes and fluid characteristics. Barry and Parlange (2018) proposed an expression of drag coefficient for spherical particle, drop, or bubble in an infinite homogeneous liquid. Terminal settling velocity and drag coefficient can be predicted accurately under different Reynolds numbers (Ma et al., 2020; Wang et al., 2020).

However, natural and artificial particles, such as organisms (Chambert and James., 2009), coal (Zhou et al., 2020), pulp (Bhutani and Brito-Parada, 2020), and fiber (Roegiers and Denys, 2019), have different shapes and sizes. Owing to the higher surface area to volume ratio, drag coefficient of the non-spherical particles is greater than those of spherical particles (Wang et al., 2014). The error occurs as the published prediction formula was applied in non-spherical particles (Ren et al., 2011), especially for particles with a high Reynolds number. Yin et al. (2003) studied the movement of columnar particles and revealed that particles will rotate when their pressure centers were inconsistent with the mass center. The flow mechanism of the non-spherical particles has not been fully understood because further research on the measuring devices and methods of particle identification and tracking was needed. Establishing precise prediction models of terminal velocity and drag coefficient for non-spherical particles remains a challenge.

Many different methods described the shape of non-spherical particles, including sphericity, circularity, flatness, and the Corey shape factor. In particular, Dellino et al. (2005) proposed a shape descriptor defined as the ratio between sphericity and circularity, which is suitable for highly irregular pumice particles. These shape factors have been used to understand and formulate the effect of particle shape on the drag better.

Few models for the prediction accuracy of terminal settling velocity and drag coefficient cover the wide range of differences in particle properties with a low prediction inaccuracy. The prediction accuracy of the models was derived for non-spherical particles (Ganser, 1993; Haider and Levenspiel, 1989; Hölzer and Sommerfeld, 2008; Ouchene et al., 2016), using the sphericity as a shape descriptor, was not significantly improved for drinking-water-related granules (Kramer et al., 2021).

In the present study, a comprehensive analytical and experimental investigation on settling process and drag coefficient of highly irregular-shaped *Oncomelania* is conducted, which is a research gap of predicting the drag coefficient and terminal settling velocity of the cone-shaped organism accurately. The settling trajectories of the *Oncomelanias* are extracted using image recognition, and the movement characteristics of the settling process are analyzed. The shape features of the *Oncomelania* are quantified. Finally, the authors develop a drag coefficient model of the *Oncomelania* and propose an explicit expression of the settling velocity.

Settling experiments and shape features

Experiment setup

Settling experiments were carried out in the vertical Plexiglas cylinder with a height of 200 cm and an inner diameter of 30 cm, as shown in Figure 1. All experiments were conducted at atmospheric pressure and at the controlled room temperatures of 17°C–20°C for all the solutions to ensure that the rheological properties of the solutions did not change greatly due to temperature variation. The cylinders were filled with the liquid solution at least 24 h prior to each experimental session to allow the escape of air bubbles.

By testing, different sized *Oncomelanias* can attain equilibrium condition after sinking 50 cm, and the trajectories with terminal settling velocities, including settling trajectories, orientation angle, and settling velocity, are collected and analyzed. The velocity in the vertical direction was obtained by center difference method from three consecutive frames.

After the settling experiment, a MATLAB program was used to analyze the images recorded by the camera to obtain various data. The temporal resolution, which depended on the reciprocal of the camera frame, was 0.04 s.

The MATLAB program can identify the centroid of the *Oncomelania* in each frame, and the movement characteristic values was calculated by center difference method.

$$u_{s,i} = \frac{x_{i+1} - x_{i-1}}{2\Delta t}, \quad w_{s,i} = \frac{y_{i+1} - y_{i-1}}{2\Delta t}, \theta_i = \arctan\left(\left|\frac{y_i - y_{ei}}{x_{ei} - x_i}\right|\right) \tag{1}$$

where $u_{s,i}$ and $w_{s,i}$ were the longitudinal and transversal instantaneous velocity of floating particles, respectively; (x_{i+1}, y_{i+1}) was the centroid coordinate in (i+1)th frame of images; (x_{i-1}, y_{i-1}) was the centroid coordinate in (i-1)th frame of images; (x_{ei}, y_{ei}) was the right endpoint in (i)th frame of images; Δt was the time interval between the two frame; and θ_i was an instantaneous vector angular.

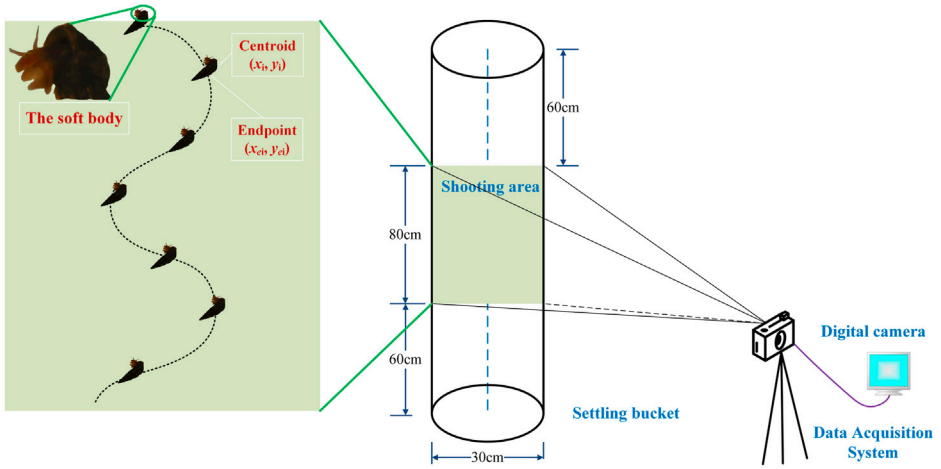

FIGURE 1
Schematic diagram of the experimental set-up and settling trajectory of the *Oncomelania*.

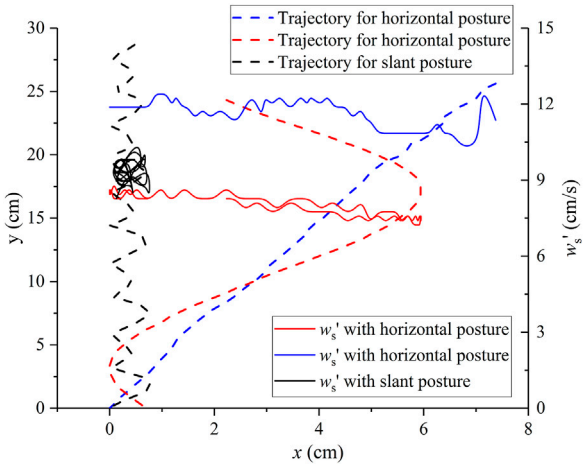

FIGURE 2
Trajectories and w_s' of the *Oncomelania* with horizontal and slant postures.

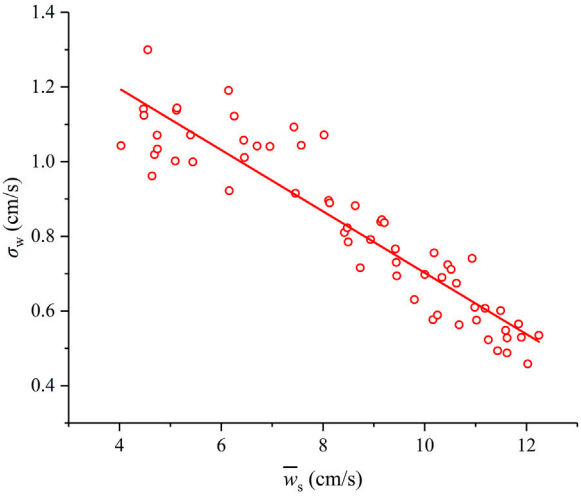

FIGURE 3
The correlation between time-average settling velocity and turbulent intensity.

Trajectory extraction

Owing to the fixed proportional relationship between pixels and actual size, the pixel unit was calibrated in advance. Based on the video image acquisition and coordinate extraction using a MATLAB program, the settling trajectories of the *Oncomelania* can be obtained. The stable settling postures of *Oncomelanias* were independent on the initial posture as water enters, most of samples sink with stable horizontal posture, some samples sink with slant posture first and last to horizontal posture, and others sink with stable slant posture.

As depicted in Figure 2, the red and blue dotted denote the sinking trajectory for the horizontal posture, and the black denotes that for the slant posture. The characteristic of trajectories can be decided by the settling posture, all of the samples sink in helix-type and only have difference in terms of stability and helical diameter. The trajectories of samples sinking with horizontal posture is instable w_s' and have lager helical diameters (twice more than the length of samples), and the trajectories of the samples sinking with slant posture are more stable w_s' and have smaller helical diameter (less than half of the length of samples).

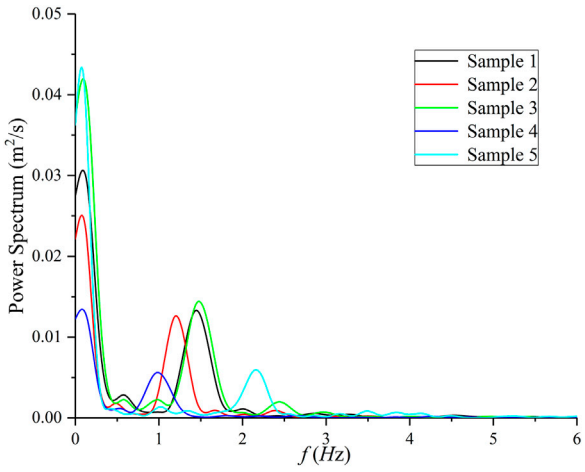

FIGURE 4
The power spectrum distribution of instantaneous settling velocities of five samples.

The vertical time-average velocity and turbulent intensity are defined as

$$\bar{w}_s = \frac{1}{N_d}\sum_{1}^{N_d} w_s' \tag{2}$$

$$\sigma_w = \sqrt{\frac{1}{N_d}\sum_{1}^{N_d}\left(w_s' - \bar{w}_s\right)^2} \tag{3}$$

where N_d is the number of trajectory dots. As shown in Figure 3, σ_w and $\bar{w}_s$ have a significantly negative linear correlation,

$$\sigma_w = -0.0822\bar{w}_s + 1.5244 \tag{4}$$

with the correlation coefficient $R^2 = 0.922$. The variation relationship is in contrast to that of open channel flow, where the turbulent intensity is proportional with discharge and the time-average velocity (Akan and Lyer, 2021). For heavy particles that sink in stable water, the faster the settling velocity, the higher conversion efficiency of gravitational potential energy to kinetic energy.

The power spectrum distribution of instantaneous settling velocities of the five samples is analyzed using wavelet analysis, as shown in Figure 4. Each sample has two peaks, the low-peak indicates the helical sinking process, and the corresponding frequency of different samples are almost same, ranging from 0.12 to 0.13 H_Z. The high-peak indicates the fluctuation around the average, and the lower time-average velocity, the corresponding frequency becomes higher. The settling postures of *Oncomelanias* affect the amplitude of helical trajectories, but have no effect on the frequency of oscillation that only depends on the shape structure of *Oncomelanias*. Analogous to stem-scale turbulence in vegetated open channel flows associated with the diameter of vegetation and flow velocity, the high-peak means the fine-scale disturbance and determined by the physical characteristics and settling velocity of *Oncomelanias*.

Shape features of the *Oncomelania*

In this study, the *Oncomelanias* are sampled from the Jingzhou fragment (the middle reach) of Changjiang River, China, as shown in Figure 5. The *Oncomelania* is amphibian, the young lives in water, and the adult generally lives on bottomland and wetland with rich nutrients. The sampling regions includes typical habitats (lake, bottomland, riverside) in the Yangtze River basin, where different growth state of *Oncomelanias* can be sampled. The shape features of the *Oncomelania* are obtained by the photographs of different angles with image processing using the MATLAB program, which mainly includes preprocessing, binarization, and morphological operation (Brueck and Wildenschild, 2020). The density of the *Oncomelanias* is measured using the Archimedes method.

The body of the *Oncomelania* can be divided into two parts at the maximum diameter, one is half a quasi-spheroid toward the mouth of the *Oncomelania*, and the other is a quasi-cone. As shown in Figure 6, the three axial lengths of the quasi-spheroid are d_1, d_2, and $2l_2$. Cross section of the quasi-spheroid approximates circle, d_1 is considered to be equivalent to d_2. The height and diameter of the quasi-cone are l_1 and d_1. The maximum and minimum project areas are the front and side of the *Oncomelania* respectively, and the maximum project area can be estimated as

$$A_{pm} = \frac{k_p d_1}{2}\left(\frac{\pi}{2}l_2 + l_1\right) \tag{5}$$

where k_p is the correction coefficient. For consistency, the total length of the *Oncomelania* is defined as $0.5\pi l_2+l_1$, and the diameter of the *Oncomelania* is d_1, which is approximately equal to d_2.

As shown in Figure 7, the parameter A_{pm} increases linearly with parameter $(0.5\pi l_2+l_1)d_1$, and k_p is a constant for the *Oncomelania* and equals to 1.424 with the correlation coefficient $R^2 = 0.966$.

The weight distribution and density of the *Oncomelania* depend on the proportion of the quasi-cone. Thus, the ratio $\gamma = l_1/l_2$ is introduced to describe the shape feature, accordingly, Eq. 5 can be written as

$$A_{pm} = 0.712\left(\gamma + \frac{\pi}{2}\right)l_2 d_1 \tag{6}$$

To obtain a definite diameter, the diameter of the volume-equivalent sphere is introduced,

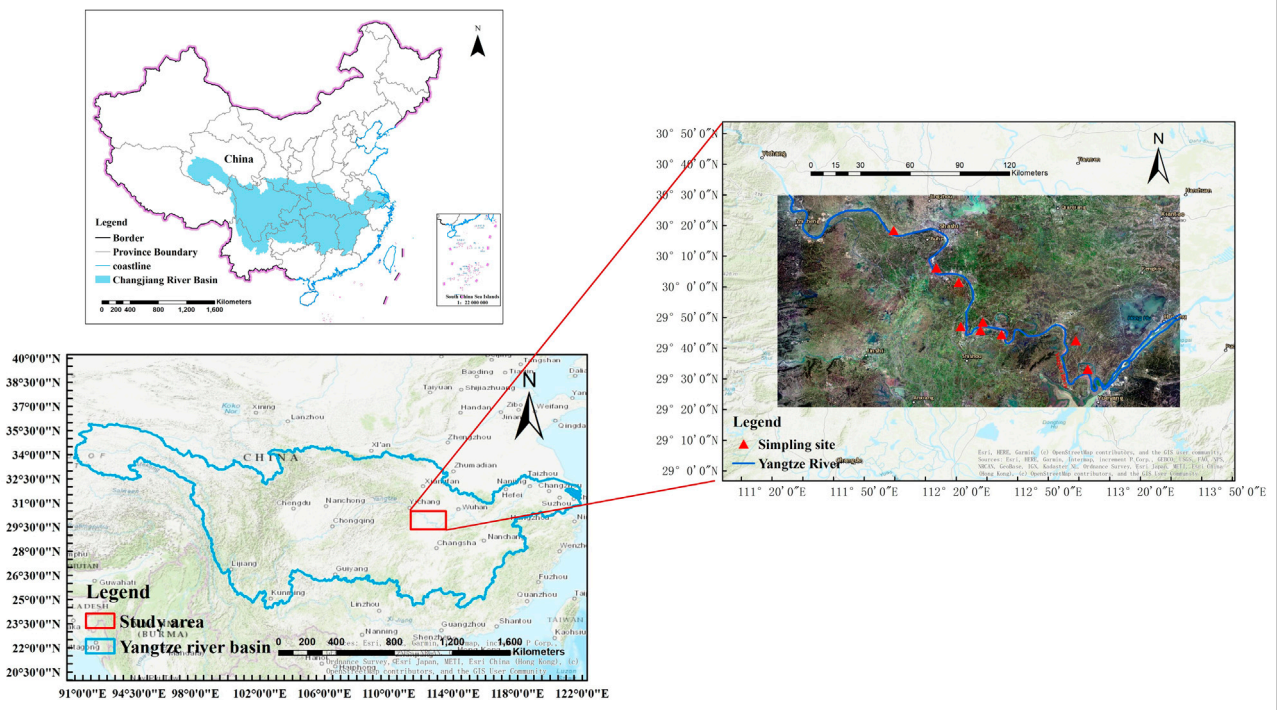

FIGURE 5
Sampling sites of experimental *Oncomelanias* of the Jingzhou fragment (the middle reach) of Changjiang River.

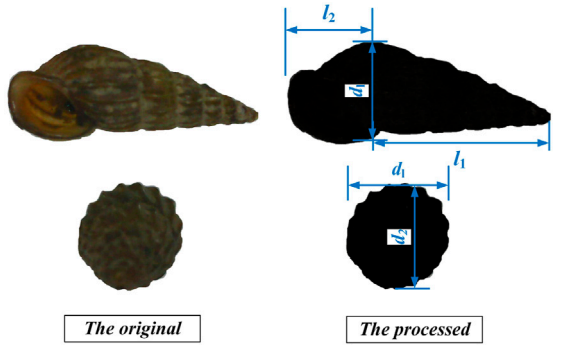

FIGURE 6
Main shape parameters of the *Oncomelania* with the original and processed images.

$$d_e = \left(6V_p/\pi\right)^{1/3} \tag{7}$$

Owing to the shape structure of the *Oncomelanias* being fixed, d_e is found to be proportion to the total length, as shown in Figure 8, the relationship between d_e and $(0.5\pi l_2+l_1)$ can be described as,

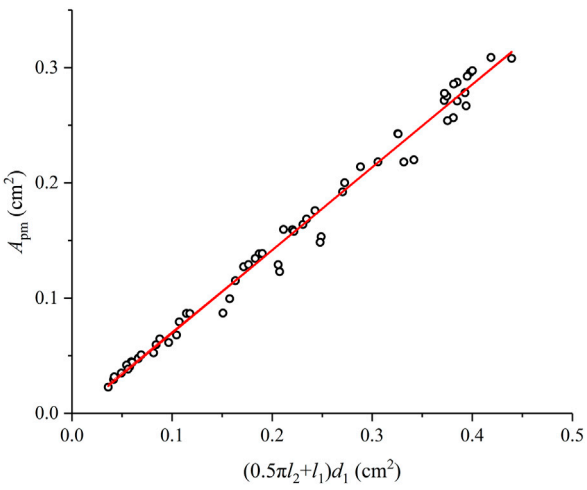

FIGURE 7
The linear relationship between A_{pm} and parameter $(0.5\pi l_2+l_1)d_1$.

$$d_e = 0.0765\left(0.5\pi l_2 + l_1\right) + 0.235 \tag{8}$$

with the correlation coefficient $R^2 = 0.988$.

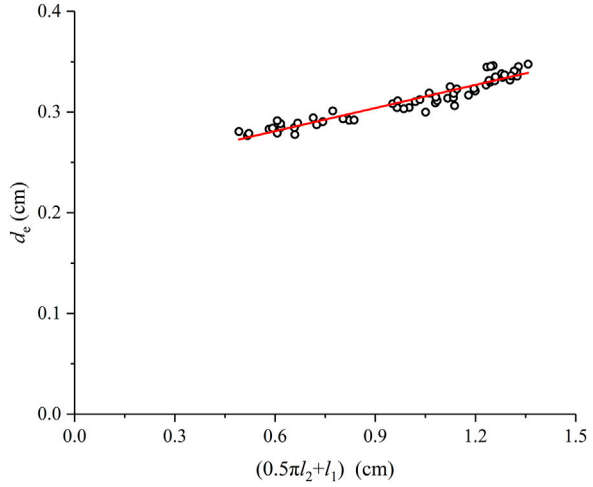

FIGURE 8
The variation relationship between the total length and the he diameter of the volume-equivalent sphere.

Sphericity is defined as the ratio between the surface area of the equivalent sphere A_{eq} and that of the actual particle A_s, which can be written as follows,

$$\phi = \frac{A_{eq}}{A_s} \tag{9}$$

Sphericity is a measure of the degree to which the shape of a particle approximates that of a true sphere, and it is very difficult to be evaluated for highly irregular particles because measuring A_s is difficult. Thus, the surface area of the *Oncomelania* is estimated, referring to quasi-spheroid and quasi-spheroid,

$$A_s = \frac{2\pi}{3}\left(d_1 d_2/4 + d_1 l_2/2 + d_2 l_2/4\right) + \frac{d_1}{2}\sqrt{l_1^2 + d_1^2/4} \tag{10}$$

The sphericity of the *Oncomelania* can be expressed as,

$$\phi = \frac{\pi\left[0.0765\left(0.5\pi l_2 + l_1\right) + 0.235\right]^3}{4\pi\left(d_1 d_2/4 + d_1 l_2/2 + d_2 l_2/4\right) + \frac{d_1}{2}\sqrt{l_1^2 + d_1^2/4}} \tag{11}$$

For highly irregular particles, the parameter Ψ, which is the ratio between phericity ϕ and a newly defined inverse circularity χ, is an effective shape descriptor.

$$\chi = \frac{P_p}{P_s} \tag{12}$$

where P_p is the maximum projection perimeter of the actual particle, and P_s is the perimeter of the circle equivalent to the maximum projection area A_s. χ is sensible to the irregularity of the contour of particles and is very suitable in evaluating the particle shape with sharp corners with large obtuse angles (Büttner et al., 2002).

Combining with Eqs 10–12, χ can be written as,

$$\chi = \frac{2\sqrt{l_1^2 + d_1^2/4} + \pi d_1/4 + 2\left(l_2 - d_1/2\right)}{\sqrt{2.8484\pi d_1\left(\frac{\pi}{2}l_2 + l_1\right)}} \tag{13}$$

which is a 2D shape factor and sensible to the irregularity of the contour of particles, and very suitable for evaluating the particle shape with sharp corners of large obtuse angles.

Models and discussion

Settling velocity model

The forces on a single particle that sinks in balance include the buoyancy force (F_b), gravitational force (F_g), and the particle-liquid interaction force (F_D). According to Newton's equation of motion, the motion of the sinking particle can be presented as

$$F_g = F_D + F_b \tag{14}$$

The gravitational force and buoyancy force are calculated respectively as

$$F_g = \rho_p V_p g \tag{15}$$

$$F_b = \rho_w V_p g \tag{16}$$

where V_p is the volume of the *Oncomelania*, ρ_p is the density of the *Oncomelania*, and ρ_w is the density of the fluid. For the *Oncomelania* uniformly settling in static water, the particle–liquid interaction force is considered the drag force, which is defined as the parallel component of the combined shear and pressure forces that act on the surface of the immersed *Oncomelania* (Fox et al., 2020) and generally expressed in terms of the drag coefficient C_D,

$$F_D = \frac{1}{2}C_D\rho_w A_p w_r^2 \tag{17}$$

where w_r is the relative velocity between particle and fluid, $w_r = w_s$ for sinking in static water, and A_p is the projected surface area of the *Oncomelania* normal to the direction of its motion. For sinking with horizontal posture, A_p equals to the maximum projected area, which is estimated by Eq. 6; for sinking with slant posture, A_p is the projected area along the settling orientation.

The force balance between the drag force and the net gravitational force (the difference of the particle weight and the particle buoyancy) is expressed as

$$\frac{1}{2}C_D\rho_w A_p w_s^2 = \left(\rho_p - \rho_w\right)g V_p \tag{18}$$

For convenient application, this study attempts to develop an explicit settling velocity equation that is suitable for different sized *Oncomelanias*.

The particle Reynolds number is defined with d_e and w_s,

$$R_{ep} = \frac{\rho_w w_s d_e}{\mu} \tag{19}$$

where μ is the dynamic viscosity coefficient of the fluid. Combining with Eq. 7, C_D can be written as

$$C_D = \frac{\pi g(\rho_p - \rho_w) d_e^3}{3\rho_w A_p w_s^2} \tag{20}$$

For the prediction of terminal settling velocity of particles of given properties, the quantity $C_D R_{ep}^2$ is introduced and convenient to be obtained, which is independent of settling velocity and can be evaluated from the physical properties of the *Oncomelanias* and the liquid (Wang et al., 2018). Combining with Eq. 19, $C_D R_{ep}^2$ can be written as,

$$C_D R_{ep}^2 = \frac{\pi g \rho_w (\rho_p - \rho_w) d_e^5}{3\mu A_p} \tag{21}$$

To reveal the effect of the physical characteristic and shape feature on the settling process and determine the terminal settling velocity of the *Oncomelania*, the variation relationship between the main influencing factor and C_D should be further discussed.

Drag coefficient for the *Oncomelanias*

Drag coefficient plays a core role in determining the drag F_D, which is a dimensionless parameter, however, that of the cone-shaped particle is rarely investigated.

According to previous studies (Dioguardi and Mele, 2015; Govindan et al., 2021; Song et al., 2017; Zhou et al., 2022), particle diameter, particle length, particle sphericity, and particle Reynolds number take effect on the drag coefficient. Thus, the drag coefficient should be the function of these effects, and can be expressed as,

$$C_D = f(l, d, \rho_p, \rho_w, w_s, A_p, \phi) \tag{22}$$

Three dimensionless parameters are refined to represent the above mentioned parameters. The shape factor ψ is defined as the ratio of the sphericity and χ, χ represents the deviation of the particle shape from the circle, and $\gamma = (l_1 + l_2)/d_1$ represents the flatness ratio of the maximum projection plane. Eq. 22 can be simplified as

$$C_D = f(\psi, \gamma, R_{ep}, S) \tag{23}$$

To apply the smooth sphere formula to irregularly-shaped particles, a shape factor needs to be introduced in the equation. Several proven methods can be referenced, where the effect of the irregular particle shape can be considered using parameter ψ in the form of power function (Dellino et al., 2005; Dioguardi and Mele, 2015; Wang et al., 2018; Zhu et al., 2017).

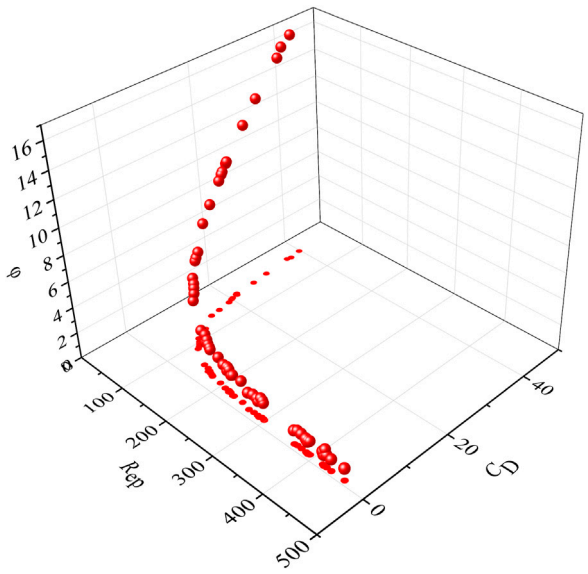

FIGURE 9
The variation relationship among the particle Reynold number, drag coefficient and Sphericity.

As shown in Figure 9, the influence of the shape feature on the variation of drag coefficient and terminal settling velocity becomes more noticeable as R_{ep} increases, which is compatible with that of Loth (2008) and Khatmullina and Isachenko (2017).

The drag coefficient of smooth sphere ($C_{D,sph}$) proposed by Clift and Gauvin (1971) is adopted in this study, which has been valid for $0 < R_{ep} < 3 \times 10^5$,

$$C_{Dsph} = \frac{24}{R_{ep}}\left(1 + 0.15R_{ep}\right)^{0.687} + 0.42 \Big/ \left(1 + 42500R_{ep}^{-1.16}\right) \tag{24}$$

Eq. 24 is appropriate for spherical particles. According to present experimental results, R_{ep} of the *Oncomelania* ranges from 30 to 400, the boundary layer around the particle separates and produces vortex shedding and wake formation, which lead to higher pressure drag and may cause the effect of shape and roundness to be dominant. To apply it to irregularly shaped particles, shape factors need to be introduced in the equation, and the effect of shape factors on C_D is affected by R_{ep} (Zhou et al., 2022). Thus, the ratio of C_D to $C_{D,\,sph}$ can be described as,

$$\frac{C_D}{C_{Dsph}} = f(\psi, \gamma, R_{ep}, S) \tag{25}$$

Further, the expression form of R_{ep} and ψ has been determined (Kramer et al., 2021; Wang et al., 2018),

$$\frac{C_D}{C_{Dsph}} \sim \psi^m R_{ep}^n \tag{26}$$

where m and n are undetermined coefficients.

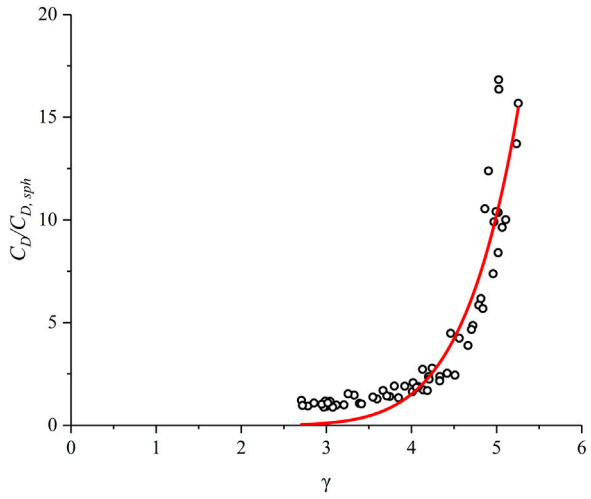

FIGURE 10
The variation relationship between parameter γ and $C_D/C_{D,\ sph}$.

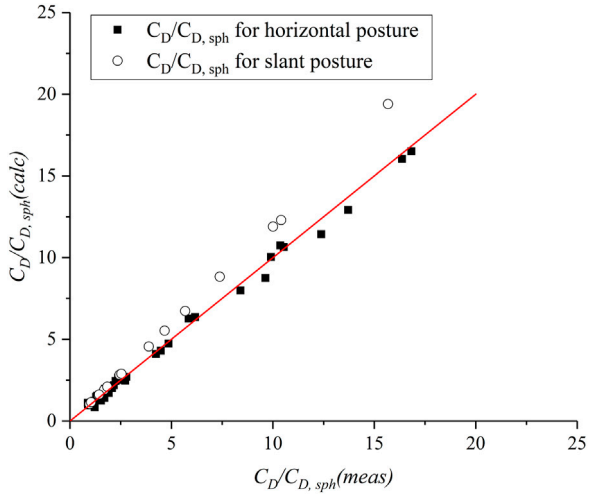

FIGURE 11
Comparison of the measured $C_D/C_{D,\ sph}$ to that of the calculated.

As shown in Figure 10, $C_D/C_{D,\ sph}$ increases with the increase of γ in the form of approximate power law function, thus, the best fit is obtained by a power form with a high correlation coefficient. Eq. 25 can be expressed as

$$\frac{C_D}{C_{D,\mathrm{sph}}} = k\psi^m R_{ep}^n \gamma^p \tag{27}$$

where p is the undetermined coefficient, and k is the scale factor.

Considering that the terminal settling velocity are obtained from the experiments, the measured drag coefficient ($C_{D,\mathrm{meas}}$) is determined using Eq. 9. The drag coefficient of smooth sphere ($C_{D,\mathrm{sph}}$) is calculated by Eq. 24. The calculated drag coefficient ($C_{D,\mathrm{calc}}$) can be obtained through the analysis of the best fitting parameters of the experimental data.

$$C_D/C_{D,sph} = \psi^{1.72}\gamma^{0.93}R_{ep}^{0.23} \tag{28}$$

The average relative error is evaluated as,

$$r = \frac{1}{N}\sum_{i=1}^{N}\frac{|C_{D,calc} - C_{D,meas}|}{C_{D,meas}} \times 100\% \tag{29}$$

where N is the total number of data points. As shown in Figure 11, the calculated and measured $C_D/C_{D,\mathrm{sph}}$ for horizontal posture match well with r = 5.2%, and the calculated $C_D/C_{D,\mathrm{sph}}$ for slant posture is significantly greater than the measured ones, suggesting that the effect of settling orientation cannot be ignored. Thus, the effect of settling orientation is represented by S, which is the ratio between equivalent sphere area (S_e) and the projected area of particle settling direction (A_p).

$$S = \frac{S_e}{A_p} \tag{30}$$

Thus, Eq. 30 can be further written as

$$\frac{C_D}{C_{D\mathrm{sph}}} = k\psi^m R_{ep}^n \gamma^p S^q \tag{31}$$

where q is the undetermined coefficient, and q = 0 is for the horizontal posture. Through nonlinear fitting with the experimental data of the slant posture, the following relationships can been derived,

$$C_D/C_{D,sphere} = 0.946\psi^{1.72}\gamma^{0.93}R_{ep}^{0.23}S^{-0.07} \tag{32}$$

The average relative error of Eq. 32 is r = 1.2%. To evaluate the accuracy and rationality of the present formula compared with other models, we evaluated C_D of the *Oncomelania* with other well-known laws available in the literature.

Isaacs and Thodos (1967) studied the free settling of cylindrical particles in the turbulent regime. The authors used the equal volume sphere as the characteristic dimension and found that the drag coefficient was independent of R_{ep}. The drag coefficient depended on the particle/fluid density ratio (ρ_p/ρ_w) and the aspect ratio (E, defined as L/d_c),

$$C_D = 0.99\left(\rho_p/\rho_w\right)^{-0.12}E^{-0.08}\ (200 < R_e \le 60000) \tag{33}$$

Chien (1994) reanalyzed the data available in the petroleum engineering and processing literature and proposed the following drag expression,

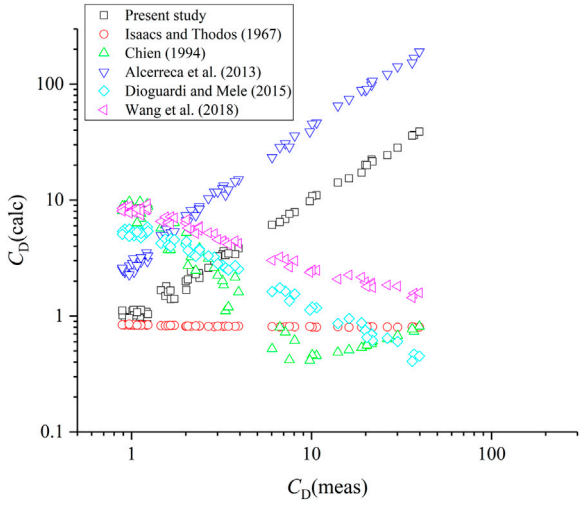

FIGURE 12
Comparisons between measured and calculated C_D for present and other related studies.

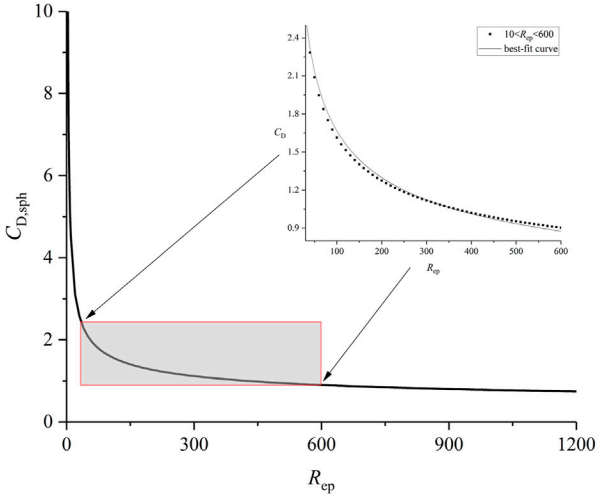

FIGURE 13
The relationship between $C_{D,\ sph}$ and R_{ep} for smooth sphere, the top right-hand corner indicates the best-fit curve with $10 < R_{ep} < 600$.

$$C_D = \frac{30}{R_{ep}} + \frac{67.289}{e^{5.030\Phi}} \tag{34}$$

where C_D and R_{ep} are based on the equal-volume sphere diameter. Eq. 34 was stated to be valid in the ranges $0.2 < \phi < 1$ and $R_{ep} < 5000$.

Alcerreca et al. (2013) derived a new equation for the computation of particle settling velocity for calcareous sand,

$$C_D = \frac{4d_e^3\left[\frac{g}{\nu^2}\left(\rho_p/\rho_w - 1\right)\right]}{3R_{ep}^2} \tag{35}$$

where ν is kinematic viscosity of water.

Dioguardi and Mele (2015) investigated the drag of non-spherical rough particles in a wide range of Reynolds numbers (0.03–10,000), the correlation has the functional form of a power law with particle Reynolds number and the shape factor. For $50 < R_{ep} < 10{,}000$, the drag coefficient can be easily written as.

$$C_D = 0.931R_{ep}^{-0.079}\psi^{-1.6} \tag{36}$$

Wang et al. (2018) developed a new model for predicting the drag coefficient of natural particles of highly irregular shapes in a wide range of particle Reynolds number (0.01–3700).

$$C_D = 0.945\frac{C_{Dshp}}{\psi^{0.641R_{ep}^{0.153}}}R_{ep}^{-0.01} \tag{37}$$

As shown in Figure 12, the other formulas of cylindrical particles (Isaacs and Thodos, 1967) and approximate isometric calcareous particles (Chien, 1994; Dioguardi and Mele, 2015; Wang et al., 2018) are not applicable for the *Oncomelania* (cone-shaped particle). The predicting values of Alcerreca et al. (2013) and Dioguardi and Mele (2015) significantly lower than the measured, the basic reason of which are the flow structure around cone-shaped particle is more complicated and skin friction coefficient is higher. The average relative errors between present experimental data and predicting formula that applied to isometric calcareous particles are larger than 100%, and the trends of C_D and R_{ep} are inconsistent with the results obtained in the present experiments. Only sphericity and circularity being considered as shape factors is not enough, especially for the irregular-shape particle with asymmetrical weight distribution. Therefore, parameter γ is essential to weight the proportion of disc-shaped and cone-shaped parts. The formula proposed by Alcerreca et al. (2013), which considered all calcareous sand types and demonstrated the best performance in predicting the settling velocity, is comparatively applicative.

In general, the drag coefficient of the *Oncomelania* with different status can be written as

$$C_D = C_{D,sph}R_{ep}^{0.23} \times \begin{cases} \psi^{1.72}\gamma^{0.93} & for\_the\_domant \\ 0.946\psi^{1.72}\gamma^{0.93}S^{-0.07} & for\_the\_active \end{cases} \tag{38}$$

The particle Reynold number of the *Oncomelania* ranges from 36 to 470, and the reported R_{ep} of the *Oncomelania* is in the range of 10–600. The relationship between the drag coefficient of smooth sphere proposed by Clift and Gauvin (1971) and R_{ep} is plotted in Figure 13. Significantly, the

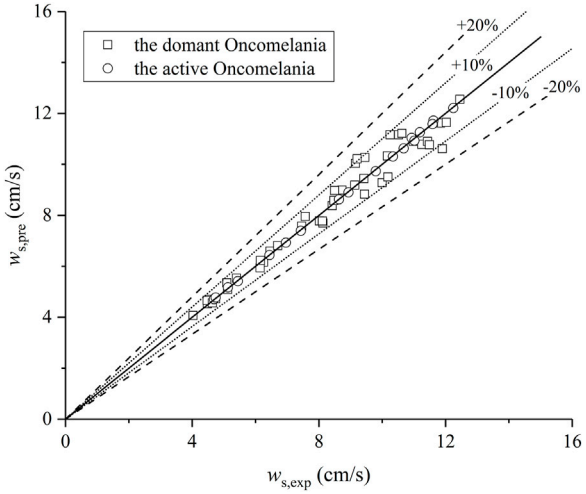

FIGURE 14
Comparison of measured and predicted settling velocity calculated by using explicit terminal settling velocity of Eq. 41.

variation of $C_{D,sph}$ with R_{ep} for $10 < R_{ep} < 600$ can be well fitted with power function, which can be described as,

$$C_{D,sph} = 8.7R_{ep}^{-0.359} \quad 10 < R_{ep} < 600 \tag{39}$$

with the correlation coefficient $R^2 = 0.9915$.

An explicit formula needs to be developed to facilitate practical application. Combining Eqs. 39, 38 can be written as:

$$C_D = \begin{cases} 8.7R_{ep}^{-0.129}\psi^{1.72}\gamma^{0.93} & for\_the\_domant \\ 8.23R_{ep}^{-0.129}\psi^{1.72}\gamma^{0.93}S^{-0.07} & for\_the\_active \end{cases} \tag{40}$$

Further, combining with Eq. 21, the explicit formula of w_s for the *Oncomelania* can be reorganized as:

$$w_s = \begin{cases} \dfrac{2.725g^{-0.5345}d_e^{-2.601}\rho_w^{-1.5345}\left(\rho_p-\rho_w\right)^{-0.5345}}{\mu^{-2.069}\psi^{-0.9193}\gamma^{-0.4971}} & for\_the\_domant \\ \dfrac{2.646g^{-0.5345}d_e^{-2.601}\rho_w^{-1.5345}\left(\rho_p-\rho_w\right)^{-0.5345}}{\mu^{-2.069}\psi^{-0.9193}\gamma^{-0.4971}S^{-0.0374}} & for\_the\_active \end{cases} \tag{41}$$

Given that the experiments in the terminal settling velocities ($w_{s,\ exp}$) are obtained using Eq. 20, the predicted terminal settling velocities ($w_{s,\ pre}$) are determined using Eq. 41. As shown in Figure 14, 95% of data points lies within the predicting error of 10%, the average relative error between the predicted and the experimental of the dormant *Oncomelanias* using Eq. 29 is 3.72%, and that of the active *Oncomelanias* is 0.48%. A general good performance of the proposed explicit formula enables the prediction of fall velocity values within the range of $10 < R_{ep} < 600$.

Conclusion

In this study, a new model for predicting the settling velocity and drag coefficient of different sized *Oncomelanias* is developed. These findings cover the particle Reynolds number range of 10–600, which are suitable for young and mature *Oncomelanias*, and can offer references for millimeter-sized cone-shaped and disc-shaped particles. The stable settling postures of *Oncomelanias* do not depend on the initial posture as entering the water, the *Oncomelania* in dormant state will sink in horizontal posture, the *Oncomelania* in active state will sink in slant posture. Turbulent intensity and time-average sinking velocity have a significantly negative linear correlation. The settling postures of *Oncomelanias* affect the amplitude of helical trajectories, but have no effect on the frequency of oscillation that only depends on the shape structure of *Oncomelanias*.

The body of the *Oncomelania* can be divided into the quasi-spheroid and the quasi-cone. Accordingly, the authors define three axial lengths. Three dimensionless shape parameters are selected using the defined lengths to predict the drag coefficient of the *Oncomelania*. As R_{ep} increases, the influence of shape features on the particle drag coefficient and terminal settling velocity become increasingly evident. The proposed model performs better in predicting drag coefficient compared with several widely used formulas. Finally, combining with the predicting formula of C_D and Eqs 20, 21 with parameters ρ_p, l_1, l_2, d_1, and d_2, an explicit formula for settling velocity is developed with several easy-to-measure parameters is and proven to be a high-precision prediction formula of settling velocity for the dormant (r = 3.72%) and active *Oncomelanias* (r = 0.48%).

This study focuses on the research gap of predicting the drag coefficient and terminal settling velocity of the cone-shaped organism accurately, and can provide a basis for further improvement for the hydraulic schistosomiasis control project.

Data availability statement

The datasets presented in this study can be found in online repositories. The names of the repository/repositories and accession number(s) can be found in the article/supplementary material.

Author contributions

XL: Conceptualization, Methodology, Formal analysis, Resources, Investigation, Writing, Validation; JW:

Methodology, Formal analysis, Writing, Supervision, Funding acquisition; ZC: Formal analysis, Writing, Supervision, Funding acquisition; XJ: Methodology, Formal analysis, Supervision; KZ: Formal analysis, Supervision; JD: Formal analysis, Supervision.

Funding

This work was mainly supported by the Fundamental Research Funds for Central Public Welfare Research Institutes (Grant Nos CKSF2021438/HL and CKSF2021530/HL), Open Foundation from the State Key Laboratory of Water Resources and Hydropower Engineering Science (Grant No. 2021HLG02), the National Natural Science Foundation of China (Grant Nos. 10802013 and 51809012) and the Program of the National Key Research and Development Plan (Grant No. 2018YFC0407803). The data that support the findings of this study is available on request from the corresponding author.

Conflict of interest

The authors declare that the research was conducted in the absence of any commercial or financial relationships that could be construed as a potential conflict of interest.

Publisher's note

References

Akan, A. O., and Iyer, S. S. (2021). *Open channel hydraulics*. Oxford, United Kingdom: Butterworth-Heinemann.

Alcerreca, J. C., Silva, R., and Mendoza, E. (2013). Simple settling velocity formula for calcareous sand. *J. hydraulic Res.* 51 (2), 215–219. doi:10.1080/00221686.2012.753645

Barry, D. A., and Parlange, J. Y. (2018). Universal expression for the drag on a fluid sphere. *Plos one* 13 (4), e0194907. doi:10.1371/journal.pone.0194907

Bhutani, G., and Brito-Parada, P. R. (2020). A framework for polydisperse pulp phase modelling in flotation. *Sep. Purif. Technol.* 236, 116252. doi:10.1016/j.seppur.2019.116252

Brueck, C. L., and Wildenschild, D. (2020). A proximity-based image-processing algorithm for colloid assignment in segmented multiphase flow datasets. *J. Microsc.* 277 (2), 118–129. doi:10.1111/jmi.12874

Büttner, R., Dellino, P., La Volpe, L., Lorenz, V., and Zimanowski, B. (2002). Thermohydraulic explosions in phreatomagmatic eruptions as evidenced by the comparison between pyroclasts and products from Molten Fuel Coolant Interaction experiments. *J. Geophys. Res.* 107 (B11), ECV 5-1–ECV 5-14. doi:10.1029/2001jb000511

Chambert, S., and James, C. S. (2009). Sorting of seeds by hydrochory. *River Res. Appl.* 25, 48–61. doi:10.1002/rra.1093

Cheng, G., Li, D., Zhuang, D., and Wang, Y. (2016). The influence of natural factors on the spatio-temporal distribution of Oncomelania hupensis. *Acta Trop.* 164, 194–207. doi:10.1016/j.actatropica.2016.09.017

Chhabra, R. P., Agarwal, L., and Sinha, N. K. (1999). Drag on non-spherical particles: An evaluation of available methods. *Powder Technol.* 101 (3), 288–295. doi:10.1016/s0032-5910(98)00178-8

Chhabra, R. P., and Richardson, J. F. (2011). *Non-Newtonian flow and applied rheology: Engineering applications*. Elsevier Science, Butterworth-Heinemann.

Chien, S. F. (1994). Settling velocity of irregularly shaped particles. *SPE Drill. Complet.* 9 (04), 281–289. doi:10.2118/26121-pa

Clift, R., and Gauvin, W. H. (1971). Motion of entrained particles in gas streams. *Can. J. Chem. Eng.* 49 (4), 439–448. doi:10.1002/cjce.5450490403

Delleur, J. W. (2001). New results and research needs on sediment movement in urban drainage. *J. Water Resour. Plan. Manag.* 127 (3), 186–193. doi:10.1061/(asce)0733-9496(2001)127:3(186)

Dellino, P., Mele, D., Bonasia, R., Braia, G., La Volpe, L., and Sulpizio, R. (2005). The analysis of the influence of pumice shape on its terminal velocity. *Geophys. Res. Lett.* 32 (21), L21306. doi:10.1029/2005gl023954

Dioguardi, F., and Mele, D. (2015). A new shape dependent drag correlation formula for non-spherical rough particles. Experiments and results. *Powder Technol.* 277, 222–230. doi:10.1016/j.powtec.2015.02.062

Fox, R. W., McDonald, A. T., and Mitchell, J. W. (2020). *Fox and McDonald's introduction to fluid mechanics*. Hoboken, NJ, USA: John Wiley & Sons.

Ganser, G. H. (1993). A rational approach to drag prediction of spherical and nonspherical particles. *Powder Technol.* 77 (2), 143–152. doi:10.1016/0032-5910(93)80051-b

Govindan, B., Mohanmani, P., Jakka, S. C. B., Tiwari, A. K., Kalburgi, A. K., Sudhakar, T. M., et al. (2021). Shape descriptors-settling characteristics of irregular shaped particles. *Chem. Eng. Commun.* 208 (3), 295–303. doi:10.1080/00986445.2019.1710494

Haider, A., and Levenspiel, O. (1989). Drag coefficient and terminal velocity of spherical and nonspherical particles. *Powder Technol.* 58 (1), 63–70. doi:10.1016/0032-5910(89)80008-7

Hölzer, A., and Sommerfeld, M. (2008). New simple correlation formula for the drag coefficient of non-spherical particles. *Powder Technol.* 184 (3), 361–365. doi:10.1016/j.powtec.2007.08.021

Hvitved-Jacobsen, T., Vollertsen, J., and Tanaka, N. (1998). Wastewater quality changes during transport in sewers—an integrated aerobic and anaerobic model concept for carbon and sulfur microbial transformations. *Water Sci. Technol.* 38 (10), 257–264. doi:10.2166/wst.1998.0409

Isaacs, J. L., and Thodos, G. (1967). The free-settling of solid cylindrical particles in the turbulent regime. *Can. J. Chem. Eng.* 45 (3), 150–155. doi:10.1002/cjce.5450450306

Jia, W. F., Zhang, S. H., Yang, Y. F., and Yi, Y. J. (2020). A laboratory investigation of the transport mechanism of floating fish eggs: A case study of asian carps. *Aquaculture* 519, 734855. doi:10.1016/j.aquaculture.2019.734855

Khatmullina, L., and Isachenko, I. (2017). Settling velocity of microplastic particles of regular shapes. *Mar. Pollut. Bull.* 114 (2), 871–880. doi:10.1016/j.marpolbul.2016.11.024

Kramer, O. J., de Moel, P. J., Raaghav, S. K., Baars, E. T., van Vugt, W. H., Breugem, W. P., et al. (2021). Can terminal settling velocity and drag of natural particles in water ever be predicted accurately? *Drink. Water Eng. Sci.* 14 (1), 53–71. doi:10.5194/dwes-14-53-2021

Liu, X., Zeng, Y., and Huai, W. (2018). Modeling of interactions between floating particles and emergent stems in slow open channel flow. *Water Resour. Res.* 54 (9), 7061–7075. doi:10.1029/2018wr022617

Loth, E. (2008). Drag of non-spherical solid particles of regular and irregular shape. *Powder Technol.* 182 (3), 342–353. doi:10.1016/j.powtec.2007.06.001

Ma, L., Xu, S., Li, X., Guo, Q., Gao, D., Ding, Y., et al. (2020). Particle tracking velocimetry of porous sphere settling under gravity: Preparation of the model

porous particle and measurement of drag coefficients. *Powder Technol.* 360, 241–252. doi:10.1016/j.powtec.2019.09.058

McManus, D. P., Gray, D. J., Ross, A. G., Williams, G. M., He, H. B., and Li, Y. S. (2011). Schistosomiasis research in the dongting lake region and its impact on local and national treatment and control in China. *PLoS Negl. Trop. Dis.* 5 (8), e1053. doi:10.1371/journal.pntd.0001053

Ouchene, R., Khalij, M., Arcen, B., and Tanière, A. (2016). A new set of correlations of drag, lift and torque coefficients for non-spherical particles and large Reynolds numbers. *Powder Technol.* 303, 33–43. doi:10.1016/j.powtec.2016.07.067

Ren, B., Zhong, W., Jin, B., Lu, Y., Chen, X., and Xiao, R. (2011). Study on the drag of a cylinder-shaped particle in steady upward gas flow. *Ind. Eng. Chem. Res.* 50 (12), 7593–7600. doi:10.1021/ie102263u

Roegiers, J., and Denys, S. (2019). CFD-modelling of activated carbon fibers for indoor air purification. *Chem. Eng. J.* 365, 80–87. doi:10.1016/j.cej.2019.02.007

Song, X., Xu, Z., Li, G., Pang, Z., and Zhu, Z. (2017). A new model for predicting drag coefficient and settling velocity of spherical and non-spherical particle in Newtonian fluid. *Powder Technol.* 321, 242–250. doi:10.1016/j.powtec.2017.08.017

Stokes, G. G. (1851). *On the effect of the internal friction of fluids on the motion of pendulums*. Cambridge, UK: Pitt Press, Cambridge Philosophical Society.

Wang, L., Zheng, K., Ding, Z., Yan, X., Zhang, H., Cao, Y., et al. (2020). Drag coefficient and settling velocity of fine particles with varying surface wettability. *Powder Technol.* 372, 8–14. doi:10.1016/j.powtec.2020.05.102

Wang, Y., Zhou, L., Wu, Y., and Yang, Q. (2018). New simple correlation formula for the drag coefficient of calcareous sand particles of highly irregular shape. *Powder Technol.* 326, 379–392. doi:10.1016/j.powtec.2017.12.004

Wang, Z., Ren, S., and Huang, N. (2014). Saltation of non-spherical sand particles. *Plos one* 9 (8), e105208. doi:10.1371/journal.pone.0105208

Yin, C., Rosendahl, L., Kær, S. K., and Sørensen, H. (2003). Modelling the motion of cylindrical particles in a nonuniform flow. *Chem. Eng. Sci.* 58 (15), 3489–3498. doi:10.1016/s0009-2509(03)00214-8

Zhou, C., Su, J., Chen, H., and Shi, Z. (2022). Terminal velocity and drag coefficient models for disc-shaped particles based on the imaging experiment. *Powder Technol.* 398, 117062. doi:10.1016/j.powtec.2021.117062

Zhou, E., Lu, J., Wang, Q., Lv, G., Zhao, Y., Dong, L., et al. (2020). Mixing and migration rule of binary medium in vibrated dense medium fluidized bed for fine coal separation. *Adv. Powder Technol.* 31 (8), 3420–3432. doi:10.1016/j.apt.2020.06.029

Zhu, X., Zeng, Y. H., and Huai, W. X. (2017). Settling velocity of non-spherical hydrochorous seeds. *Adv. Water Resour.* 103, 99–107. doi:10.1016/j.advwatres.2017.03.001

frontiers | Frontiers in Environmental Science

TYPE Original Research
PUBLISHED 23 November 2022
DOI 10.3389/fenvs.2022.1033160

OPEN ACCESS

EDITED BY
Matteo Rubinato,
Coventry University, United Kingdom

REVIEWED BY
Sitong Liu,
Peking University, China
Baozhu Pan,
Xi'an University of Technology, China

*CORRESPONDENCE
Yuefei Huang,
yuefeihuang@tsinghua.edu.cn
Shuo Zhang,
zhangs2019@tsinghua.edu.cn

SPECIALTY SECTION
This article was submitted to Freshwater Science, a section of the journal Frontiers in Environmental Science

RECEIVED 31 August 2022
ACCEPTED 14 October 2022
PUBLISHED 23 November 2022

CITATION
Wang D, Huang Y, Zhang S, Liu S, Wang T and Yang H (2022), Differences in bacterial diversity, composition, and community networks in lake water across three distinct regions on the Qinghai-Tibet Plateau.
Front. Environ. Sci. 10:1033160.
doi: 10.3389/fenvs.2022.1033160

Differences in bacterial diversity, composition, and community networks in lake water across three distinct regions on the Qinghai-Tibet Plateau

Dandan Wang[1], Yuefei Huang[1,2,3]*, Shuo Zhang[3]*, Shufeng Liu[4], Ting Wang[4] and Haijiao Yang[1]

[1]School of Water Resources and Electric Power, Key Laboratory of Ecological Protection and High Quality Development in the Upper Yellow River, Key Laboratory of Water Ecological Remediation and Protection at Headwater Regions of Big Rivers, Ministry of Water Resources, Qinghai University, Xining, Qinghai, China, [2]State Key Laboratory of Plateau Ecology and Agriculture, Qinghai University, Xining, Qinghai, China, [3]State Key Laboratory of Hydroscience and Engineering, Department of Hydraulic Engineering, Tsinghua University, Beijing, China, [4]College of Environmental Sciences and Engineering, Peking University, The Key Laboratory of Water and Sediment Sciences, Ministry of Education, Beijing, China

We analyze bacterial composition, diversity, geographical distribution, and their community networks in lake water in three adjacent regions on the Qinghai-Tibet Plateau (QTP). Results show that bacterial alpha-diversity indices are much lower in the Hoh Xil (HX) than that in the Yellow River Headwater (YRH) regions and the Qaidam (QD) region. The dominant phyla in QD and YRH are Proteobacteria which account for 42.45 % and 43.64 % of all detected phyla, while Bacteroidetes is the dominant bacterial taxa in HX (46.07 %). Redundancy analysis results suggest that the most important factors in driving bacterial community composition in the three regions are altitude (QD), total nitrogen (YRH), and pH (HX), respectively. Both environmental factors and spatial factors significantly affect the bacterial community composition in QD and HX, while only environmental factors are the major drivers in YRH. Finally, network analyses reveal that the bacterial network structure in QD is more complex than those in YRH and HX, whereas the bacterial network in HX is the most stable, followed by those in QD and YRH.

KEYWORDS

bacterial community, lake ecosystem, Qinghai-Tibet Plateau, biogeographic patterns, co-occurrence network

Introduction

The Qinghai-Tibet Plateau (QTP), considered as "the Third Pole", is located in the northwest of China with an average elevation of 3000 m. The climate is arid/semi-arid with a mean annual precipitation less than 400 mm and an average annual air temperature lower than 5°C (Liu et al., 2021). The lake ecosystem at the QTP is the

largest and one of the most representative oligotrophic and mesotrophic lake ecosystems in the world (Wen et al., 2019). Large variations in water chemistry occur in the plateau lakes due to incomplete water mixing over multi-year intervals (Wen et al., 2019). Numerous bacteria are found in lake water bodies, which are vital parts of the aquatic ecosystem and play important functional roles in nutrient and energy cycling in the lakes (Zinger et al., 2011; Chen et al., 2019; Zhang et al., 2020b; Wang et al., 2020; Xie et al., 2020). For example, denitrifying bacteria and anammox bacteria are related to nitrogen loss in aquatic ecosystems (Wang et al., 2019). Many studies have been conducted on the bacterial community harbored in the surface water in areas of the QTP and it has been found that the bacterial communities in these lakes are highly sensitive to environmental differences such as salinity, elevation and human activities (Wu et al., 2006; Xiong et al., 2012; Yang et al., 2016a; Liu et al., 2019c; Zhong et al., 2016; Ji et al., 2019; Liu et al., 2021). For example, recent studies have reported that water salinity is a major driving force in shaping community structure of bacteria in the Tibetan lakes (Xing et al., 2009; Liu et al., 2019a; Liu et al., 2020).

The Qaidam lake and the Qinghai lake, with hypersaline (>35%) and saline water, a relatively low elevation (~3000 m), affected by intensive human activities, are located at a gigantic inland river region on the QTP (Supplementary Figure S1), surrounded by the Kunlun, Riyue, and Qilian Mountains (Zhong et al., 2016). Several studies have reported the bacterial community structure and its influencing factors in lake water bodies in the Qaidam region (QD) (Jiang et al., 2010; Wang et al., 2011; Yang et al., 2016b; Han et al., 2017; Ren et al., 2017). A previous study reported that salinity, pH, dissolved oxygen concentration and total nitrogen concentration are the most important environmental factors that affect the prokaryotic community in these lakes (Yang 2015).

The Yellow River Headwater region (YRH, Supplementary Figure S1) has freshwater (salinity <1%), an average elevation of 4500 m (Luo et al., 2020) and less disturbance from human activities. Only two studies have reported bacterioplankton in lake waters within YRH. Previous research found that the bacterial communities in water have a significant correlation with water conductivity, total nitrogen, and total phosphorus in the thermokarst lakes from the YRH region (Ren et al., 2021a).

One study has been undertaken to investigate the response of archaea to climate change in Kusai lake at the northern Hoh Xil region (HX, Supplementary Figure S1), which has an intermediate salinity (1% < salinity <35%) and an average elevation of 4500 m (Yang 2015; Liu et al., 2019b).

These three neighboring regions, while being close geographically, are characterized by significantly different environmental conditions, providing an opportunity to study the differences of bacterial communities and their driving forces in these three typical habitats (Li et al., 2020). In this study, we systematically examine the bacterial diversity and community composition, their geographical distributions, and co-occurrence network in the three regions using 16S rRNA gene sequencing. The objectives of our investigation are: 1) to analyze the differences in bacterial diversity, community structure, and biomarkers in the lakes in the three distinct regions, 2) to identify contributions of environmental and spatial factors to variations of bacterial community composition in the three regions, and 3) to reveal bacterial co-occurrence patterns in each region. The results of this study provide insight into differences of bacterial features at the regional scale, and provide guidance for the protection and management of the plateau lake ecosystems.

Materials and methods

Sampling and processing

About 5L surface (top 0.5 m) water samples were obtained in three replicates at each sampling point of the 19 investigated lakes including six lakes in QD, seven lakes in YRH, and six lakes in HX in June 2020. For larger lakes more than two sampling points were chosen at different functional (i.e., central-C/shore-S, or inlet/outlet areas) zones (Figure 1 and Supplementary Table S1). The lakes were selected to cover most of the major lakes in each region. Water samples were saved in sterile narrow-necked glass bottles and immediately kept in a portable refrigerator. After mixing the 5L of water from each sampling point, about 3L of water sample was filtered through 0.22 μm pore polycarbonate membrane (47 mm, Millipore S-Pak, Germany) using a vacuum pump within 12 h. Filters were transferred into 50 ml sterile conical centrifuge tubs, and then stored at −20°C in a portable refrigerator until transported back to our laboratory for total DNA extraction. The residual water samples were saved at dark and cold conditions at 4°C until they were used for physicochemical parameter analyses.

Water sample analysis

At each sample site, water temperature (Temp), pH, dissolved oxygen (DO), salinity (SAL), electrical conductivity (EC), oxidation-reduction potential (ORP), turbidity (NTU), and Chlorophyll-a concentration (Chl-a) were measured *in-situ* using a portable multi-parameter water quality monitor (EXO™2 Sonde, SY1, United States). Additionally, total nitrogen (TN), ammonia nitrogen (NH_4^+-N), nitrate nitrogen (NO_3^--N), nitrite nitrogen (NO_2^--N), and total phosphorus (TP) of the water samples were analyzed using standard methods as described in previous studies (Zhao et al., 2017; Meng et al., 2020). After filtered through a 0.45 μm membrane, concentrations of dissolved organic carbon (DOC) in water samples were measured according to the Chinese National Standard HJ 501-2009 by a TOC elemental analyzer (TOC-L, Shimadzu, Japan). Geospatial

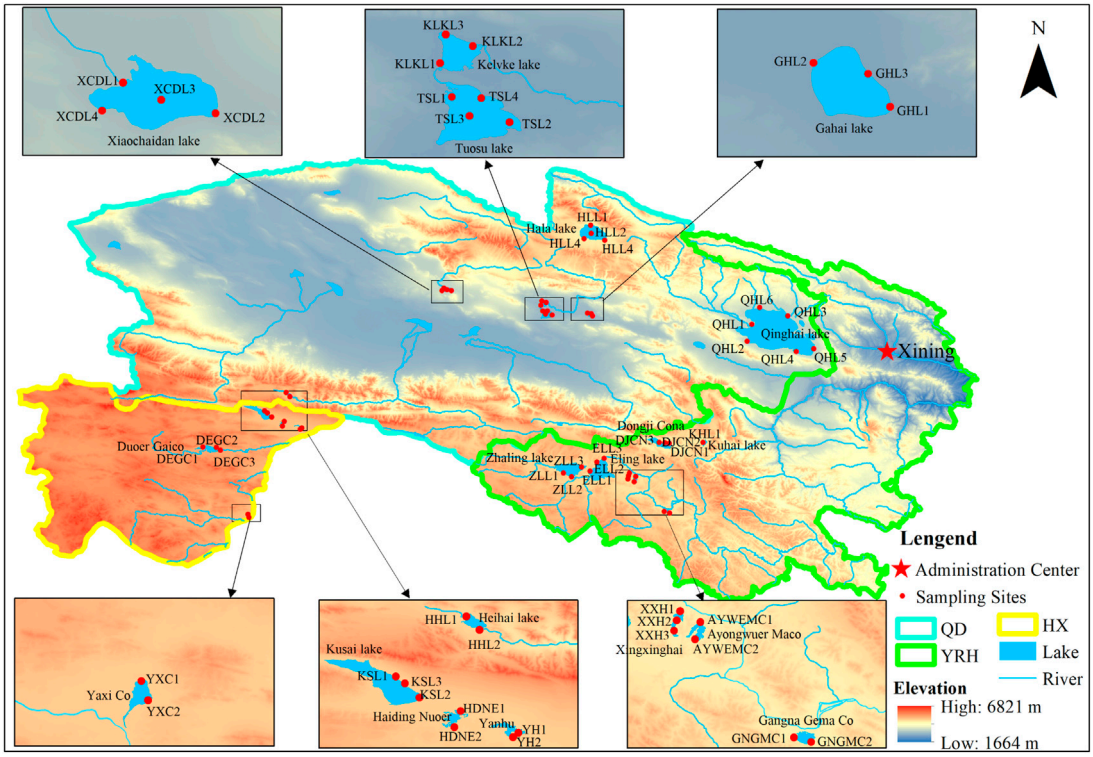

FIGURE 1
Locations of studied lakes and sampling sites on the Qinghai-Tibet Plateau.

parameters, such as longitude, latitude, and altitude were recorded with a portable global position system where water samples were collected (GPS-China), which were used to calculate the Euclidean distance between sampled sites for analysis of the spatial patterns (Mora-Ruiz et al., 2018). All these detected environmental parameters were measured three times and the average values were used for subsequent analysis.

DNA extraction, 16S rRNA genes amplification and sequence bioinformatics analysis

The total DNA information of microbial community in each water sample was extracted using the CTAB methods (Kubo et al., 2014). DNA was purified using 1% (w/v) agarose gel electrophoresis for further amplification reactions. The fragment of V4 region of bacterial 16S rRNA genes were amplified using the universal primers 515F (5′-GTGCCAGCMGCCGCGGTTA-3′) and 806R (5′-GGACTACHVGGGTWTCTAAT-3′) (Caporaso et al., 2010). All DNA PCR reactions were carried out in a 50 μl reaction volume, containing 25 μl of 2x Taq PCR mix, 3 μl Primer F (10 μM), 3 μl Primer FR (10 μM), 3 μl diluted DNA and 16 μl double distilled H_2O. The cycling processes include pre-denaturation for 60 s at 98°C, followed by 34 cycles of denaturation at 94°C for 60 s, annealing at 57°C for 45 s, extension at 72°C for 60 s, and a final extension at 72°C for 10 min. After the amplification reactions, PCR products were checked in 2% (w/v) agarose gel by electrophoresis and purified using AxyPrep DNA gel extraction Kit (AxyGEN, Union City, CA, United States). Amplicons were stored at −20°C and sequenced on an Illumina HiSeq platform using the 2 bp × 250 bp paired-end read protocol at Novogene bioinformatics technology Co., Ltd. (Beijing, China). The raw sequencing data of each sample were trimmed and merged using Trimmomatic (v.0.33) and FLASH (v1.2.7, http://ccb.jhu.edu/software/FLASH/) (Wang et al., 2021). The low-quality sequencing data with average quality scores less than 20 and with a sequence length less than 75% of the tag length were removed from the obtained raw sequence. Subsequently, the corrected sequences were arranged into the same operational taxonomic units (OTUs) at a 3% threshold of sequence dissimilarity level ($OTU_{0.03}$) using UPARSE (v7.0.1001, http://www.drive5.com/uparse/) and the singletons were removed. The effective sequences for each OTU were packed for annotating corresponding taxonomic information using the

SILVA v138 high quality ribosomal RNA database by the ribosomal data project (RDP) classifiers (threshold 0.8) using the "*cluster*" command in MOTHUR (Zhao et al., 2016; Jiao et al., 2020). The raw sequencing data were submitted to the NCBI (http://www.ncbi.nlm.nih.gov) Sequence Read Archive under Bioproject number PRJNA728144.

Statistics analysis

Non-parametric (Kruskal-Wallis) test was employed to test the difference of physicochemical parameters of water. Before performing sequence statistical analysis, the number of sequences was normalized by the sample with the smallest number (60779) of sequences (Zhong et al., 2016). Hill numbers including Richness index, Shannon index, Simpson index and Pielou evenness index were calculated to evaluate the α-diversities of bacterial communities in each geographical region (QD, YRH, and HX) using the packages of "hilldiv" (Hill 1973; Chao et al., 2010). The Mann-Whitney *U* test was used to examine the difference of alpha diversity between any two regions and the results of p-value < 0.05 were considered as significant (Li et al., 2019). The rarefaction curves were used to identify the sampling depth of a community, and to evaluate the reliability of sequences data of each water sample (Mania et al., 2019). The Pearson's and Spearman's correlations between environmental factors and alpha-diversity indices and relative abundances of top 10 phyla in the bacterial community in the three regions were calculated respectively using the "vegan" packages.

Principal coordinate analysis (PCoA) and permutational multivariate analysis of variance (PERMANOVA) were performed to reveal the regional differences in bacterial community structures based on the Bray-Curtis distance (Xia et al., 2020). We used permutation multivariate dispersion (PERMDISP) to test the dispersions of the data (Banerjee et al., 2019; Cadena et al., 2019). The taxa of the water bacterial biomarkers were identified using linear discriminant analysis (LDA) and the effect size algorithm (LEfSe) in the Novogene analysis platform. Variance inflation factors (VIFs) were used to identify the multi-collinearity among abiotic factors. Based on the results of calculated detrended correspondence analysis (DCA), the abiotic factors with VIFs values less than 10 were selected for redundancy analysis (RDA) to investigate the relationship between environmental factors and bacterial community composition (Zeng et al., 2019). Variation partitioning analysis (VPA) was used to evaluate the importance of water physicochemical and geographical factors in determining bacterial community composition with spatial factors generated using the principal coordinates of neighbor matrices (PCNM) analysis (Liu et al., 2020). Furthermore, Mantel and partial Mantel tests with 999 permutations were performed to test the contributions of water physicochemical/geospatial factors to the bacterial community composition variability in each region (Li et al., 2019).The geographic distances and the Bray-Curtis similarity of bacterial community for two pairing sampling points were calculated to reveal the distance decay patterns of bacterial community structures in the three regions and all regions using the "geosphere" and "vegan" packages (Zeng et al., 2019).

For bacterial networks, only OTUs with average of relative abundance larger than 0.01% that exist in at least 50% of all samples in each region were chosen to construct the bacterial network (Zeng et al., 2019). Furthermore, the relationships between OTUs with Spearman's correlation coefficient $r > 0.8$ or $r < -0.8$ and Benjamini-Hochberg $p < 0.01$ were selected for network construction (Zhao et al., 2016; Ji et al., 2019; Ren et al., 2021b). Networks were analyzed and visualized using the "igraph" package and Gephi platform (https://gephi.org/) (Zhou et al., 2019). Mean degree, clustering coefficient, modularity, average path length, network diameter, graph density, and robustness were calculated to describe topological characteristic of the networks. The nodes in networks represent OTUs and the edge represent relationships between two OTUs. Mean degree is the average number of connected edges of each node (Jiao et al., 2020). Clustering coefficient refers to the degree of nodes which tend to cluster together in network. Modularity is the degree that a network can be divided into modules. A modularity value larger than 0.4 indicates that network have a modular structure (Jiao et al., 2020; Tu et al., 2020). Average path length and network diameter are the mean of the length of the shortest path and the largest distance between any two nodes in a network, respectively (Banerjee et al., 2019; Jiao et al., 2020). Graph density is the ratio of the edge number over the possible edge number (Jiao et al., 2020). Robustness and vulnerability are estimated to reflected network stability (representing the ability of network to resist external interference) by randomly removing 50% of nodes and the nodes with maximal vulnerability in each region (Chen and Wen 2021; Liu et al., 2022).

We used among module connectivity (Pi) and within module connectivity (Zi) plot to reveal the topological roles of network nodes (Jiao et al., 2020). According to the values of Zi and Pi, all OTUs in network could be divided into peripherals ($Pi \leq 0.62$; $Zi \leq 2.5$), connectors (nodes in networks connecting different modules, $Pi > 0.62$; $Zi \leq 2.5$), module hubs (highly connected nodes in modules, $Pi \leq 0.62$; $Zi > 2.5$), and network hubs (highly connected nodes in network, $Pi > 0.62$; $Zi > 2.5$) (Deng et al., 2012; Li et al., 2021). Network hubs, module hubs, and connectors are defined as keystones in network, so OTUs associated with these nodes are considered as the keystone species in the bacterial community (Olesen et al., 2007). All the above analyses are calculated in R (v. 4.1.3) except the LEfSe analysis.

TABLE 1 Water physicochemical parameters of three regional groups on the QTP in July 2020. The data represent the mean values of samples in each regional group with standard deviation.

Parameters (units)	QD mean ± SD	YRH mean ± SD	HX mean ± SD	*P*
	Min—Max	Min—Max	Min—Max	
Temp	11.22 ± 3.17	10.25 ± 2.64	7.14 ± 4.67	< 0.01
(°C)	5.48–18.17	6.63–15.27	1.78–17.09	
pH	9.41 ± 0.38	9.30 ± 0.10	9.59 ± 0.40	> 0.05
—	8.80–10.10	8.53–9.83	9.03–10.16	
DO	5.89 ± 1.88	7.25 ± 1.92	6.74 ± 1.15	> 0.05
(mg. L^{-1})	1.56–8.56	3.02–10.04	4.59–9.93	
EC	24.06 ± 24.71	0.82 ± 1.33	3.88 ± 3.06	< 0.001
($mS.cm^{-1}$)	0.23–75.10	0.27–5.96	0.40–11.05	
ORP	153 ± 208	114 ± 55	79 ± 32	< 0.05
(mV)	−108–814	−83–167	-23–118	
TDS	20562 ± 21167	771 ± 1327	4111 ± 3343	< 0.001
(mg. L^{-1})	200–63275	244–5886	397–11490	
Turb	113.87 ± 143.49	58.26 ± 92.36	106.09 ± 182.48	> 0.05
(NTU)	1.84–482.18	2.45–371.52	1.23–655.75	
SAL	21.27 ± 23.50	0.62 ± 1.15	3.50 ± 2.98	< 0.001
(ppt)	0.15–69.88	0.18–5.06	0.3–10.33	
Chl-a	8.71 ± 15.60	3.41 ± 5.46	1.71 ± 1.37	> 0.05
(μg. L^{-1})	0.41–68.17	0.52–22.71	0.53–4.49	
TP	0.02 ± 0.01	0.05 ± 0.13	0.05 ± 0.14	> 0.05
(mg. L^{-1})	0.01–0.05	0.01–0.55	0.01–0.54	
TN	1.86 ± 1.05	1.03 ± 0.22	0.81 ± 0.27	< 0.001
(mg. L^{-1})	0.56–4.60	0.67–1.44	0.52–1.49	
NH_4^+-N	0.17 ± 0.01	0.11 ± 0.06	0.07 ± 0.02	< 0.001
(mg. L^{-1})	0.06–0.39	0.05–0.25	0.04–0.12	
NO_3^--N	0.32 ± 0.28	0.13 ± 0.16	0.06 ± 0.06	< 0.01
(mg. L^{-1})	0.001–1.17	0.004–0.72	0.006–0.20	
NO_2^--N	0.003 ± 0.003	0.002 ± 0.001	0.001 ± 0.001	< 0.01
(mg. L^{-1})	0.001–0.016	0.001–0.005	0.001–0.003	
DOC	9.57 ± 6.61	4.07 ± 1.83	2.42 ± 1.25	< 0.001
(mg. L^{-1})	0.85–22.66	1.31–7.35	0.83–5.05	

Temp, DO, EC, ORP, TDS, turb; SAL, Chl-a, TP, TN, NH_4^+-N, NO_3^--N, NO_2^--N, and DOC represent temperature, dissolved oxygen, electrical conductivity, oxidation reduction potential, total dissolved solids, turbidity, salinity, chlorophyll-a, total phosphorus, total nitrogen, ammonia nitrogen, nitrate nitrogen, nitrite nitrogen, and dissolved organic carbon, respectively. The $mS.cm^{-1}$ and the NTU are the abbreviations of MiliSiemens.cm^{-1} and nephelometric turbidity unit. Bold indicates significant differences of environmental parameters among three regions using the Kruskal-Wallis test. QD: The Qaidam region; YRH: The yellow river headwater region; HX: The hoh xil region.

Results

Physicochemical properties of lake water in the three regions

The values of fifteen physicochemical factors for all water samples in the three regions were summarized in Table 1. Significant differences in water physicochemical parameters were observed in the three regions. Specially, Temp, EC, ORP, and TDS were significantly higher in QD compared to those in YRH and HX ($p < 0.05$), while no significant differences of pH, DO, and Turb were found in the three regions ($p > 0.05$). Moreover, DOC content in QD varied over a wide range from 0.85 to 22.66 mg/L, but less so in YRH (1.31–7.35 mg/L) and HX (0.83–5.05 mg/L). Mean concentrations of TN and TP showed remarkable differences among the three regions ($p < 0.001$). In summary, environmental parameters suggested a large habitat heterogeneity across the three regions.

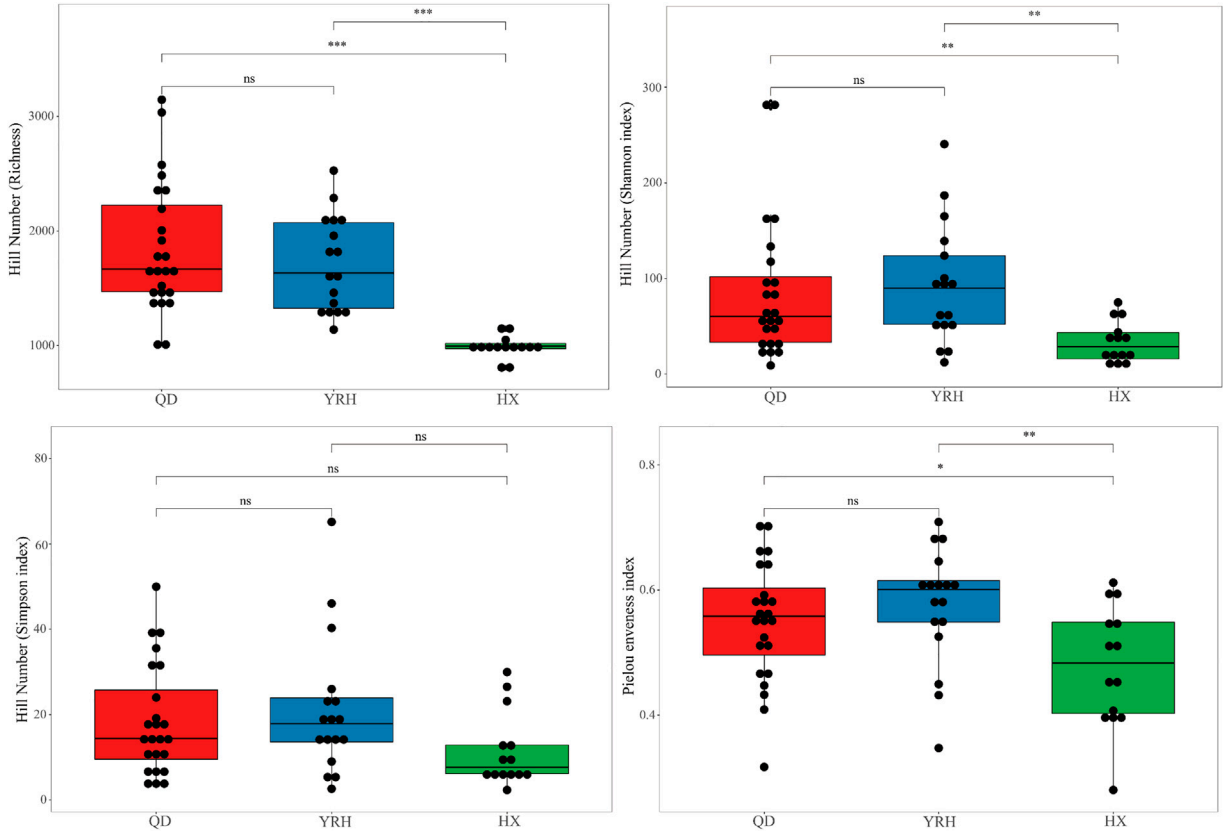

FIGURE 2
Boxplots showing the comparisons of alpha-diversity indices based on Hill numbers in the three regions. *, **, and *** represent the significant level of $p < 0.05$, $p < 0.01$, and $p < 0.001$ using Maun-Whitney U test., respectively. The ns indicates no significant difference in two regions.

Bacterial diversity and composition in the three investigated regions

Analysis of rarefaction curves confirmed that the samples were able to represent the species of each lake (Supplementary Figure S2A) with the observed species numbers reach plateaus. After checking and removing the low-quality sequences, a total number of 4,843,690 effective reads were obtained from all water samples in the three regions. These effective reads were clustered into a total of 20,222 OTUs distributed among 83 phyla. As shown in Supplementary Figure S2B, the total number of OTUs for QD, YRH, and HX regions were 9,594, 6,868, and 3,760, respectively. According to Supplementary Figure S2B, the proportion of shared OTUs numbers was 13.28% in the three investigated regions. The proportions of shared OTUs numbers were 26.07% between QD and YRH, 22.57% between QD and HX, and 29.71% between YRH and HX, respectively. The proportions of unique OTUs were 24.60% in QD, 10.41% in YRH, and 1.35% in HX.

Comparison analysis of four alpha diversity indices in the three regions, including the Hill Richness, Hill Shannon index, Hill Simpson index and Pielou's evenness index, were presented in Figure 2. The highest Hill Shannon index, Hill Simpson index, and Pielou's evenness index indicated high diversity and even distribution of the bacterial community in YRH. The highest Hill Richness reflected high abundance of bacterial in QD. The four alpha diversity indices of bacterial community were the lowest in HX (Figure 2). The indices for the bacterial community in HX were significantly lower than those in QD and YRH except the Hill Simpson index (Mann-Whitney U test $p < 0.05$). The four alpha diversity indices in QD and YRH did not have significant differences (Mann-Whitney U test $p > 0.05$).

The top 10 phyla consist of Bacteroidetes (mean relative abundance, QD = 21.12%, YRH = 19.46%, and HX = 46.06%), Proteobacteria (QD = 42.45%, YRH = 43.64%, and HX = 38.13%), Cyanobacteria (QD = 3.5%, YRH = 20.57%, and HX = 4.47%), Firmicutes (QD = 12.13%, YRH = 1.24%, and HX = 0.99%), Actinobacteria (QD = 15.07%, YRH = 8.08%, and HX = 8.69%), Verrucomicrobia (QD = 1.27%, YRH = 3.48%, and HX = 1.04%), Planctomycetes (QD = 0.59%, YRH = 1.29%, and HX = 0.16%), Acidobacteria (QD = 0.41%, YRH =

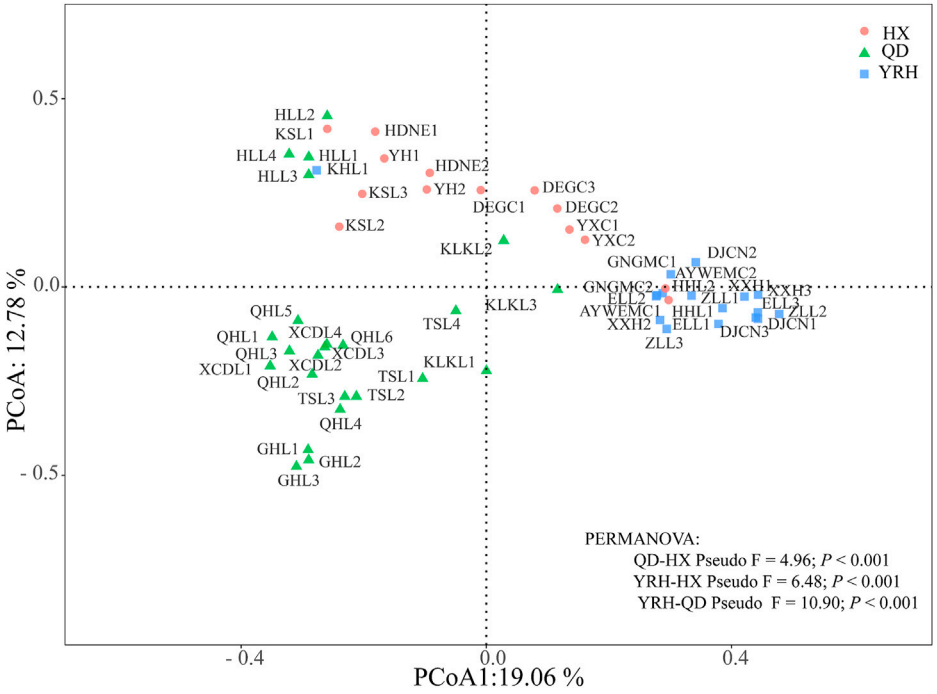

FIGURE 3
Principal coordinate analysis (PCoA) showing the compositional difference of bacteria community in the three regions based on the OTU level.

0.61%, and HX = 0.08%), Chloroflexi (QD = 0.78%, YRH = 0.57%, and HX = 0.09%), and Gemmatimonadetes (QD = 0.28%, YRH = 0.25%, and HX = 0.05%) (Supplementary Figure S3A). Proteobacteria was the dominated phylum in QD and YRH, while Bacteroidetes was the dominated phylum in HX. Meanwhile, bacterial communities also exhibited compositional differences at different sample points within the same lake. For example, the dominant phylum at QHL4 (sampling point 4 of the Qinghai lake) was Firmicutes (64.36%), but was Proteobacteria (42.62%) at QHL6 (Supplementary Figure S4), which suggested that the distributions of bacteria was heterogeneous in larger lakes.

The results of PCoA indicated that bacterial community compositions tend to cluster together in each region and the first two axes of the PCoA contributed 19.06% and 12.78% of the variance observed among three regions. PERMANOVA results also supported this observation and confirmed the significant differences of bacterial community compositions among three regions (Figure 3). Pairwise comparison with PERMDISP indicated that bacterial community compositions of lakes were significantly different between QD and YRH ($F = 16.25$, $p = 0.001$), and QD and HX ($F = 11.15$, $p = 0.004$). It is suggested that bacterial community in QD had different spatial dispersion compared with YRH and HX. However, there were insignificant difference between YRH and HX ($F = 1.24$, $p = 0.282$), indicating homogenous dispersion of bacterial community composition in these two regions.

Four phyla, eleven orders and nine families were screened out across all water samples for determining the indicator and biomarkers of bacterial communities using the LEfSe algorithm (Figure 4A). At the phylum level, Firmicute was found as the indicator in QD, Cyanobacteria and Verrucomicrobia were two phyla indicators in YRH, and Bacteroidetes was the indicator in HX. There are 10 biomarkers (taxonomic) in YRH, 14 biomarkers in QD, and 19 biomarkers in HX (i.e., colored circles in Figure 4A) with significantly different abundances identified (Figure 4B).

Effects of environmental parameters on bacterial diversity and composition in the three regions

Pearson's correlations between bacterial alpha diversity indices and environmental variables of sampled lakes for all three regions were calculated as shown in Supplementary Figure S5. For all three regions, bacterial diversity and richness had negative correlations with altitude and pH ($p < 0.01$), but positive relationships with longitude, Temp, ORP, TN, DOC, and NH_4^+-N ($p < 0.05$). The

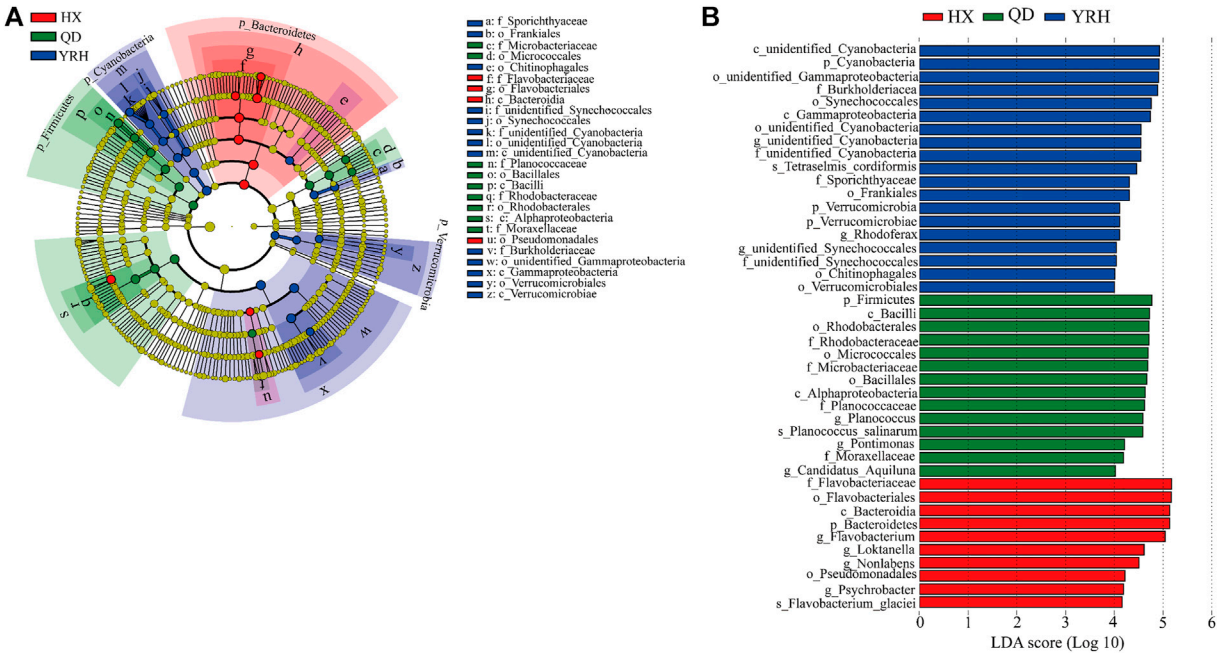

FIGURE 4
(A): Taxa cladogram comparison of bacterial communities in the three regions. (The circles from innermost to outermost represent the phylum level to the species level); **(B)** Linear discriminant analysis (LDA) of effective size of bacterial communities in the three regions.

environmental variables influencing bacterial diversity indices in each region were different. Latitude, DO, and altitude had significant negative relationship with bacterial richness and diversity, whereas Temp, ORP, Chl-a, and DOC showed positive relationship with bacterial richness and diversity in QD. In YRH, longitude, altitude, EC, TDS, and SAL had significant influences on bacterial diversity and richness. DO, EC, TDS, SAL, pH, and Chl-a were the significant factors in affecting bacterial diversity and richness in HX.

Results of redundancy analysis revealed that 40.94%, 52.92%, and 73.84% of the total variability of bacterial community in QD, YRH, and HX were explained by the first two principal components (RDA1 and RDA2, Supplementary Figure S7). Among all environmental factors assessed, altitude (*envfit* test: $r^2 = 0.513$, $p = 0.003$), TN (*envfit* test: $r^2 = 0.436$, $p = 0.021$), and pH (*envfit* test: $r^2 = 0.702$, $p = 0.003$) had the greatest impact on community structure of bacterial in QD, YRH, and HX, respectively (Supplementary Figure S7). Combining water samples from all of the three regions, the first two principal components in RDA explained 37.59% of the overall variability of bacterial community structure and altitude had the greatest influence on the bacterial community structure (*envfit* test: $r^2 = 0.702$, $p = 0.001$). To decouple the effects of geographical factors and water physicochemical factors on water bacterial compositions, variance partition analysis (VPA) was performed at the OTU level. The results showed that

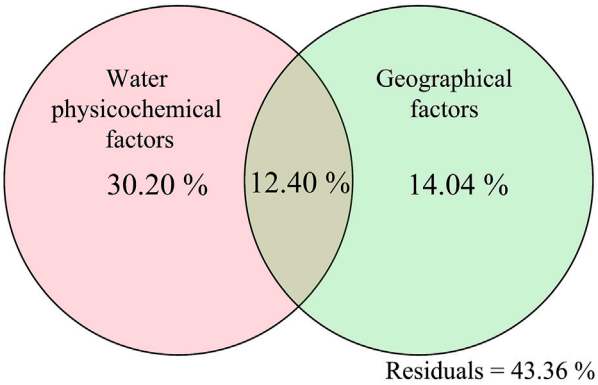

FIGURE 5
Variation partition analysis (VPA) diagram of geographical factors and water physicochemical factors in determining bacterial composition variations.

physicochemical properties of water had larger effects on water bacterial abundances (30.20%) compared to geographical factors (14.04%, Figure 5). Additionally, Mantel and partial Mantel tests confirmed that the bacterial community composition in QD and HX regions were related to both geographical factors (QD: $r = 0.221$; $p = 0.018$ and HX: $r = 0.505$; $p = 0.001$) and water physicochemical factors (QD: $r = 0.420$; $p = 0.001$ and HX: $r = 0.536$; $p = 0.001$,

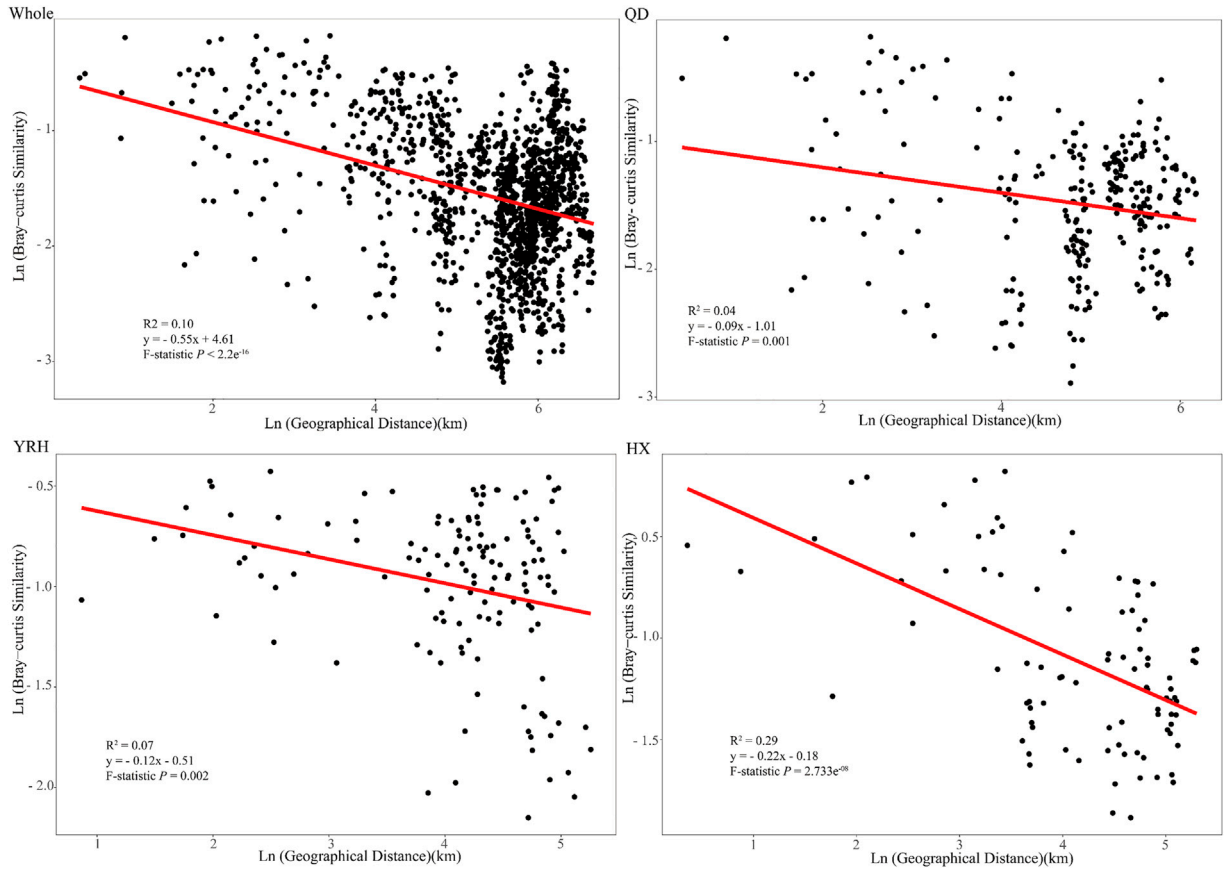

FIGURE 6
The relationship between bacterial community similarity (Bray-Curtis) and geographic distance (Euclidean distance) between any two sampling sites in each region.

Supplementary Table S2). However, the geographical factors showed insignificant impact on bacterial community structure in YRH (Supplementary Table S2), which might be due to the small geographical range of the sampled lakes in this region. It was worth noting that the contribution of uncertain factors reached 43.36%, implying that some unmeasured environmental factors might be vital as well in affecting the bacterial community composition of the lakes (Williams 1998; Chakraborty et al., 2020; Gu et al., 2020; Liu et al., 2021).

Distance decay patterns of bacterial community are the results of environmental filtering (environmental factors) and dispersal limitation (geographic factors). In general, the slope of the distance decay relationship can reflect the turnover rate of bacterial community spatially. Our results showed that the Bray-Curtis similarity of bacterial communities in each region decayed with geographic distance. This suggested that the bacterial community was not randomly dispersed in each region. The slope in HX was the steepest compared to those in QD and YRH (Figure 6), which indicated that there was the highest turnover rate of bacterial communities in HX.

Bacterial networks in the three regions

To explore the relationship among OTUs, we constructed networks in each region using species-species correlations and calculated characteristic values of network topology, as shown in Figure 7 and Supplementary Table S3. Bacterial networks in the three regions consisted of 196 nodes and 812 edges (QD), 135 nodes and 421 edges (YRH), and 102 nodes and 329 edges (HX), respectively (Figure 7). Overall, there were more positive relationships than negative ones in each region, which suggested that taxa tended to co-occur rather than exclude each other. Zi-Pi plots showed that Firmicutes and Bacteroidetes phyla were the keystone taxa (module hubs) in QD and HX, but the nodes in YRH did not reach the threshold for module hubs. There were 29, 20, and 20 connectors in QD, YRH, and HX.

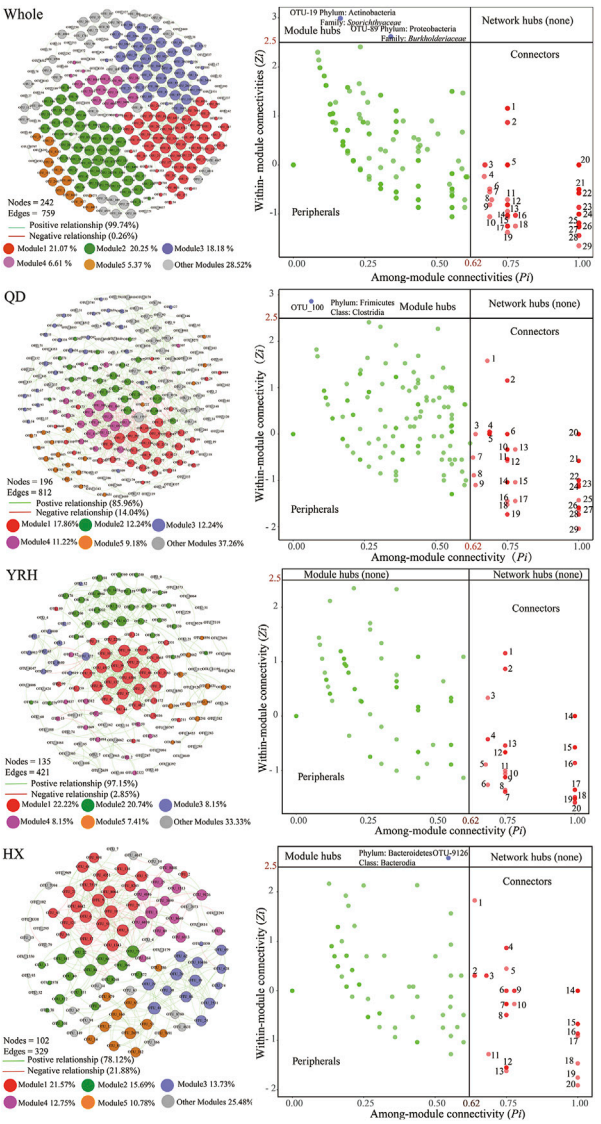

FIGURE 7
The co-occurrence networks among OTUs (left panel) and Zi-Pi plot showing the distribution of OTUs (right panel) in the whole and the three regions based on Spearman's rank correlations ($r > 0.8$ or $r < -0.8$ $p < 0.01$) and their topological roles, respectively. The size of each node is proportional to the number of connections (i.e., degree), and the nodes are colored according to different types of modularity classes. Each node represents an OTU. Edges with green or red colors represent positive or negative relationship between any two OTUs.

Furthermore, the results demonstrated different topological characteristics among the three regions and the network in QD was more complex than those in YRH and HX (represented by numbers of nodes and edges) (Wang et al., 2021). The bacterial community had the highest robustness and lowest vulnerability values in HX (Supplementary Table S3). This indicated that the bacterial network in this region was more stable compared to those in the other two regions.

Discussion

Relationship between bacterial alpha diversity and environmental factors and their differences in the different regions

There are significant differences in salinity in the three regions (averagely 21.27 ppt in QD, 3.50 in HX, and 0.62 in YRH), and we suspect that salinity is the main driving force on the bacterial diversity in the three regions as also suggested in previous studies (Yang et al., 2016a; Zhong et al., 2016). Salinity had different effects on the bacterial diversity indices of lakes in QD, YRH, and HX according to our data (Supplementary Figure S5). Salinity was positively correlated with bacterial alpha diversity in QD, but negatively correlated with bacterial alpha diversity in YRH and HX regions (Supplementary Figure S5). The response of bacterial abundance and diversity to changes in salinity in YRH and HX regions follows the "general survival theory" that more extreme habitats lead to loss of microbial diversity. Generally, higher salinity in habitats increases extracellular osmosis pressure in bacteria, making the bacteria less active or even leading bacterial death. These further lead to loss of bacterial richness and diversity (Mo et al., 2021). However, the positive relationship between bacterial alpha diversity and salinity in QD is not consistent with the "general survival theory". Possible explanations are as follows: 1) the niche availability for halotolerant bacterial in lakes in QD increased with increasing salinity (Wang et al., 2011); 2) some bacterial groups can adapt to the high salinity habitats in lakes in QD which have survived under the stress of extreme salinity for a long time (Mo et al., 2021).

Bacterial community composition and drivers

Our data showed that the top four bacteria phyla were Proteobacteria (42.43%), Bacteroidetes (21.51%), Actinobacteria (15.07%), and Firmicutes (12.13%) in QD, Proteobacteria (43.64%), Cyanobacteria (20.57%), Bacteroidetes (19.46%), and Actinobacteria (8.08%) in YRH, and Bacteroidetes (46.07%), Proteobacteria (38.13%), Actinobacteria (8.70%), and Cyanobacteria (4.48%) in HX (Supplementary Figure S3A). The relative abundance of Proteobacteria in the three regions was relatively high, which indicated that Proteobacteria were not sensitive to the extreme habitat of the plateau. This was consistent with the result of many previous studies which found Proteobacteria to be the dominant phylum in lakes (Jiang et al., 2019; Chakraborty et al., 2020). The

relative abundance of Proteobacteria in HX was lower than those in QD and YRH (Supplementary Figure S3A). As shown in Supplementary Figure S8, the relative abundances of Proteobacteria in QD and YRH were significantly correlated with ORP and NO_3^--N, and with TN and NO_3^--N in HX. In addition, the concentrations of ORP and NO_3^--N in QD and YRH were significantly different and the TN and NO_3^--N concentrations in HX were lower than those in QD and YRH (Table1). Therefore, the difference in the relative abundance of Proteobacteria in the three regions might be caused by the significant differences in ORP, NO_3^--N, and TN concentrations in different regions.

Bacteroidetes was the most abundant phylum in HX possibly because protorhodopsin in their cells could enhance their adaptability to the oligotrophic conditions of lakes in HX (Wang et al., 2020). The relative abundances of Actinobacteria in YRH and HX regions were similar, but were lower than that in QD. The relative abundance of Actinobacteria had significant negative relationships with DO and pH, but significant positive relationships with SAL, DOC, and TN (Supplementary Figure S8). Thus, the lower DO concentration and higher concentrations of SAL, DOC, and TN in QD may be beneficial to the survival of Actinobacteria leading to their higher relative abundance. It is worth noting that the relative abundance of Firmicutes, which can be used as an indicator of fecal pollution, is relatively high in the Qinghai lake, the Tuosu lake, and the Kelvke lake in QD (Supplementary Figure S6), implying that water quality of these lakes are threatened by livestock fecal (Zhang et al., 2020a). The concentrations of TN and NO_3^--N in these three lakes are the highest when compared with all other sampling sites in QD (Supplementary Table S1).

At the class level, the dominant bacteria in the QD and YRH regions were *Gamma-proteobacteria*, and the dominant bacteria in HX was *Bacteroidia* (Supplementary Figure S3B). The class of *Gamma-Proteobacteria*, one member of Proteobacteria phyla, was known as the typical anti-disturbance taxa and the most abundant class present in eutrophic lakes, which contributed to nitrogen fixation, sulfur metabolism, methane metabolism, and salinity reduction of brackish lakes (Zhang et al., 2020b; Chakraborty et al., 2020; Wang et al., 2020). However, previous research reported that the dominant species was *Beta-proteobacteria* (37.2%) in a Tibet glacial stream and lake (Gu et al., 2020). Further analysis of the differences between the bacterial habitats in our study and in Gu et al. (2020) showed that the mean water temperature, TN, and DOC concentrations in QD and YRH regions were higher than those in Gu et al. (2020). We suspect that the inconsistency of the results may be due to the differences in habitat conditions, hydrological characteristics, and recharge water sources (Freimann et al., 2015).

Consistent with previous studies (Zhong et al., 2016; Gu et al., 2020; Tolotti et al., 2020; Yang et al., 2020), our findings showed that altitude, TN, and pH were the most important factors in determining bacterial composition variations in the three regions. In general, the effect of different altitudes on bacterial community structure is manifested in two aspects. Firstly, the changes in altitude lead to changes in the physicochemical factors of water (such as water temperature and DO concentration) (Supplementary Figure S5). Secondly, geographic isolation between habitats caused by altitude hinders the dispersal of bacteria between habitats, resulting in differences in bacterial community between lakes (Zhang et al., 2020c; Shi et al., 2020). It could be seen that altitude and the related environmental factors had significant correlations with the bacterial abundance of lakes in QD from Supplementary Figure S8. It is likely that the altitudinal effect on bacterial community structure of lakes in QD is through changing physicochemical properties of the lake water bodies. TN was the most robust driver in determining bacterial community composition in the investigated lakes in YRH (Supplementary Figure S7). Nitrogen is considered as the most important macronutrient for bacterial cellular processes (i.e., photosynthesis, respiration, energy storage and transfer, and cell division) responsible for primary production and formation of algal blooms (Wang et al., 2020; Xia et al., 2020). Variance of bacterial community structure in HX was mainly driven by pH (Supplementary Figure S7). The variations of pH value can alter the availability of nutrients and the characteristics of DOC in the habitat, and therefore affect the growth and metabolism of heterotrophic bacteria (Wang et al., 2020).

Biogeography distribution patterns and their differences in the different regions

With the increases of geographical distances, the Bray-Curtis similarity of bacterial communities decreased significantly in each region and in all the three regions (Figure 6). This was consistent with a previous study which reported geographic patterns of bacterial community in 23 lakes on the western of the Tibetan Plateau (Liu et al., 2020). However, the spatial turnover rate (represented by the slope of the fitted curve: 0.55) of bacterial community in our study was much higher than that in Liu et al. (2020), which was 0.14, indicating that bacterial community of lakes in this study are subject to stronger dispersal limitation and environmental filtering (Liu et al., 2018). The salinity gradient (0.15-69.88) between lakes in our study was larger than that in Liu et al. (2020) (0.01-47.8), and range of geographical distance in our study (1.4–799 km) is smaller than that in Liu et al. (2020) (0.5–1000 km). This indicated that the effects of salinity gradient on the bacterial community geographic patterns in the plateau lakes was greater compared to geographical distance, which was further supported by VPA results (Figure 5).

Further analysis of the distance decay relationship of bacterial community in each region showed that the order of bacterial community spatial turnover rate in the three regions were as follow: HX > YRH > QD (Figure 6), indicating that the

bacterial community in HX was highly sensitive to changes in geographical factors and water physicochemical factors compared to those in YRH and QD. This could be further confirmed by the Mantel and Partial results (HX: Mantel r = 0.469; YRH: Mantel r = 0.369; QD: r = 0.434, Supplementary Table S2). Furthermore, our result showed that the variation of salinity in QD was largest, followed by HX and YRH regions and only changes of Temp and Turb in HX were largest (Table1), which implied that the higher bacterial community spatial turnover rate in HX was related to the higher Temp and Turb gradients. Interestingly, the spatial turnover rate of bacterial community in QD was the smallest, while the correlation coefficient between bacterial community and environmental factors in QD was greater than that in YRH. Therefore, we speculated that it might be attributed to larger hydraulic connectivity of different sampling lakes in QD (Figure 1). Larger hydraulic connectivity created more homogenous environmental conditions for bacteria among different lakes, which led to less taxonomic differences spatially in QD (Liu et al., 2018).

Co-occurrence network of bacterial community and their differences in the different regions

Bacterial interactions play key roles in affecting bacterial community composition and its geographical distribution. We constructed bacterial networks to analyze the relationship between bacterial species as well as their ecological roles (Liu et al., 2020). The value of topological parameters reflects the complexity of network. The positive relationships represent mutual symbiosis and parasitism relationships and the negative correlations reflect predation and competition among bacterial species (Mo et al., 2021; Wang et al., 2021). We found that the proportion of positive correlations (99.74%) between bacterial species in the plateau lakes was much higher than the proportion of negative ones (0.26%), which indicated that there was niche sharing among bacterial species in the plateau lakes (Zeng et al., 2019). Compared with the bacterial network in low-altitude lakes (Jiao et al., 2020), the proportion of negative correlations between nodes in bacterial network in high-altitude lakes was smaller, indicating that there was less competition among bacterial species in high-altitude lakes. According to a previous study (Zeng et al., 2019), a higher proportion of competitive correlations among bacterial species may enhance the stability of the network under environmental perturbations. Hence, bacterial networks in high-altitude lakes may be more susceptible to environmental changes than bacterial networks in low-altitude lakes.

Additionally, we found that the complexity of bacterial network in QD was much higher than those in YRH and HX regions by comparing the bacterial networks in the three regions. We speculate that there are several possible reasons for this. Frist, the higher bacterial richness and diversity in QD can increase the interaction between bacterial species and complicate their network. Second, based on the findings of Ji et al. (2019), we suggest that the high salinity of lakes in QD increase the complexity of the bacterial network in their lakes. Complexity of bacterial network was proposed to be affected by high salinity through increasing cooperation or competition among bacterial species (Yang et al., 2020).

Key species (nodes with the most connections to other nodes in a network) in bacterial networks play an important role in maintaining the network structure (Deng et al., 2012). Relevant research results showed that removal or disappearance of key species in bacterial network could cause the bacterial network structure to change rapidly and even lead to network collapse (Zhou et al., 2020). Our results showed that the key species in QD and HX regions were *Clostridia* and *Bacterodia*, while the nodes in the bacterial network in YRH did not reach the threshold for key species. This suggests an increased possibility of disappearance of modules or decomposition of network in YRH owing to the absence of key species. The key species of the bacterial network in QD (*Clostridia*) can tolerate higher salinity in the habitat and decompose carbohydrates into organic acids. The protorhodopsin produced by the key species of the bacterial network in HX (*Bacterodia*) helps it to survive in the lakes in HX with low nutrient concentrations (Table1) and promote decomposition and fermentation of organic matter in its habitat (Wang et al., 2020).

Conclusion

We analyzed the differences in bacterial diversity, composition, geographical distribution, and their driving factors in three distinct neighboring regions on the QTP. The results showed that alpha diversity indices of bacterial community in HX were the lowest. The dominant species at the phylum and class levels in QD and YRH were the same, but with different relative abundances. The most abundant species in HX at the phylum and class levels were Bacteroidetes, *Bacteroidia*, and *Flavobacterium*, respectively. Further, community compositions of bacterial were significantly different in QD, YRH, and HX, owing to environmental heterogeneity in the three regions.

The most important factors in driving bacterial community composition at QD, YRH, and HX were altitude, TN, and pH, respectively. Both water physicochemical factors and geographical factors had significant impacts on bacterial community structure in QD and HX, but geographical factors had very small impact on the bacterial community in YRH. Correlation between geographical distance and bacterial similarity in HX was stronger than those in QD and YRH. Network analysis revealed that the bacterial community

networks in the three regions were different in their structure, complexity, and stability. Bacterial communities in QD and HX had the most complex and stable networks, respectively.

Data availability statement

The datasets presented in this study can be found in online repositories. The names of the repository/repositories and accession number(s) can be found in the article/Supplementary Material.

Author contributions

DW performed investigation, visualization, and writing of the original draft. YH performed conceptualization, writing, supervision and funding acquisition. SZ performed conceptualization, writing, and supervision. SL, TW, and HY reviewed and revised the mansucript.

Funding

This study was supported by Major Basic Research Development Program of the Science and Technology Agent, Qinghai Province (2019-SF-146), The Young & Mid-aged Scientific Research Fund Project of the Qinghai university (2018-QGY-9) and the Open Research Foundation Supported by State Key Laboratory of Hydroscience and Engineering-Tsinghua University (sklhse-2019-A-04).

Conflict of interest

The authors declare that the research was conducted in the absence of any commercial or financial relationships that could be construed as a potential conflict of interest.

The reviewer SL declared a shared affiliation with the authors SL and TW to the handling editor at the time of review.

Publisher's note

Supplementary material

The Supplementary Material for this article can be found online at: https://www.frontiersin.org/articles/10.3389/fenvs.2022.1033160/full#supplementary-material

References

Banerjee, S., Walder, F., Buchi, L., Meyer, M., Held, A. Y., Gattinger, A., et al. (2019). Agricultural intensification reduces microbial network complexity and the abundance of keystone taxa in roots. *ISME J.* 13, 1722–1736. doi:10.1038/s41396-019-0383-2

Cadena, S., Aguirre-Macedo, M. L., Cerqueda-García, D., Cervantes, F. J., Herrera-Silveira, J. A., and Garcia-Maldonado, J. Q. (2019). Community structure and distribution of benthic bacteria and archaea in a stratified coastal lagoon in the southern gulf of Mexico. *Estuar. Coast. Shelf Sci.* 230, 106433. doi:10.1016/j.ecss.2019.106433

Caporaso, J. G., Kuczynski, J., Stombaugh, J., Bittinger, K., Bushman, F. D., Costello, E. K., et al. (2010). Qiime allows analysis of high-throughput community sequencing data. *Nat. Methods* 7 (5), 335–336. doi:10.1038/nmeth.f.303

Chakraborty, J., Sapkale, V., Shah, M., Rajput, V., Mehetre, G., Agawane, S., et al. (2020). Metagenome sequencing to unveil microbial community composition and prevalence of antibiotic and metal resistance genes in hypersaline and hyperalkaline lonar lake, India. *Ecol. Indic.* 110, 105827. doi:10.1016/j.ecolind.2019.105827

Chao, A., Chiu, C. H., and Jost, L. (2010). Phylogenetic diversity measures based on hill numbers. *Phil. Trans. R. Soc. B* 365, 3599–3609. doi:10.1098/rstb.2010.0272

Chen, L. M., Liu, S. T., Chen, Q., Zhu, G. B., Wu, X., Wang, J. W., et al. (2019). Anammox response to natural and anthropogenic impacts over the yangtze river. *Sci. Total Environ.* 665, 171–180. doi:10.1016/j.scitotenv.2019.02.096

Chen, W. D., and Wen, D. H. (2021). Archaeal and bacterial communities assembly and co-occurrence networks in subtropical mangrove sediments under spartina alterniflora invasion. *Environ. Microbiome* 16, 10. doi:10.1186/s40793-021-00377-y

Deng, Y., Jiang, Y. H., Yang, Y. F., He, Z. L., Luo, F., and Zhou, J. Z. (2012). Molecular ecological network analyses. *BMC Bioinforma.* 113, 113. doi:10.1186/1471-2105-13-113

Freimann, R., Burgmann, H., Findlay, S. E., and Robinson, C. T. (2015). Hydrologic linkages drive spatial structuring of bacterial assemblages and functioning in alpine floodplains. *Front. Microbiol.* 6, 1221. doi:10.3389/fmicb.2015.01221

Gu, Z. Q., Liu, K. S., Pedersen, M. W., Wang, F., Chen, Y. Y., Zeng, C., et al. (2020). Community assembly processes underlying the temporal dynamics of glacial stream and lake bacterial communities. *Sci. Total Environ.* 761, 143178. doi:10.1016/j.scitotenv.2020.143178

Han, R., Zhang, X., Liu, J., Long, Q. F., Chen, L. S., Liu, D. L., et al. (2017). Microbial community structure and diversity within hypersaline keke salt lake environments. *Can. J. Microbiol.* 63, 895–908. doi:10.1139/cjm-2016-0773

Hill, M. O. (1973). Diversity and evenness: A unifying notation and its consequences. *Ecology* 54, 427–432. doi:10.2307/1934352

Ji, M. K., Kong, W. D., Yue, L. Y., Wang, J. B., Deng, Y., and Zhu, L. P. (2019). Salinity reduces bacterial diversity, but increases network complexity in Tibetan plateau lakes. *FEMS Microbiol. Ecol.* 95, fiz190. doi:10.1093/femsec/fiz190

Jiang, H. C., Deng, S. C., Huang, Q. Y., Dong, H. L., and Yu, B. S. (2010). Response of aerobic anoxygenic phototrophic bacterial diversity to environment conditions in saline lakes and daotang river on the Tibetan plateau, nw China. *Geomicrobiol. J.* 27, 400–408. doi:10.1080/01490450903480269

Jiang, Y. M., Huang, H. Y., Ma, T. L., Ru, J. L, Blank, S., Kurmayer, R., et al. (2019). Temperature response of planktonic microbiota in remote alpine lakes. *Front. Microbiol.* 10, 1714. doi:10.3389/fmicb.2019.01714

Jiao, C. C., Zhao, D. Y., Zeng, J., Guo, L., and Yu, Z. B. (2020). Disentangling the seasonal co-occurrence patterns and ecological stochasticity of planktonic and benthic bacterial communities within multiple lakes. *Sci. Total Environ.* 740, 140010. doi:10.1016/j.scitotenv.2020.140010

Kubo, K., Kojima, H., and Fukui, M. (2014). Vertical distribution of major sulfate-reducing bacteria in a shallow eutrophic meromictic lake. *Syst. Appl. Microbiol.* 37, 510–519. doi:10.1016/j.syapm.2014.05.008

Li, J., Zhu, L. P., Li, M. H., Wang, J. B., and Ma, Q. F. (2020). Origin of modern dolomite in surface lake sediments on the central and Western Tibetan plateau. *Quat. Int.* 544, 65–75. doi:10.1016/j.quaint.2020.02.018

Li, L., Ning, D. L., Jeon, Y., Ryu, H., Santo Domingo, J. W., Kang, D. W., et al. (2021). Ecological insights into assembly processes and network structures of bacterial biofilms in full-scale biologically active carbon filters under ozone implementation. *Sci. Total Environ.* 751, 141409. doi:10.1016/j.scitotenv.2020.141409

Li, Y., Gao, Y., Zhang, W. L., Wang, C., Wang, P. F., Niu, L. H., et al. (2019). Homogeneous selection dominates the microbial community assembly in the sediment of the three gorges reservoir. *Sci. Total Environ.* 690, 50–60. doi:10.1016/j.scitotenv.2019.07.014

Liu, K. S., Hou, J. Z., Liu, Y. Q., Hu, A. Y., Wang, M. D., Wang, F., et al. (2019a). Biogeography of the free-living and particle-attached bacteria in Tibetan lakes. *FEMS Microbiol. Ecol.* 95, fiz088. doi:10.1093/femsec/fiz088

Liu, K. S., Liu, Y. Q., Han, B. P., Xu, B. Q., Zhu, L. P., Ju, T. T., et al. (2019c). Bacterial community changes in a glacial-fed Tibetan lake are correlated with glacial melting. *Sci. Total Environ.* 651, 2059–2067. doi:10.1016/j.scitotenv.2018.10.104

Liu, K. S., Liu, Y. Q., Hu, A. Y., Wang, F., Chen, Y. Y., Gu, Z. Q., et al. (2020). Different community assembly mechanisms underlie similar biogeography of bacteria and microeukaryotes in Tibetan lakes. *FEMS Microbiol. Ecol.* 96, fiaa071. doi:10.1093/femsec/fiaa071

Liu, K. S., Yao, T. D., David, P. A., Jiao, N. Z., Zeng, Y. H., Guo, B. X., et al. (2021). Bacteria in the lakes of the Tibetan plateau and polar regions. *Sci. Total Environ.* 754, 142248. doi:10.1016/j.scitotenv.2020.142248

Liu, S. W., Yu, H., Yu, Y. H., Huang, J., Zhou, Z. Y., Zeng, J. X., et al. (2022). Ecological stability of microbial communities in lake donghu regulated by keystone taxa. *Ecol. Indic.* 136, 108695. doi:10.1016/j.ecolind.2022.108695

Liu, T., Zhang, A. N., Wang, J. W., Liu, S. F., Jiang, X. T., Dang, C. Y., et al. (2018). Integrated biogeography of planktonic and sedimentary bacterial communities in the yangtze river. *Microbiome* 6, 16. doi:10.1186/s40168-017-0388-x

Liu, W. H., Xie, C. W., Zhao, L., Wu, T. H., Wang, W., Zhang, Y. X., et al. (2019b). Dynamic changes in lakes in the hoh xil region before and after the 2011 outburst of zonag lake. *J. Mt. Sci.* 16, 1098–1110. doi:10.1007/s11629-018-5085-0

Luo, D. L., Jin, H. J., Du, H. Q., Li, C., Ma, Q., Duan, S. Q., et al. (2020). Variation of alpine lakes from 1986 to 2019 in the headwater area of the yellow river, Tibetan plateau using Google Earth engine. *Adv. Clim. Change Res.* 11, 11–21. doi:10.1016/j.accre.2020.05.007

Mania, I., Gorra, R., Colombo, N., Freppaz, M., Martin, M., and Anesio, A. M. (2019). Prokaryotic diversity and distribution in different habitats of an alpine rock glacier-pond system. *Microb. Ecol.* 78, 70–84. doi:10.1007/s00248-018-1272-3

Meng, L., Zuo, R., Wang, J. S., Yang, J., Li, Q., Chen, M. H., et al. (2020). The spatial variations of correlation between microbial diversity and groundwater quality derived from a riverbank filtration site, northeast China. *Sci. Total Environ.* 706, 135855. doi:10.1016/j.scitotenv.2019.135855

Mo, Y. Y., Peng, F., Gao, X. F., Xiao, P., Logares, R., Jeppesen, E., et al. (2021). Low shifts in salinity determined assembly processes and network stability of microeukaryotic plankton communities in a subtropical urban reservoir. *Microbiome* 9, 128. doi:10.1186/s40168-021-01079-w

Mora-Ruiz, M. D. R., Cifuentes, A., Font-Verdera, F., Perez-Fernandez, C., Farias, M., Gonzalez, B., et al. (2018). Biogeographical patterns of bacterial and archaeal communities from distant hypersaline environments. *Syst. Appl. Microbiol.* 41, 139–150. doi:10.1016/j.syapm.2017.10.006

Olesen, J. M., Bascompte, J., Dupont, Y. L., and Jordano, P. (2007). The modularity of pollination networks. *Proc. Natl. Acad. Sci. U. S. A.* 104, 19891–19896. doi:10.1073/pnas.0706375104

Ren, Z., Wang, F., Qu, X. D., Elser, J. J., Liu, Y., and Chu, L. M. (2017). Taxonomic and functional differences between microbial communities in qinghai lake and its input streams. *Front. Microbiol.* 8, 2319. doi:10.3389/fmicb.2017.02319

Ren, Z., Zhang, C., Li, X., Ma, K, Feng, K. X, Zhang, Z., et al. (2021a). Abundant and rare bacterial taxa structuring differently in sediment and water in thermokarst lakes in the yellow river source area, qinghai-tibet plateau. *bioRxiv Prepr*.

Ren, Z., Zhang, C., Li, X., Ma, K., Zhang, Z., Feng, K. X., et al. (2021b). Bacterial communities present distinct co-occurrence networks in sediment and water of the thermokarst lakes in the yellow river source area. *Front. Microbiol.* 12, 716732. doi:10.3389/fmicb.2021.716732

Shi, Y., Jiang, Y. Y., Wang, S. Y., Wang, X. M., and Zhu, G. B. (2020). Biogeographic distribution of comammox bacteria in diverse terrestrial habitats. *Sci. Total Environ.* 717, 137257. doi:10.1016/j.scitotenv.2020.137257

Tolotti, M., Cerasino, L., Donati, C., Pindo, M., Rogora, M., Seppi, R., et al. (2020). Alpine headwaters emerging from glaciers and rock glaciers host different bacterial communities: Ecological implications for the future. *Sci. Total Environ.* 717, 137101. doi:10.1016/j.scitotenv.2020.137101

Tu, Q. C., Yan, Q. Y., Deng, Y., Michaletz, S. T., Buzzard, V., Weiser, M. D., et al. (2020). Biogeographic patterns of microbial co-occurrence ecological networks in six American forests. *Soil Biol. Biochem.* 148, 107897. doi:10.1016/j.soilbio.2020.107897

Wang, B. H., Zheng, X. F., Zhang, H. J., Xiao, F. S., Gu, H., Zhang, K. K., et al. (2020). Bacterial community responses to tourism development in the xixi national wetland park, China. *Sci. Total Environ.* 720, 137570. doi:10.1016/j.scitotenv.2020.137570

Wang, J. J., Yang, D. M., Zhang, Y., Shen, J., van der Gast, C., Hahn, M. W., et al. (2011). Do patterns of bacterial diversity along salinity gradients differ from those observed for macroorganisms? *PLoS One* 6, e27597. doi:10.1371/journal.pone.0027597

Wang, S. Y., Liu, W. Y., Zhao, S. Y., Wang, C., Zhuang, L. J., Liu, L., et al. (2019). Denitrification is the main microbial n loss pathway on the qinghai-tibet plateau above an elevation of 5000m. *Sci. Total Environ.* 696, 133852. doi:10.1016/j.scitotenv.2019.133852

Wang, Y. B., Hu, X. K., Sun, Y. Y., and Wang, C. X. (2021). Influence of the cold bottom water on taxonomic and functional composition and complexity of microbial communities in the southern yellow sea during the summer. *Sci. Total Environ.* 759, 143496. doi:10.1016/j.scitotenv.2020.143496

Wang, W. J., Yi, Y. J., Yang, Y. F., Zhou, Y., Zhang, S. H., Wang, X., et al. (2020). Impact of anthropogenic activities on the sediment microbial communities of baiyangdian shallow lake. *Int. J. Sediment Res.* 35, 180–192. doi:10.1016/j.ijsrc.2019.10.006

Wen, Z. D., Song, K. S., Liu, G., Shang, Y. X., Hou, J. B., Lyu, L., et al. (2019). Impact factors of dissolved organic carbon and the transport in a river-lake continuum in the tibet plateau of China. *J. Hydrol. X.* 579, 124202. doi:10.1016/j.jhydrol.2019.124202

Williams, W. D. (1998). Salinity as a determinant of the structure of biological communities in salt lakes. *Hydrobiologia* 381, 191–201. doi:10.1023/a:1003287826503

Wu, Q. L., Zwart, G., Schauer, M., Kamst-van Agterveld, M. P., and Hahn, M. W. (2006). Bacterioplankton community composition along a salinity gradient of sixteen high-mountain lakes located on the Tibetan plateau, China. *Appl. Environ. Microbiol.* 72, 5478–5485. doi:10.1128/AEM.00767-06

Xia, P. H., Yan, D. B., Sun, R. G., Song, X., Lin, T., and Yi, Y. (2020). Community composition and correlations between bacteria and algae within epiphytic biofilms on submerged macrophytes in a plateau lake, southwest China. *Sci. Total Environ.* 727, 138398. doi:10.1016/j.scitotenv.2020.138398

Xie, G. J., Tang, X. M., Shao, K. Q., Hu, Y., Liu, H., Martin, R. M., et al. (2020). Spatiotemporal patterns and environmental drivers of total and active bacterial abundances in lake taihu, China. *Ecol. Indic.* 114, 106335. doi:10.1016/j.ecolind.2020.106335

Xing, P., Hahn, M. W., and Wu, Q. L. (2009). Low taxon richness of bacterioplankton in high-altitude lakes of the eastern Tibetan plateau, with a predominance of bacteroidetes and synechococcus spp. *Appl. Environ. Microbiol.* 75, 7017–7025. doi:10.1128/AEM.01544-09

Xiong, J. B., Liu, Y. Q., Lin, X. G., Zhang, H. Y., Zeng, J., Hou, J. Z., et al. (2012). Geographic distance and ph drive bacterial distribution in alkaline lake sediments across Tibetan plateau. *Environ. Microbiol.* 14, 2457–2466. doi:10.1111/j.1462-2920.2012.02799.x

Yang, J., Jiang, H. C., Sun, X. X., Huang, J. R., Han, M. X., and Wang, B. C. (2020). Distinct co-occurrence patterns of prokaryotic community between the waters and sediments in lakes with different salinity. *FEMS Microbiol. Ecol.* 97, fiaa234. doi:10.1093/femsec/fiaa234

Yang, J., Jiang, H. C., Wu, G., Liu, W., and Zhang, G. J. (2016a). Distinct factors shape aquatic and sedimentary microbial community structures in the lakes of Western China. *Front. Microbiol.* 7, 1782. doi:10.3389/fmicb.2016.01782

Yang, J., Ma, L., Jiang, H. C., Wu, G., and Dong, H. L. (2016b). Salinity shapes microbial diversity and community structure in surface sediments of the qinghai-Tibetan lakes. *Sci. Rep.* 6, 25078. doi:10.1038/srep25078

Yang, J. (2015). *Microbial response to environmental changes in qinghai-Tibetan lakes and its environmental implications*. Wuhan: China university of Geosciences. (In Chinese).

Zeng, J., Jiao, C. C., Zhao, D. Y., Xu, H. M., Huang, R., Cao, X. Y., et al. (2019). Patterns and assembly processes of planktonic and sedimentary bacterial community differ along a trophic gradient in freshwater lakes. *Ecol. Indic.* 106, 105491. doi:10.1016/j.ecolind.2019.105491

Zeng, Q. C., An, S. S., Liu, Y., Wang, H. L., and Wang, Y. (2019). Biogeography and the driving factors affecting forest soil bacteria in an arid area. *Sci. Total Environ.* 680, 124–131. doi:10.1016/j.scitotenv.2019.04.184

Zhang, L., Wang, K. F., Li, X. C., Gao, G., and Jiang, J. H. (2020b). Linking bacterial community shifts with changes in the dissolved organic matter pool in a eutrophic lake. *Sci. Total Environ.* 719, 137387. doi:10.1016/j.scitotenv.2020.137387

Zhang, L., Zhao, F., Li, X. C., and Lu, W. J. (2020a). Contribution of influent rivers affected by different types of pollution to the changes of benthic microbial community structure in a large lake. *Ecotoxicol. Environ. Saf.* 198, 110657. doi:10.1016/j.ecoenv.2020.110657

Zhang, S. B., Qin, W., Xia, X. H., Xia, L. Z., Li, S. L., Zhang, L. W., et al. (2020c). Ammonia oxidizers in river sediments of the qinghai-tibet plateau and their adaptations to high-elevation conditions. *Water Res.* 173, 115589. doi:10.1016/j.watres.2020.115589

Zhao, D. Y., Cao, X. Y., Huang, R., Zeng, J., Shen, F., Xu, H. M., et al. (2017). The heterogeneity of composition and assembly processes of the microbial community between different nutrient loading lake zones in taihu lake. *Appl. Microbiol. Biotechnol.* 101, 5913–5923. doi:10.1007/s00253-017-8327-0

Zhao, D. Y., Shen, F., Zeng, J., Huang, R., Yu, Z. B., and Wu, Q. L. (2016). Network analysis reveals seasonal variation of co-occurrence correlations between cyanobacteria and other bacterioplankton. *Sci. Total Environ.* 573, 817–825. doi:10.1016/j.scitotenv.2016.08.150

Zhong, Z. P., Liu, Y., Miao, L. L., Wang, F., Chu, L. M., Wang, J. L., et al. (2016). Prokaryotic community structure driven by salinity and ionic concentrations in plateau lakes of the Tibetan plateau. *Appl. Environ. Microbiol.* 82, 1846–1858. doi:10.1128/AEM.03332-15

Zhou, H., Gao, Y., Jia, X. H., Wang, M. M., Ding, J. J., Cheng, L., et al. (2020). Network analysis reveals the strengthening of microbial interaction in biological soil crust development in the mu us sandy land, northwestern China. *Soil Biol. Biochem.* 144, 107782. doi:10.1016/j.soilbio.2020.107782

Zhou, L., Zhou, Y. Q., Hu, Y., Cai, J., Liu, X., Bai, C. R., et al. (2019). Microbial production and consumption of dissolved organic matter in glacial ecosystems on the Tibetan plateau. *Water Res.* 160, 18–28. doi:10.1016/j.watres.2019.05.048

Zinger, L., Amaral-Zettler, L. A., Fuhrman, J. A., Horner-Devine, M. C., Huse, S. M., Welch, D. B. M., et al. (2011). Global patterns of bacterial beta-diversity in seafloor and seawater ecosystems. *PLoS One* 6, e24570. doi:10.1371/journal.pone.0024570

frontiers | Frontiers in Environmental Science

TYPE Original Research
PUBLISHED 28 November 2022
DOI 10.3389/fenvs.2022.1060703

OPEN ACCESS

EDITED BY
Li Zhang,
Tsinghua University, China

REVIEWED BY
Hongjie Wen,
South China University of Technology, China
Dong Wang,
Dalian Maritime University, China

*CORRESPONDENCE
Yanggui Li,
liyanggui@126.com

SPECIALTY SECTION
This article was submitted to Freshwater Science,
a section of the journal
Frontiers in Environmental Science

RECEIVED 03 October 2022
ACCEPTED 07 November 2022
PUBLISHED 28 November 2022

CITATION
Li Y, Wang L, Zhao Y, Wang H, Li S and Jia J (2022), Numerical investigation of the flow characteristics of Bingham fluid on a slope with corrected smooth particle hydrodynamics.
Front. Environ. Sci. 10:1060703.
doi: 10.3389/fenvs.2022.1060703

Numerical investigation of the flow characteristics of Bingham fluid on a slope with corrected smooth particle hydrodynamics

Yanggui Li[1]*, Lei Wang[2], Yun Zhao[3], Heping Wang[4], Shengshan Li[5] and Jinfang Jia[5]

[1]State Key Laboratory of Plateau Ecology and Agriculture, Qinghai University, Xining, China, [2]State Key Laboratory of Solidification Processing, Northwestern Polytechnical University, Xi'an, China, [3]School of Chemical Engineering, Qinghai University, Xining, China, [4]School of Sciences, Nanchang Institute of Technology, Nanchang, China, [5]Department of Computer Technology and Applications, Qinghai University, Xining, China

The Bingham model can effectively describe the flow behavior of viscoplastic fluid. It is important to study the flow characteristics of Bingham fluid to understand the dynamic mechanism of viscous debris flow. In this study, the Bingham fluid flow on a slope is numerically researched using a corrected smooth particle hydrodynamics (CSPH) method based on periodic density re-initialization and artificial stress. First, the accuracy and stability of the improved SPH method are verified by the benchmark problem impacting droplets. Then, the flow characteristics of the Bingham fluid on the slope and the influence of the slope inclination angle on the Bingham fluid movement process are studied with the improved SPH method. The numerical results show that the improved SPH numerical scheme has higher accuracy and better stability and can deal with the complex flow behavior of the unsteady Bingham fluid.

KEYWORDS

Bingham fluid, corrected smooth particle hydrodynamics, rheological property, viscoplastic fluid, flow characteristics

1 Introduction

The Bingham model can effectively describe the transient flow behavior of viscoplastic fluid, which is often used in the study of viscous debris flow. Therefore, the investigation of the flow characteristics of the Bingham fluid has important significance for protecting against and mitigating debris flow disasters. Due to the high cost and difficulty of performing a physical test, numerical simulation has gradually become an important research method. It is implemented by establishing mathematical models based on the physical mechanism, designing numerical algorithms, and then realizing the models via computer programming.

Many mathematical models of viscoplastic fluid have been established by scholars in the early stage, and the Bingham model is one of the most well-developed and widely used constitutive relationship models. Whipple (1997) analyzed the mud-rich debris flows and

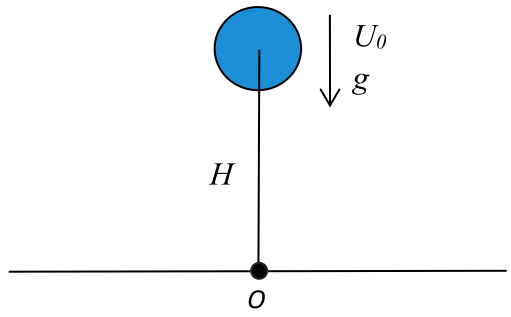

FIGURE 1
Schematic diagram of the droplet impacting the horizontal solid wall.

their routes and deposits by using a finite element numerical simulation of the open-channel flow of Bingham fluids. Chen and Lee (2002) simulated natural transient slurry flows with the Bingham model and the numerical method of the Lagrangian finite element. Their developed numerical model was validated with available experimental results, and a back-analysis of the dynamic behavior of the 1997 Lai Ping Road landslide in Hong Kong was conducted with the model. De Blasio et al. (2004) applied the Bingham model to investigate the Storegga slide in the Norwegian Sea and, in particular, the sub-region called Ormen Lange. Based on the Bingham model, the governing equations of debris flow were solved using the Lagrange difference method, and the effects of material parameters, Earth pressure coefficient, and inclination angle on the runout characteristics, such as velocity distribution, runout distance, and deposit shape, were analyzed by Wu et al. (2015). Chen et al. (2018) chose the Bingham fluid as the constitutive model of this debris flow and used finite volume method (FVM) software based on computational fluid dynamics (CFD) to simulate the fields of flow velocity, pressure, and mud depth of the Zoumaling debris flow. Moreno et al. (2021) considered the numerical modeling of spillage and debris floods as Newtonian and viscoplastic Bingham flows with free surface using mixed stabilized finite elements. Their main objective was to determine the location of the free surface of the flow. Their work presented a simplified Eulerian method solved on a fixed mesh to track the movement of the free surface, which was done by transporting the free surface with a stabilized level set method. Olshanskii (2009) designed a finite difference scheme for Bingham flow problems. The finite difference scheme used a non-staggered grid for velocity approximation, and a special stabilization was introduced to ensure the well-posedness and optimal approximation properties of the scheme. Roquet and Saramito (2003) presented the numerical modeling of the steady flow of a yield stress fluid around a cylinder. In their work, the resolution of variational inequalities describing the flow was based on the augmented Lagrangian method and a mixed finite element method (FEM), and the localization of yield surfaces was approximated by an anisotropic auto-adaptive mesh procedure. Mahmood et al. (2017) performed numerical simulations in a single and double-lid-driven square cavity to study the flow of a Bingham viscoplastic fluid. All implementations were performed in the open-source software package FEATFLOW, which was a general-purpose finite element-based solver package for solving partial differential equations. Mahmood et al. (2018) presented the stationary Bingham fluid flow simulations past a circular cylinder placed in a channel. In their work, the governing equations of motion were discretized using the mixed FEM.

Most of the numerical methods mentioned above are grid-based, such as the finite difference method (FDM), FVM, and FEM, applied to solve the control equations of the Bingham fluid. However, mesh-based numerical methods often encounter difficulties such as mesh reconstruction and distortion. Moreover, when these grid-based numerical methods are used to simulate the flow problem with a free surface, additional interface capture methods are generally required, such as the volume-of-fluid (VOF) method and level set method (Zheng et al., 2007; Zhao et al., 2008; Zheng et al., 2009), which further increases the difficulty in the numerical simulation. Therefore, various meshless particle methods are proposed in the Lagrangian framework, among which the smooth particle hydrodynamics (SPH) method is one of the most popular pure particle methods in numerical simulation applications (Shao et al., 2006; Shao, 2010; Huang et al., 2015a; Ye et al., 2019). Because it does not need additional interface tracking technology and the program design is easier to implement for dealing with large deformation and complex flow problems with a free interface, the SPH method is widely used in many fields (Shao and Gotoh, 2005; Shao, 2011; Canelas et al., 2015; Lind et al., 2015), such as viscous flow, incompressible fluid, heat transfer, multiphase flow, turbulence, and viscoelastic fluid. In recent years, the SPH method has been applied to the study of viscoplastic fluid.

There are a series of results in the numerical simulation of the Bingham fluid using the SPH method. Zhu et al. (2010) conducted a numerical study on the flow of Bingham-like fluids in two-dimensional vane and cylinder rheometers with the SPH method. To overcome the weaknesses of traditional flow analysis methods for liquefied soils that exhibit fluidization and large deformation characteristics, Huang et al. (2011) adopted SPH to analyze the flow processes of liquefied soils, in which the Bingham model incorporating the Mohr–Coulomb yield criterion, the concepts of equivalent Newtonian viscosity, and the Verlet neighbor list method were introduced into the SPH framework to build an algorithm for the analysis of flowing liquefied soils. In order to identify the areas potentially at risk and predict the flow severity, Huang et al. (2015b) proposed an SPH modeling technique to simulate the post-earthquake debris flows

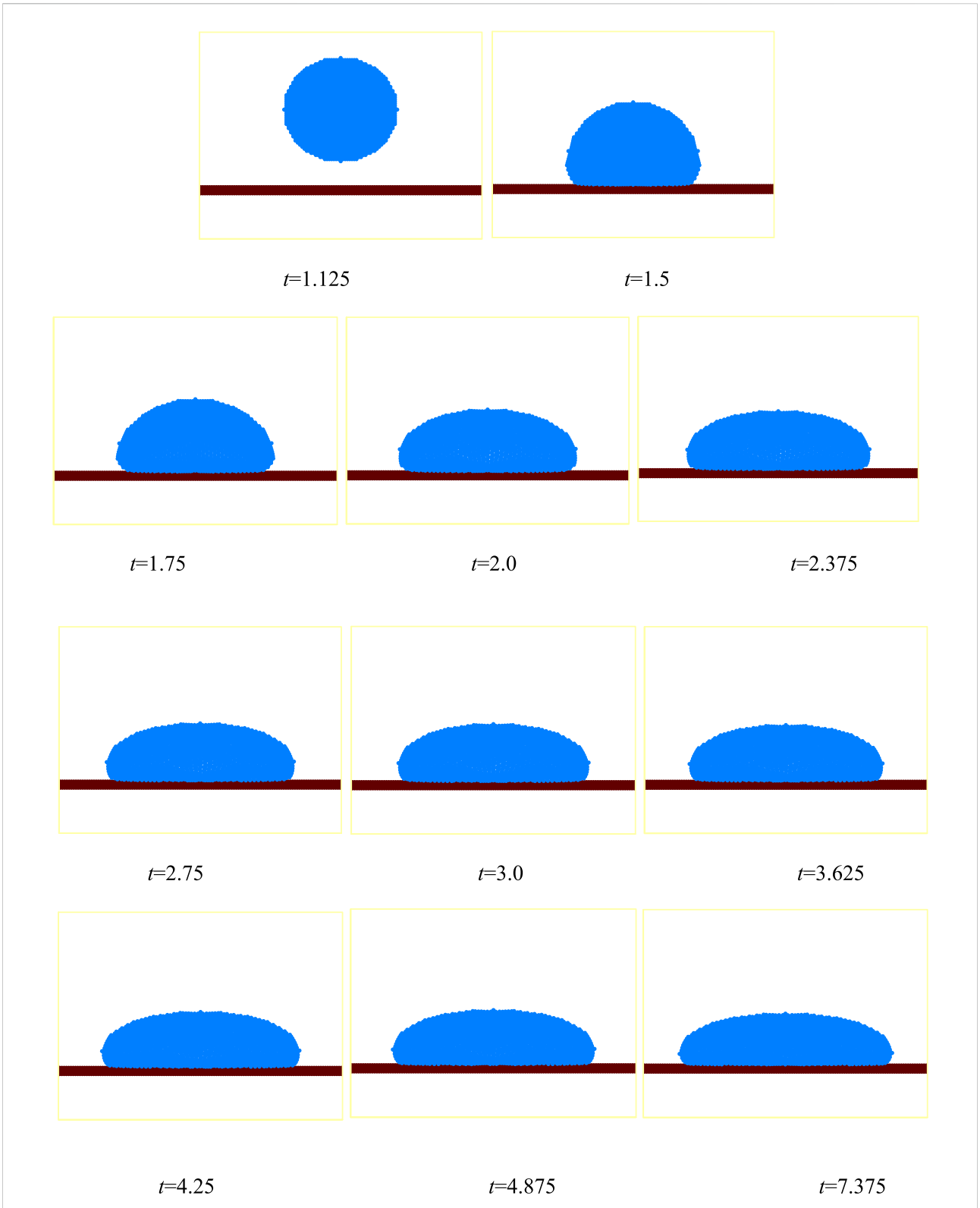

FIGURE 2
Evolution process of the Newtonian droplet impacting the horizontal solid wall.

in the Wenchuan earthquake disaster areas, in which the Bingham model is introduced to analyze the relationship between material stress rates and particle motion velocity. Wang et al. (2016) employed a Cross model and introduced the rheological parameters from the Bingham model and the Mohr–Coulomb yield criterion. In their work, the governing equations with the revisional rheological model were numerically built in the SPH framework, and the 2010 Yohutagawa debris-flow event in Japan was chosen as a case study to illustrate its performance. Wang et al. (2019) proposed a solid-fluid-coupled SPH model to investigate the behavior of the pipe in the liquefied sand after failure. Their model simulated the liquefied soil as a Bingham fluid material combined with the equivalent Newtonian viscosity. Most of the above SPH simulations are based on the traditional SPH method.

However, the traditional SPH method often produces larger errors in numerical calculation. In order to improve the accuracy and stability of calculation, this study proposes a corrected smooth particle hydrodynamics (CSPH) method based on periodic density re-initialization and applies it to the numerical study of the Bingham fluid flow process on a slope. The remaining part of this study is organized as follows. The governing equations for the flow of Bingham fluid are presented in Section 2. Section 3 describes the discretization of the governing equations for the Bingham fluid with the standard SPH and the improved SPH method, respectively. Section 4 tests the validity of the corrected SPH with the benchmark example impacting droplets. In the same section, further numerical results are given by simulating the flow of Bingham fluid in a slope with the improved SPH method. Some conclusions are summarized in Section 5.

2 Governing equations for the Bingham fluid

2.1 Governing equations

In a Lagrangian frame, the Bingham fluid is governed by the conservation of mass and momentum equations together with a Bingham constitutive equation. In this work, the conservation of mass and momentum equations are written as

$$\frac{\mathrm{D}\rho}{\mathrm{D}t} = -\rho\frac{\partial v^{\beta}}{\partial x^{\beta}}, \tag{1}$$

$$\frac{\mathrm{D}v^{\alpha}}{\mathrm{D}t} = \frac{1}{\rho}\frac{\partial \sigma^{\alpha\beta}}{\partial x^{\beta}} + g^{\alpha}, \tag{2}$$

where ρ is the fluid density, t is time, x^{β} denotes the spatial coordinate, v^{β} denotes the $\beta - th$ component of the flow velocity, $\sigma^{\alpha\beta}$ denotes the $(\alpha, \beta) - th$ component of the Cauchy stress tensor, g denotes the gravitational acceleration, and $\mathrm{D}/\mathrm{D}t = \partial/\partial t + v^{\beta} \cdot (\partial/\partial x^{\beta})$ is the material derivative.

The Cauchy stress tensor in Eq. 2 commonly contains the isotropic pressure p and the components of extra stress tensor $\tau^{\alpha\beta}$:

$$\sigma^{\alpha\beta} = -p\delta^{\alpha\beta} + \tau^{\alpha\beta}, \tag{3}$$

where $\delta^{\alpha\beta} = 1$ if $\alpha = \beta$ and $\delta^{\alpha\beta} = 0$ if $\alpha \neq \beta$. In order to investigate Bingham fluid, the related constitutive equation must be provided.

2.2 Bingham model

In order to investigate the flow behavior of the Bingham fluid, we adopt the following Bingham model to describe its rheological properties:

$$\tau^{\alpha\beta} = \tau^{\beta\alpha} = \mu_B \varepsilon^{\alpha\beta} + \tau_y, \tag{4}$$

where $\tau^{\alpha\beta}$ and $\tau^{\beta\alpha}$ are shear stress tensors, μ_B is the Bingham viscosity coefficient, and $\varepsilon^{\alpha\beta}$ is the strain rate tensor defined as

$$\varepsilon^{\alpha\beta} = \frac{1}{2}\left(\frac{\partial v^{\alpha}}{\partial x^{\beta}} + \frac{\partial v^{\beta}}{\partial x^{\alpha}}\right), \tag{5}$$

where τ_y is the yield stress of fluid. In the study of large deformation of soil, the yield stress τ_y can be calculated by the molar Coulomb yield criterion:

$$\tau_y = coh + p\tan\varphi, \tag{6}$$

where coh is the cohesion of soil, φ is the internal friction angle, and p is normal stress.

Uzuoka et al. (1998) proposed the concept of equivalent viscosity coefficient, which equivalently transformed the Bingham model into the expression form of a Newtonian fluid. The equivalent viscosity coefficient is defined as

$$\mu_{\mathrm{eff}} = \mu_B + \frac{\tau_y}{\dot{\gamma}}, \tag{7}$$

where μ_{eff} is equivalent viscosity coefficient and $\dot{\gamma}$ is shear strain rate defined as

$$\dot{\gamma} = \sqrt{2\mathrm{tr}\left(\varepsilon^{\alpha\beta}\varepsilon^{\alpha\beta}\right)} = \sqrt{2\left[\left(\frac{\partial v^{\alpha}}{\partial x^{\alpha}}\right)^2 + \left(\frac{\partial v^{\beta}}{\partial x^{\beta}}\right)^2\right] + \left(\frac{\partial v^{\alpha}}{\partial x^{\beta}} + \frac{\partial v^{\beta}}{\partial x^{\alpha}}\right)^2}. \tag{8}$$

The symbol "tr" denotes the trace of the matrix. According to Eq. 7, Eq. 4 can be equivalently converted to the representation form of a Newtonian fluid:

$$\tau^{\alpha\beta} = \tau^{\beta\alpha} = \mu_{\mathrm{eff}}\,\varepsilon^{\alpha\beta}. \tag{9}$$

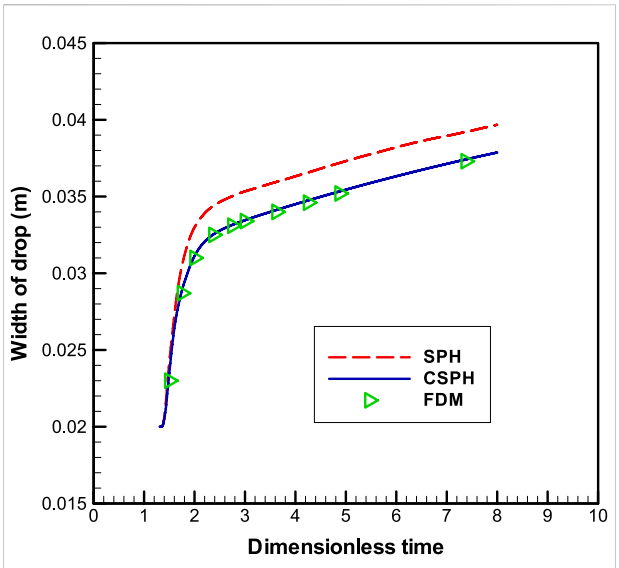

FIGURE 3
Comparison of droplet widths calculated using SPH and CSPH (the FDM result is obtained by Tome et al.).

The constitutive equation describing the rheological properties of the Bingham fluid is given above. It also requires the equation of state, which describes the relationship between density and pressure. Sometimes, incompressible fluid can be treated as a weakly compressible fluid (Monaghan, 1994), and the relationship between density and pressure is described by the equation of state as follows:

$$p = c^2(\rho - \rho_0), \tag{10}$$

where c denotes the artificial sound velocity and ρ_0 denotes the initial density of the particles.

3 Corrected smooth particle hydrodynamics formulation

3.1 Discretization schemes of standard smooth particle hydrodynamics

In the standard SPH scheme, a function and its derivative can be expressed in the form of summation by kernel approximation and particle approximation. Thus, at the particle i, the particle discretization schemes for the conservation of mass and momentum equations can be expressed as follows:

$$\left(\frac{\mathrm{D}\rho}{\mathrm{D}t}\right)_i = \rho_i \sum_j \frac{m_j}{\rho_j}\left(v_i^\beta - v_j^\beta\right)\frac{\partial W_{ij}}{\partial x_i^\beta}, \tag{11}$$

$$\left(\frac{\mathrm{D}v^\alpha}{\mathrm{D}t}\right)_i = \sum_j m_j\left(\frac{\sigma_i^{\alpha\beta}}{\rho_i^2} + \frac{\sigma_j^{\alpha\beta}}{\rho_j^2}\right)\frac{\partial W_{ij}}{\partial x_i^\beta} + g^\alpha. \tag{12}$$

The velocity gradient is marked as

$$\kappa_i^{\alpha\beta} = \left(\frac{\partial v^\alpha}{\partial x^\beta}\right)_i = \sum_j \frac{m_j}{\rho_j}\left(v_j^\alpha - v_i^\alpha\right)\frac{\partial W_{ij}}{\partial x_i^\beta}; \tag{13}$$

then, the particle approximation scheme for the constitutive equation of the Bingham model can be expressed as

$$\sigma_i^{\alpha\beta} = -p_i\delta^{\alpha\beta} + \mu_{\mathrm{eff}}(\dot{\gamma}_i)\left(\kappa_i^{\alpha\beta} + \kappa_i^{\beta\alpha}\right), \tag{14}$$

$$\dot{\gamma}_i = \sqrt{2\left[\left(\kappa_i^{\alpha\alpha}\right)^2 + \left(\kappa_i^{\beta\beta}\right)^2\right] + \left(\kappa_i^{\alpha\beta} + \kappa_i^{\beta\alpha}\right)^2}. \tag{15}$$

3.2 Density re-initialization method

In the standard SPH method, the mass of each particle is fixed. If the particle number is constant, the conservation of mass is naturally satisfied. However, the density obtained by the continuity equation often cannot accurately meet the consistency among the mass, density, and occupied volume (Benz, 1990; Morris et al., 1997). Morris et al. (1997) tried to alleviate the above problems using the density summation formula:

$$\rho_i = \sum_j m_j W_{ij}. \tag{16}$$

However, it did not get satisfactory results, especially in boundary regions or irregularly distributed particles.

To overcome the problem more effectively, in the present work, we employ a second-order exact particle approximation scheme based on the Taylor series expansion (Chen and Beraun, 2000; Liu and Liu, 2006) to periodically re-initialize density:

$$\rho_i = \sum_j m_j W_{ij}^{Tay}, \tag{17}$$

where W_{ij}^{Tay} is the corrected kernel function given by

$$W_{ij}^{Tay} = \mathrm{B}\left[\sum_j \mathrm{A}(\mathrm{r}_i)V_j\right]^{-1}\mathrm{W}, \tag{18}$$

$$A(r_i) = \begin{pmatrix} W_{ij} & x_{ji}\cdot W_{ij} & y_{ji}\cdot W_{ij} \\ \dfrac{\partial W_{ij}}{\partial x_i} & x_{ji}\cdot\dfrac{\partial W_{ij}}{\partial x_i} & y_{ji}\cdot\dfrac{\partial W_{ij}}{\partial x_i} \\ \dfrac{\partial W_{ij}}{\partial y_i} & x_{ji}\cdot\dfrac{\partial W_{ij}}{\partial y_i} & y_{ji}\cdot\dfrac{\partial W_{ij}}{\partial y_i} \end{pmatrix},\ \mathrm{B} = (1,0,0),$$
$$\mathrm{W} = \begin{pmatrix} W_{ij} \\ \partial W_{ij}/\partial x_i \\ \partial W_{ij}/\partial y_i \end{pmatrix}, \tag{19}$$

where $x_{ji} = x_j - x_i$, $y_{ji} = y_j - y_i$ and V_j is replaced by m_j/ρ_j in performing calculation.

In the implementation of the SPH method with density re-initialization, it is necessary to solve an inversion matrix of 3×3 for each fluid particle. Therefore, the calculation time increases slightly. Considering the computational cost, we should re-

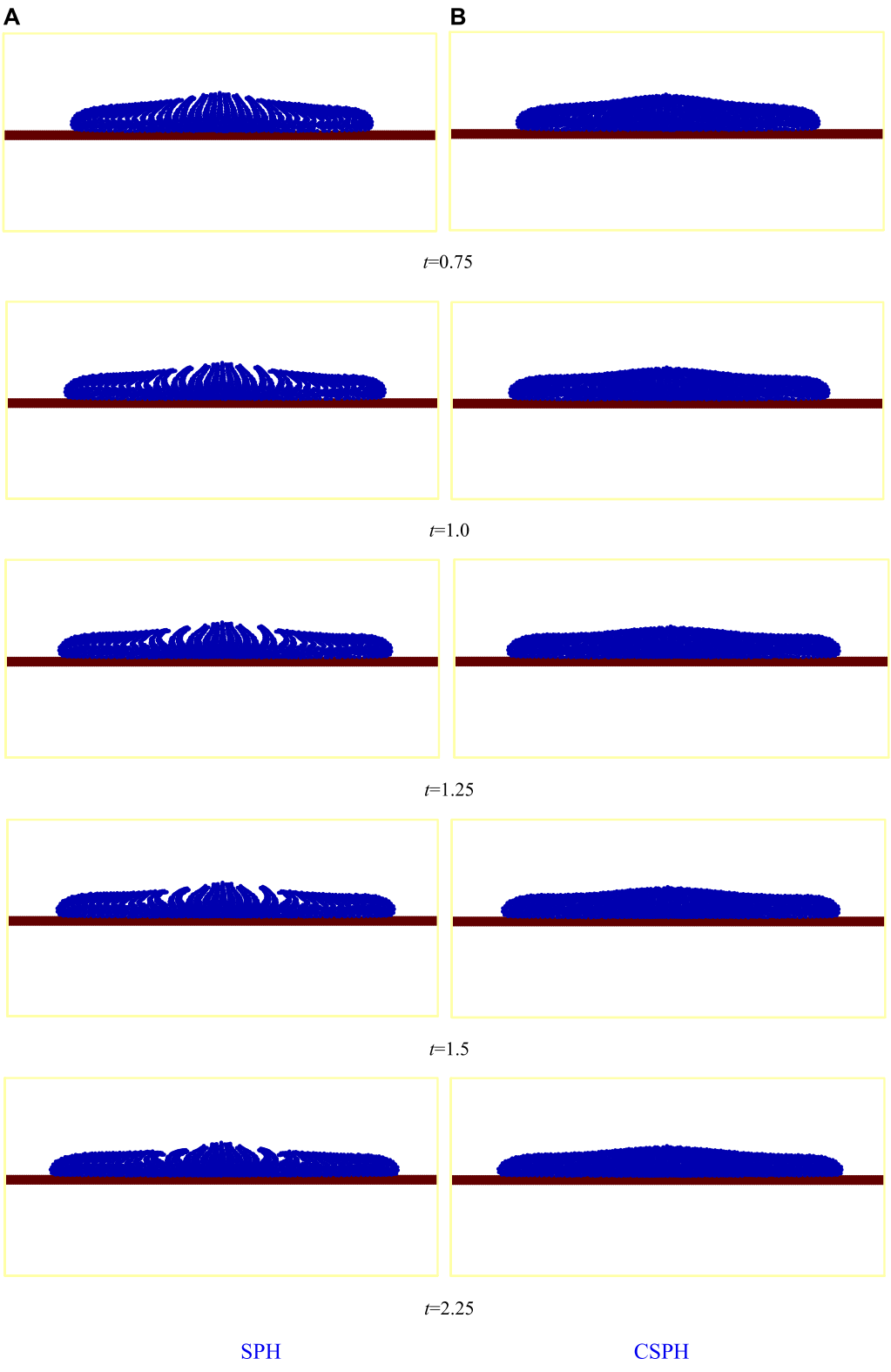

FIGURE 4
Bingham droplet impacting the horizontal solid wall with SPH and CSPH: **(A)** SPH and **(B)** CSPH.

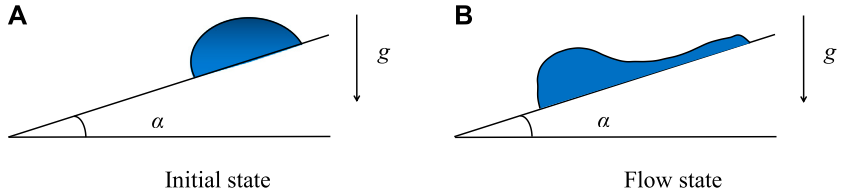

FIGURE 5
Schematic diagram of fluid flow on a slope: **(A)** initial state and **(B)** flow state.

initialize the density every several steps in the numerical simulation. In this work, density re-initializing is implemented every 20 steps.

3.3 Artificial viscosity model

In order to increase the stability of numerical schemes, an artificial viscosity is usually adopted in the SPH method (Monaghan, 2005; Fang et al., 2006; Fang et al., 2009). In this study, the artificial viscosity (Monaghan, 1992) is also considered in the momentum equation. The mathematical expression for the artificial viscosity is

$$\Pi_{ij} = \begin{cases} \dfrac{-\alpha_\Pi \bar{c}_{ij}\phi_{ij} + \beta_\Pi \phi_{ij}^2}{\bar{\rho}_{ij}} & \mathrm{v}_{ij}\cdot \mathrm{r}_{ij} < 0 \\ 0 & \mathrm{v}_{ij}\cdot \mathrm{r}_{ij} \geq 0 \end{cases}, \tag{20}$$

Where

$$\phi_{ij} = \frac{h\mathrm{v}_{ij}\cdot \mathrm{r}_{ij}}{|\mathrm{r}_{ij}|^2 + 0.01h^2},\ \bar{c}_{ij} = \frac{c_i + c_j}{2},\ \bar{\rho}_{ij} = \frac{\rho_i + \rho_j}{2} \text{ and}$$
$$\mathrm{v}_{ij} = \mathrm{v}_i - \mathrm{v}_j, \mathrm{r}_{ij} = \mathrm{r}_i - \mathrm{r}_j. \tag{21}$$

In Eq. 20, the first term with coefficient α_Π produces shear and bulk viscosity, whereas the second term with β_Π is similar to the von Neumann–Richtmyer viscosity used in FDM, which prevents unphysical particle penetration. For preventing numerical divergence when two particles get too close to each other, the term 0.01h2 is used in Eq. 21.

3.4 Artificial stress model

The phenomenon of "tensile instability (Swegle et al., 1995)" often occurs when the standard SPH method is used for solids because small clumps of particles lead to unrealistic fracture behavior of the material when the material is in a state of stretching. Some methods have been proposed to solve this problem, and the artificial stress method proposed by Monaghan (2000) and Gray et al. (2001) is one of the most successful methods. Bingham fluid is a mixture of solid soil and liquid water with solid and fluid properties. The problem of tensile instability is also prone to occur when the standard SPH method is applied to the Bingham fluid. In order to alleviate this problem, the artificial stress method is employed in the SPH numerical simulation of the Bingham fluid. The artificial stress term can effectively prevent two particles from getting too close when they are in a state of tensile stress. The artificial stress term is expressed as

$$K_{ij} = f_{ij}^n\left(S_i^{\alpha\beta} + S_j^{\alpha\beta}\right), \tag{22}$$

where $n = W(0,h)/W(d_0,h)$ and $f_{ij} = W_{ij}(|\mathrm{r}_i - \mathrm{r}_j|,h)/W_{ij}(d_0,h)$. The components of the artificial stress tensor $S_i^{\alpha\beta}$ is computed by the expression

$$S_i^{\alpha\beta} = \begin{cases} -b\sigma_i^{\alpha\beta}\Big/\rho^2 & if\left(\sum_j W''^{\alpha\beta}_{ij}\right)\cdot\sigma_i^{\alpha\beta} > 0 \\ 0 & other \end{cases}, \tag{23}$$

where b is a positive parameter with a value between 0 and 1 ($0 < b < 1$) and $W''^{\alpha\beta}_{ij} = \partial^2 W_{ij}/(\partial x^\alpha \partial x^\beta)$.

By adding the artificial viscosity term Eq. 20 and the artificial stress term Eq. 22, the discretization numerical scheme Eq. 12 of the momentum equation can be modified as

$$\left(\frac{\mathrm{D}v^\alpha}{\mathrm{D}t}\right)_i = \sum_j m_j\left(\frac{\sigma_i^{\alpha\beta}}{\rho_i^2} + \frac{\sigma_j^{\alpha\beta}}{\rho_j^2} - \Pi_{ij}\delta^{\alpha\beta} + K_{ij}\right)\frac{\partial W_{ij}}{\partial x_i^\beta} + g^\alpha. \tag{24}$$

Finally, the particle positions are updated by the following formula:

$$\frac{\mathrm{D}x_i^\alpha}{\mathrm{D}t} = v_i^\alpha. \tag{25}$$

The system of ordinary differential equations 11, 24, 25 is solved with the predictor-corrector scheme due to its second-order accuracy and better stability, in which the Courant–Friedrichs–Lewy (CFL) condition (Morris et al., 1997) is satisfied for ensuring the numerical stability.

3.5 Boundary condition treatment

The treatment method of the boundary conditions is important, and several algorithms have been proposed and

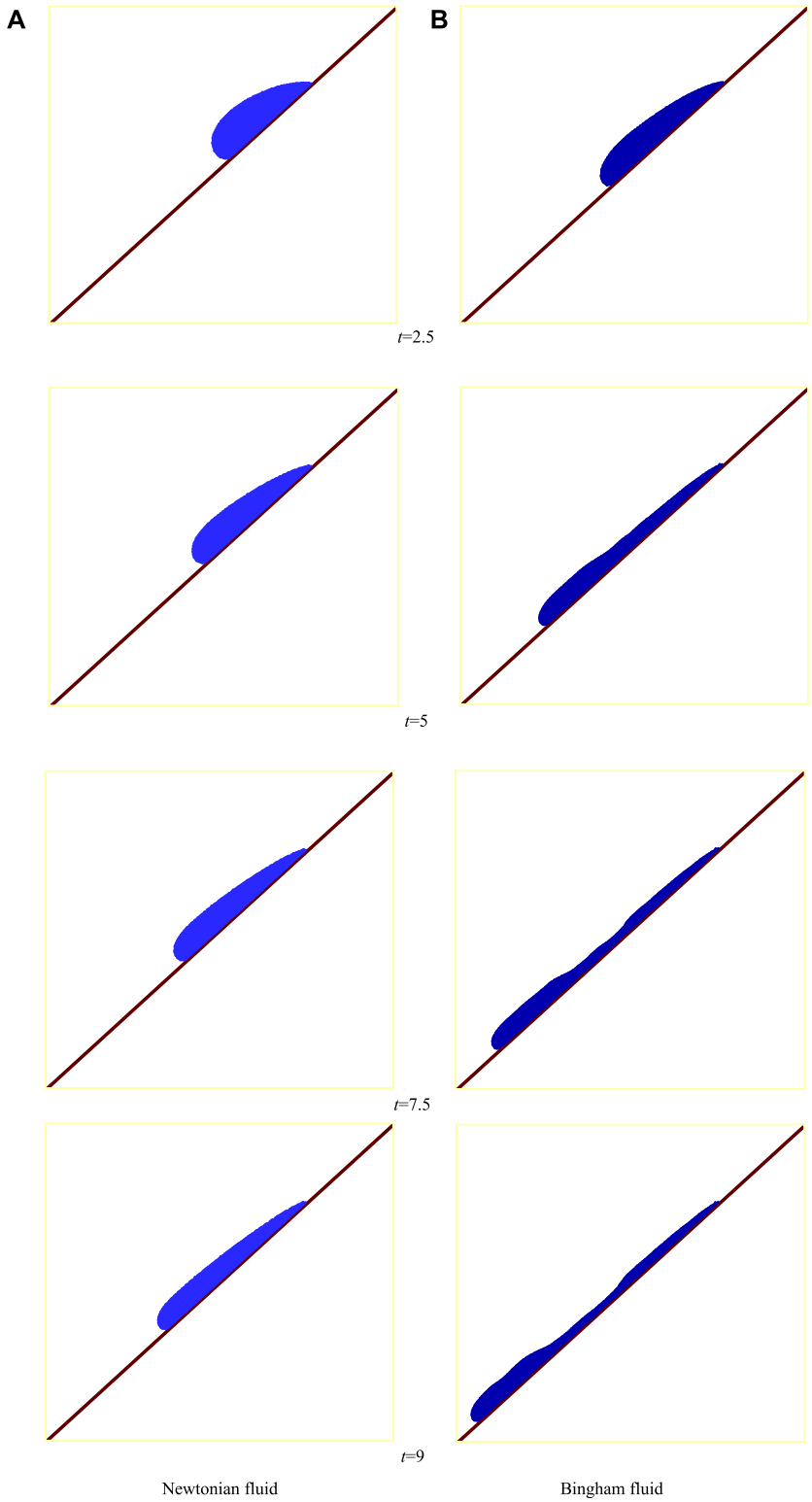

FIGURE 6
Fluid flow on a slope: **(A)** Newtonian fluid and **(B)** Bingham fluid.

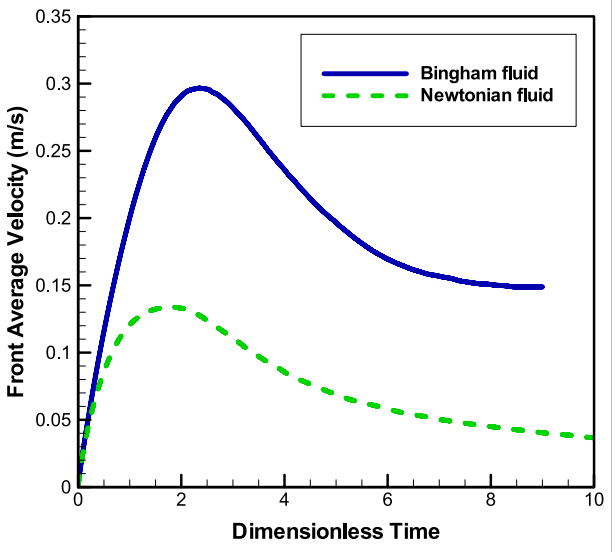

FIGURE 7
Front average velocity.

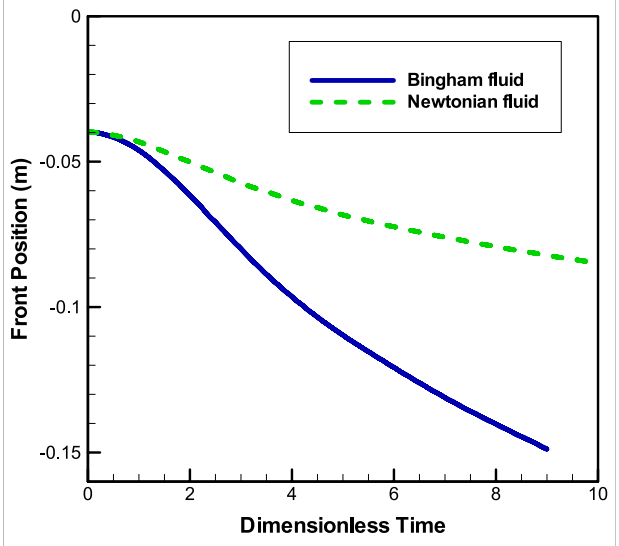

FIGURE 8
Front position of the *x* direction.

applied in the SPH model (Morris et al., 1997; Zhu et al., 2010; Ren et al., 2014; Wen et al., 2018; Wen et al., 2020). In the present work, the boundary condition is treated with the virtual particle method designed by Morris et al. (1997). The solid boundary is filled with equispaced virtual particles, and the thickness of the solid boundary is equal to or slightly greater than the support length scale of the weight function. The velocity of the boundary virtual particles is deduced from those of the fluid particles adjacent to the solid boundary. The derivation formula is

$$\mathrm{v}_j^g = \mathrm{v}_i^f - \left(1 + \frac{d_j^g}{d_i^f}\right)\mathrm{v}_i^f, \tag{26}$$

where v_j^g is the velocity of the boundary virtual particle j and v_i^f is the velocity of the fluid particle i. For every boundary virtual particle j, a normal distance d_j^g to the boundary surface is defined. This is applied to construct a tangent line to the surface in a two-dimensional region, and d_i^f is the normal distance to this tangent line for a selected fluid particle i. Thus, the physical quantities of boundary particles contribute to the SPH expressions for velocity, pressure, and stress gradients.

4 Numerical results

4.1 Validity of corrected smooth particle hydrodynamics

In order to verify the stability and accuracy of CSPH and the effectiveness of boundary treatment, the evolution process of the Newtonian droplet impacting a horizontal solid wall is shown in this section. Figure 1 shows the schematic diagram.

Here, the Newtonian droplet is considered to be two-dimensional, and its initial diameter and velocity are $D = 0.02$ m and $U_0 = -1\ \mathrm{ms}^{-1}$, respectively. The center of the droplet is initially at position $(0.0, 0.0)$ with the height $H = 0.04$ m to the horizontal rigid wall. The initial particle spacing is set to $d_0 = 0.0004$ m, and the time-step is set to $\Delta t = 1 \times 10^{-5}$ s. The gravitational acceleration acts downward with $g = -9.81\ \mathrm{ms}^{-2}$. The reference density is $\rho_0 = 10^3\ \mathrm{kgm}^{-3}$, the total viscosity is $\eta = 4\ \mathrm{Pa} \cdot \mathrm{s}$, and the speed of sound is $c = 12.5\ \mathrm{ms}^{-1}$. The artificial viscosity parameter $\alpha_{\Pi} = 1.0$ and $\beta_{\Pi} = 2.0$. The droplet contains 1,961 fluid particles, and the solid wall consists of 251 wall particles and 753 ghost particles.

Figure 2 shows the symmetrical evolution process of Newtonian droplets along the wall after impacting. The figures show that the droplet surface evolves smoothly, indicating good numerical stability. For the evolution of the droplet width with dimensionless time, Figure 3 shows a comparison of numerical results obtained using the SPH and CSPH methods. The dimensionless time is $t^\star = (U/L)\,t$, where $U = |U_0|$ and $L = H$. For ease of expression, the dimensionless time in the study is still recorded as t. Figure 3 shows that the result using CSPH is closer to the result by Tomé et al. (2002) compared to that using SPH. Thus, the results obtained by the CSPH method are more accurate than those obtained by the SPH method.

The tension instability occurs in the numerical simulations of Newtonian and Bingham fluids using the traditional SPH method, which leads to particle clustering

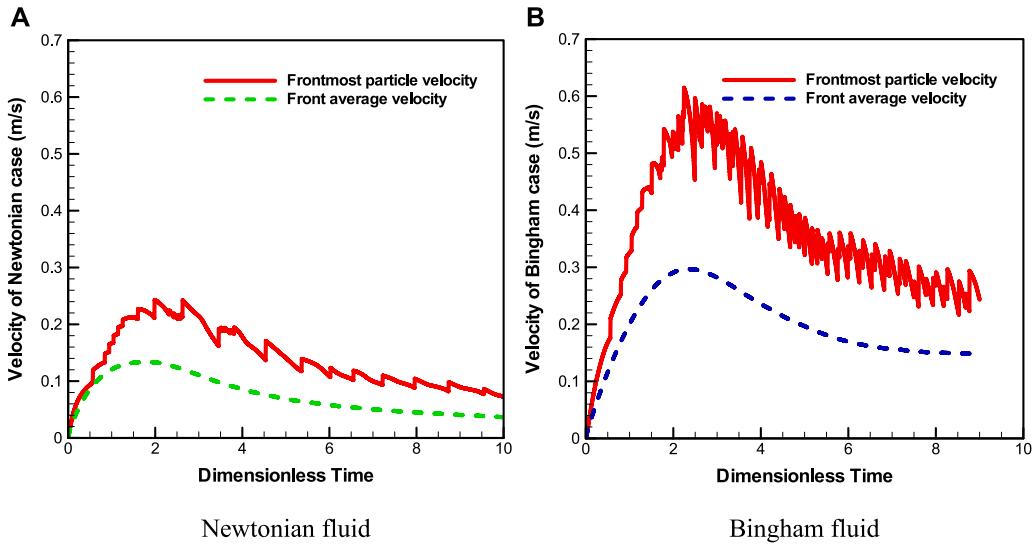

FIGURE 9
Velocity: **(A)** Newtonian fluid and **(B)** Bingham fluid.

or fractal phenomenon. The influence of tension instability on the numerical simulation of Bingham fluid is more serious than that of the Newtonian fluid. In order to solve this problem, the CSPH method in this study adds the artificial stress item. Figure 4 shows the numerical results of the Bingham droplet impacting the solid wall using the traditional SPH and CSPH methods. For the Bingham model, $\mu_B = 4 \times 10^{-4}$ m^{2}s^{-1}, $\tau_y = 3.6 \times 10^{-3}$ Pa, and the other parameter values are the same as those in the Newtonian fluid. Figure 4Ashows that due to the tension instability, the fluid particles show serious clustering and fractal phenomena in the numerical simulation of Bingham liquid drops hitting the solid wall with the traditional SPH method. Although Figure 4B shows no obvious fluid particle clustering and fractal phenomenon, the fluid particles are evenly distributed, and the droplet surface is smooth during the simulation of Bingham droplet impacting the solid wall with the CSPH method. Thus, the CSPH method can overcome the problem of tension instability well.

4.2 Numerical simulation of the Bingham fluid flow on a slope

This section considers the flow characteristics of Bingham fluid on a slope under the action of gravity. The flow process of the corresponding Newtonian case is also considered for comparison. In addition, the influence of slope angle on the flow behavior of the Bingham fluid is analyzed.

Figure 5 shows the schematic diagrams of fluid flow on a slope with an inclination angle α. For simplicity, the initial state of the fluid on the slope is a semicircle with the center of the circle at the origin $O(0, 0)$ on the slope, as shown in Figure 5A. The fluid flows down the slope under the action of gravity, as shown in Figure 5B.

4.2.1 Fluids flow on a slope with Bingham and Newtonian models

The initial state of the fluid is shown in Figure 5A. In this state, the diameter of the semicircle is $D = 0.04$ m and the inclination angle is $\alpha = 45^\circ$. In addition to the flow evolution process of the Bingham fluid on the slope, the corresponding Newtonian case is also shown in this section for comparison. For the Bingham model, $\mu_B = 4 \times 10^{-4}$ m^{2}s^{-1} and $\tau_y = 3.6 \times 10^{-3}$ Pa. Generally, the density of the Bingham fluid is larger than that of water. Here, in order to compare the fluid flow behaviors described by the Bingham and Newtonian models, the same reference density $\rho_0 = 10^3$ kgm^{-3} is adopted for both, and the other parameter values are the same as those in the case of the Newtonian fluid. Namely, the number of fluid particles is 3,852, the number of wall particles is 501, and the number of ghost particles is 1,503. The initial spacing $d_0 = 0.0004$ m, and the time-step $\Delta t = 1 \times 10^{-5}$ s. The gravitational acceleration is $g = -9.81$ ms^{-2}, and the speed of sound is $c = 10$ ms^{-1}. The artificial viscosity parameter $\alpha_{\Pi} = 1.0$ and $\beta_{\Pi} = 2.0$. In addition, the Newtonian fluid has the changeless total viscosity $\eta = 4$ Pa · s.

Figures 6A,B show the flow evolution process on a slope for Newtonian and Bingham fluids, respectively. A comparison of the two cases shows that the flow deformation of the Bingham fluid is more obvious than that in the Newtonian case. Besides, the flow velocity of the Bingham fluid is larger than that in the

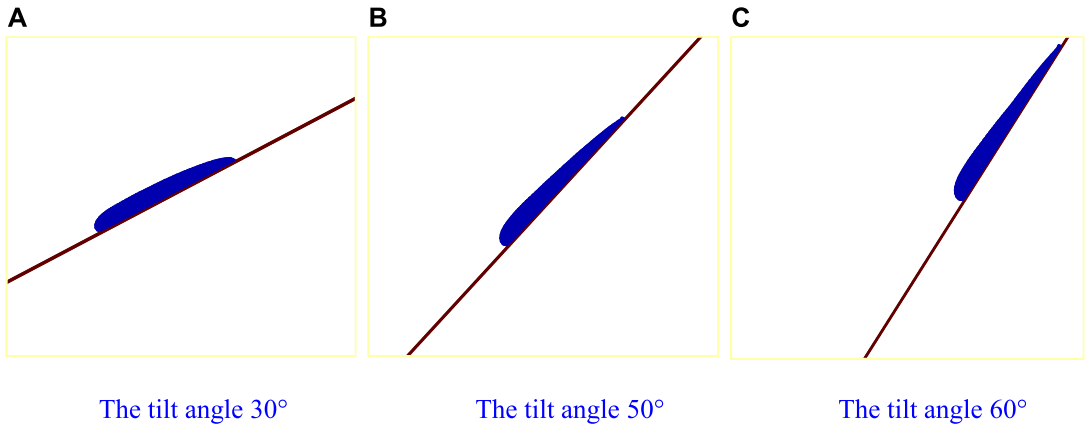

FIGURE 10
Bingham fluid flow on a slope at t = 3.75 with tilt angles of 30°, 50°, and 60°. **(A)** The tilt angle of 30°. **(B)** The tilt angle of 50°. **(C)** The tilt angle of 60°.

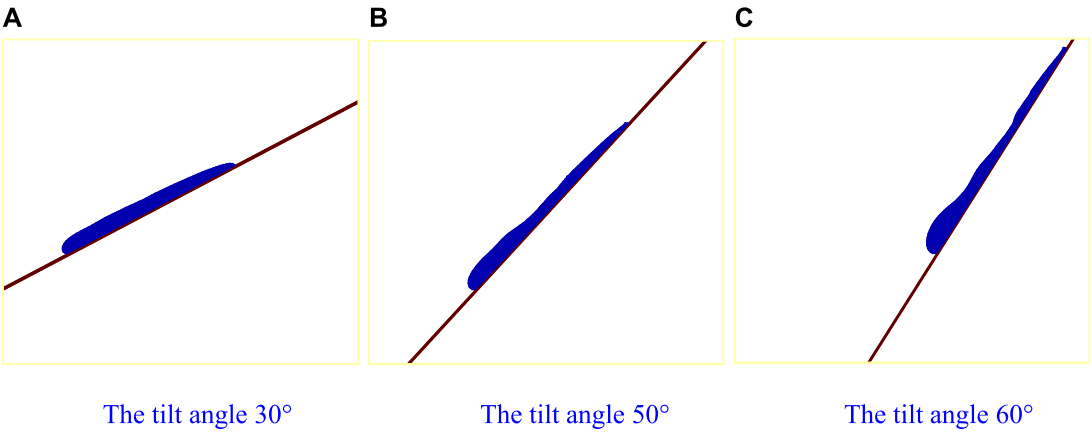

FIGURE 11
Bingham fluid flow on a slope at t = 5.75 with tilt angles of 30°, 50°, and 60°. **(A)** The tilt angle of 30°. **(B)** The tilt angle of 50°. **(C)** The tilt angle of 60°.

Newtonian case (see Figures 7, 8). Here, the frontmost particle velocity and the front average velocity are calculated to describe the flow velocity. The frontmost particle velocity refers to the velocity of the particle in the forefront of fluid, and the front average velocity refers to the statistical average of the velocities of some particles in the flow front. These flow characteristics of the Bingham fluid are the manifestation of a shear thinning behavior. Figure 6B shows that the Bingham fluid flow develops into a multi-crest pattern, similar to the intermittent flow. As shown in Figure 7, the flow rate of the Newtonian fluid reaches the peak at about t = 1.8, whereas that of the Bingham fluid reaches the peak at about t = 2.5. Subsequently, as the mass of the front fluid decreases, the influence of viscous resistance on the slope surface becomes obvious, and the velocity decreases gradually. Figure 9 shows that the frontmost particle velocity is higher than the front average velocity because the bottom particles are affected by the viscous resistance of the slope surface, which reduces the front average velocity.

4.2.2 Fluid flow on a slope with different tilt angles

The steepness of the slope will have a significant effect on the flow behavior of the Bingham fluid. In order to test the ability of CSPH simulation under a wide range of inclination angles and analyze the flow characteristics of the Bingham fluid on slopes with different inclination angles, the CSPH method is used to simulate the flow process of the Bingham fluid on the slopes with inclination angles of 30°, 50°, and 60°, respectively. Here, the reference density of the Bingham fluid is taken as $\rho = 1100\ \mathrm{kgm}^{-3}$, and the other physical parameter values are the same as those in Section 4.2.1.

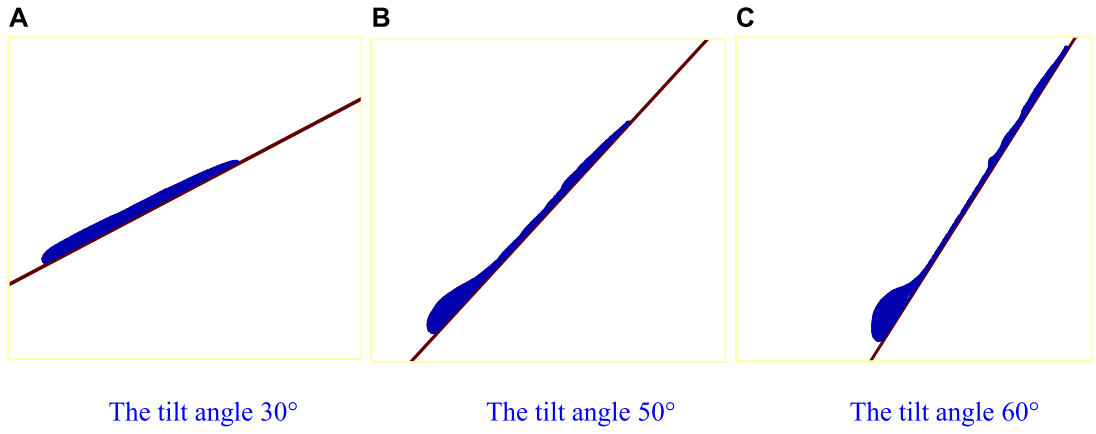

FIGURE 12
Bingham fluid flow on a slope at t = 8.5 with tilt angles of 30°, 50°, and 60°. **(A)** The tilt angle of 30°. **(B)** The tilt angle of 50°. **(C)** The tilt angle of 60°.

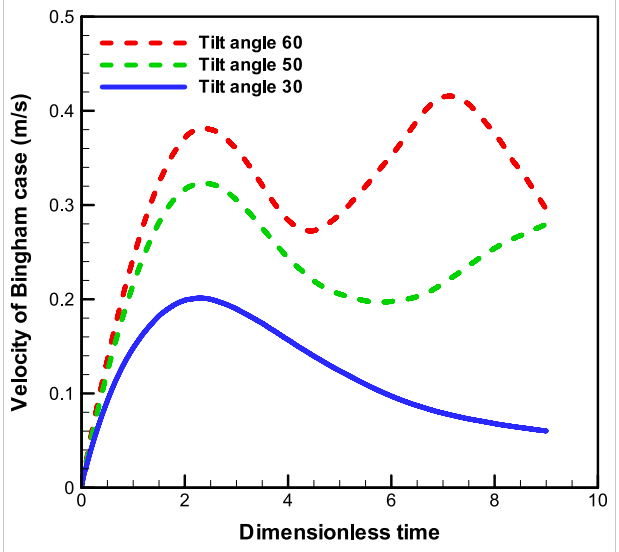

FIGURE 13
The front average velocity of Bingham fluid flow on a slope with the tilt angles of 30°, 50°, and 60°.

Figures 10–12 show the flow characteristics of the Bingham fluid at different tilt angles (α=30°, 50°, 60°), and Figure 13 shows their front average velocity. The figures show that the fluid accumulation in front becomes more obvious with the tilt angle enlarging. The accumulation changes the fluid flow behavior. When the fluid accumulation in front is small, the viscous force on the slope surface greatly influences the flow, and the front flow velocity is small. In this case, as the slope surface that the fluid has flowed through has been wetted, the viscous resistance of the slope surface behind the fluid front is reduced, and the subsequent fluid gradually catches up and accumulates in front. When the front fluid accumulates to a certain amount, the volume force increases to a sufficient degree and plays a leading role and the influence of slope viscous resistance decreases. Thus, the front fluid accelerates to flow forward and distances itself from the fluid behind, which forms a multi-crest flow pattern (see Figure 11C). As the front fluid flows forward, fluid adhesion on the slope surface leads to fluid loss in the front. Thus, the volume force of the front fluid decreases, and the influence of viscous resistance on the slope surface increases, leading to the front velocity decrease. Under the lubrication of the slope surface, the rear crests catch up with the front crest and overlap (see Figures 11C, 12C). The downward flow of the Bingham fluid on a slope is a competition process between gravity and viscous friction. In the case of a small slope, viscous friction plays a dominant role, and in the case of large slopes, gravity plays a dominant role, resulting in different flow patterns at different slopes.

5 Conclusion

To understand the motion characteristics of viscoplastic fluid, we introduced the improved SPH method to investigate the flow process of the Bingham fluid on a slope in this study. Firstly, we add the artificial stress term to the momentum equation to relieve the tension instability. Consequently, the SPH method based on the periodic re-initialization of density is improved to keep the consistency between mass, density, and occupied volume. The higher accuracy and stability of the improved SPH method are validated by droplet examples of Newtonian and Bingham fluids. Secondly, we numerically investigate the flow characteristic of the Bingham fluid on a slope using the improved SPH method and compare the results to those of the Newtonian case. The computational results show that the

corrected SPH method can accurately simulate the rheological behavior of the Bingham fluid, such as shear thinning. Furthermore, the numerical results with a large range of incline angles are given to prove the effectiveness and stability of the improved SPH method, which can effectively capture the complex transient flow behavior of Bingham fluid and be applied to large-scale and real scene debris flow numerical simulation with parallel technology.

Data availability statement

The original contributions presented in the study are included in the article/supplementary material. Further inquiries can be directed to the corresponding author.

Author contributions

All authors listed have made a substantial, direct, and intellectual contribution to the work and approved it for publication.

Funding

The National Natural Science Foundation of China (no. 61962051) and the National Natural Science Foundation of China (no. 12161058). This research was funded by the National Natural Science Foundation of China (No. 61962051), the Open Project of State Key Laboratory of Plateau Ecology and Agriculture, Qinghai University (No. 2021-ZZ-02), the Jiangxi Provincial Natural Science Foundation (No. 20212BAB201020), the National Natural Science Foundation of China (No. 12161058), the Jiangxi Provincial Education Department (No. GJJ190961), the Youth Foundation Program of Qinghai University (No. 2020-QGY-11), and the Chunhui project of the Ministry of Education (No. QDCH2018001).

Conflict of interest

The authors declare that the research was conducted in the absence of any commercial or financial relationships that could be construed as a potential conflict of interest.

Publisher's note

All claims expressed in this article are solely those of the authors and do not necessarily represent those of their affiliated organizations or those of the publisher, the editors, and the reviewers. Any product that may be evaluated in this article, or claim that may be made by its manufacturer, is not guaranteed or endorsed by the publisher.

References

Benz, W. (1990). Smooth particle hydrodynamics: A review. *The Numerical Modelling of Nonlinear Stellar Pulsations*. Heidelberg: Springer, 269–288.

Canelas, R. B., Domínguez, J. M., Crespo, A. J. C., Gómez-Gesteira, M., and Rui, M. L. F. (2015). A Smooth Particle Hydrodynamics discretization for the modelling of free surface flows and rigid body dynamics. *Int. J. Numer. Methods Fluids* 78 (9), 581–593. doi:10.1002/fld.4031

Chen, H., and Lee, C. F. (2002). Runout analysis of slurry flows with bingham model. *J. Geotech. Geoenviron. Eng.* 128 (12), 1032–1042. doi:10.1061/(asce)1090-0241(2002)128:12(1032)

Chen, J. K., and Beraun, J. E. (2000). A generalized smoothed particle hydrodynamics method for nonlinear dynamic problems. *Comput. Methods Appl. Mech. Eng.* 190 (1-2), 225–239. doi:10.1016/s0045-7825(99)00422-3

Chen, Y., Qiu, Z., Li, B., and Yang, Z. (2018). Numerical simulation on the dynamic characteristics of a tremendous debris flow in sichuan, China. *Process. (Basel).* 6 (8), 109. doi:10.3390/pr6080109

De Blasio, F. V., Elverhøi, A., Issler, D., Harbitz, C. B., Bryn, P., and Lien, R. (2004). Flow models of natural debris flows originating from overconsolidated clay materials. *Mar. Geol.* 213 (1-4), 439–455. doi:10.1016/j.margeo.2004.10.018

Fang, J., Owens, R. G., Tacher, L., and Parriaux, A. (2006). A numerical study of the SPH method for simulating transient viscoelastic free surface flows. *J. Newt. Fluid Mech.* 139 (1-2), 68–84. doi:10.1016/j.jnnfm.2006.07.004

Fang, J., Parriaux, A., Rentschler, M., and Ancey, C. (2009). Improved SPH methods for simulating free surface flows of viscous fluids. *Appl. Numer. Math.* 59 (2), 251–271. doi:10.1016/j.apnum.2008.02.003

Gray, J. P., Monaghan, J. J., and Swift, R. P. (2001). SPH elastic dynamics. *Comput. Methods Appl. Mech. Eng.* 190 (49-50), 6641–6662. doi:10.1016/s0045-7825(01)00254-7

Huang, C., Lei, J. M., Liu, M. B., and Peng, X. Y. (2015). A kernel gradient free (KGF) SPH method. *Int. J. Numer. Methods Fluids* 78, 691–707. doi:10.1002/fld.4037

Huang, Y., Cheng, H., Dai, Z., Xu, Q., Liu, F., Sawada, K., et al. (2015). SPH-based numerical simulation of catastrophic debris flows after the 2008 Wenchuan earthquake. *Bull. Eng. Geol. Environ.* 74 (4), 1137–1151. doi:10.1007/s10064-014-0705-6

Huang, Y., Zhang, W., Mao, W., and Jin, C. (2011). Flow analysis of liquefied soils based on smoothed particle hydrodynamics. *Nat. Hazards (Dordr).* 59 (3), 1547–1560. doi:10.1007/s11069-011-9851-3

Lind, S. J., Stansby, P. K., Rogers, B. D., and Lloyd, P. M. (2015). Numerical predictions of water-air wave slam using incompressible-compressible smoothed particle hydrodynamics. *Appl. Ocean Res.* 49, 57–71. doi:10.1016/j.apor.2014.11.001

Liu, M. B., and Liu, G. R. (2006). Restoring particle consistency in smoothed particle hydrodynamics. *Appl. Numer. Math.* 56 (1), 19–36. doi:10.1016/j.apnum.2005.02.012

Mahmood, R., Kousar, N., Usman, K., and Mehmood, A. (2018). Finite element simulations for stationary Bingham fluid flow past a circular cylinder. *J. Braz. Soc. Mech. Sci. Eng.* 40 (9), 459. doi:10.1007/s40430-018-1383-2

Mahmood, R., Kousar, N., Yaqub, M., and Jabeen, K. (2017). Numerical simulations of the square lid driven cavity flow of bingham fluids using nonconforming finite elements coupled with a direct solver. *Adv. Math. Phys.* 2017, 1–10. doi:10.1155/2017/5210708

Monaghan, J. J. (1994). Simulating free surface flows with SPH. *J. Comput. Phys.* 110 (2), 399–406. doi:10.1006/jcph.1994.1034

Monaghan, J. J. (1992). Smoothed particle hydrodynamics. *Annu. Rev. Astron. Astrophys.* 30 (1), 543–574. doi:10.1146/annurev.aa.30.090192.002551

Monaghan, J. J. (2005). Smoothed particle hydrodynamics. *Rep. Prog. Phys.* 68 (8), 1703–1759. doi:10.1088/0034-4885/68/8/r01

Monaghan, J. J. (2000). SPH without a tensile instability. *J. Comput. Phys.* 159 (2), 290–311. doi:10.1006/jcph.2000.6439

Moreno, E., Dialami, N., and Cervera, M. (2021). Modeling of spillage and debris floods as Newtonian and Viscoplastic Bingham flows with free surface with mixed stabilized finite elements. *J. Newt. Fluid Mech.* 290 (2), 104512. doi:10.1016/j.jnnfm.2021.104512

Morris, J. P., Fox, P. J., and Zhu, Y. (1997). Modeling low Reynolds number incompressible flows using SPH. *J. Comput. Phys.* 136 (1), 214–226. doi:10.1006/jcph.1997.5776

Olshanskii, M. A. (2009). Analysis of semi-staggered finite-difference method with application to Bingham flows. *Comput. Methods Appl. Mech. Eng.* 198 (9-12), 975–985. doi:10.1016/j.cma.2008.11.010

Ren, B., Wen, H., Dong, P., and Wang, Y. (2014). Numerical simulation of wave interaction with porous structures using an improved smoothed particle hydrodynamic method. *Coast. Eng.* 88, 88–100. doi:10.1016/j.coastaleng.2014.02.006

Roquet, N., and Saramito, P. (2003). An adaptive finite element method for Bingham fluid flows around a cylinder. *Comput. Methods Appl. Mech. Eng.* 192 (31-32), 3317–3341. doi:10.1016/s0045-7825(03)00262-7

Shao, S., and Gotoh, H. (2005). Turbulence particle models for tracking free surfaces. *J. Hydraulic Res.* 43 (3), 276–289. doi:10.1080/00221680509500122

Shao, S. (2011). Incompressible smoothed particle hydrodynamics simulation of multifluid flows. *Int. J. Numer. Methods Fluids* 69 (11), 1715–1735. doi:10.1002/fld.2660

Shao, S. (2010). Incompressible SPH flow model for wave interactions with porous media. *Coast. Eng.* 57 (3), 304–316. doi:10.1016/j.coastaleng.2009.10.012

Shao, S., Ji, C., Graham, D. I., Reeve, D. E., James, P. W., and Chadwick, A. J. (2006). Simulation of wave overtopping by an incompressible SPH model. *Coast. Eng.* 53 (9), 723–735. doi:10.1016/j.coastaleng.2006.02.005

Swegle, J. W., Hicks, D. L., and Attaway, S. W. (1995). Smoothed particle hydrodynamics stability analysis. *J. Comput. Phys.* 116 (1), 123–134. doi:10.1006/jcph.1995.1010

Tomé, M. F., Mangiavacchi, N., Cuminato, J. A., Castelo, A., and McKee, S. (2002). A finite difference technique for simulating unsteady viscoelastic free surface flows. *J. Newt. Fluid Mech.* 106 (2-3), 61–106. doi:10.1016/s0377-0257(02)00064-2

Uzuoka, R., Yashima, A., Kawakami, T., and Konrad, J.-M. (1998). Fluid dynamics based prediction of liquefaction induced lateral spreading. *Comput. Geotechnics* 22 (3-4), 243–282. doi:10.1016/s0266-352x(98)00006-8

Wang, W., Chen, G., Han, Z., Zhou, S., Zhang, H., and Jing, P. (2016). 3D numerical simulation of debris-flow motion using SPH method incorporating non-Newtonian fluid behavior. *Nat. Hazards (Dordr).* 81 (3), 1981–1998. doi:10.1007/s11069-016-2171-x

Wang, Z., Yu, X., Zhang, W., Zhang, F., Zhou, Y., and Gao, Y. (2019). SPH-based analysis on the lateral response of pipe culverts in the flowing process of liquefied sand. *Math. Problems Eng.* 2019, 43515011–43515012. doi:10.1155/2019/4351501

Wen, H., Ren, B., Dong, P., and Zhu, G. (2020). Numerical analysis of wave-induced current within the inhomogeneous coral reef using a refined SPH model. *Coast. Eng.* 156, 103616. doi:10.1016/j.coastaleng.2019.103616

Wen, H., Ren, B., and Yu, X. (2018). An improved SPH model for turbulent hydrodynamics of a 2D oscillating water chamber. *Ocean. Eng.* 150, 152–166. doi:10.1016/j.oceaneng.2017.12.047

Whipple, K. X. (1997). Open-channel flow of bingham fluids: Applications in debris-flow research. *J. Geol.* 105 (2), 243–262. doi:10.1086/515916

Wu, H., He, N., and Zhang, X. (2015). Numerical model of viscous debris flows with depth-dependent yield strength. *J. Geoengin.* 10 (1), 1–10.

Ye, C., Mota, P., Li, J., Lin, K., and Qian, W.-L. (2019). On the boundary condition and related instability in the smoothed particle hydrodynamics. *Commun. Theor. Phys.* 11, 1281–1292. doi:10.1088/0253-6102/71/11/1281

Zhao, Z., Ouyang, J., Zhang, L., and Liu, D. (2008). Numerical simulation of branched polymer melts through planar contraction with inset based on XPP model. *J. Chem. Industry Eng.* 59 (4), 843–850.

Zheng, S., Ouyang, J., Zhang, L., and Zhang, H. (2007). Dynamic simulation of fusion process and analysis of flow field. *J. Reinf. Plastics Compos.* 26 (17), 1781–1792. doi:10.1177/0731684407080479

Zheng, S., Ouyang, J., Zhang, L., and Zhao, Z. (2009). Research on a numerical schemes for capturing free front during injection molding. *Polymer-Plastics Technol. Eng.* 48 (4), 446–454. doi:10.1080/03602550902725456

Zhu, H., Martys, N. S., Ferraris, C., and Kee, D. D. (2010). A numerical study of the flow of Bingham-like fluids in two-dimensional vane and cylinder rheometers using a smoothed particle hydrodynamics (SPH) based method. *J. Newt. Fluid Mech.* 165 (7-8), 362–375. doi:10.1016/j.jnnfm.2010.01.012

frontiers | Frontiers in Environmental Science

TYPE Original Research
PUBLISHED 13 January 2023
DOI 10.3389/fenvs.2022.1114448

OPEN ACCESS

EDITED BY
Xiaoning Zhao,
Nanjing University of Information Science and Technology, China

REVIEWED BY
Li Jian,
China University of Geosciences Wuhan, China
Limo Tang,
Hohai University, China

*CORRESPONDENCE
Shanghong Zhang,
zhangsh928@126.com

SPECIALTY SECTION
This article was submitted to Freshwater Science, a section of the journal Frontiers in Environmental Science

RECEIVED 02 December 2022
ACCEPTED 30 December 2022
PUBLISHED 13 January 2023

CITATION
Ruan Q, Li W, Zhang S, Tang C and Hou J (2023), Effects of dam construction on the reproduction of the Yellow River carp (*Cyprinus carpio*) in lower reaches of the Yellow River, China.
Front. Environ. Sci. 10:1114448.
doi: 10.3389/fenvs.2022.1114448

Effects of dam construction on the reproduction of the Yellow River carp (*Cyprinus carpio*) in lower reaches of the Yellow River, China

Qiongyao Ruan, Wenda Li, Shanghong Zhang*, Caihong Tang and Jun Hou

School of Water Resources and Hydropower Engineering, North China Electric Power University, Beijing, China

The construction of dams changes the natural flow of rivers, affects the integrity of river ecosystems, and causes a series of ecological and environmental problems, such as habitat fragmentation and reduction in fish resources. This study took a section of the Yellow River in China from the Xiaolangdi Dam to Gaocun as the research area. The Yellow River carp (*Cyprinus carpio*) was selected as an indicator species for its economic value. A habitat suitability model for the Yellow River carp coupled with a one-dimensional hydrodynamic model was built. It was used to simulate dynamic changes in the reproductive habitat suitability of the Yellow River carp before and after the construction of the Xiaolangdi Dam. We demonstrated the spatial distribution of the carp's spawning reaches before and after the Xiaolangdi Dam construction and investigated its influence on the spawning activity and larval development of the species accordingly. The results apparently showed that the construction and operation of the Xiaolangdi Dam delayed the breeding time of the Yellow River carp and decreased its quality by 5.28%. In particular, the larval fish development was greatly affected by the dam, with the quality being reduced by 8.95%. Furthermore, the habitat suitability of the spawning reaches slightly decreased as the extent of spawning reaches decreased by 16.23%, and several spawning reaches were lost entirely. This study shed light on the response of the Yellow River carp to hydrological and physical changes in the period 1980–1990 before the construction of the Xiaolangdi Dam and 2006–2018 after the construction. Thus, it is a valuable reference for the ecological scheduling of discharges of the Xiaolangdi Dam.

KEYWORDS

fish habitat, habitat suitability model, hydrodynamic model, spawning reach, Xiaolangdi Dam

1 Introduction

The construction of dams brings great social and economic benefits to human beings but strongly interferes with river ecosystems, resulting in a variety of ecological problems (Liu et al., 2013). Dams as obstructions on rivers, to a certain extent, change the hydrological conditions and impact the environmental geology and biodiversity of rivers (Collier et al., 1996; Fantin-Cruz et al., 2015; Wang et al., 2016). Up to 60% of river habitats worldwide might be affected by dams, disrupting fish migration, fragmenting, or even disappearing aquatic habitats (Morita and Yamamoto, 2002; Yi et al., 2014). Investigating the ecological effects of dams helps protect

the river ecosystem, guide the ecological scheduling at the macro level, and achieve a balance between development and ecological protection.

Fish are top aquatic food chain animals in freshwater river basins (Muñoz-Mas et al., 2012) yet sensitive to environmental changes. Individual aquatic species are taken as an indicator of the physical and biological environment of rivers (Karr, 1981) and play an important role in ecosystems (Sun and Sheng, 2000). The Yellow River carp (*Cyprinus carpio*) inhabits mainly in the Ning–Meng section, Xiaobei mainstream, and the lower reaches of the Yellow River; meanwhile, it is an economically important species of the Yellow River. However, since the 1950s, due to human activities, climate change, and other factors, the natural spawning grounds of fish have been disconnected, and the migration channels have been blocked, which seriously damaged the ecological balance of the Yellow River. By 2008, the total number of fish species recorded in the Yellow River had decreased by 71.72% (Han et al., 2013). Biodiversity loss and ecology destruction can seriously endanger sustainable development, economy, and environmental functions. The scale and quantity of the fish habitat is important to the ecosystem and the high-quality development of the Yellow River Basin. Fish habitat assessment helps understand the impact of dam construction on carp reproduction in the Yellow River. Furthermore, it makes a potential contribution to the restoration of the fish habitat, ecological quality, and biodiversity in the Yellow River Basin.

Hydrological and habitat simulations are mainly used to assess the habitat status, in which physical habitat models are widely applied for the protection and restoration of river ecosystems affected by water conservancy projects. Mouton et al. (2007) applied a physical habitat model built by HEC-RAS and CASiMiR software applications to the Zwalm River in northern Belgium and assessed the impact of dam removal on the habitat quality of the bullhead (*Cottus gobio* L.). Yi and Yue (2011) established a fish habitat suitability function combined with ecological factors to evaluate the impact of dams on the four major Chinese carps in the Yangtze River; Chang et al. (2013) studied the short-term and long-term effects of spur dikes on the extent of the fish habitat; Im et al. (2018) used an adaptive neuro-fuzzy inference system (ANFIS) to simulate the physical habitat of fish populations downstream of a dam. Habitat simulation is considered a complex and scientific method (Ahmadi-Nedushan et al., 2010), which takes into account the physical habitat requirements of organisms and establishes the assessment index between indicator species and habitats.

Researchers have carried out many studies on the survival and reproduction of the Yellow River carp through habitat simulation. Wang et al. (2020) established a habitat model of the Yellow River carp on two reaches of the Yellow River (Huayuankou and Lijin), explored the quantitative response relationship between the habitat area and flow, and determined the downstream ecological flow. Jiang et al. (2010a) applied the River2D hydrodynamic model to reveal the relationship between the ecological habitats of the Yellow River carp and the discharge. They studied habitat areas of the carp under different flow conditions and found that from April to June, after the Xiaolangdi Dam construction, the large flow decreased significantly, which was not conducive to spawning of the Yellow River carp. Zhang et al. (2008) took the Lanzhou to Shizuishan section of the main Yellow River as the research area and the Yellow River carp as the indicator species. They calculated the available ecological flow before flooding through hydraulic factors such as the flow velocity and the water depth. The studies on the influencing factors of the Yellow River carp reproduction are mostly based on the two-dimensional hydrodynamic model of characteristic section flow simulation. There are few measured inflow processes to reflect the complex inflow of a continuous reach. As a one-dimensional hydrodynamic model has generalized the hydrological conditions of the same section, its calculation efficiency for a long river is far higher than that of the two-dimensional model, which realizes the flow simulation of a long river reflected by a measured inflow process. Furthermore, there is a lack of study on changes in the locations, scale, and habitat quality of fish spawning grounds before and after dam construction on the Yellow River.

It is crucial to analyze the status of fish habitats before and after the dam construction to reveal the impact of dams on river ecosystems. In this study, the river section between Xiaolangdi and Gaocun in the lower reaches of the Yellow River in China is selected as the study area. In addition, the Yellow River carp, a typical economically valued fish, is selected as the indicator species of river ecology. A habitat suitability model coupled with a one-dimensional non-constant flow hydrodynamic model is built to study the carp's breeding period. We analyzed the changes in the Yellow River carp reproduction before and after dam construction based on the habitat suitability index and assessed the impact of the dam on species' reproduction.

2 Materials and methods

2.1 Study area

The Xiaolangdi–Gaocun reach in the lower part of the Yellow River is selected as the study area with a total length of 337 km (shown in blue in the Figure 1). The reach is wide and shallow, with dense sandbars and variable water flow, and the broad beaches along the river are rich in food organisms. These conditions provide fish with foraging and spawning habitats, making them ideal for studying the ecology of rivers under the dam. The Yellow River Carp National Aquatic Germplasm Resource Reserve (YRCNAGRR) in the Zhengzhou section of the lower Yellow River was established in 2008 and chosen as a part of our study area (shown in gray in the Figure 1). Its main protection objects are the Yellow River carp and its spawning grounds, feeding grounds, and wintering grounds, as well as the aquatic ecology and terrestrial ecosystems (Zhang and Han, 2016), among which the Huayuankou reach is one of the important spawning grounds. For our study area, it is necessary to select a sufficiently long enough reach downstream of the dam as the study area in order to explore the influence of the dam on the different reaches. Meanwhile, there should be many relatively stable spawning grounds in the study area, which could make it a representative reach of the lower part of the Yellow River for studying fish and their habitats. The natural hydrological cycle of the river has changed since the construction of the Xiaolangdi Dam at the end of 2001, thereby affecting the quality and scale of aquatic habitats and the breeding activities of fish in the study area.

2.2 One-dimensional hydrodynamic modeling

In simulating the physical characteristics of river flows, one-dimensional hydrodynamic modeling can be used to calculate the

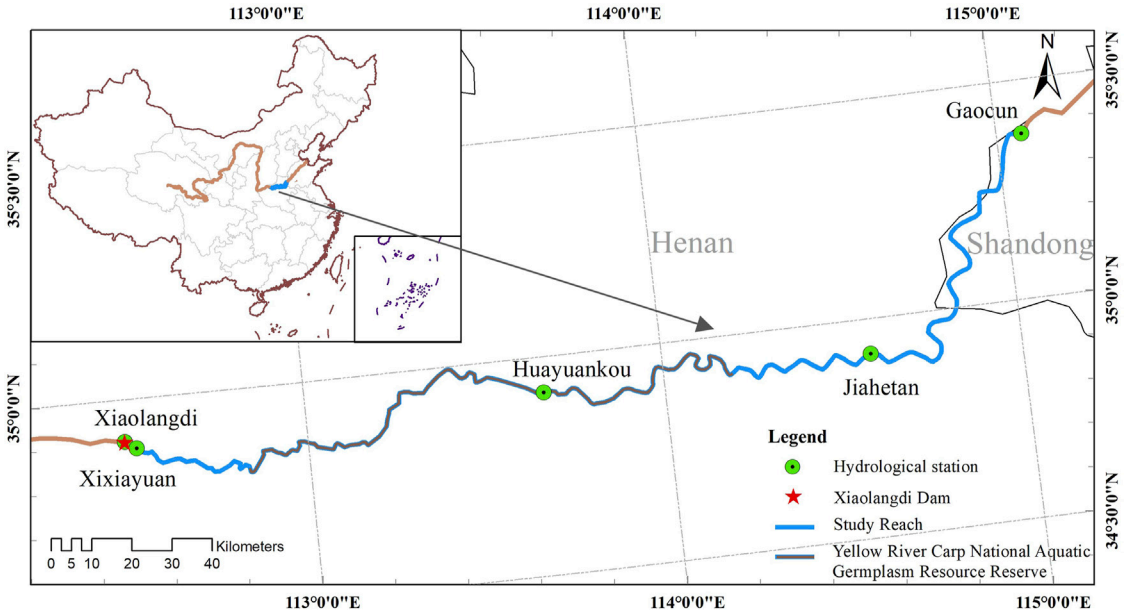

FIGURE 1
Geographical location of the Yellow River in China and the study area comprised the Yellow River downstream of the Xiaolangdi Dam, between Xiaolangdi and Gaocun.

hydrological and hydrodynamic parameters of different sections at various times and, therefore, provide data to gauge fish habitat suitability. In this study, a one-dimensional hydrodynamic model of the lower Yellow River was constructed based on MIKE11 software, which could simulate the vertical homogeneous water flow of the river according to the terrain and the boundary of the water flow. The Saint-Venant equations and the Abbott–Ionscu 6-point implicit scheme are applied for the numerical simulation. Thus, the governing equations for the one-dimensional hydrodynamic model are as follows:

$$B\frac{\partial Z}{\partial t}+\frac{\partial Q}{\partial x}=q, \tag{1}$$

$$\frac{\partial Q}{\partial t}+\frac{\partial}{\partial x}\left(\frac{Q^2}{A}\right)+gA\left(\frac{\partial Z}{\partial x}+\frac{Q|Q|}{K^2}\right)=0, \tag{2}$$

where x (m) is the distance along the river; t (s) is the time; Z (m) and Q (m^3/s) are the water level and water flow of the section, respectively; A (m^2) is the cross-sectional area; q (m^2/s) is the lateral inflow per unit length; B (m) is the river width; g (m/s^2) is gravitational acceleration; and K (m^3/s) is the flow modulus.

The data files of the MIKE11 hydrodynamic model mainly include files of sections, river networks, boundaries, and model parameters. The HD (hydrodynamic) module is the basic calculation module of MIKE11, and its module parameters are mainly numerical and physical parameters. Numerical parameters are related to the iterative solution of the equations, such as the number of iterations and iterative calculation accuracy. The physical parameter is mainly the roughness of the river bed. There are 152 measured post-flood sections in the study area. After considering that the two tributaries in the study area have little influence on the model simulation results, no tributaries are added to the one-dimensional hydrodynamic model. The measured flows at the Xiaolangdi Hydrological Station and water levels at the Gaocun Hydrological Station are used as the upper and lower boundary conditions, respectively. The time step of the hydrodynamic model is 1 min. We adjust the roughness of the river bed as model calibrations to improve the simulation accuracy. The outputs of MIKE11 are hydrological elements, such as the water level, flow, and velocity at each moment for 152 sections of the study area.

2.3 Habitat suitability model for the Yellow River carp

The habitat suitability index (*HSI*) is for evaluating the suitability and quality of wildlife habitats, and it is the biological basis of habitat simulations (Boavida et al., 2015; Morales-Marín et al., 2019; Sharma et al., 2022). Habitat suitability curves present the relationship between a species' growth and its influencing factors (Cho et al., 2012; Knudson et al., 2015), which is generally determined by the appearance frequency and distribution of the species. The *HSI* varies from 0 to 1 to quantitatively indicate the habitat suitability. In this study, the Yellow River carp is selected as the indicator species for the habitat in the lower reaches of the Yellow River. For the breeding period (including the parent fish spawning period and the larval fish development period), four important habitat factors are selected to determine the habitat suitability of the Yellow River carp. They are water depth h, flow velocity v, water temperature t, and water-level rise dz, and their definitions are as follows.

(1) Flow velocity v: The Yellow River carp is a kind of benthic omnivorous fish and mostly inhabits on the soft riverbed or in water with plentiful aquatic plants. It can lay sticky eggs in various water bodies but prefers slow-flowing or still water with aquatic plants. Its hatching time is 3–7 days in general. Then, its larval fish usually requires a stable water flow for 3–4 days to stay alive. The suitable flow velocity for larval development is in the range of 0–0.15 m/s (Wang et al., 2020).

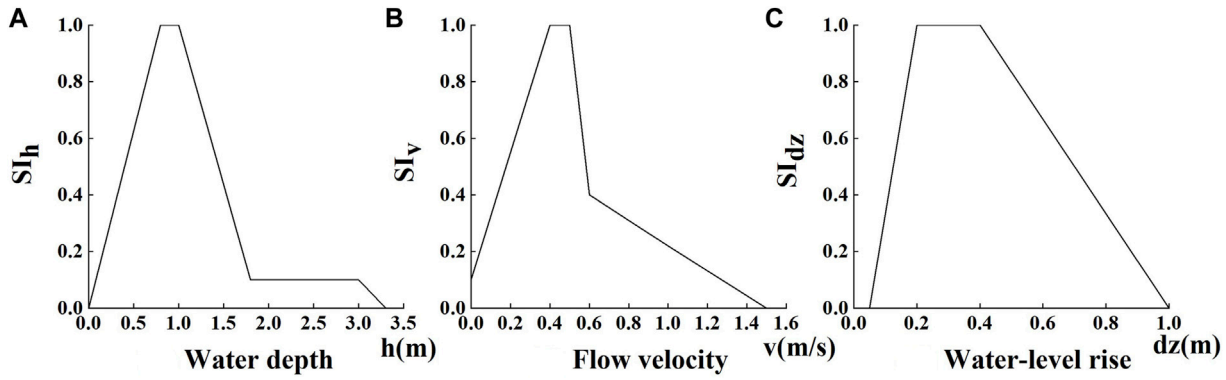

FIGURE 2
Parent fish spawning suitability index of the Yellow River carp in the study area. **(A)** Water depth *h*; **(B)** flow velocity *v*; **(C)** water-level rise *dz*.

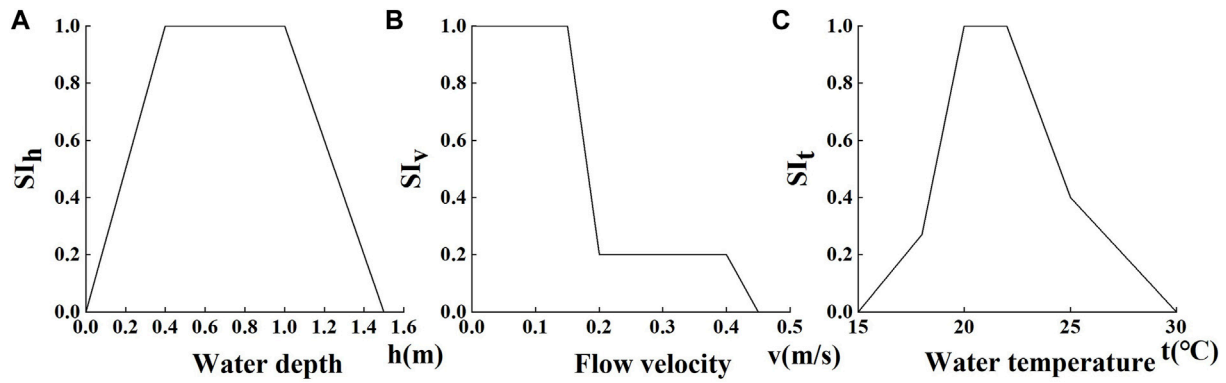

FIGURE 3
Larval fish development suitability index of the Yellow River carp in the study area. **(A)** Water depth *h*; **(B)** flow velocity *v*; **(C)** water temperature *t*.

(2) Water depth *h*: Neither too shallow nor too deep waters are suitable for fish movements; thus, the water depth of spawning grounds should generally be deeper than 1 m (Jiang et al., 2010b). Larval fish are survivable with a water depth in a free range of .2 m–1.5 m. In addition, a tiny fluctuation of water levels is more conducive to larval fish growth.

(3) Water temperature *t*: Water temperature is a crucial factor in the process of fish spawning because of its dependence for its occurrence, duration, and its temporal and spatial distribution of the spawning activity (Li et al., 2021). The Yellow River carp can spawn in water with temperatures of 18°C–28°C, and its optimum spawn temperature range is 18°C–24°C. The water temperature of 18°C is a critical value for Yellow River carp hatching. The water temperatures above 18°C could greatly improve the hatching, survival, and emergence rates.

(4) Water-level rise *dz*: The process of rising water is a necessary condition for stimulating fish to spawn. The rise of water levels is more important for fish dynamics processes no matter what its initial water level is. A certain flow pulse and water-level rise can promote fish spawning, reduce dystocia, and shorten the time of spawning and fertilization. It is also productive for the spawning quantity, spawning rate, and fertilized egg development (Li and Gao, 2013).

To summarize, the four different habitat factors of parent fish and larval fish are obtained, and its suitability curves of each single index are represented by step functions (as shown in Figures 2, 3). Then, the parent fish spawning suitability index (HSI_{pf}) is formulated of water depth *h*, flow velocity *v*, and water-level rise *dz* by Eq. 3, and the larval fish development suitability index (HSI_{lf}) is formulated of the flow velocity *v*, water depth *h*, and water temperature *t* by Eq. 4. In this paper, we propose the Habitat Suitability Index *HSI* of the Yellow River carp by the mean values of HSI_{pf} and HSI_{lf} in Eq. 5 as follows.

$$HSI_{pf} = \frac{(SI_h + SI_v + SI_{dz})}{3}, \tag{3}$$

$$HSI_{lf} = \frac{(SI_h + SI_v + SI_t)}{3}, \tag{4}$$

$$HSI = \frac{HSI_{pf} + HSI_{lf}}{2}, \tag{5}$$

where HSI_{pf}, HSI_{lf}, and HSI represent the parent fish spawning suitability index, larval fish development suitability index, and habitat suitability index of the Yellow River carp, respectively, and SI_h, SI_v, SI_t, and SI_{dz} represent the water depth index, flow velocity index, water temperature index, and water-level rise index, respectively.

TABLE 1 Suitability for the Yellow River carp under different values of the habitat suitability index (*HSI*).

HSI	Suitability
0–0.5	Poor
0.5–0.8	Generally suitable
0.8–1	Suitable

We have the water temperature t, and we calculate the water depth h and flow velocity v of the river cross section using the one-dimensional hydrodynamic model. Then, the values of SI_h, SI_v, SI_{dz}, and SI_t can be pointed out according to Figures 2, 3. It can be seen that even under the same hydrological conditions, the suitability of parent fish and larval fish is different, and the comprehensive habitat suitability index *HSI* is obtained by Eqs 3, 4, 5. Different *HSI* values represent the different suitability of the habitat (Table 1) (Jiang et al., 2019; Tang et al., 2022). We find that all river suitable sections with a *HSI* value greater than .5 are suitable for carp's reproduction, according to Table 1. The reach between these two continuous suitable habitat sections is defined as a suitable spawning reach. The reach length is defined as L_{sr}, and the average *HSI* value of up and down reach sections is defined as HSI_{sr}. L_{sr} and HSI_{sr} are used to describe the scale and quality of a spawning reach, respectively.

In this study, the habitat suitability index is used to build the habitat suitability model of the Yellow River carp. Furthermore, it is combined with the one-dimensional hydrodynamic modeling for habitat factors to define the habitat suitability and assess the suitability of the habitat.

2.4 Statistical analysis

The Nash–Sutcliffe efficiency (NSE) and the root mean square error (RMSE) are selected to evaluate the accuracy of the hydrodynamic model. The NSE is a statistical parameter that describes the fitting degree between simulation and measurement. The more it closes to 1, the better the simulation of the hydrodynamic model is. The RMSE represents the deviation between the simulated and the measured value. The more it closes to 0, the smaller the model error is.

3 Results and discussions

3.1 Calibration and verification of the hydrodynamic model

The flood from August 16 to September 11 in the year 2018 was chosen to calibrate the riverbed roughness in the study area, and another flood from September 15 to October 10, 2018, was chosen to verify the hydrodynamic model. If the model can well simulate the flood process, it shows that the model has good applicability at all water levels and can also well reflect the hydrodynamic characteristics during the spawning period.

Three hydrological stations (Xixiayuan, Huayuankou, and Jiahetan) were selected to calibrate and verify this model. The range of riverbed roughness in this study was determined as .020 to .032. The water-level calibration and verification results of the three hydrological stations are shown in Figure 4, which well-fitted the water flow under different incoming waters and captured the process of water-level fluctuation, such as the rise and fall in 8.28–9.4. We listed the NSE and RMSE in Table 2 for the results of Figure 4. The minimum NSE for calibration and verification was .769, and the maximum RMSE was .161 m. This means that the model can accurately reflect the process of hydrodynamic changes and can be used for the construction of habitat models.

3.2 Validation of the habitat suitability model for the Yellow River carp

April to June is the spawning period of the Yellow River carp every year. It is the most critical and vulnerable stage for the Yellow River carp to spawn and develop. To breed successfully, the Yellow River carp has extremely high requirements on the ecological and hydraulic conditions of the habitat during its spawning period. There are 16 spawning grounds marked by stars (Figure 5), which are measured spawning locations in the Henan section of the Yellow River studied by Hui et al. (2019). To verify the simulation of the habitat model, the habitat factors from April 1 to June 30 of the year 2014 were chosen. The daily *HSI* values of 152 sections were calculated by these habitat factors, according to Eqs 3, 4, 5, and then, the daily average *HSI* values of each section from April to June were obtained. There were 19 suitable spawning reaches shown in red lines (Figure 5). Their size L_{sr} and spawning habitat quality HSI_{sr} are displayed in Supplementary Table S1. Most of the 16 measured spawning grounds studied by Hui et al. (2019) (black stars) fell within the spawning reaches (red lines) simulated by the habitat suitability model (Figure 5). This indicates that the habitat suitability model of the Yellow River carp can simulate accurately the positions of spawning habitats. For a measured spawning ground, its *HSI* value is the *HSI* value of the nearest section among 152 sections. 87.5% of the 16 measured spawning grounds had their *HSI* values greater than .5 except grounds 7 and 10 (Table 3). The spawning area is simulated by the average value of *HSI* from April to June; the measured spawning grounds only need to meet their reproductive requirements for a long enough time in April–June rather than the whole 3 months, so the model simulation results have a certain deviation from the measured spawning ground. These spawning grounds are generally suitable for the Yellow River carp, which is consistent with Hui's findings (Table 1). This indicates that the habitat suitability model of the Yellow River carp has a good simulation effect and can well represent the quality of spawning habitats.

3.3 Effects of the Xiaolangdi Dam on the Yellow River carp reproduction

3.3.1 Dynamic changes of *HSI* for the Yellow River carp before and after dam construction

The Xiaolangdi Dam was built in 2001. Hence, April–June every year in the 1980–1990 period was selected as the representative period before the dam construction, and April–June in the 2006–2018 period was selected as the representative period after dam construction. In this study, we defined the *HSI*, HSI_{pf}, and HSI_{lf} values of the whole

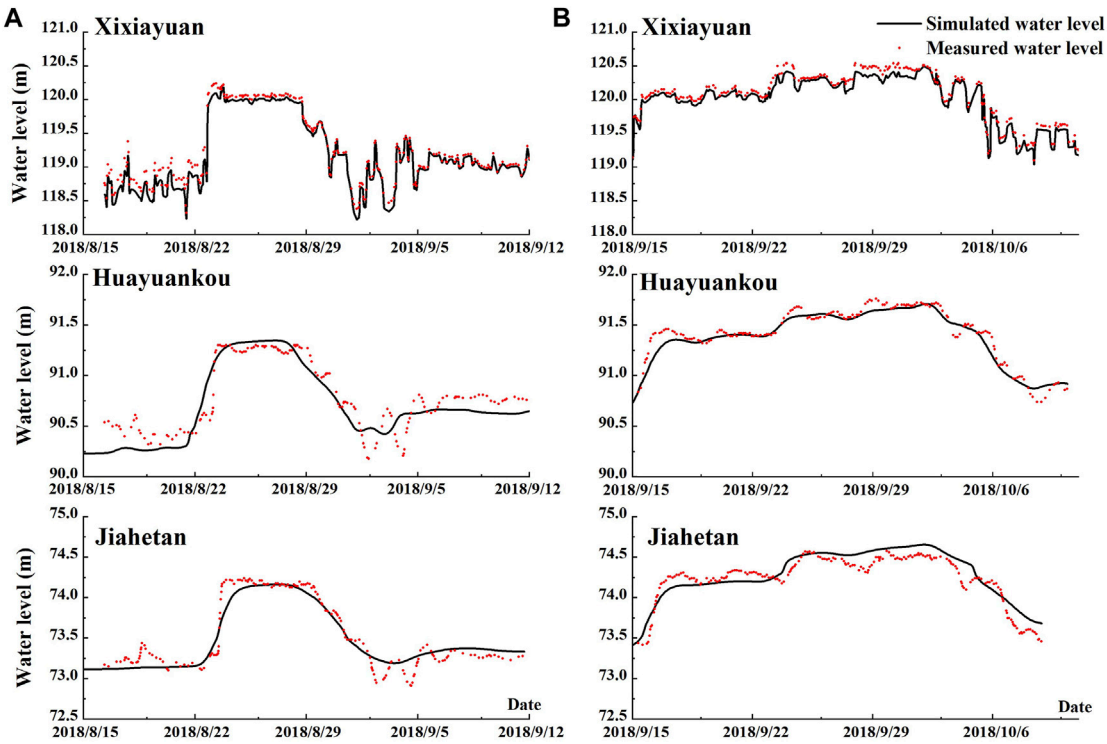

FIGURE 4
Calibration and verification results of the measured and simulated water levels of the three hydrological stations (Xixiayuan, Huayuankou, and Jiahetan) in the study area during 2018.8.16–2018.9.11 and 2018.9.15–2018.10.10 periods. **(A)** Water-level calibration results; **(B)** water-level verification results.

TABLE 2 Criteria of fit for the simulation of the hydrological stations of the Yellow River. NSE = Nash–Sutcliffe efficiency; RMSE = root mean square error.

Hydrological station	NSE		RMSE (m)	
	Calibration	Verification	Calibration	Verification
Xixiayuan	0.958	0.973	0.100	0.079
Huayuankou	0.769	0.919	0.161	0.084
Jiahetan	0.901	0.880	0.136	0.130

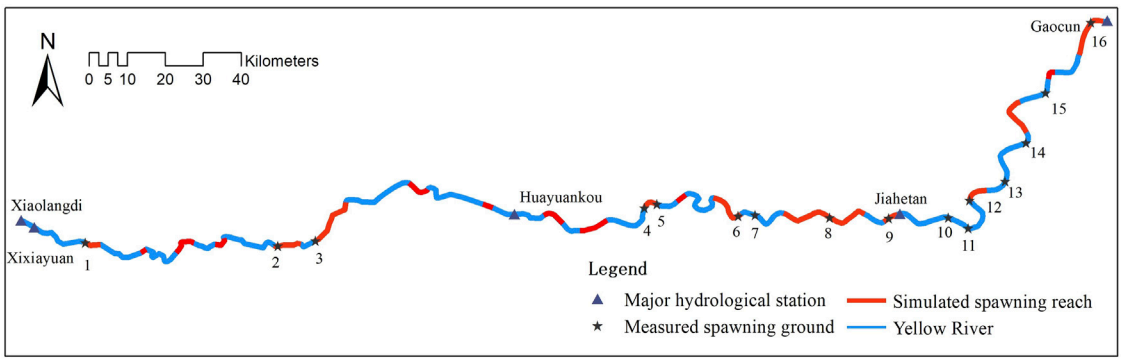

FIGURE 5
Predicted spawning ground map by the habitat suitability model of the Yellow River carp in the reach from Xiaolangdi to Gaocun of the Yellow River from April 1 to June 30, 2014.

TABLE 3 ***HSI*** **values of the spawning grounds of the Yellow River carp from April 1 to 30 June 2014.**

Spawning ground No.	*HSI*	Spawning ground no.	*HSI*
1	0.504	9	0.549
2	0.534	10	0.426
3	0.555	11	0.576
4	0.526	12	0.562
5	0.531	13	0.563
6	0.617	14	0.547
7	0.424	15	0.561
8	0.555	16	0.571

study area, i.e., the Xiaolangdi–Gaocun section of the lower Yellow River by the average value of 152 cross sections located in it. The *HSI*, HSI_{pf}, and HSI_{lf} daily values from April 1 to June 30 in these two representative periods were simulated by the habitat suitability model and are presented in Figure 6. Furthermore, it was quantitatively described by the variations, as shown in Table 4.

From Table 4, the following could be observed: 1) the discharge of the Xiaolangdi Dam from April to June is regulated. However, the water-level rise index SI_{dz} of the parent fish dropped significantly by 35.75% after the dam construction (Table 4). It meant that the water-level rise was no longer suitable for the spawning activities of the Yellow River carp, and it led to a decrease in the parent fish spawning suitability index HSI_{pf} by 1.89%; 2) the low-temperature water released by the Xiaolangdi Reservoir could affect the water temperature under the dam. The water temperatures of the Xiaolangdi hydrological station in April, May, and June are generally lower than that before the dam construction (Table 5). Thus, the water temperature suitability index SI_t decreased by 26.41% after the dam construction (Table 4). This caused the decrease by 8.95% of the larval fish developmental suitability index HSI_{lf}. 3). It could be seen that the habitat suitability index *HSI* for the Yellow River carp in the study area decreased by 5.28% after the construction of the Xiaolangdi Dam, which was caused by the 1.89% decrease of the fish spawning suitability index HSI_{pf} and 8.95% decrease of the larval fish developmental suitability index HSI_{lf} (Table 4). Therefore, we can get the conclusion that the construction of the Xiaolangdi Dam reduced the reproductive quality of the Yellow River carp and limited the larval fish development more. We explain the dynamic changes and reasons of *HSI* before and after dam construction in details as follows.

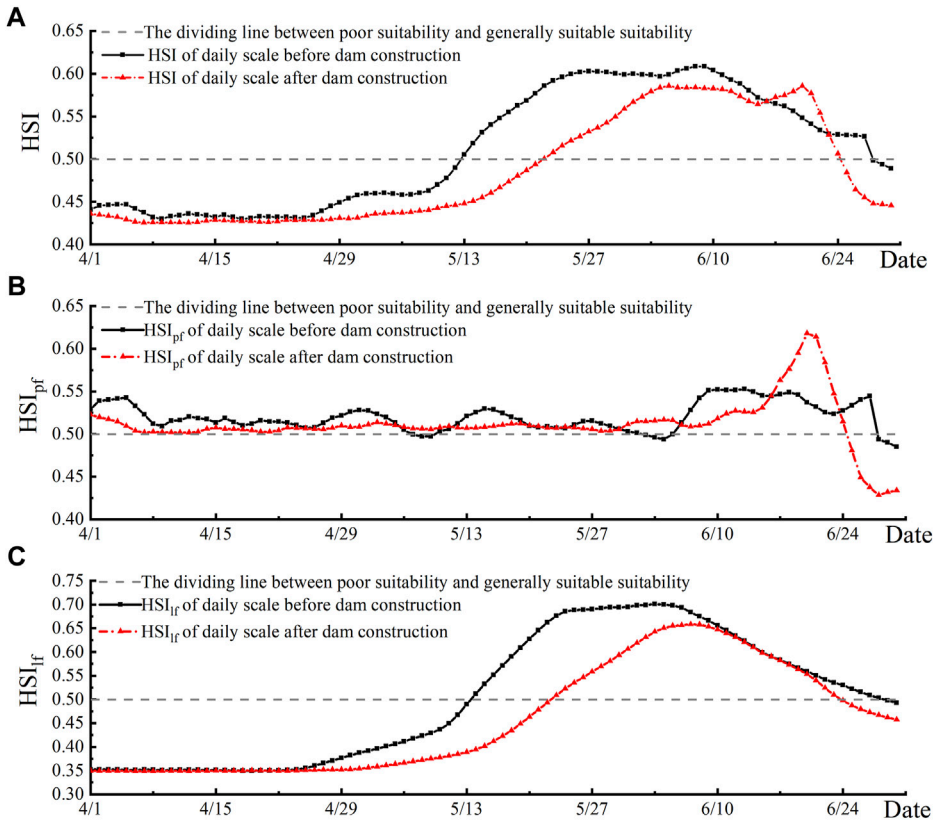

FIGURE 6
Simulation of the habitat suitability index (*HSI*), parent fish spawning suitability index (HSI_{pf}), and larval fish development suitability index (HSI_{lf}) of the Yellow River carp at a daily scale during April 1–June 30 from 1980–1990 (before dam construction) to 2006–2018 (after dam construction). **(A)** Comparison of the daily-scale habitat suitability index (*HSI*); **(B)** comparison of the daily-scale parent fish spawning suitability index (HSI_{pf}); **(C)** comparison of the daily-scale larval fish development suitability index (HSI_{lf}).

TABLE 4 Percentage variation of each suitability index (*SI*) for the Yellow River carp of the whole study area before and after the dam construction.

Parent fish spawning suitability	Variation	Larval fish development suitability	Variation
SI_h	−.49%	SI_h	−.66%
SI_{dz}	−35.75%	SI_t	−26.41%
SI_v	.49%	SI_v	−12.65%
HSI_{pf}	−1.89%	HSI_{lf}	−8.95%
Habitat suitability		Variation	
HSI		−5.28%	

Note: The variation is the relative change of the multi-year daily average of the whole study area from April to June before and after the dam construction.

TABLE 5 Multi-year monthly average water temperature of the Xiaolangdi Hydrological Station from April to June before and after dam construction.

	April (°C)	May (°C)	June (°C)
Before	14.07	19.02	23.80
After	6.30	13.40	21.30

3.3.1.1 The influence of the water level and the water-level rise on *HSI*

The period from mid-June to early-July after dam construction is the pre-flood water and the sediment regulation period of the Xiaolangdi Reservoir. The Xiaolangdi Reservoir releases its clear water during this period, and its reservoir water level drops sharply accordingly (Wang et al., 2019). Thus, released water creates a rapid increase in the water level of the downstream river, as shown in the red line in Figure 7A from June 15 to June 22. The continuous rising time of the water level from June 15 to June 22 (Figure 7A) coincides with the timing of the Yellow River carp spawning and hatching cycle, which is bound to have an impact on the reproduction of the Yellow River carp. The continuously rising water level creates the increasing water-level rise index (SI_{dz}) from June 15 to June 22, as shown by the red line in Figure 7B. It also causes an increasing effect on the parent fish spawning suitability index HSI_{pf} (Figure 6B). We can get the conclusion that the continuous increase in the water level from June 15 to June 22 has improved the reproductive ability of the Yellow River carp. In late June, the average water level begins to drop from June 22 to June 29 (Figure 7A), which leads to corresponding decreases in the water-level rise suitability index SI_{dz} and the parent fish spawning suitability index HSI_{pf}. Figure 6A accurately figures out the increase of habitat suitability *HSI* from June 15 to June 22 that is caused by the continuous rise of the water level and the decrease of habitat suitability *HSI* from June 22 to June 29 that is caused by the decline of the water-level rise.

The continuous increase of the water level from June 15 to June 22 is beneficial to the breeding of the Yellow River carp. However, on the whole, the operation of the Xiaolangdi Dam makes the flow downstream of the dam smoother from April to June (excluding pre-flood water and the sediment regulation period), resulting in a 35.75% decrease in the water-level rise index (SI_{dz}) (Table 4).

3.3.1.2 The influence of water temperature on *HSI*

After the completion of the dam, the low-temperature water discharge from the Xiaolangdi Reservoir in April and May had a greater impact on the water temperature downstream of the dam but had a less impact in June (Table 5). There is a huge gap between the water temperature suitability index SI_t before and after the dam construction (Figure 8). This is because the water temperature downstream of the dam in May is primarily controlled by the

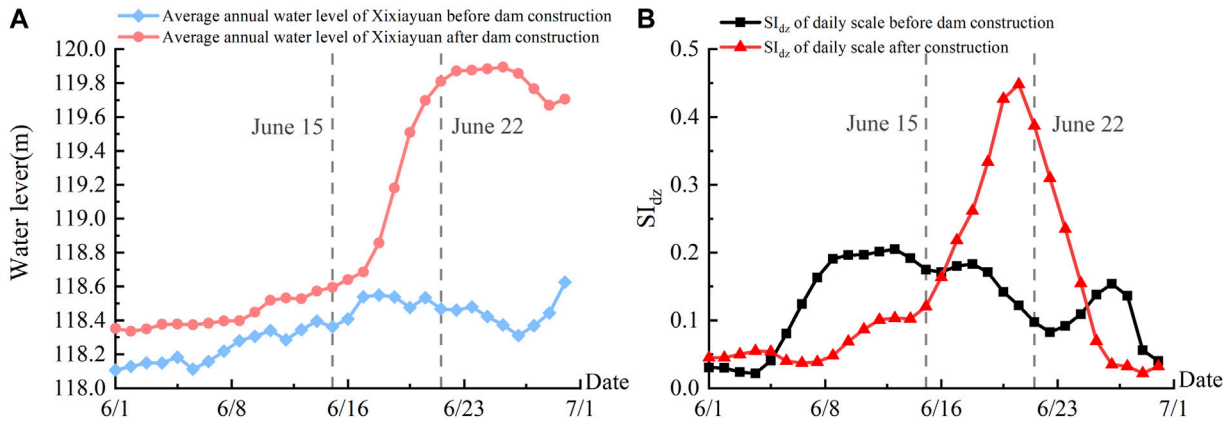

FIGURE 7
Simulated average water level of the Xixiayuan Hydrological Station over the years and the daily-scale water-level rise index (SI_{dz}) of the Yellow River carp from June 1 to June 30 in 1980–1990 (before dam construction) and 2006–2018 (after dam construction). **(A)** Average water level of the Xixiayuan Hydrological Station simulated by MIKE11; **(B)** the daily-scale water-level rise index (SI_{dz}) of the Yellow River carp.

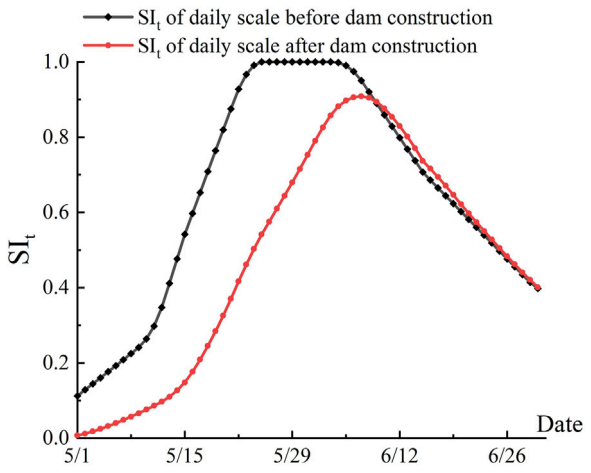

FIGURE 8
Comparison of the daily-scale water temperature index (SI_t) of the Yellow River carp before and after dam construction.

construction and operation of the Xiaolangdi Reservoir. After the dam construction, the water temperature suitability index SI_t shows a significant lag and a decrease from May 1 to June 12 compared with the pre-dam construction period (Figure 8). This inevitably causes the corresponding decrease of the larval fish developmental suitability index HSI_{lf} from May 1 to June 10 and the corresponding lag of the habitat suitability index *HSI* from mid-May to early June (Figures 6A, C).

3.3.2 Changes in the spawning reaches of the Yellow River carp before and after dam construction

The period of April, May, and June in the years 1980–1990 was chosen as the representative period before the dam construction, and April, May, and June in the years 2006–2018 was chosen as the representative period after dam construction. The daily average *HSI* values of each section for many years were calculated in representative periods by the habitat suitability model, and the habitat suitability index HSI_{sr} and spawning reach size L_{sr} of the Yellow River carp spawning reach were obtained (Table 6). The corresponding spawning reaches are depicted in Figure 9.

From Table 6 and Figure 9, it is clear that the establishment of the Xiaolangdi Dam has changed the size and locations of the spawning reaches of the Yellow River carp. There were 22 spawning reaches simulated in the study area before dam construction in 1980–1990, with a total length of 101.757 km and an average habitat suitability index (HSI_{sr}) value (the average of all spawning reach HSI_{sr} values) of .565 (Table 6). However, after the dam construction, the number of spawning reaches was predicted as 16, with their size reduced to 85.241 km, and the average habitat suitability index (HSI_{sr}) value was .546 during the years 2006–2018. The average habitat suitability index (HSI_{sr}) decreased slightly from .565 before dam construction to .546 after dam construction, but the extent of the spawning reaches decreased sharply by 16.23%, and some spawning reaches even disappeared. We can also see the differences in size and locations of the Yellow River carp spawning reaches (Figure 9). Thus, we demonstrate that the establishment of the Xiaolangdi Dam has changed the locations of the spawning reaches of the Yellow River carp and likely reduced their size.

It can be seen that before and after dam construction, the spawning reaches located in the Xiaolangdi–Huayuankou section, which is directly downstream of the dam, have undergone great changes (Figure 9). There are five spawning reaches that have completely disappeared, which are reach No. 1, No. 3, No. 4, No. 6, and No. 7 marked in blue in Table 6. This is the direct result of the Xiaolangdi Dam construction. These five disappearing reaches are the principal domains affected by the low-temperature water released from the Xiaolangdi Reservoir. After all, they are presumably no longer suitable for the carp due to the low-temperature habitat condition. In addition, the further downstream section from Huayuankou to Gaocun is significantly less affected by the dam. Its distribution of spawning reaches has only one spawning reach, i.e., reach No. 16, that disappeared completely, and its average habitat suitability index (HSI_{sr}) drops slightly from .564 to .547.

3.4 Impact of dam construction on fish reproduction

Based on the one-dimensional hydrodynamic model and the habitat suitability model of the Yellow River carp, the simulation of the habitat suitability before the dam construction (1980–1990) and after the dam construction (2006–2018) shows that the habitat suitability index reduces generally (Figure 6A), and the scale of the Yellow River carp spawning reaches in the lower reaches of the Yellow River decreases after the dam construction (Table 6; Figure 9).

3.4.1 Impact of dam construction on the water-level rises

Water-level rises increase the chance of shoal flooding and the extent of still-water areas. It is not only conducive to the spawning of the Yellow River carp but also to the transfer of food organisms between nearshore areas and the main river trough, thereby expanding the habitat for fish. After the dam construction, the operation of the Xiaolangdi Reservoir makes the flow downstream of the dam smoother from April to June (excluding pre-flood water and the sediment regulation period). This reduces the water-lever rise suitability index (SI_{dz}) from April to June each year (Figure 7B) and makes the carp lose its spawning stimulation, which is one of the unfavorable factors for its reproduction. Therefore, the parent fish spawning suitability index HSI_{pf} of the Yellow River carp, which characterizes the reproductive ability, is correspondingly reduced after the dam construction (Figure 6C).

3.4.2 Impact of dam construction on water temperature

The water temperatures above 18°C are critical for the Yellow River carp to spawn and hatch. The appropriate temperature can greatly improve its hatching, survival, and emergence rates. Otherwise, it will be another unfavorable factor for reproduction. After the dam construction, the large heat capacity of the impoundment in the Xiaolangdi Reservoir causes a significant difference in temperature between the discharged water and the natural river water. The low-temperature discharged water released from the Xiaolangdi Reservoir can influence hundreds of kilometers downstream. It delays and flattens the water temperature downstream. The Xiaolangdi–Huayuankou reach is the main affected section of the released low-temperature water, and the impact period is mainly from November to June (Jiao and Lei, 2021), coinciding with the usual breeding period of the Yellow

TABLE 6 Habitat suitability index of the spawning reach HSI_{sr} and the size of spawning reaches L_{sr} for the Yellow River carp, before and after the construction of the Xiaolangdi Dam.

Spawning reach no.	Before dam construction		After dam construction	
	HSI_{sr}	L_{sr}/km	HSI_{sr}	L_{sr}/km
1	0.526	3.922	—	0
2	0.583	1.465	0.529	1.465
3	0.546	9.284	—	0
4	0.567	2.352	—	0
5	0.589	5.05	0.549	5.05
6	0.555	7.138	—	0
7	0.559	1.543	—	0
8	0.599	4.106	0.567	4.106
9	0.573	4.659	0.537	4.659
10	0.587	3.412	0.558	3.412
11	0.568	10.061	0.534	10.061
12	0.546	2.711	0.517	2.711
13	0.603	1.287	0.565	1.287
14	0.586	7.251	0.563	7.251
15	0.582	18.966	0.555	18.966
16	0.551	0.705	—	0
17	0.539	1.049	0.532	0.486
18	0.568	2.586	0.55	2.586
19	0.589	8.856	0.553	8.856
20	0.536	1.414	0.528	1.414
21	0.563	1.066	0.563	1.066
22	0.518	2.874	0.54	12.138

Note: The spawning reaches marked blue in the table are the spawning reaches that disappeared after the dam was built.

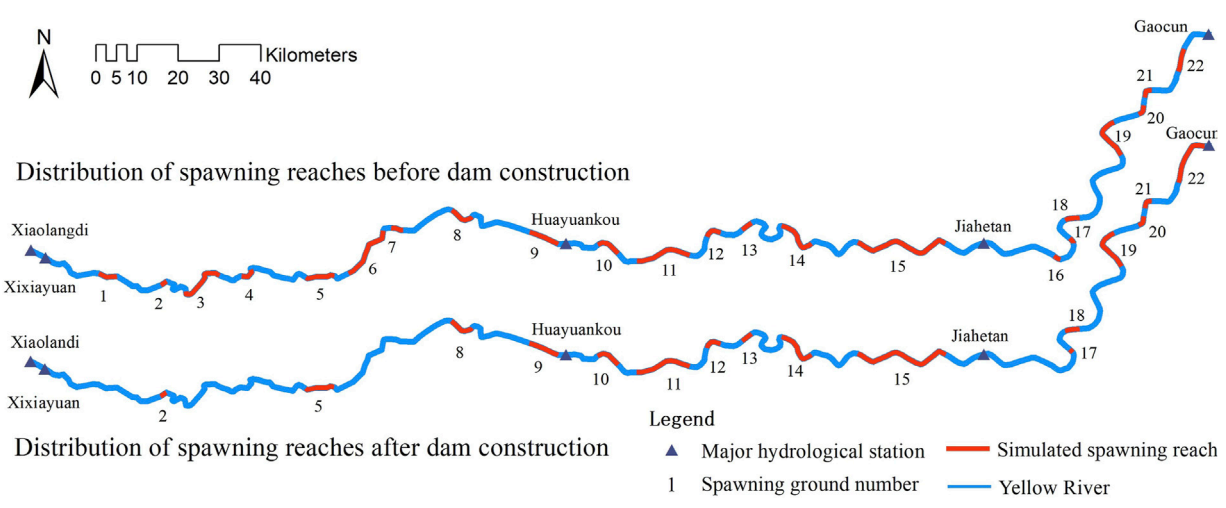

FIGURE 9
Simulated distribution of the Yellow River carp spawning reaches from April 1 to June 30 in 1980–1990 (before dam construction) and 2006–2018 (after dam construction).

River carp. This released low-temperature water results in a decline and lag in the water temperature suitability index (SI_t) downstream which directly delays spawning and affects the growth of larval fish. Therefore, the Xiaolangdi Dam has delayed and hindered the development and reproduction of the Yellow River carp in the downstream reaches, which has reflected in the corresponding reduction of the habitat suitability index (*HSI*) for the Yellow River carp, as shown in Figure 6A.

3.5 Impact of the dam on river ecology

The impact of the construction and operation of the Xiaolangdi Dam on the river ecology is two-fold. The Xiaolangdi Reservoir has changed the hydrological regime of the river downstream. The notably changed flow velocity, water levels, water-level rises, and water temperatures result in a decline in the quality of the Yellow River carp reproduction and a reduction in the size of the spawning reaches. The release of the lower-temperature bottom water from the reservoir has a direct impact on the development and reproduction of fish downstream of the dam. Furthermore, the dam has blocked channels used by migratory species for feeding and reproduction, with sharp declines for these fishes. For instance, some fishes in the Yellow River, like the migratory *Coreius septentrionalis* (Nichols) and *Coilia nasus*, are now endangered (Han et al., 2013).

However, the completion and operation of the Xiaolangdi Dam also plays a role in improving the ecological environment to some extent. It now ensures a continuous river flow downstream and increases the guarantee rate of ecological flow (Gao et al., 2014). Meanwhile, the sediment from the reservoir constantly scours the riverbed downstream, the floodplain flux is increased, and the river morphology tends to be stable. All of these changes provide a more stable habitat for organisms. There are complex interactions among these factors which affect the fish growth, and the responses of fish are also unclear, which makes it more difficult to establish clear correlations between fish habitat factors and habitat suitability. Deep research on the impact of multiple factors on fish habitats is still merited.

4 Conclusion

This study implemented a one-dimensional hydrodynamic model and built a habitat suitability model for the Yellow River carp to depict dynamic changes of reproduction suitability in the lower reaches of the Yellow River before and after the construction of the Xiaolangdi Dam. By simulating and analyzing the habitat suitability and spawning reaches of the Yellow River before and after the dam construction, we get the main conclusions as follows:

(1) After the dam construction, the artificially controlled discharges of the Xiaolangdi Reservoir mainly result in the water-level rise and the water temperature drop. This operation reduces the habitat suitability *HSI* of the Yellow River carp by 5.28% in average, including 1.89% for the parent fish spawning suitability index HSI_{pf} and 8.95% for the larval fish developmental suitability index HSI_{lf}. It suggests that the larval fish development is more affected by the dam.
(2) Dam construction reduces the habitat quality of spawning reaches and may even lead to the disappearance of spawning reaches. Compared with the periods of 1980–1990 before dam construction and 2006–2018 after construction, the number of spawning reaches downstream of the dam reduces from 22 to 16, their extent reduces by 16.23%, and their habitat suitability decreases from .564 to .547. In particular, the effect of dam construction on the Yellow River carp reproduction is more pronounced in the downstream section close to the dam from Xiaolangdi to Huanakou, where five spawning reaches disappear. However, in the reach between Huayuankou and Gaocun farther away downstream from the dam, the effect works weaker.

This paper has studied the response of the Yellow River carp to hydrological rhythm changes after dam construction. It also provides a reference for restoring the spawning habitat of the Yellow River carp and constructing the Xiaolangdi Reservoir's ecological dispatch, which considers the reproductive needs of the Yellow River carp. Furthermore, the response and feedback relationship between the hydrological situation, habitat demand, and fish behavior under dam construction and operation will be further clarified. In the future, the reservoir regulation mechanism that is conducive to fish survival and river ecological health could be explored to serve the optimization of the Xiaolangdi Reservoir and other large reservoirs.

Data availability statement

The datasets presented in this article are not readily available because the data are obtained from the project and used under the permission of the current research. Requests to access the datasets should be directed to Qiongyao Ruan, 120202238021@ncepu.edu.cn.

Author contributions

QR: data curation, formal analysis, methodology, software, and writing—original draft. WL: methodology, software, reviewing, and editing. SZ: resources, conceptualization, writing—reviewing and editing, supervision, funding acquisition, and project administration. CT: methodology and validation. JH: data curation and formal analysis.

Funding

This study was supported by the National Natural Science Foundation of China (52061135104) and the Joint Funds of the National Natural Science Foundation of China (U2243236).

Acknowledgments

The authors thank Cynthia Kulongowski from Liwen Bianji (Edanz) (www.liwenbianji.cn/) for editing the English text of a draft of this manuscript.

Conflict of interest

The authors declare that the research was conducted in the absence of any commercial or financial relationships that could be construed as a potential conflict of interest.

Publisher's note

References

Ahmadi-Nedushan, B., St-Hilaire, A., Bérubé, M., Robichaud, E., Thiemonge, N., and Bobee, B. (2010). A review of statistical methods for the evaluation of aquatic habitat suitability for instream flow assessment. *River Res. Appl.* 22 (5), 503–523. doi:10.1002/rra.918

Boavida, I., Santos, J. M., Ferreira, T., and Pinheiro, A. (2015). Barbel habitat alterations due to hydropeaking. *J. hydro-environment Res.* 9 (2), 237–247. doi:10.1016/j.jher.2014.07.009

Chang, Y. L., Hsieh, T. Y., Chen, C. H., and Yang, J. C. (2013). Two-dimensional numerical investigation for short-and long-term effects of spur dikes on weighted usable area of Rhinogobius candidianus (Goby). *J. Hydraulic Eng.* 139 (12), 1297–1303. doi:10.1061/(asce)hy.1943-7900.0000789

Cho, Y., Lee, W. C., Hong, S., Kim, H. C., and Kim, J. B. (2012). GIS-based suitable site selection using habitat suitability index for oyster farms in Geoje-Hansan Bay, Korea. *Ocean Coast. Manag.* 56, 10–16. doi:10.1016/j.ocecoaman.2011.10.009

Collier, M., Webb, R. H., and Schmidt, J. C. (1996). *Dams and rivers: A primer on the downstream effects of dams. US department of the interior, US geological survey*. Pennsylvania: DIANE.

Fantin-Cruz, I., Pedrollo, O., Girard, P., Zeilhofer, P., and Hamilton, S. K. (2015). Effects of a diversion hydropower facility on the hydrological regime of the Correntes River, a tributary to the Pantanal floodplain, Brazil. *J. Hydrology* 531, 810–820. doi:10.1016/j.jhydrol.2015.10.045

Gao, G., Li, X., and Ma, Y. (2014). Research on ecological scheduling of Xiaolangdi reservoir. *Yellow River* 36 (9), 76–79. doi:10.3969/j.issn.1000-1379.2014.09.025

Han, T., Xiong, Y., and Sun, X. (2013). The impact of the Yellow River Xiaolangdi Project on aquatic biological resources and the reflection on the conservation of resources. *China Fish.* (6), 28–29. doi:10.3969/j.issn.1002-6681.2013.06.013

Hui, J., Jie, Z., and He, H. (2019). Spawning ground status of fish that release benthic eggs in the henan section of Yellow River. *J. Hydroecology* 40 (4), 108–114. doi:10.15928/j.1674-3075.2019.04.014

Im, D., Choi, S. U., and Choi, B. (2018). Physical habitat simulation for a fish community using the ANFIS method. *Ecol. Inf.* 43, 73–83. doi:10.1016/j.ecoinf.2017.09.001

Jiang, N., Jiang, B., and Lei, G. (2019). Influence of waterway regulation project on habitat suitability index of Four Major Chinese Carps in Dongliu channel in lower Yangtze River. *Yangtze River* 50 (5), 5–9. doi:10.16232/j.cnki.1001-4179.2019.05.002

Jiang, X., Arthington, A., and Changming, L. (2010b). Environmental flow requirements of fish in the lower reach of the Yellow River. *Water Int.* 35 (4), 381–396. doi:10.1080/02508060.2010.506261

Jiang, X., Zhao, W., and Zhang, W. (2010a). The impact of Xiaolangdi Dam operation on the habitat of Yellow River Carp (Cyprinus(Cyprinus) carpio haematopterus Temminck et Schlegel). *Acta Ecol. Sin.* 30 (18), 4940–4947.

Jiao, R., and Lei, G. (2021). "Research on water temperature monitoring and evaluation along the lower reaches of the Yellow River. Hohai university, xi'an university of Technology, China dredging association, shanxi water conservancy society," in Proceedings of the 9th China Water Ecology Conference in 2021, 241–249.

Karr, J. R. (1981). Assessment of biotic integrity using fish communities. *Fisheries* 6 (6), 21–27. doi:10.1577/1548-8446(1981)006<0021:aobiuf>2.0.co;2

Knudson, M. D., VanLooy, J. A., and Hill, M. J. (2015). A habitat suitability index (HSI) for the Western prairie fringed orchid (Platanthera praeclara) on the Sheyenne National Grassland, North Dakota, USA. *Ecol. Indic.* 57, 536–545. doi:10.1016/j.ecolind.2015.05.011

Li, B., and Gao, J. (2013). Factors affecting the gonadal development of Yellow River Carp broodstock. *Fish. Guide be Rich* (17), 30–31.

Li, T., Mo, K., Wang, J., Chen, Q., Zhang, J., Zeng, C., et al. (2021). Mismatch between critical and accumulated temperature following river damming impacts fish spawning. *Sci. Total Environ.* 756, 144052. doi:10.1016/j.scitotenv.2020.144052

Liu, J., Zang, C., Tian, S., Yang, H., Jia, S., You, L., et al. (2013). Water conservancy projects in China: Achievements, challenges and way forward. *Glob. Environ. Change* 23 (3), 633–643. doi:10.1016/j.gloenvcha.2013.02.002

Morales-Marín, L., Rokaya, P., Sanyal, P., Sereda, J., and Lindenschmidt, K. (2019). Changes in streamflow and water temperature affect fish habitat in the Athabasca River basin in the context of climate change. *Ecol. Model.* 407, 108718. doi:10.1016/j.ecolmodel.2019.108718

Morita, K., and Yamamoto, S. (2002). Effects of habitat fragmentation by damming on the persistence of stream-dwelling charr populations. *Conserv. Biol.* 16 (5), 1318–1323. doi:10.1046/j.1523-1739.2002.01476.x

Mouton, A. M., Schneider, M., Depestele, J., Goethals, P. L., and De Pauw, N. (2007). Fish habitat modelling as a tool for river management. *Ecol. Eng.* 29 (3), 305–315. doi:10.1016/j.ecoleng.2006.11.002

Muñoz-Mas, R., Martínez-Capel, F., Schneider, M., and Mouton, A. M. (2012). Assessment of Brown trout habitat suitability in the jucar River Basin (Spain): Comparison of data-driven approaches with fuzzy-logic models and univariate suitability curves. *Sci. Total Environ.* 440, 123–131. doi:10.1016/j.scitotenv.2012.07.074

Sharma, A., Baruah, A., Mangukiya, N., Hinge, G., and Bharali, B. (2022). Evaluation of Gangetic dolphin habitat suitability under hydroclimatic changes using a coupled hydrological-hydrodynamic approach. *Ecol. Inf.* 69, 101639. doi:10.1016/j.ecoinf.2022.101639

Sun, G., and Sheng, L. (2000). Theory of keystone species in ecosystems: New idea, new mechanism, new approach. *J. Northeast Normal Univ. Nat. Sci. Ed.* 32 (3), 73–77. doi:10.16163/j.cnki.22-1123/n.2000.03.017

Tang, C., Yan, Q., Li, W., Yang, X., and Zhang, S. (2022). Impact of dam construction on the spawning grounds of the four major Chinese carps in the Three Gorges Reservoir. *J. Hydrology* 609, 127694. doi:10.1016/j.jhydrol.2022.127694

Wang, R., Huang, J., and Ge, L. (2020). Study of ecological flow based on the relationship between cyprinusy carpio habitat hydrological and ecological response in the lower Yellow River. *J. Hydraulic Eng.* 51, 1175–1187. doi:10.13243/j.cnki.slxb.20200184

Wang, T., Li, X., and Qu, S. (2019). "Water and sediment regulation of Xiaolangdi reservoir in medium and small floods during recent pre-flood season," in *Yellow River* (New Haven: Yale University Press), 47–50.

Wang, Y., Rhoads, B. L., and Wang, D. (2016). Assessment of the flow regime alterations in the middle reach of the Yangtze river associated with dam construction: Potential ecological implications. *Hydrol. Process.* 30 (21), 3949–3966. doi:10.1002/hyp.10921

Yi, Y., Tang, C., Yang, Z., and Chen, X. (2014). Influence of manwan reservoir on fish habitat in the middle reach of the lancang river. *Ecol. Eng.* 69, 106–117. doi:10.1016/j.ecoleng.2014.03.026

Yi, Y., and Yue, S. (2011). Habitat suitability function of four major Chinese Carps spawning sites in the Yangtze River. *J. Basic Sci. Eng.* 19, 117–122. doi:10.3969/j.issn.1005-0930.2011.s1.013

Zhang, C., and Han, X. (2016). The current situation and protection strategies of carp germplasm resources in the Yellow River in Zhengzhou. *Henan Fish.* (1), 4–6.

Zhang, W., Huang, Q., and Jiang, X. (2008). Mechanistic insight into the biological nanopore in tetragonal lysozyme crystal. *Adv. Water Sci.* 19 (2), 192–197. doi:10.1016/j.memsci.2008.07.013

frontiers | Frontiers in Environmental Science

TYPE Original Research
PUBLISHED 19 January 2023
DOI 10.3389/fenvs.2023.1093413

OPEN ACCESS

EDITED BY
Biyun Guo,
Zhejiang Ocean University, China

REVIEWED BY
Pengfei Hei,
Minzu University of China, China
Hongbin Yin,
Nanjing Institute of Geography and Limnology (CAS), China

*CORRESPONDENCE
Man Zhang,
zhangman86@tsinghua.edu.cn

SPECIALTY SECTION
This article was submitted to Freshwater Science,
a section of the journal
Frontiers in Environmental Science

RECEIVED 09 November 2022
ACCEPTED 09 January 2023
PUBLISHED 19 January 2023

CITATION
Li H, Zhou J and Zhang M (2023), Regime of fluvial phosphorus constituted by sediment.
Front. Environ. Sci. 11:1093413.
doi: 10.3389/fenvs.2023.1093413

Regime of fluvial phosphorus constituted by sediment

Huali Li, Jianjun Zhou and Man Zhang*

Department of Hydraulic Engineering, Tsinghua University, Beijing, China

Phosphorus (P) is a crucial macronutrient, and recently a venture agent of pollutant, in aquatic systems worldwide. Most of P circulates with sediment through rivers, and the relationship between P and sediment is the basis for understanding the biogeochemical processes in rivers. Although studies of fluvial P have been carried out at specific sites and for particular problems, the general regime by which sediment affects P recirculation still warrants attention. In this study, a series of water samples were collected from six different rivers in China whose sediment concentration and size distribution vary widely and their P properties were analyzed in the laboratory. From this analysis of field samples, a highly consistent comet shaped pattern of sediment effects on P is revealed, i.e., generally the range of the concentration of total P has a diverge-converge trend as the sediment concentration increases. It is further supported by examining the strictly composed samples from P adsorption experiments. Furthermore, case analyses were performed on the basis of the above relationships to illustrate the impact of sediment on P cycling in rivers. The results can infer the following: 1) There is a strong positive correlation between total P and sediment concentration, indicating that sediment is a crucial agent in the movement and fate of P. 2) The negative correlation between dissolved P and sediment concentration indicates a buffering effect of sediment, especially fine sediment, on dissolved P, interpreting the intricate phenomena of increased dissolved P concentration caused by sediment reduction. Hence, natural sediment has the prevailing advantage in moderating the water quality of rivers, which is directly relevant to mitigating the present pollution and eutrophication of waters. 3) River damming causes a P blockage tendency, altering the fluvial nourishment to contamination in the river.

KEYWORDS

phosphorus, sediment, regime, river environment, river ecology

1 Introduction

Phosphorus (P), one of the most critical macronutrient elements affecting aquatic environments and their ecology, mainly circulates with sediment *via* rivers (Smil, 2000). In the global P cycle, the atmospheric deposition amounts to only 3–4 Mt, while the amount transported to the ocean *via* erosion and runoff is as high as 25–30 Mt (Smil, 2000). Importantly, P has a strong affinity to sediment (Müller et al., 2006), and the P of the world's large rivers is mostly attached to sediment (i.e., 80%–90%) (Zhou et al., 2018). Therefore, the river sediment transport largely determines the destination and circulation path of P.

In recent decades, sediment has been intensively disturbed by human activities, such as river damming and inter-basin water diversion projects (Vörösmarty et al., 2003; Syvitski et al., 2005; Best, 2019; Grill et al., 2019), which inevitably affects P transport and transformation processes in rivers (Zhou et al., 2013; Maavara et al., 2015; Zhou et al., 2015; Li et al., 2022). For instance, the substantial reduction in total P (TP) trapped by dams is widely observed in rivers, reaching

77% in the Yangtze River (Zhou et al., 2013), 40% in the Madeira River (Almeida et al., 2015), and 60% in the Zambezi River (Kunz et al., 2011), mainly due to the reduced sediment loads. Additionally, the self-purification capacity of natural rivers is gradually changing, as manifested by the continuously increasing dissolved P (DP) level detected in large rivers (Chai et al., 2009; Pan et al., 2013; Zhou et al., 2018; Chen et al., 2020; Zeng et al., 2022; Zhang et al., 2022). Although the dramatic shifts in sediment and the ecological and environmental risks of basin-wide fluvial P changes are acknowledged, our understanding of how sediment impacts P cycling in rivers is still incomplete.

The relationship between P and sediment is the cornerstone for understanding the process of P cycling in rivers, and basic knowledge of this relationship has been reported, such as that between P and sediment load (Q_s) (Zhou et al., 2013; Huang et al., 2015), sediment concentration (S) (Uusitalo et al., 2000; Yu et al., 2010; Zhou et al., 2013; Almeida et al., 2015; Zeng et al., 2022; Zhang et al., 2022), and sediment grain size (Yao et al., 2015; Zhou et al., 2015). However, most of these studies were limited to a specific situation, such as an individual river. To our best knowledge, no study has yet integrated the general regime of fluvial P constituted by sediment with the wide disparity in the concentration and size distribution of sediment at the scale of different rivers. Moreover, previous studies mostly focus on the effect of S on P, while the effects of sediment grain size on P were rarely considered. Actually, the adsorption behaviors of natural sediment would be significantly affected by sediment grain size (Meng et al., 2014), and the grain size is crucially important for the transport of P in the flow (Zhou et al., 2015). Therefore, sediment grain size should also be considered when investigating the effects of sediment on P. Furthermore, most of the experimental studies on P adsorption/desorption focused on the maximum adsorption capacity of P by sediment (Zhou et al., 2005; Omari et al., 2019; Li et al., 2021), paying little attention to the buffering effects of river sediment against P pollution. Moreover, most experiments only explored a narrow range of values of sediment and P concentrations, while these values are generally one or two orders of magnitude higher than those in the natural rivers (Zhou et al., 2005; Wang et al., 2009; Omari et al., 2019). Hence, the findings of those studies cannot directly reflect the natural conditions, limiting their practical applicability. Accordingly, although notable field surveys and laboratory studies have been carried out recently for specific sites and problems, the general regime underpinning the effects of sediment on P cycling deserves further investigation.

In this study, a series of water samples from six rivers in China differing widely in their sediment concentration and size distribution were collected and their P properties were analyzed in the laboratory to derive the relationship between P and sediment. The regimes of fluvial P constituted by sediment spanning a low to high S and from a large to small grain size were explored. Then, laboratory experiments were also conducted for further verification of these relationships. Finally, case analyses were conducted to discuss changes in P cycling as caused by sediment reduction and its impact on the ecology and environment of rivers. This study differs from previous works (Zhou et al., 2013; Zhou et al., 2015) in that 1) here the range of sediment concentration was much wider as samples from six rivers were used instead of from only the Three Gorges Reservoir region, 2) phosphorus adsorption experiments were conducted in this study to further explain the effects of sediment grain size on P.

2 Materials and methods

2.1 Field measurements

The sampling locations are shown in Figure 1 and the sampling periods are listed in Table 1. About 2–5 L of water samples were collected at each site. Every sample was divided into two subsamples, one for sediment (A) and the other for P (B) analysis in laboratory. Sub-sample A was further divided into two parts, one for sediment concentration (measured according to China national standard GB11901-89) and the other for the grain size distributions (measured using the HORIBA LA-920 Laser Particle Size Analyzer). Sub-sample B was also subdivided into one unfiltered part and the other filtered through a 0.45-μm filter, all of the subsamples were digested with potassium persulfate to analyze P using the ammonium metamolybdate spectro-photometric method (Environment Protection Administration of China (EPA China), 1989).

We define TP concentration (C_{tp}, mg/L) and DP concentration (C_{dp}, mg/L) as the measured value in the unfiltered samples and the value after filtration through a 0.45-μm filter, respectively; and particulate P (PP) concentration (C_{pp}, mg/L) as the difference between C_{tp} and C_{dp} (i.e., $C_{pp} = C_{tp} - C_{dp}$) (Zhou et al., 2013). For the sediment properties, S (g/L) denotes the sediment concentration; D_{50} (μm) is the median particle size of sediment; C_a (m^2/L) is the surface area concentration of sediment ($C_a = 6 \times 10^{-2} S/\gamma_s \sum p_i/d_i$), where γ_s is the specific weight of the sediment (kg/m^3), and p_i (%) and d_i (mm) are the percentage and grain diameter of the fractions, respectively (Zhou et al., 2015); $d_{pp} = C_{pp}/S$ (mg/g) is the P content per Gram of sediment, called the PP mass density (Zhou et al., 2013); and $d_a = C_{pp}/C_a$ (mg/m^2) is the density of PP on per unit area of sediment grain surface, called the PP areal density (Zhou et al., 2015).

In addition to field surveys, we also collected long-term data for flow and sediment at key hydrological stations, the Yichang and Datong stations in the Yangtze River as well as the Huayuankou and Lijin stations in the Yellow River (Figure 1). This included daily average data of the flow discharge and sediment concentration (1950–2020) and monthly average data for the sediment grain size distribution (1960–2019), which was provided by the Ministry of Water Resources of China (MWR).

2.2 Laboratory experiments

In the laboratory, P adsorption experiments were tested to verify the results from the rivers. Three sediment samples collected from the Yellow River were used: fine sediment (D_{50} = 4.61 μm), median sediment (D_{50} = 20.89 μm), and coarse sediment (D_{50} = 51.56 μm) (grain size distribution of these three sediment samples see Supplementary Figure S1). These sediment samples were naturally air-dried and their native P content (d_{pp0}) was 0.59, 0.49 and 0.27 mg/g, respectively. A batch of strictly composed samples was prepared by adding a different amount of sediment (0.3, 0.6, 1.5, 3, 6, 15, 30, 60, 150 or 300 mg) to 30 mL of a P solution with initial P concentrations (denoted as C_{dp0}) of 0.001, 0.01, 0.1, 0.5, 1, and 10 mg/L. These samples were then processed in an incubator shaker and shaken continuously for 24 h to achieve an equilibrium adsorption (Li et al., 2021). Next, the C_{dp} under equilibrium conditions was measured after passing each sample through a

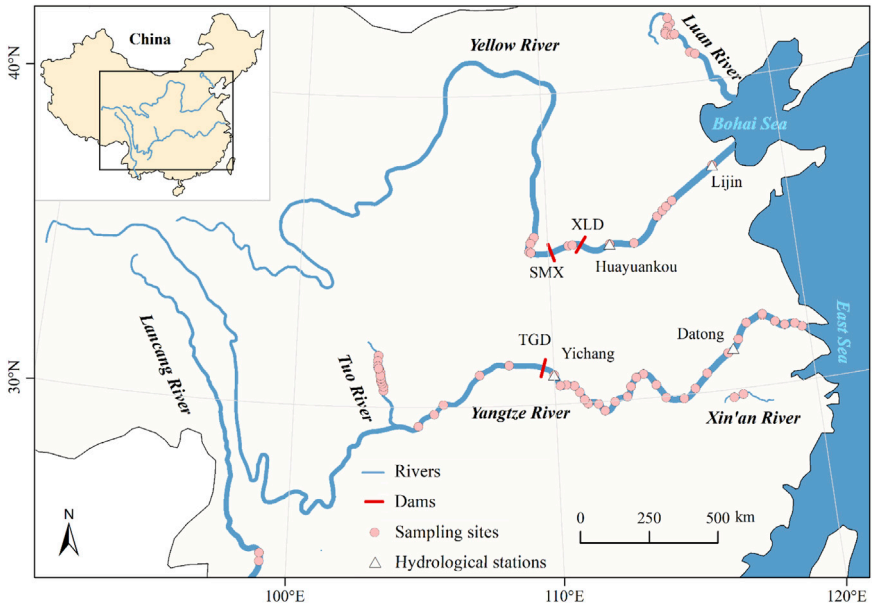

FIGURE 1
The sampling sites along six different rivers in China and the relevant locations used in this study. TGD, SMX, and XLD respectively denote the dams for the Three Gorges, Sanmenxia, and Xiaolangdi reservoirs.

TABLE 1 Basic characteristics of the six different rivers in China selected for this study and their sampling periods.

River	Long-term average runoff (km^3/a)	Long-term average sediment load (Mt/a)	Long-term average S (g/L)	Statistical period (year)	Sampling period
Yangtze River	905.1	433	0.486	1951–2000[a]	2004–2012[b], 2015–2016[b], November 2019, July 2021
Yellow River	33.12	839.2	25.2	1950–2000[a]	May 2021–June 2022
Luan River	4.453	20.1	4.44	1929–1984[c]	August 2019, October 2019, April 2020, September 2020
Tuo River	12.53	11.2	0.89	1957–1992[d]	December 2020, July 2021
Lancang River	57	91.4	1.55	1965–2003[e]	April 2021, August 2021
Xin'an River	6.92	1.51	0.22	1956–2000[f]	June 2020, October 2020

[a]From the Ministry of Water Resources of the People's Republic of China.
[b]From Jiang et al. (1986).
[c]From Li et al. (2002).
[d]From Liu et al. (2013).
[e]From Cheng & Zhang (2005).
[f]Sampling campaigns were undertaken monthly by the Upper Changjiang River Bureau of Hydrological and Water Resources Survey.

0.45-μm filter (see section 2.1) and the C_{tp} was calculated according to the conservation of matter ($C_{tp} = C_{dp0} + Sd_{pp0}$).

3 Results

3.1 Relations between the sediment and P in rivers

As seen in Table 1, the selected six rivers in China differs substantially in terms of their sediment properties, especially S. The long-term average S of the Yellow River (25.2 g/L) is about two orders of magnitude higher than that of the Xin'an River (0.22 g/L), and the long-term average S of the Luan River (4.44 g/L) is about one order of magnitude higher than that of the Yangtze River (0.486 g/L). As expected, the samples collected from these six rivers in this study has a wide disparity in their S (0.001–41.8 g/L) and D_{50} (1.49–195.62 μm) (Figure 2A). Similar to sediment, a wide disparity in the P properties is evident, especially for C_{tp} (0.02–21.66 mg/L) (Figure 2B). It is worth noting that the peaks of S (41.8 g/L) and C_{tp} (21.66 mg/L) both appear in the Yellow River, being comparable to that of previous study (47.94 g/L and 30.98 mg/L) (Yu et al., 2010).

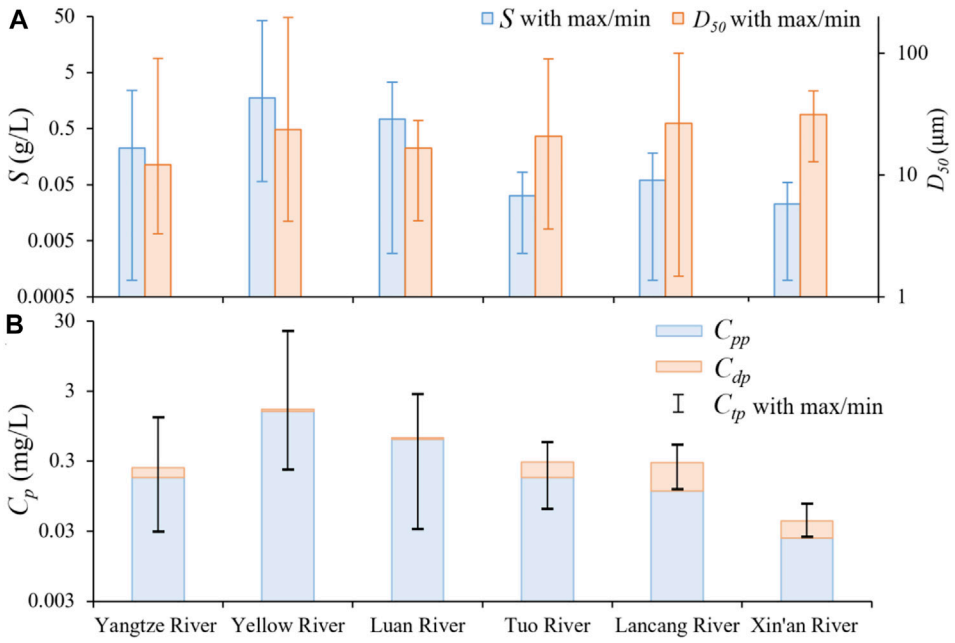

FIGURE 2
Sediment and phosphorus conditions of six different rivers in China during the sampling period. The height of the column denotes average values of sediment concentration (S) **(A)**, median grain size (D_{50}) **(A)**, Total P concentration (C_{tp}) **(B)**, dissolved P concentration (C_{dp}) **(B)** and particulate P concentration (C_{pp}) **(B)**. The error bars denote the maximum and minimum values of S **(A)**, D_{50} **(A)** and C_{tp} **(B)**.

Like most rivers in the world (Zhou et al., 2018), TP is dominated by PP (the average proportion of C_{dp} to C_{tp} of all samples is 68%).

Figure 3 shows the relationships between P and sediment in the six rivers that have a wide disparity in their sediment concentration and size distribution. There is a highly consistent positive relationship between C_{tp} and S in these six rivers (Figure 3A), indicating that sediment is a crucial agent in the movement and fate of P. This positive pattern is consistent with other rivers like the Pearl River (Duan and Zhang, 1999), the Mississippi River (Welch et al., 2014) and Aurajoki River (Uusitalo et al., 2000), and even lakes such as Poyang Lake (Pu et al., 2020). Notably, the relationship between C_{tp} and S shows a clear comet shaped pattern from divergence to convergence with increasing S. For instance, the regression relationship between C_{tp} and S in the area with low S (like $S \leq 0.1$ g/L, $R^2 = 0.04$) is much worse than that in the area with high S ($S > 0.1$ g/L, $R^2 = 0.92$) (Supplementary Figure S3). It indicates that P is mainly attached to the sediment and C_{tp} is controlled by sediment in high sediment laden rivers like the Yellow River and Luan River.

By contrast, the proportion of DP (C_{dp}/C_{tp}) is negatively related to S (Figure 3C), indicating a buffering effect of sediment on DP. The comet shaped pattern is more evident from the relationship between C_{dp}/C_{tp} and S. Specifically, in those areas with high S, sediment has a strong buffering effect, thus C_{dp}/C_{tp} is close to zero (i.e., the DP level is mainly controlled by S). However, with the decreases of S, the buffering effect of sediment gradually diminishes, and C_{dp}/C_{tp} varies widely (i.e., 3.7%–93.3%), being affected mainly by other factors like the riparian P input. Values of C_{dp}/C_{tp} in areas with low S in this study (e.g., Yangtze River and Lancang River) are similar to those reported for some low-sediment water bodies, like lakes (C_{dp}/C_{tp} = 10%–97%) (Pu et al., 2020) and estuaries (C_{dp}/C_{tp} = 50%–90%) (Fang and Wang, 2020).

Sediment PP density d_{pp} is also inversely proportional to S (Figure 3E), which indicates that sediment has a strong adsorption potential in areas with high S or small grain size (Zhou et al., 2018), when considering the competitive mechanism between sediment particles (Müller et al., 2006). For example, the markedly lower d_{pp} due to high S of the Yellow River than the other rivers implies that the sediment still has a strong adsorption potential, a view supported by experimental findings that most of the Yellow River's suspended sediment acts as a sink for additional phosphate input (Pan et al., 2013).

The highly consistent relationships between P and S from six rivers with varying S convincingly demonstrate the dependence of fluvial P on sediment (Figures 3A, C, E). The specific surface area of sediment affecting P adsorption varies with its particle size (Goldberg and Sposito, 1985; Boström et al., 1988). Therefore, we propose that C_a might better reflect the effect of sediment on P after a comprehensive consideration of S and grain size. The correlation results are shown in Figures 3B, D, F, where the effect of C_a on fluvial P displays a similar pattern to that from S, but PP has a slightly better relationship with C_a (Figure 3F) than its relationship with S (Figure 3E). However, there is no significant improvement in the relationship between TP (or DP) and sediment. One possible reason is that flocculation may affect the effective surface area of fine sediment in natural waters, which may raise inaccuracy when calculating C_a in this study. This effect is discussed in detail in the next section with experimental results.

3.2 P adsorption experiments on natural sediment

For a better understanding of the P partition regime (denoted mainly as the ratio C_{dp}/C_{tp}) constituted by sediment of natural water

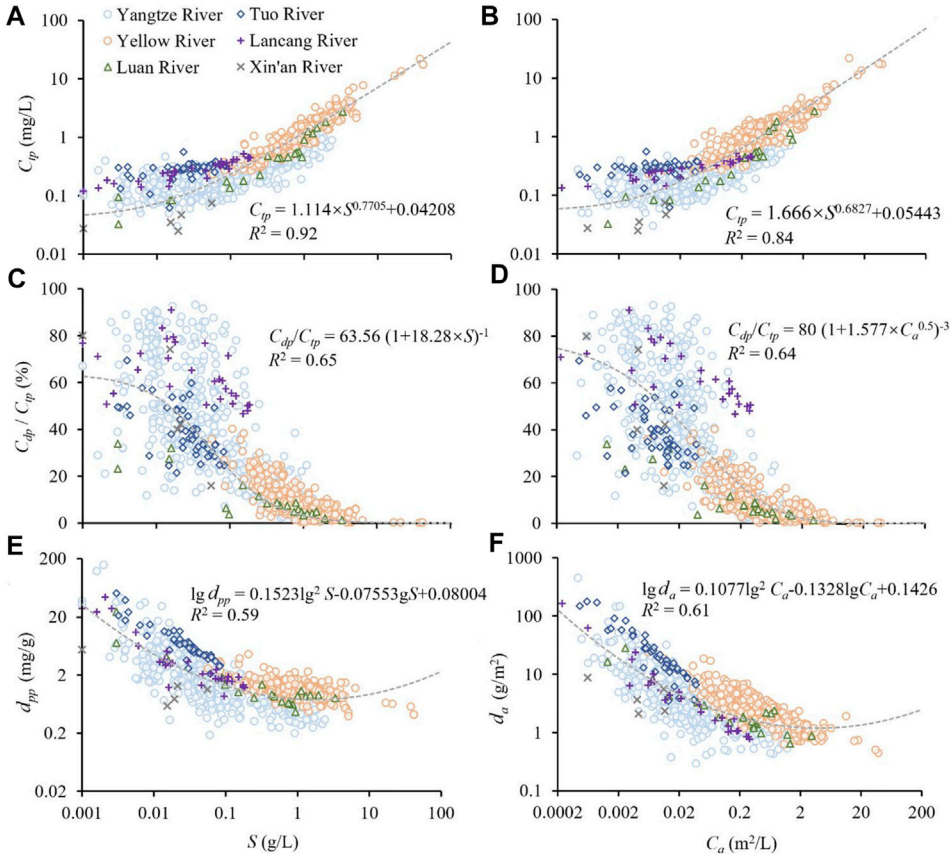

FIGURE 3
Relationships between fluvial P and natural sediment based on the field data collected from six different rivers in China. **(A)** Total P concentration (C_{tp}), **(C)** proportion of dissolved P (C_{dp}/C_{tp}), and **(E)** mass density of particulate P (d_{pp}) *versus* sediment concentration (S); and **(B)** C_{tp}, **(D)** C_{dp}/C_{tp}, and **(F)** areal density of particulate P (d_a) *versus* the surface area concentration of sediment (C_a). The grey dotted lines represent the fitted regression of P *versus* sediment.

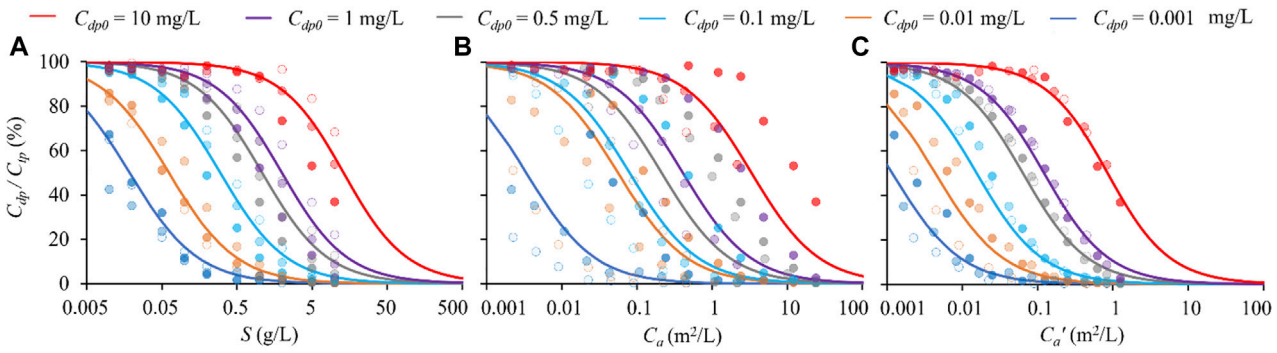

FIGURE 4
Relationship between the proportion of dissolved P at adsorption equilibrium (C_{dp}/C_{tp}) and total sediment concentration (S) **(A)**, total area concentration of sediment (C_a) **(B)** and the total effective surface area concentration of sediment (C_a') **(C)** for graded sediment under different initial dissolved P concentration (C_{dp0}), based on the data from laboratory experiments (colored symbols) and equilibrium adsorption model (solid line). The color symbols in full, half and empty refer to the fine (D_{50} = 4.61 μm), median (D_{50} = 20.89 μm), and coarse (D_{50} = 51.56 μm) sediment used in the experiment.

samples, strictly composed samples is analyzed in this section. Figure 4 shows the relationship between C_{dp}/C_{tp} and sediment of the strictly composed samples from the P adsorption experiments. We can see that C_{dp}/C_{tp} is overall inversely proportional to S and C_a, and it also exhibits a consistent comet shaped pattern (Figures 4A, B), corroborating the field-based results for the rivers (Figure 3C). This

comet-like pattern is also supported by the equilibrium adsorption model. These general results confirm that the comet shaped buffer phenomenon in field measurements (Figures 3C, D) is a reasonable and natural law. As shown in Figures 4A, B, the relationship between C_{dp}/C_{tp} and C_a is more diffuse than the relationship between C_{dp}/C_{tp} and S. As mentioned in Section 3.1, flocculation of sediment, especially fine sediment, may raise inaccuracy when calculating C_a. Here, the effective surface area (C_a') is proposed by introducing a reduction factor that represents the effect of fine sediment flocculation (Supplementary Equation S2.1). As shown in Figure 4C, by introducing C_a', the experimental data from fine to coarse sediment are closely unified into the same equilibrium adsorption curve; Figure 4; Supplementary Table SA1 also indicate that C_a' performs better in optimizing the correlation of P partition between PP and DP for graded sediment. This further suggests that the surface area is the essential determinant of the effect of sediment on P. Therefore, in order to indicate the P content of sediment in rivers, the true state of sediment in rivers needs to be considered. In this research, we suggest that C_a should be determined by sedimentation particle size (flocculated sediment as a whole).

4 Discussion

Our results present a highly consistent comet shaped pattern of sediment effects on P based on the analysis of field samples from six rivers in China, and it is further supported by examinations of the strictly composed samples. The comet shaped pattern indicates that P is mainly attached to the sediment and C_{tp} and C_{dp}/C_{tp} are controlled by sediment in the area with high S. But as S decreases, C_{tp} and C_{dp}/C_{tp} perhaps are affected relatively more by other factors, such as the P input level and the sediment grain size. Considering that low sediment content and high pollution load are the current and future status of most rivers, the divergence phenomenon in areas with low S deserves more attention. In this section, we further discuss the mechanism behind these obtained relationships and possible ecological and environmental effects. After that, we apply the obtained relationships between P and sediment to estimate long-term variability of P in rivers caused by sediment reduction, by using the Yangtze River and Yellow River as examples.

4.1 Mechanism and impact of the relationships between P and sediment

Our results uncover negative relationship between C_{dp}/C_{tp} and S, indicating a strong buffering effect of sediment on DP. However, the divergence phenomenon in the comet tail region implies that this buffering effect is not only controlled by S. Taking the Yangtze River as an example (Figure 5), the statistical results of the measured data show that C_{dp}/C_{tp} gradually increase as the group-average D_{50} increase, indicating that C_a decrease. Thus, assuming a relatively constant P input level during the sampling period, C_{dp}/C_{tp} shifts from being S-controlled to sediment grain size-controlled with declining S. In particular, in areas with low S, the advantage of fine sediment over coarse sediment is most prominent in terms of the buffering effect on DP.

The outstanding buffering effect of fine sediment is due to its stronger ability to adsorb P compared to coarse sediment. As evinced by Figure 6, sediment can restrain the increase in DP caused by increasing C_{dp0} through adsorption. The extent that the slope deviates from one can be used to quantify the restraining effect of sediment on C_{dp} levels in solution. Sediment grain size is a key factor responsible for the restraining effect. Specifically, despite the same S, the amount of phosphate remaining in solution can vary greatly among these three sediment types. Especially, for fine sediment, at the highest S (10 g/L), most of the added P is removed by adsorption ($k_3 = 0.15$), whereas the effect of coarse sediment under the same S is not discernible ($k_3 = 0.81$). This is because C_a of the latter (0.75 m^2/L) is less than 10% that of the former (12.4 m^2/L).

It is important to note that, for all of the three sediment size types, the relationship between C_{dp} and C_{dp0} becomes linear with a slope of 1 as S is reduced below 0.1 g/L (Figure 6). This can further interpret the above-mentioned divergence phenomenon in the relationship between C_{tp} and S ($S < 0.1$ g/L, $R^2 = 0.04$). These relationships all indicate that an S value of 0.1 g/L may be a critical threshold for the buffering effect of natural sediment, below which most phosphate cannot be removed by sediment. Actually, for some natural sediment collected from river bed, this threshold value of S is even higher (0.2–1.0 g/L) (Pan et al., 2013). However, in recent years, the natural S in many rivers may fail to reach this threshold. For instance, the average S of the Tuo River (0.03 g/L), Lancang River (0.06 g/L) and Xin'an River (0.02 g/L) during the sampling period in this study are all far below this threshold. This indicates that the buffering effect of sediment on DP in these rivers is gradually disappearing.

DP (especially dissolved inorganic phosphate, DIP) is easily used by primary producers (Maruo et al., 2015) and is often a pollutant for a local or stationary system. In recent years, the significant DP-elevating phenomena has been widely reported in the context of sediment reduction (Chai et al., 2009; Dai et al., 2011; Pan et al., 2013; Chen et al., 2020). Our results suggest that adsorption of dissolved phosphate onto sediment, particularly fine sediment, is a key process to keep C_{dp} at a relatively low level and to improve the river water quality.

4.2 Estimation of changes in P cycling in rivers caused by sediment reduction

To illustrate the impact of sediment reduction on P cycling in a river, the Yangtze River and the Yellow River are taken as examples for further discussion. The relationship between P and S and that between the P and C_a in the Yellow River are proposed in this study (Supplementary Figure S3). The relationship between P and S (Zhou et al., 2013) and that between the P and C_a (Zhou et al., 2015) in the Yangtze River reported in previous studies are used directly. First, according to the relationship between P and S and the sediment data, long-term variation in the cumulative TP flux (L_{tp}) in the Yangtze River (Figure 7C) and Yellow River (Figure 7D) is estimated. Then, combined with sediment grading data, long-term variation in the C_{tp} and C_{dp} in the Yangtze River (Figure 7E) and Yellow River (Figure 7F) are roughly modeled using the obtained relationships between P and C_a.

Estimates show that the growth rate of cumulative L_{tp} (Figure 7C) and C_{tp} (Figure 7E) related to sediment in the Yangtze River has declined slightly since 1990 in the context of sediment reduction (Figure 7A). In particular, an obvious inflection point appears in 2003 just after the Three Gorges Reservoir (TGR) became operational.

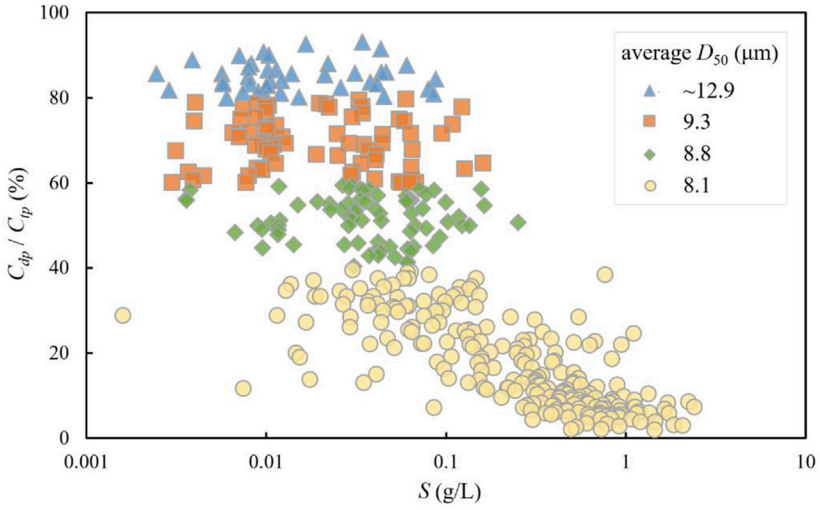

FIGURE 5
The proportion of dissolved P (C_{dp}/C_{tp}) *versus* sediment concentration (S) based on the measured data collected from the Three Gorges Reservoir area of the Yangtze River (2004–2012 and 2015–2016). Different symbols represent artificial groups with C_{dp}/C_{tp} of 80%–100%, 60%–80%, 40%–60% and 0%–40%, respectively.

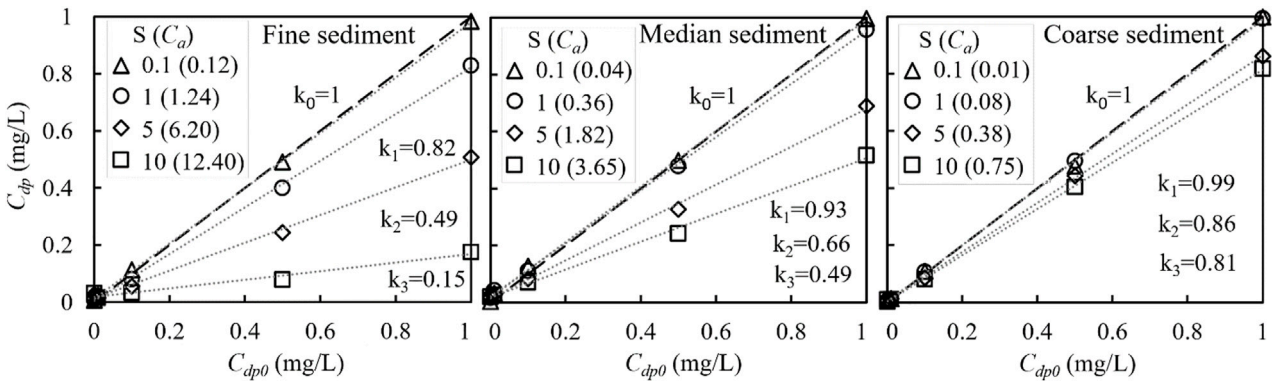

FIGURE 6
Effect of P pollution condition (indicated by the initial dissolved P concentration, C_{dp0}) on dissolved P concentration (C_{dp}) at adsorption equilibrium. The k_0~k_3 denotes the slope between C_{dp0} and C_{dp} when S = 0 (clear water, meaning no adsorption occurs), 1, 5, and 10 g/L, respectively. The units of sediment concentration (S) and surface area concentration of sediment (C_a) are g/L and m^2/L, respectively. Panels correspond to fine (D_{50} = 4.61 μm), median (D_{50} = 20.89 μm), and coarse (D_{50} = 51.56 μm) sediment.

The average growth rate of cumulative L_{tp} through Yichang falls to 0.04 MT/a in 2003–2020, only accounting for 20% of that in 1951–1990 (0.2 MT/a) and the C_{tp} during wet season at Yichang falls to 0.14 mg/L in 2003–2019, only accounting for 22% of that in 1951–1990 (0.63 mg/L). Like the Yangtze River, the estimated growth rate of cumulative L_{tp} (Figure 7D) and C_{tp} (Figure 7F) related to sediment in the Yellow River has declined slightly since 1960 (Figure 7B), relating to the implementation of dams and other hydraulic projects along the river. In particular, the average growth rate of cumulative L_{tp} through Huayuankou falls to 0.08 MT/a in 2000–2020, being less than 7% of that in 1950–1959 (1.15 MT/a) (Figure 7D). The estimated decreasing trend of L_{tp} and C_{tp} in the Yangtze River and Yellow River in this study is consistent with other rivers in the world, such as the Madeira River (decline by 40%) (Almeida et al., 2015) and the Zambezi River (60% trapped) (Kunz et al., 2011). The above estimates for long-term TP are rough but have a physical basis, i.e., sediment has a strong affinity to P due to its great specific surface areas and active surface sites (Davis and Kent 1990; Huang et al., 2016). In this study, this physical basis is further illustrated by both the strong positive correlation between TP and S in the field measurements and the strong P adsorption for natural sediment in the laboratory experiments. Long-term measurements show that since the TGR begins operating in 2003, 93% of the sediment normally delivered to the middle and lower Yangtze River through Yichang has been trapped; it decreased to only 35 Mt/a (2003–2020) compared with 517 Mt/a over the long term

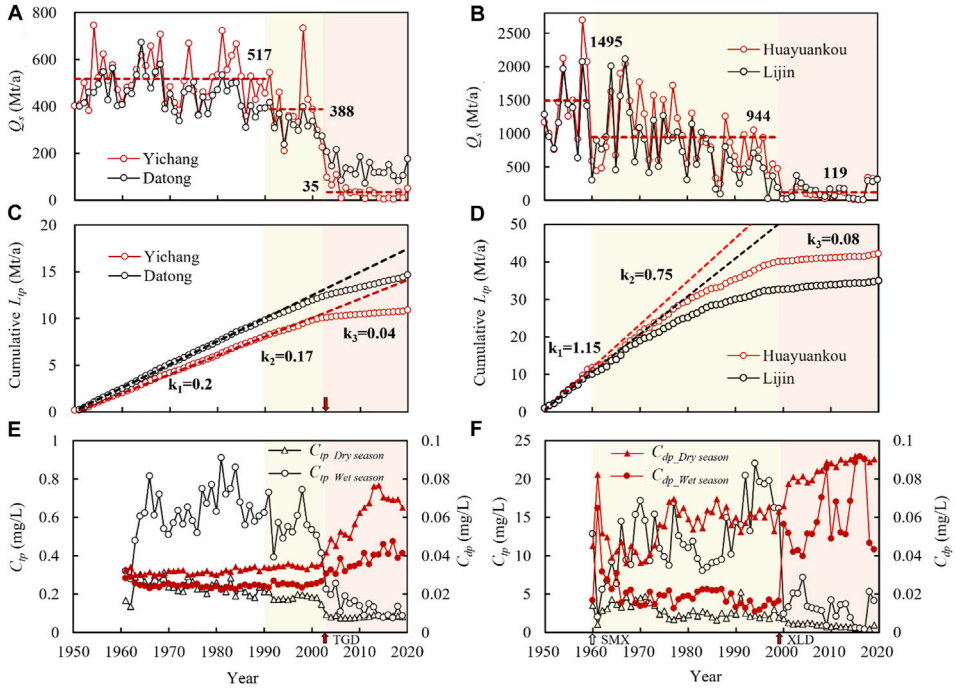

FIGURE 7
Long-term variation in the annual sediment load (Q_s) and accumulative total P flux (L_{tp}) at Yichang and Datong in the Yangtze River **(A** and **C)**, and at Huayuankou and Lijin in the Yellow River **(B** and **D)** (1950–2020). Long-term variation of the simulated total P concentration (C_{tp}) and dissolved P concentration (C_{dp}) at Yichang in the Yangtze River **(E)** and at Huayuankou in the Yellow River **(F)** during the dry season (October–May in the Yangtze River and November–June in the Yellow River) and the wet season (June–September in the Yangtze River and July–October in the Yellow River) (1960–2019). The dashed lines indicate the average value of the corresponding process at Yichang **(A)** and Huayuankou **(B)**, and the slope of the cumulative L_{tp} at Yichang and Datong (1951–1990) **(C)**, and at Huayuankou and Lijin (1950–1959) **(D)**. k_1~k_3 denotes the average growth rate of L_{tp} in 1951–1990, 1991–2002, and 2003–2020 at Yichang **(C)**, and 1950–1959, 1960–1999, and 2000–2020 at Huayuankou **(D)**. Arrows indicate when the Three Gorges Reservoir (TGR) in the Yangtze and Sanmenxia (SMX) and Xiaoliangdi (XLD) reservoirs in the Yellow River became operational.

(1951–1990) (Figure 7A). Similarly, a stepwise decline in sediment is observed as the implementation of dams and other hydraulic projects along the Yellow River and the average Q_s through Huayuankou in 2000–2020 (119 MT/a) constituted just 8% of that in 1950–1959 (1495 MT/a) prior to the implementation of Sanmenxia Dam (1960) and Xiaoliangdi Dam (1999) (Figure 7B). In fact, the percentage of sediment interception in these rivers far exceeds that of other major rivers globally (Vörösmarty et al., 2003). Therefore, the dramatic decrease in TP estimated in this study is reasonable, which is also consistent with the global trend (Maavara et al., 2015).

Like most rivers in the world, P in the Yangtze River and Yellow River occurs mainly in particulate form (Zhou et al., 2018). In fact, PP is likely strongly adsorbed to iron and aluminum oxide surfaces and is not readily bioavailable (Berner and Rao, 1994). However, PP can be released from sediment and may become mobilized and bioavailable after undergoing transformation under certain chemical conditions (e.g., low pH and low oxygen concentration) (Silva and Sampaio, 1998). Numerous studies have shown that PP is the key source of potentially bioavailable P (BAP) and the ratio BAP/PP is 19%–31% in the Yellow River (Yao et al., 2015) and 45.6% in the Yangtze River (Wei et al., 2010). Thus, from a long-term ecological perspective, maintaining the long-term stability of both the sediment and TP load is critical for the primary productivity of estuary and coast, where P is often the limiting nutrient for bioactivity (Wang et al., 2021). To our knowledge, the ratio of nitrogen (N) to P (N/P) has far surpassed the normal value (15–16) in either the Yangtze River (192.5–317.5) (Shen & Liu, 2009) or Yellow river (700–1480), being much higher than that of other major rivers worldwide (Pan et al., 2013; Wang et al., 2021). This very high N/P ratio means that both the two rivers are extreme P-limited ecosystems and their productivity is severely limited by P (Elser et al., 2007; Shen and Liu, 2009). On the one hand, such significant reductions in L_{tp} and C_{tp} will not only further reduce the bioavailability of P but also augment the existing high N/P, altering the nutrient structure of downstream rivers. On the other hand, dam trapping causes P accumulation in the reservoirs that changes fluvial nourishment to contamination within the river.

Conversely, evident increases in C_{dp} against a background of decreasing C_{tp} are found in both the Yangtze River (Figure 7E) and the Yellow River (Figure 7F). Especially in the dry season, C_{dp} increases to 0.08 mg/L at Yichang and 0.09 mg/L at Huayuankou, respectively, in recent years. The inferred trend of rising C_{dp} is supported further by additional observations from the Yangtze River and the Yellow River; for example, (i) recently, Zhang et al. (2022) reported that the C_{dp} rose from 0.05 mg/L (2003–2012) to 0.1 mg/L (2013–2017) under the background of decreasing TP at Yichang in the Yangtze River; (ii) earlier, Pan et al. (2013) found the DIP (important components of the DP) increasing from 0.29 μmol/L (1980–1992) to 0.43 μmol/L (2007) due to *S* decreasing in the Yellow River. The abnormally increased DP level indicates that the decreasing sediment may have nearly lost its ability to buffer P pollutant (Figure 6). In fact, our estimates of how much P cycling could be affected by sediment reduction are likely to be conservative

and poorly constrained because TP and DP are not only affected by sediment but also directly affected by pollutant emissions (Zeng et al., 2022). In recent decades, anthropogenic P emissions from both point and non-point sources, particularly fertilizers applied to support agriculture, have greatly enhanced the P load to watersheds (Jarvie et al., 2006). For instance, long-term (1980–2015) net anthropogenic phosphorus input to the Yangtze River Basin has progressively increased (by ~1.4-fold) (Hu et al., 2020). Such high phosphate input would further promote a rising DP according to our laboratory experiments results (Figure 6). Therefore, maintaining a certain degree of turbidity in rivers plays an important role in the health of water bodies. Major strategies of the Yangtze River and Yellow River require that ecological protection of rivers be put in the first place, and it is recommended for the reservoirs to properly increase the amount of fine sediment released downstream to sustain the health of the downstream ecology.

5 Conclusion

In this study, the regime of fluvial P constituted by sediment was systematically investigated by collecting a series of samples from six rivers of China having a disparate sediment concentration and size distribution, combined with laboratory experiments. The main conclusions are as follows:

1) A highly consistent comet shaped pattern of sediment effects on P is found based on the analysis of field samples. It is further supported by examining the strictly composed samples from P adsorption experiments. Specifically, in areas with high S, there is strong dependence of fluvial P on sediment, and C_{tp} and C_{dp}/C_{tp} are mainly controlled by S. However, as S declines, the regime of fluvial P changes from S-controlled to the one affected more by other factors such as the P input level and sediment grain size.
2) A strong positive correlation between C_{tp} and S is obtained, thus indicating that sediment is a crucial agent in the movement and fate of P. Moreover, C_{dp} is negatively related to S, indicating a buffering effect of sediment on dissolved P and interpreting the intricate phenomena of increased C_{dp} caused by sediment reduction.
3) On the basis of the above relationships obtained, we roughly estimate changes in P cycling in rivers caused by sediment reduction and present a P blockage tendency in both the Yangtze River and Yellow River. Dam trapping causes P accumulation in the reservoirs would not only alter the nutrient structure of downstream river and estuary but also increases contamination within the river. Furthermore, the estimated long-term C_{dp} shows a trend of increase, which suggests the ability of sediment to buffer DP may have been eliminated by dams.

Anthropogenic activities are altering the path and nature of sediment in rivers in various ways, arguably adversely affecting the transport and transformation of fluvial P. The regime of fluvial P constituted by sediment obtained in this study servers as a knowledge base for further investigation of this fundamental biogeochemical cycle.

Data availability statement

The original contributions presented in the study are included in the article/Supplementary Material, further inquiries can be directed to the corresponding author.

Author contributions

HL: Field sampling, experimental tests, analysis and draft manuscript preparation. JZ: Conceptual idea, project administration, funding acquisition, reviewing and editing, supervision. MZ: Field sampling, project administration, data curation, reviewing and editing. All authors contributed to the article and approved the submitted version.

Funding

This work has been financially supported by the National key research and development program of China, (2022YFC3202701) (co-authors: JZ and MZ).

Acknowledgments

The constructive suggestions of the editors and reviewers are gratefully acknowledged.

Conflict of interest

The authors declare that the research was conducted in the absence of any commercial or financial relationships that could be construed as a potential conflict of interest.

Publisher's note

Supplementary material

The Supplementary Material for this article can be found online at: https://www.frontiersin.org/articles/10.3389/fenvs.2023.1093413/full#supplementary-material

References

Almeida, R. M., Tranvik, L., Huszar, L. M. V., Sobek, S., Mendonça, R., Barros, N., et al. (2015). Phosphorus transport by the largest Amazon tributary (Madeira River, Brazil) and its sensitivity to precipitation and damming. *Inland Waters Print.* 5 (3), 275–282. doi:10.5268/IW-5.3.815

Berner, R. A., and Rao, J.-L. (1994). Phosphorus in sediments of the Amazon River and estuary: Implications for the global flux of phosphorus to the sea. *Geochimica Cosmochimica Acta* 58 (10), 2333–2339. doi:10.1016/0016-7037(94)90014-0

Best, J. (2019). Anthropogenic stresses on the world's big rivers. *Nat. Geosci.* 12, 7–21. doi:10.1038/s41561-018-0262-x

Boström, B., Andersen, J. M., Fleischer, S., and Jansson, M. (1988). Exchange of phosphorus across the sediment-water interface. *Hydrobiologia* 170 (1), 229–244. doi:10.1007/BF00024907

Chai, C., Yu, Z., Shen, Z., Song, X., Cao, X., and Yao, Y. (2009). Nutrient characteristics in the Yangtze River estuary and the adjacent east China sea before and after impoundment of the three Gorges dam. *Sci. Total Environ.* 407 (16), 4687–4695. doi:10.1016/j.scitotenv.2009.05.011

Chen, Q., Shi, W., Huisman, J., Maberly, S. C., Zhang, J., Yu, J., et al. (2020). Hydropower reservoirs on the upper Mekong River modify nutrient bioavailability downstream. *Natl. Sci. Rev.* 7 (9), 1449–1457. doi:10.1093/nsr/nwaa026

Cheng, X., and Zhang, C. (2005). Analysis of hydrological characteristics of Xin'an River Basin in anhui province. *Water Conservancy Sci. Technol. Anhui Prov.* 2 , 11–13. [in Chinese].

Dai, Z., Du, J., Zhang, X., Su, N., and Li, J. (2011). Variation of riverine material loads and environmental consequences on the Changjiang (Yangtze) estuary in recent decades (1955–2008). *Environ. Sci. Technol.* 45 (1), 223–227. doi:10.1021/es103026a

Davis, J. A., and Kent, D. B. (1990). Surface complexation modeling in aqueous geochemistry. *Rev. Mineral. Geochem* 23, 177–260.

Duan, S. W., and Zhang, S. (1999). The variations of nitrogen and phosphorus concentrations in the monitoring stations of the three major rivers in China [in Chinese]. *Sci. Geogr. Sin.* 19 (5), 411–416. doi:10.13249/j.cnki.sgs.1999.05.411

Elser, J. J., Bracken, M. E., Cleland, E. E., Gruner, D. S., Harpole, W. S., Hillebrand, H., et al. (2007). Global analysis of nitrogen and phosphorus limitation of primary producers in freshwater, marine and terrestrial ecosystems. *Ecol. Lett.* 10 (12), 1135–1142. doi:10.1111/j.1461-0248.2007.01113.x

Fang, T.-H., and Wang, C. W. (2020). Dissolved and particulate phosphorus species partitioning and distribution in the danshuei river estuary, northern taiwan. *Mar. Pollut. Bull.* 151, 110839. doi:10.1016/j.marpolbul.2019.110839

Goldberg, S., and Sposito, G. (1985). On the mechanism of specific phosphate adsorption by hydroxylated mineral surfaces: A review. *Commun. Soil Sci. Plant Analysis* 16 (8), 801–821. doi:10.1080/00103628509367646

Grill, G., Lehner, B., Thieme, M., Geenen, B., Tickner, D., Antonelli, F., et al. (2019). Mapping the world's free-flowing rivers. *Nature* 569, 215–221. doi:10.1038/s41586-019-1111-9

Hu, M., Liu, Y., Zhang, Y., Shen, H., Yao, M., Dahlgren, R. A., et al. (2020). Long-term (1980–2015) changes in net anthropogenic phosphorus inputs and riverine phosphorus export in the Yangtze River basin. *Water Res.* 177, 115779. doi:10.1016/j.watres.2020.115779

Huang, L., Fang, H., Fazeli, M., Chen, Y., He, G., and Chen, D. (2015). Mobility of phosphorus induced by sediment resuspension in the Three Gorges Reservoir by flume experiment. *Chemosphere* 134, 374–379. doi:10.1016/j.chemosphere.2015.05.009

Huang, L., Fang, H., He, G., and Chen, M. (2016). Phosphorus adsorption on natural sediments with different pH incorporating surface morphology characterization. *Environ. Sci. Pollut. Res. Int.* 23 (18), 18883–18891. doi:10.1007/s11356-016-7093-3

Jarvie, H. P., Neal, C., and Withers, P. J. A. (2006). Sewage-effluent phosphorus: A greater risk to river eutrophication than agricultural phosphorus? *Sci. Total Environ.* 360 (1), 246–253. doi:10.1016/j.scitotenv.2005.08.038

Jiang, T., Fang, X., Xu, H., and Guo, W. (1986). Runoff and sediment transport analysis at the estuary of the Luan River. *Adv. Mar. Sci.* 4, 100–113.

Kunz, M. J., Wüest, A., Wehrli, B., Landert, J., and Senn, D. B. (2011). Impact of a large tropical reservoir on riverine transport of sediment, carbon, and nutrients to downstream wetlands. *Water Resour. Res.* 47 (12), W12531. doi:10.1029/2011WR010996

Li, C., Wang, Z., Liu, H., Zuo, L., Lu, Y., Wu, P., et al. (2022). Impact of a water-sediment regulation scheme on nutrient variations at the Lijin station of the Yellow River. *Front. Environ. Sci.* 10, 900508. doi:10.3389/fenvs.2022.900508

Li, C., Liu, X., Cao, S., He, W., and Zhang, Z. (2002). Development of water powerre source in Sichuan and soil-water conservation in upper reaches of Yangtze River. *Resour. Enuironment Yangtza Basin* 11 (2), 117–122.

Li, X., Huang, L., Fang, H., Chen, M., Cui, Z., Sun, Z., et al. (2021). Phosphorus adsorption by sediment considering mineral composition and environmental factors. *Environ. Sci. Pollut. Res.* 28, 17495–17505. doi:10.1007/s11356-020-12206-9

Liu, C., He, Y., Des Walling, E., and Wang, J. (2013). Changes in the sediment load of the Lancang-Mekong River over the period 1965–2003. *Sci. China Technol. Sci.* 56 (4), 843–852. doi:10.1007/s11431-013-5162-0

Maavara, T., Parsons, C. T., Ridenour, C., Stojanovic, S., Dürr, H. H., Powley, H. R., et al. (2015). Global phosphorus retention by River Damming. *Proc. Natl. Acad. Sci. U. S. A.* 112, 15603–15608. doi:10.1073/pnas.1511797112

Maruo, M., Ishimaru, M., Azumi, Y., Kawasumi, Y., Nagafuchi, O., and Obata, H. (2015). Comparison of soluble reactive phosphorus and orthophosphate concentrations in river waters. *Limnology* 17 (1), 7–12. doi:10.1007/s10201-015-0463-6

Meng, J., Yao, Q., and Yu, Z. (2014). Particulate phosphorus speciation and phosphate adsorption characteristics associated with sediment grain size. *Ecol. Eng.* 70, 140–145. doi:10.1016/j.ecoleng.2014.05.007

Müller, B., Stierli, R., and Wüest, A. (2006). Phosphate adsorption by mineral weathering particles in oligotrophic waters of high particle content. *Water Resour. Res.* 42 (10), W10414. doi:10.1029/2005wr004778

Omari, H., Dehbi, A., Lammini, A., and Abdallaoui, A. (2019). Study of the phosphorus adsorption on the sediments. *J. Chem.* 2019, 1–10. doi:10.1155/2019/2760204

Pan, G., Krom, M. D., Zhang, M., Zhang, X., Wang, L., Dai, L., et al. (2013). Impact of suspended inorganic particles on phosphorus cycling in the Yellow River (China). *Environ. Sci. Technol.* 47 (17), 9685–9692. doi:10.1021/es4005619

Pu, J., Wang, S., Ni, Z., Wu, Y., Liu, X., Wu, T., et al. (2020). Implications of phosphorus partitioning at the suspended particle-water interface for lake eutrophication in China's largest freshwater lake, Poyang Lake. *Chemosphere* 263, 128334. doi:10.1016/j.chemosphere.2020.128334

Shen, Z.-L., and Liu, Q. (2009). Nutrients in the Changjiang River. *Environ. Monit. Assess.* 153 (1–4), 27–44. doi:10.1007/s10661-008-0334-2

Silva, C., and Sampaio, L. S. (1998). Speciation of phosphorus in a tidal floodplain forest in the Amazon estuary. *Mangroves Salt Marshes* 2 (1), 51–57. doi:10.1023/A:1009950208582

Smil, V. (2000). Phosphorus in the environment: Natural flows and human interferences. *Annu. Rev. Energy Environ.* 25 (1), 53–88. doi:10.1146/annurev.energy.25.1.53

Syvitski, J. P., Vörösmarty, C. J., Kettner, A. J., and Green, P. (2005). Impact of humans on the flux of terrestrial sediment to the global coastal ocean. *Science* 308 (5720), 376–380. doi:10.1126/science.1109454

Uusitalo, R., Yli-Halla, M., and Turtola, E. (2000). Suspended soil as a source of potentially bioavailable phosphorus in surface runoff waters from clay soils. *Water Res. Oxf.* 34 (9), 2477–2482. doi:10.1016/S0043-1354(99)00419-4

Vörösmarty, C. J., Meybeck, M., Fekete, B., Sharma, K., Green, P., and Syvitski, J. P. M. (2003). Anthropogenic sediment retention: Major global impact from registered river impoundments. *Glob. Planet. Change* 39 (1–2), 169–190. doi:10.1016/s0921-8181(03)00023-7

Wang, J., Bouwman, A. F., Liu, X., Beusen, A., and Yu, Z. (2021). Harmful algal blooms in Chinese coastal waters will persist due to perturbed nutrient ratios. *Environ. Sci. Technol. Lett.* 8, 276–284. doi:10.1021/acs.estlett.1c00012

Wang, Y., Shen, Z., Niu, J., and Liu, R. (2009). Adsorption of phosphorus on sediments from the Three-Gorges Reservoir (China) and the relation with sediment compositions. *J. Hazard. Mater.* 162 (1), 92–98. doi:10.1016/j.jhazmat.2008.05.013

Wei, J. F., Chen, H. T., Liu, P. X., Li, R. H., and Yu, Z. G. (2010). Phosphorus forms in suspended particulate matter of the Yangtze River [in Chinese]. *Adv. Water Sci.* 121 (1), 107–112.

Welch, H. L., Coupe, R. H., and Aulenbach, B. T. (2014). Concentrations and transport of suspended sediment, nutrients, and pesticides in the lower Mississippi-Atchafalaya River subbasin during the 2011 Mississippi River flood, April through July *(Report No. 2014–5100; Scientific Investigations Report*. Reston, Virginia: USGS Publications Warehouse, 54. doi:10.3133/sir20145100

Yao, Q.-Z., Du, J.-T., Chen, H.-T., and Yu, Z.-G. (2015). Particle-size distribution and phosphorus forms as a function of hydrological forcing in the Yellow River. *Environ. Sci. Pollut. Res. Int.* 23 (4), 3385–3398. doi:10.1007/s11356-015-5567-3

Yu, T., Wei, M., Ongley, E., Li, Z., and Chen, J. (2010). Long-term variations and causal factors in nitrogen and phosphorus transport in the Yellow River, China. *Estuar. Coast. Shelf Sci.* 86 (3), 345–351. doi:10.1016/j.ecss.2009.05.014

Zeng, X., Huang, L., He, G., Wang, D., Wu, X., and Fang, H. (2022). Phosphorus transport in the Three Gorges Reservoir over the past two decades. *J. Hydrology* 609, 127680. doi:10.1016/j.jhydrol.2022.127680

Zhang, S., Zeng, Y., Zha, W., Huo, S., Niu, L., and Zhang, X. (2022). Spatiotemporal variation of phosphorus in the Three Gorges Reservoir: Impact of upstream cascade reservoirs. *Environ. Sci. Pollut. Res. Int.* 29, 56739–56749. doi:10.1007/s11356-022-19787-7

Zhou, A., Tang, H., and Wang, D. (2005). Phosphorus adsorption on natural sediments: Modeling and effects of pH and sediment composition. *Water Res.* 39 (7), 1245–1254. doi:10.1016/j.watres.2005.01.026

Zhou, J., Zhang, M., and Li, Z. (2018). Dams altered Yangtze River phosphorus and restoration countermeasures [in Chinese]. *Hupo Kexue* 30 (4), 865–880. doi:10.18307/2018.0401

Zhou, J., Zhang, M., Lin, B., and Lu, P. (2015). Lowland fluvial phosphorus altered by dams. *Water Resour. Res.* 51 (4), 2211–2226. doi:10.1002/2014wr016155

Zhou, J., Zhang, M., and Lu, P. (2013). The effect of dams on phosphorus in the middle and lower Yangtze river. *Water Resour. Res.* 49 (6), 3659–3669. doi:10.1002/wrcr.20283

frontiers | Frontiers in Environmental Science

TYPE Original Research
PUBLISHED 25 January 2023
DOI 10.3389/fenvs.2023.1106181

OPEN ACCESS

EDITED BY
Biyun Guo,
Zhejiang Ocean University, China

REVIEWED BY
Shuo Zhang,
Tsinghua University, China
Xuefei Chen,
Guangzhou Institute of Geochemistry (CAS), China

*CORRESPONDENCE
Binkai Li,
libk@isl.ac.cn

SPECIALTY SECTION
This article was submitted to Freshwater Science, a section of the journal Frontiers in Environmental Science

RECEIVED 23 November 2022
ACCEPTED 11 January 2023
PUBLISHED 25 January 2023

CITATION
Ren Q, Li B, Zhang Y and Wu H (2023), Origin and evolution of intercrystalline brine in the northern Qaidam Basin based on hydrochemistry and stable isotopes. *Front. Environ. Sci.* 11:1106181. doi: 10.3389/fenvs.2023.1106181

Origin and evolution of intercrystalline brine in the northern Qaidam Basin based on hydrochemistry and stable isotopes

Qianhui Ren[1,2,3], Binkai Li[4]*, Yan Zhang[5] and Haitao Wu[1,2,3]

[1]School of Water Resources and Electric Power, Qinghai University, Xining, China, [2]Laboratory of Ecological Protection and High-Quality Development in the Upper Yellow River, Xining, China, [3]Key Laboratory of Water Ecology Remediation and Protection at Headwater Regions of Big Rivers, Ministry of Water Resources, Xining, China, [4]Qinghai Institute of Salt Lakes, Chinese Academy of Sciences, Xining, China, [5]The Third Qinghai Nonferrous Metals Geological Exploration Institute, Xining, China

The Kunteyi Basin, located in northern Qaidam, is known as a significant potash ore deposit in China. It is of great significance to study the origin of the potassium-rich intercrystalline brine to support the exploitation of potassium salts. In this study, the major ion concentrations and isotopic ratios (δ^2H, $\delta^{18}O$, and $\delta^{11}B$) of intercrystalline brine were used to analyze the evolution of the brine. The results show that the intercrystalline brine has a much higher concentration of total dissolved solids compared with the oil-field brine. Most of the ions are enriched except Ca^{2+} and Br^-. The value of δ^2H and $\delta^{18}O$ are much negative while the $\delta^{11}B$ values are positive. The analysis of C_{Na}/C_{Cl}, C_{Br}/C_{Cl}, Cl/(Na + K + Mg) and isotopes ratios, indicate that (1) Atmospheric precipitation is the primary source of water in brine; (2) The salinity of the brine is mainly influenced by halite dissolution; (3) The study area was influenced by the deep hydrothermal fluids. The thermal water recharged the Pleistocene layer, reacted with polyhalite, and formed Mg- and K-rich brine. The solution rose along the channel formed by the Shuangqiquan Fault and was supplied to the shallow intercrystalline brine.

KEYWORDS

Qaidam Basin, Kunteyi Playa, intercrystalline brine, origination, isotopes

1 Introduction

The origin of brines in the sedimentary basin has a significant implication for understanding the processes of water migration, sedimentary deposition, salt separation, and variation of paleoclimates (Farber et al., 2007; Bershaw et al., 2012; Ye et al., 2015; Basyoni and Aref, 2016). Two questions need to be answered to identify the brine origin, i.e., where the water comes from and how salinity enriches (Bagheri et al., 2014). Two main hypotheses answer the first question. One suggestion is that water came from the residual paleo-seawater, whereas others have suggested the influence of meteoric water and mantle water. The source of salinity in the brine is more complex than that of the proposed origin waters. It can be transformed by many factors, such as seawater concentration, sedimentary weathering or dissolution, and thermal water supply. However, under evaporation and salt crystallization, brines of different origins have similar chemical compositions and associated minerals (Vengosh et al., 1995), which complicates research on brine evolution.

The Qaidam Basin, a Cenozoic sedimentary basin, is a typical interior basin. There are dozens of different sizes of salt lakes, salinas, and playas in the Qaidam Basin. The

sedimentary sequence and tectonic deformation of the Qaidam Basin have recorded the evolution and growth history of the Tibetan Plateau since the Indian–Eurasian plate collision (Yin and Harrison, 2000; Tapponnier et al., 2001; Royden et al., 2008). Under the influence of deep water, volcanic hydrothermal water, and the surrounding rock, the brines of different locations have different hydrochemical characteristics and sources (Ye et al., 2015). In addition, many mineral resources, such as petroleum, potassium, boron, and strontium, exceed the Chinese industrial grade (Tan et al., 2011). Brine is a special kind of water with a total dissolved solid (TDS) content greater than 50 g/L. The intercrystalline brine indicates that the brine remains in the pore structure of the stratum and has undergone a similar evolution process as the formation of minerals. Therefore, research on the origin of brine also helps in understanding the process of mineral formation and improves the efficiency of mineral exploitation.

As playas and hypersaline lakes account for one-quarter of the Qaidam Basin, the origin of these brines has attracted considerable attention (Yu et al., 2013). These researchers agree on two evolutionary mechanisms, i.e., evaporation and dissolution. Analyzing the ion content and isotopic compositions of $\delta^{18}O$, $\delta^{2}H$, and $\delta^{37}Cl$, Du et al. (2016) suggested that the shallow brine of the Qaidam Basin originated from evaporation and was influenced by rainwater that dissolved halite. However, sources of water and salinity are highly controversial. For example, the $\delta^{18}O$ and $\delta^{2}H$ values of brines in the Qaidam Basin, near the meteoric water line, indicate that the brine originated from paleo-meteoric water (Fan et al., 2010; Han et al., 2013; Ye et al., 2015). However, based on the tectonic movement of the Tibetan Plateau, Li et al. (2013b) explained the high $\delta^{11}B$ value of brines in Xiaoliangshan using modified paleo-seawater. In addition, the chemical composition and elemental ratios indicated the influence of thermal water or magmatic fluids. In general, most researchers agree that the evolution of brines is associated with non-marine evaporation. However, these studies did not discuss the origin of water and salinity separately and there is still doubt regarding brine circulation in different regions and depths.

The study area, Kunteyi Salt Lake, located in the western Qaidam Basin, is a vital potash ore deposit containing several Cenozoic brines. In this study, we used $\delta^{18}O$, $\delta^{2}H$, and $\delta^{11}B$ isotopes and ion chemistry to explain the origin of the brine. Traditional elemental geochemical analysis methods have been used to study brine sources. The application of conventional and non-conventional isotope methods makes brine source research more accurate (Vengosh et al., 1995). In this method, we attempt to understand water and salinity sources of the brine.

2 Regional geology

The Qaidam Basin, located in the northern part of the Tibetan Plateau, is a typical arid interior basin. It is a Cenozoic extensional basin that is surrounded by mountains. The Qilian Mountains, Kunlun Ranges, and Altun Mountains are the basin boundaries on the north, south, and northwest, respectively (Xia et al., 2001; Jolivet et al., 2003; Cowgill, 2007). During the Caledonian, a soft collision intensified the paleo-oceanic trough uplift, followed by an underthrusting period on the northern and southern fringes (Xia et al., 2001). After this period, the Qaidam Basin was limited between the Kunlun and Qilian ranges. In the Mesozoic, there was a series of mantle plume uplift and regional compression, resulting in a structural inverted rift basin in this area (Cheng et al., 2019; Cheng et al., 2021). The embryonic Qaidam Basin was formed by sinistral strike-slip faulting on the Altun Mountains in the late Eocene (Lu and Xiong, 2009). Then, the Altyn Tagh continued to rise and the basin continued to sink, leading to a complete separation between the Qaidam Basin and the Tarim Basin, indicating the formation of the modern Qaidam Basin. After this period, the basin reached a mega-lake environment that evolved into modern salt lakes (Vengosh et al., 1995).

Regarding Xitaijinaier and Dongdabuxun lakes as demarcation points, the Qaidam Basin can be divided into three parts: the eastern, central, and western parts (Figure 1A). The western Qaidam Basin is located between 38° and 39°N and 91° and 93°E, close to the Kunlun mountain fault zone and the Altyn Tagh Fault zone, which is the most intense deformation and tectonic form of the Qaidam Basin.

The Kunteyi Basin is a typical dry sabkha located in the western part of Qaidam and is a crucial potash deposit in China. All intercrystalline brine samples were collected from the central Dayantan Basin, the best ore-forming and largest potash deposit in Kunteyi (Li et al., 2021). It is surrounded by the Eboliang structure in the west, the Hulushan structure in the south, and the Lenghu structure in the east, forming a semi-closed secondary basin. The study area is covered by middle Pleistocene and upper Pleistocene strata, and the old to new strata exposed in the area are the Proterozoic, Ordovician, Devonian, Carboniferous, Jurassic, Tertiary, and Quaternary strata. Four groups of fault structures exist in the region. Three are large in scale, the Shuangqiquan Fault in the west, the remote sensing F_6 Fault in the northeast, and the remote sensing F_5 Fault in the middle of Kunteyi, which may supply the channel for the inflow of hydrothermal water (Figure 1B). Since the beginning of the Archean Luliang Movement, the Dayantan Basin has experienced long-term and complex tectonic movements and has formed well-developed fault blocks and substantial folds (Li et al., 2020). These structures block the surface water supply to the mining area and create conditions for brine formation. The occurrence state of the brine in Kunteyi is mainly the intercrystalline brine, and a small amount of oilfield water is distributed along the eastern Lenghu Fault. The intercrystalline brine in the study area is divided into five layers. Except for the shallow intercrystalline brine distributed in the Holocene series or the upper Pleistocene series, the other four confined aquifers correspond to the Pleistocene salt layer. In this study, we collected the shallow intercrystalline brine and analyzed its hydrochemical and isotopic compositions to explore the evolutionary process of the brine.

3 Method

In this study, 11 samples were collected, including nine intercrystalline brines and two salt lake brines. The sampling point locations are shown in Figure 1C. All the intercrystalline brine samples were collected from the existing engineering boreholes in the mining area 1 m below the water surface.

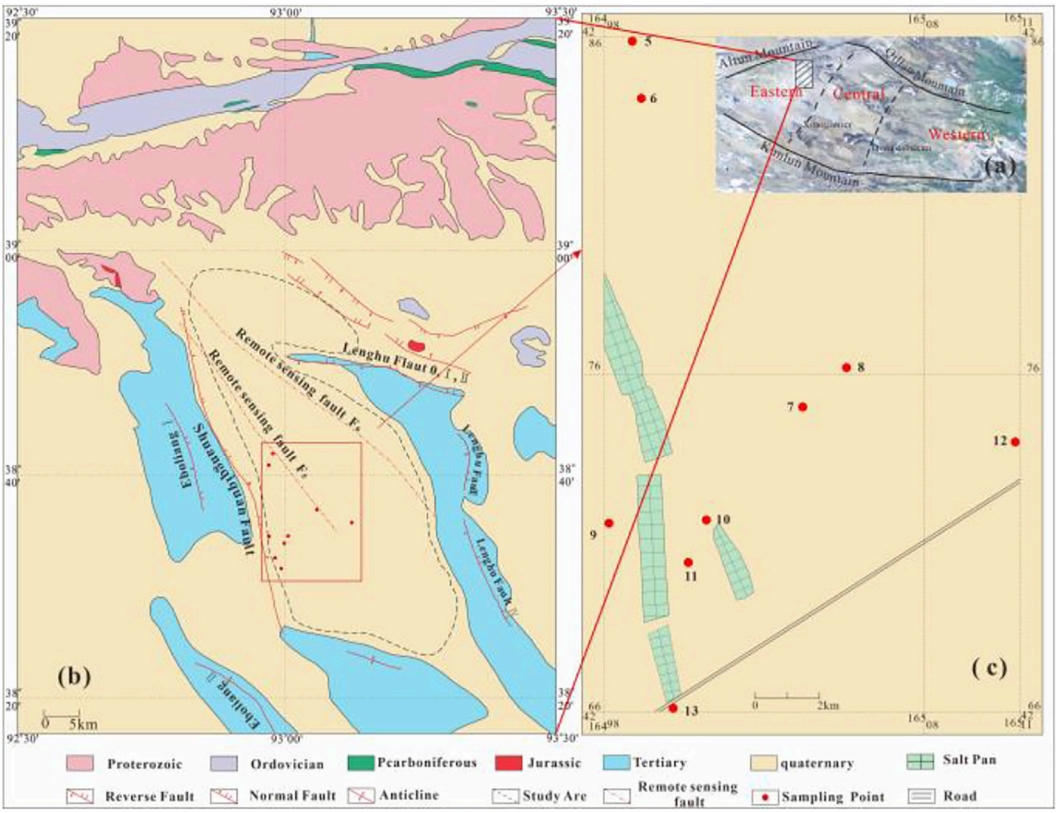

FIGURE 1
(A) Framework of the Qaidam Basin and the location of study area; **(B)** General tectonic features of the study area; **(C)** Location of sampling points.

Therefore, these brine samples belonged to the submersible aquifer. The sample measurements were completed at the analysis and testing center of the Qinghai Institute of Salt Lakes, Chinese Academy of Sciences.

3.1 Element concentration analyses

The concentrations of K^+ and SO_4^{2-} ions and TDS were measured using gravimetric analysis, Ca^{2+} and Mg^{2+} ion concentrations were measured through EDTA titration, Cl^- concentration was measured using $AgNO_3$ titration, and Na^+ ion concentration was assessed *via* subtraction. An inductively coupled plasma emission spectrometer (ICP-MS) was used to analyze the B and Br concentrations. Analytical uncertainties are less than ±5% for B and Br, less than ±2% for Na^+, and less than ±0.5% for all other elements. The results are presented in Table 1.

3.2 Hydrogen and oxygen isotopic analyses

Hydrogen and oxygen isotopic analyses were performed using a stable isotope mass spectrometer (MAT253), and the analytical uncertainties were less than ±0.2% and ±2%, respectively.

3.3 Boron isotopic analysis

The B isotopes were measured at the Chinese Academy of Geological Sciences. The determination process included B purification and isotope determination. In the purification stage, the prepared sample was first diluted with ultrapure water and a solution of low-B boron water, with a B concentration of 10 μg and pH of 6–7. The diluted solutions were passed through a B-specific resin column at a flow rate of 2.5 mL/L for B adsorption. Column elution and B extraction were performed by adding 12 mL of a 0.1 mol/L HCl solution to the resin column at 75°C. The eluent was evaporated and concentrated in a 60-°C purification furnace, and excess ions were removed using an anion and cation-mixed exchange resin column. Then, it was further purified using an eluent without B; the diluted eluents were evaporated, dried at 60°C, and then prepared for isotopic analysis. During the two evaporation processes, mannitol and cesium carbonate (Cs_2CO_3) were added to the eluents to inhibit evaporation.

All B^{11}/B^{10} ratios were determined using a Triton thermal ionization mass spectrometer (Thermo Fisher Company). Our analyses showed a standard deviation of less than 0.2‰ (2σ), as determined by the coeval studies of NIST SRM-951 replicates. Isotope ratios are reported here as a per mil deviation ($\delta^{11}B$) in the B^{11}/B^{10} ratios relative to those of the standard NBS SRM 951:

$$\delta^{11}B(‰) = \left[\left(B^{11}/B^{10}\right)_{sample} / \left(B^{11}/B^{10}\right)_{standard} - 1 \right] \times 1000.$$

TABLE 1 Concentration of major elements, trace elements, hydrogen isotopes, oxygen isotopes, and boron isotopes of brines in the study area.

Sample No.	Type	TDS g/L	K^+ g/L	Na^+ g/L	Mg^{2+} g/L	Ca^{2+} g/L	Cl^- g/L	SO_4^{2-} g/L	HCO_3^- g/L	Br^- mg/L	B mg/L	δ^2H	$\Delta^{18}O$	$\delta^{11}B$	Data source
1	Oilfield brine	43.34	0.25	12.53	0.62	3.61	25.12	0.46	0.69	4.52	55.82	−56.4	−6.5		Li et al. (2019)
2		49.18	0.09	13.18	1.38	3.29	30.85	0.28	0.08	4.77	20.13	−48	0.1		
3		42.43	0.08	11.56	1.09	2.58	26.61	0.06	0.15	19.01	119.5	−39.7	3		
4		33.79	0.07	8.95	1.41	1.88	21.35	0.02	0.09	5.92	11.02	−39.5	3.9		
5	Intercrystalline brine	332.75	4.54	116.44	5.75	0.36	189.59	15.64	0.15	16.98	260	−49	−5.1	21.27	
6		331.75	5.46	113.39	7.05	0.36	189.94	15.06	0.13	13.62	351.5	−47	−4.7	21.67	
7		328.39	2.62	117.37	5.11	0.29	188.21	14.41	0.17	12.78	200.9	−38	−2.6	24.87	
8		328.21	1.66	121.30	2.97	0.44	188.21	13.34	0.18	8.14	110.5	−34	−3.2	21.61	
9		339.32	8.34	96.53	17.69	0.18	186.32	29.88	0.19	9.03	200.9	−33	−2	18.49	
10		344.50	10.43	99.11	15.86	0.44	184.76	33.34	0.32	22.26	221	−39	−4.1	22.58	
11		341.49	10.34	103.39	12.86	0.29	186.66	27.41	0.19	15.16	331.4	−47	−5.1	21.22	
12		331.01	5.50	111.98	7.71	0.36	189.25	15.72	0.17	10.71	301.3	−41	−4	22.37	
13		331.46	6.55	109.78	8.11	0.73	184.59	21.16	0.13	21.23	401.7	−48	−3.3	15.77	
14	Potassium Lake	311.71	3.71	79.22	24.49	2.14	198.56	3.05	0.22	8.34	301.3	−30	1.8	9.25	
20	Sugan Lake	68.37	0.33	20.26	1.00	0.04	0.47	46.10	0.17	4.23	15.06	−69	−9.4	5.27	
21	Seawater	32.00	0.34	9.89	1.19	0.38	17.53	2.42	0.13	61	4.3	0	0		Chen (1983)

10.3389/fenvs.2023.1106181

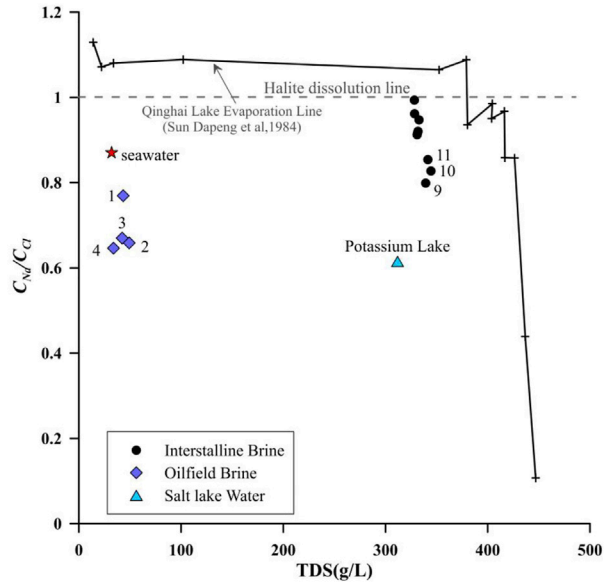

FIGURE 2
Comparative C_{Na}/C_{Cl} ratio distribution and total dissolved solids (TDS) of the intercrystalline brine, oilfield brine, and salt lake water.

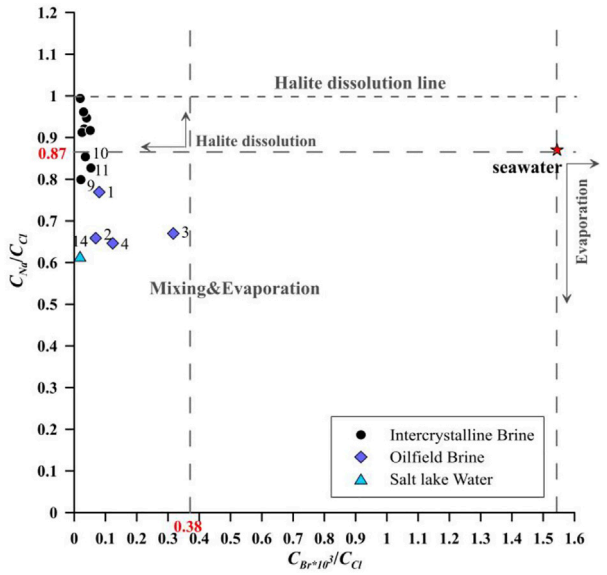

FIGURE 3
Relationship between the C_{Na}/C_{Cl} ratio and C_{Br}/C_{Cl} ratio of the intercrystalline brine, oilfield brine, and salt lake water. Data for oilfield brine are extracted from Li et al. (2019).

The mean of the absolute B^{11}/B^{10} ratios of NIST SRM-951 replicates analyzed alongside the samples was 4.05262 ± 0.00077 (2σ = 0.02%; n = 9).

4 Results

The chemical and isotopic compositions of the samples in the study area are listed in Table 1. The data on the intercrystalline brine and salt lake brine were measured in this study. Data from seawater and the oilfield brine of the Kunteyi Salt Lake, reported by Chen (1983) and Li et al. (2019), were selected as a comparison (Table 1) to understand the formation process of the brine.

4.1 Water chemistry

The average value of TDS in the intercrystalline brine of Kunteyi is 334.04 g/L. It is almost ten times higher than the TDS value of seawater and the oilfield brine from Kunteyi but is similar to the TDS value of the brine from the oilfield of northern Qaidam (Tan et al., 2011). The major anions and cations of the brine in Kunteyi are Cl^- (184,589.9–198,563.5 mg/L) and Na^+ (96,527.64–121,296.22 mg/L) ions, respectively, which together account for 90% of TDS. Compared with the oilfield brine, the intercrystalline brine has a much higher K^+ and SO_4^{2-} concentration, indicating a possible influence of the evaporation stage of halite sedimentation (Liu et al., 2016). According to the sequence of mineral precipitation in Qinghai Lake evaporated during the experiment given by Sun et al. (2002), the K^+ and SO_4^{2-} concentrations continued to increase until the end of evaporation. However, the Cl^- concentration in the intercrystalline brine was much higher than that in the residual solution after halite deposition. The brine of the Potassium Lake, located near the study area, is rich in Mg^{2+}, Ca^{2+}, and Cl^-. These

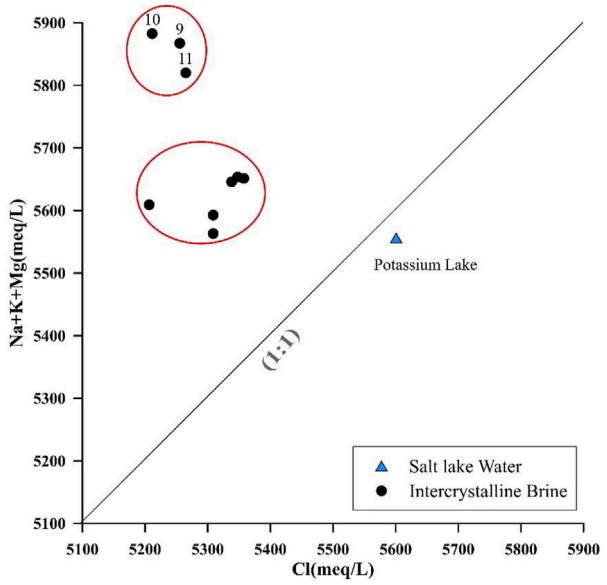

FIGURE 4
Relationship between (Na + K + Mg) and Cl in intercrystalline brines and salt lake water in the study area.

phenomena indicate that the evolution of the brine may be simultaneously controlled by evaporation and influenced by the Ca–Cl-type water.

Boron and bromine are ideal elements for identifying the origin of the salinity. Therefore, the concentrations of these two elements were tested in this study. The results show that the Br concentration of the intercrystalline brine ranges from 8.14 to 22.26 mg/L, considerably lower than the initial Br concentration of seawater caused by

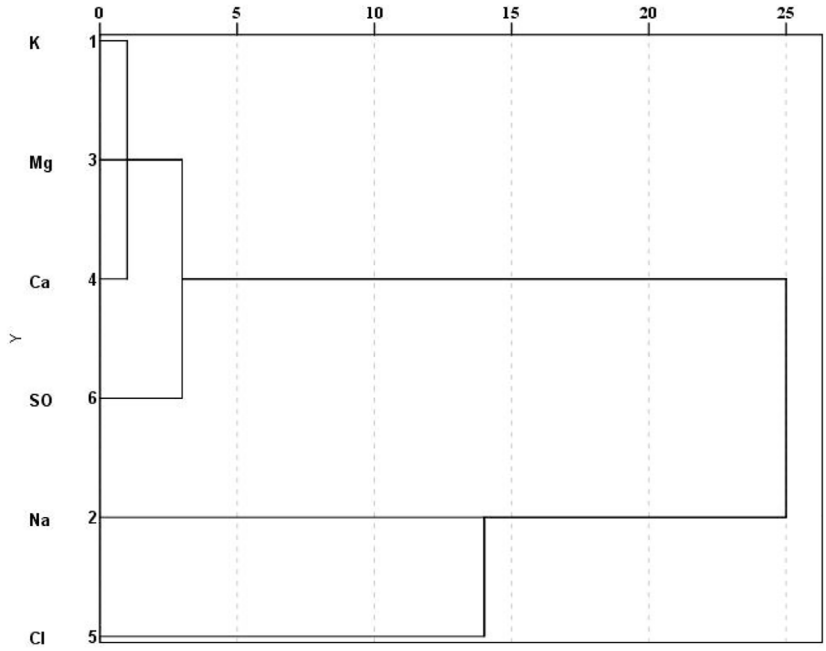

FIGURE 5
Cluster analysis of the major ions of the intercrystalline brine.

evaporation. The concentration of B ranges from 110.50 to 401.70 mg/L, while the concentration of B in seawater is only 4.30 mg/L (Chen, 1983). These results indicate that the intercrystalline brine of Kunteyi is of non-marine origin.

4.2 Isotopic ratios of the intercrystalline brine

It can be seen from Table 1 that the characteristics of the H, O, and B isotopic compositions are considerably different between brine, oilfield water, and salt lake water. The δ^2H and $\delta^{18}O$ values of the intercrystalline brine range from −49 to −33‰ (average −41.7‰) and from −5.1 to −2.0‰ (average −3.8‰), respectively. The oilfield water has a positive $\delta^{18}O$ value, with an average 0.12‰, and a similar δ^2H, with an average −45.9‰, which may indicate that the intercrystalline brine underwent a more intense evaporation process than the oilfield water.

As B isotopes do not react with other elements during the water cycle, these often are used to distinguish the different sources of salinity, such as eluviation and ancient brine precipitation (Fan et al., 2010). In this study, the average $\delta^{11}B$ value of the intercrystalline brine is 21.09‰, whereas that of the Potassium Lake is 9.26‰.

5 Discussion

5.1 Chemical evolution of the brine

The ratios of the chemical compositions are valuable tools for tracing the sources of brine salinity and its evolution. The relationship between the molar concentration ratio C_{Na}/C_{Cl} and TDS can reveal the salinity enrichment process (Engle and Rowan, 2013). During evaporation, the TDS of the solution increased continuously (Ye et al., 2015). The oilfield brine is far from the evaporation line and halite dissolution line and instead has a similar C_{Na}/C_{Cl} ratio to that of seawater, as shown in Figure 2. In contrast to the oilfield brine, the C_{Na}/C_{Cl} ratio of the intercrystalline brine in this study showed a similar trend to that of the Qinghai Lake evaporation line but had a lower TDS concentration, suggesting that evaporation is the main factor in the formation of the intercrystalline brine but not the only factor. The lower TDS concentration is likely caused due to the simultaneous freshwater intrusion. Halite dissolution is another crucial process that results in Na^+ enrichment, maintaining a C_{Na}/C_{Cl} ratio of approximately 1 (Han et al., 2014; Llewellyn, 2014). However, the C_{Na}/C_{Cl} ratio of all the samples was less than 1, and the minimum value of the intercrystalline brine is 0.79. The processes that can cause this phenomenon include cation exchange and absorption, mixing of Ca–Cl water, and dissolution of other Cl-containing minerals (Liu et al., 2016). Therefore, the C_{Na}/C_{Cl} ratio alone cannot clearly explain the origin of the salinity.

Like other halogens, bromide exists in nature only in an oxidation state (Gupta et al., 2012). The chemical properties of Br^- are relatively conservative, and Br^- is not easily absorbed by coprecipitation. In the process of seawater evaporation, the concentration of Br^- increases because it is difficult for Br^- to enter the crystal lattice of halite and coprecipitate with it (Liu et al., 2016). In contrast, brines formed by the dissolution of non-marine evaporites had a much smaller content of Br^-. Therefore, the C_{Br}/C_{Cl} ratio commonly helps in identifying the source of salts during the leaching of halite and other minerals (Li et al., 2015). Figure 3 plots the relationship between the C_{Na}/C_{Cl} ratio and C_{Br}/C_{Cl} ratio to analyze the evolution process of the brine. The seawater had C_{Na}/C_{Cl} = 0.87 and C_{Br}/C_{Cl} = 1.54. With evaporation, Na^+ and Cl^- were precipitated continuously with the increasing Br^- concentration. Therefore, the sedimentary brine usually shows $C_{Na}/$

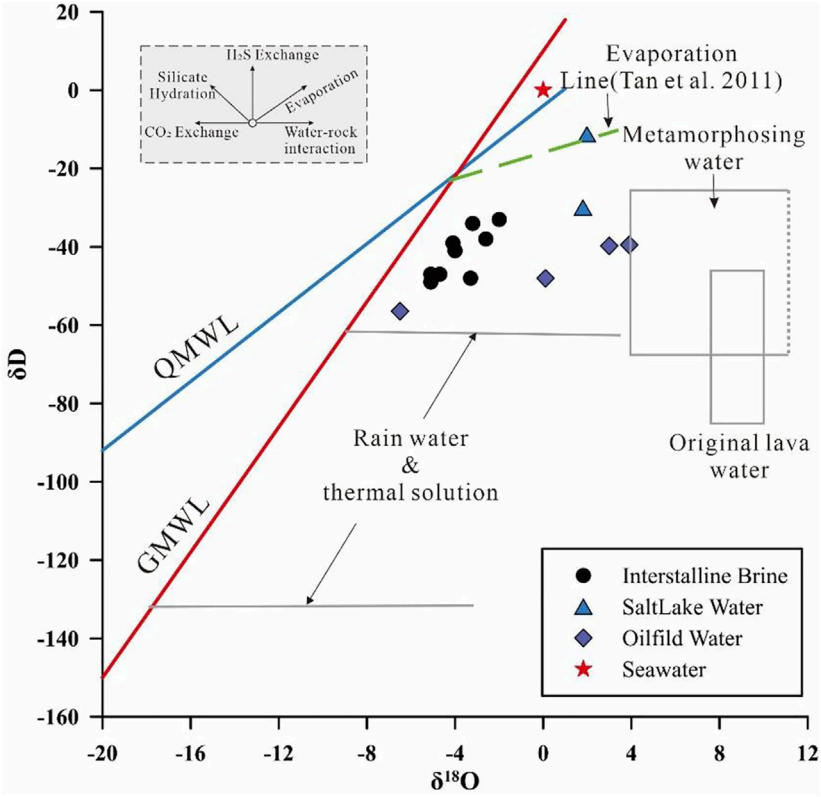

FIGURE 6
Relationship between δ^2H and $\delta^{18}O$ of the intercrystalline brine, oilfield brine, and salt lake water. Data for the oilfield brine are extracted from Li et al. (2019).

C_{Cl} <0.87 and C_{Br}/C_{Cl} >1.54. For the halite dissolution brine, the C_{Na}/C_{Cl} ratio is higher than 0.87 and the C_{Br}/C_{Cl} ratio is smaller than 0.38 (Li et al., 2013a). The characteristic coefficients of most intercrystalline brines conform to the process of halite dissolution, as shown in Figure 3. However, points 9 to 11 have C_{Na}/C_{Cl} ratios less than 0.87 and C_{Br}/C_{Cl} ratios less than 0.38, which plot in the same area as the oilfield brine. The oilfield brine of Kunteyi is affected by a Ca–Cl-type hydrothermal fluid (Li et al., 2019). This process may increase Ca^{2+} simultaneously, but the intercrystalline brine in this area has a low Ca^{2+} content. Two possible modes of evolution may lead to an increase in the concentration of Cl^- ions accompanied by a low Ca^{2+} ion concentration. In the first mode, the Ca–Cl-type water intrudes into the study area, and Ca^{2+} ions react with CO_3^{2-} ions and deposit, whereas the second mode may involve the dissolution of other Cl-bearing minerals, such as sylvine.

The dissolution of Cl-bearing minerals would elevate the Cl^- concentration and give a Cl/(Na + K + Mg) ratio of approximately 1 in groundwater. However, this ratio of the intercrystalline brine plot is scattered, and all points are above the 1:1 line (Figure 4). These samples can be divided into two groups, and points 9, 10, and 11 have significantly higher (Na + K + Mg) concentrations, proving that there may be other mineral dissolution processes providing more cations without chlorine to the intercrystalline brine.

Cluster analysis divides the data on unknown categories into different classes or clusters through statistical methods and then identifies the data changed with the same rule. This method has been used widely to classify groundwater and identify groundwater flow and geochemical processes (Lyu et al., 2019). Cluster analysis was used on the major ion concentration of all intercrystalline brines in the study area to find the similarity of different ion concentration variation trends and identify which mineral participates in the dissolution quickly. The cluster analysis results are presented as a dendrogram (Figure 5). In this study, the ions were divided into two groups. One group included Na^+ and Cl^-, which resulted in the dissolution of the halite. This result was obtained by analyzing the C_{Na}/C_{Cl} and C_{Br}/C_{Cl} ratios. The other group includes K^+, Ca^{2+}, Mg^{2+}, and SO_4^{2-}, which are contained in polyhalite ($K_2Ca_2Mg\ [SO_4]_4{\cdot}2H_2O$). A large amount of polyhalite is buried in the Pleistocene strata of Kunteyi. However, this mineral is difficult to develop because of its insoluble characteristics and deeply buried layers (Yuan et al., 2021). All brines analyzed in this study were collected during the Holocene, and it needs to be further confirmed whether polyhalite buried in the Pleistocene can influence K^+ and Mg^{2+} concentrations in the superficial layer. There are three deep faults, F_5, F_6, and Shuangqiquan faults, located in the middle and western boundaries of Kunteyi. They provide a channel for deep water to recharge the shallow brine. Most hydrothermally, Ca–Cl brines are known to dissolve polyhalite effectively (Li et al., 2020). Therefore, in the process of brine evolution, Cl^--containing water from the deep layer may have been trapped in the Pleistocene and may have dissolved the polyhalite in this layer. The solution was then replenished upward along the deep faults and flowed into the Holocene, improving the K^+ and Mg^{2+}

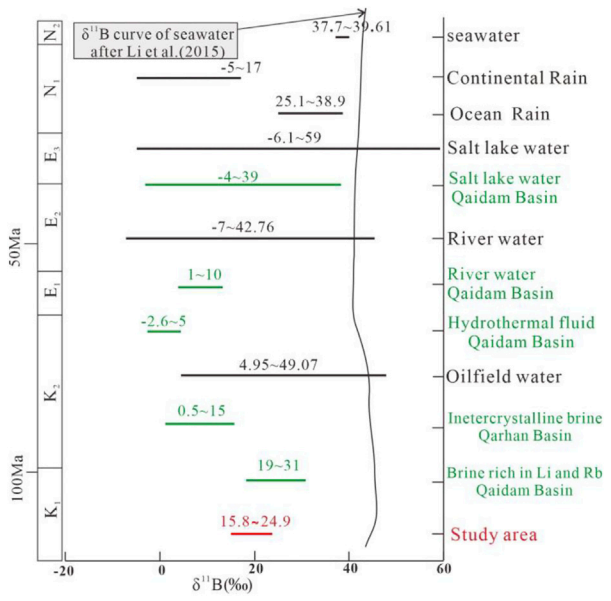

FIGURE 7
Comparison of $\delta^{11}B$ values of different solutions. The salt lake water data in the Qaidam Basin are extracted from Xiao et al. (1999), the river water data in the Qaidam Basin are extracted from Hussain et al. (2021), the oilfield water data are extracted from Li et al. (2013b), the intercrystalline brine data in the Qarhan Basin are extracted from Fan et al. (2015), and the data on the brine rich in Li and Rb in the Qarhan Basin are extracted from Li et al. (2022).

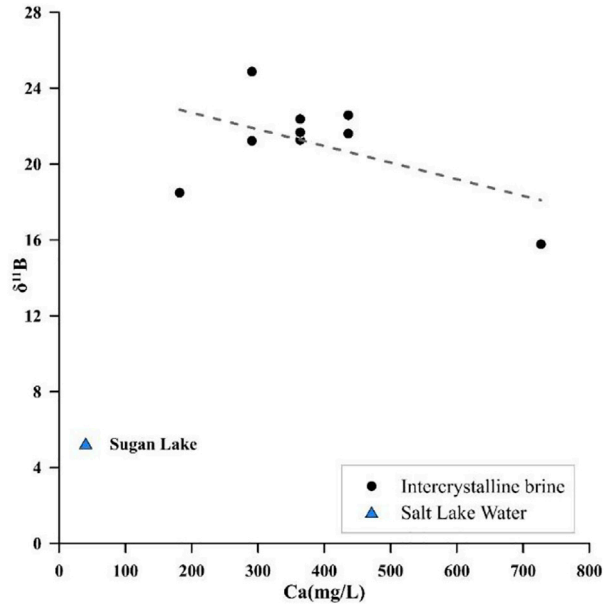

FIGURE 8
Relationship between $\delta^{11}B$ values and the Ca content of the intercrystalline brine and salt lake water.

concentrations of the intercrystalline brine. Simultaneously, the high concentration of Cl^- in the solution inhibited halite dissolution and led to a C_{Na}/C_{Cl} ratio smaller than 1.

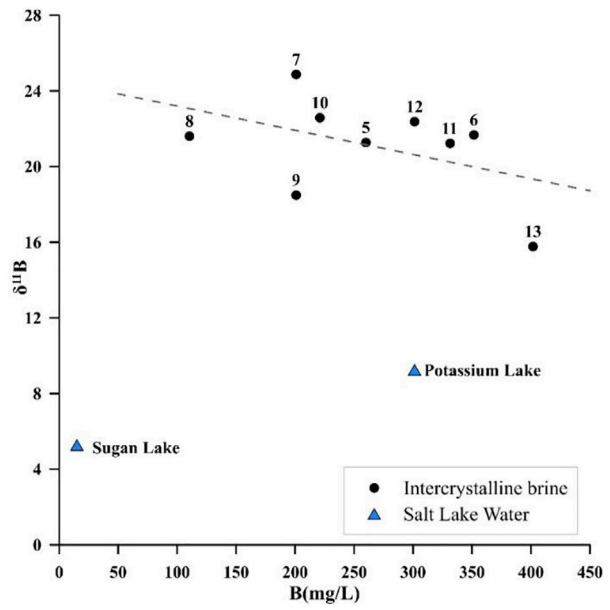

FIGURE 9
Relationship between $\delta^{11}B$ values and the B content of the intercrystalline brine and salt lake water.

From the aforementioned analysis, points 9, 10, and 11 (Figure 4) showed many different hydrochemical characteristics compared to the other points. The brine sampled from these three points has a lower C_{Na}/C_{Cl} ratio and Cl/(Na + K + Mg) ratio because the brine is rich in K^+ and Mg^{2+} and poor in Na^+. These three points are located near the Shuangqiquan Fault and may receive more polyhalite dissolution water containing high K^+ and Mg^{2+} ion concentrations than polyhalite water received by other intercrystalline brine points.

5.2 Hydrogen and oxygen isotopes

The isotopes δ^2H and $\delta^{18}O$ are good conservative tracers for identifying recharge sources because they are the part of the water molecule itself, which can reflect its history and origin before infiltration (Clark and Fritz, 2013). The $\delta^{18}O$ isotopes of intercrystalline brines are relatively lighter, ranging from −5.1 to −2‰, compared to those of the oilfield brines of Kunteyi, and almost similar δ^2H isotopes, ranging from −49 to −33‰. As Figure 6 shows, all the isotopic data lie on the right of the Global Meteoric Water Line (GMWL, $\delta^2H = 8 \times \delta^{18}O - 46$) and Qaidam Meteoric Water Line (QMWL, $\delta^2H = 4.4 \times \delta^{18}O - 4.0$) in the plot of δ^2H vs. $\delta^{18}O$ (Craig, 1961; Fan et al., 2010). The apparent positive shift in $\delta^{18}O$ may be caused by water–rock interactions (Cartwright et al., 2004; Boschetti et al., 2020). The equation of the fitting curve for the intercrystalline brine ($\delta^2H = 4.3 \times \delta^{18}O - 25$) is almost parallel to the QMWL, indicating an atmospheric water origin of the water source of the intercrystalline brine. However, owing to the evaporation effect, the light isotope (H) migrates to the gas phase, whereas the heavy isotope (D) tends to be enriched in the weakly active phase and retained in the original brine solution. Thus, the surface brine has a heavier δ^2H value than the δ^2H values of all intercrystalline plots below the evaporation line. Evaporation is not a primary process

in brine evolution. The oilfield brine will have frequent water–rock interactions, leading to a much heavier $\delta^{18}O$ value, owing to the enclosed space compared to that of the intercrystalline brine. Notably, the oilfield water in the study area is close to the hydrothermal distribution area (Figure 6). The oilfield brine of Kunteyi has been proven to be affected by deep hydrothermal water influxes (Tan et al., 2011), and therefore, the comparatively lighter $\delta^{2}H$ of the intercrystalline brine may also be caused by the inflow of hydrothermal water, which has a negative $\delta^{2}H$ value. Simultaneously, the positive $\delta^{18}O$ value may have been influenced by the water–rock interaction and evaporation, consistent with the conclusions obtained from the chemical analyses.

5.3 Boron isotopes

Natural boron exists as either tetrahedral (i.e., $B(OH)_3$) or trigonal complexes (i.e., $B(OH)_4^-$) (Barth, 1993). Differences in their reduced partition function ratios and relative masses result in two stable isotopes, B^{11} and B^{10}, showing significant isotopic fractionation (Ren et al., 2018), leading to considerable variations in natural $\delta^{11}B$ (Figure 7). Thus, boron isotopes can readily distinguish the evolution of brines. All the intercrystalline brine samples exhibited $\delta^{11}B$ values of 15.77‰–25.87‰, with an average value of 21.1‰. These values are considerably higher than those of the intercrystalline brine from the Qarhan Basin and similar to those of brines rich in Li and Rb, identified to be influenced by thermal water, as shown in Figure 7. Compared with the brine from the Potassium Lake and Sugan Lake (values 9.25‰ and 5.27‰), which represent the $\delta^{11}B$ value of the residual brine of evaporation, the $\delta^{11}B$ values of the intercrystalline brine are much higher. During the evaporation of seawater, $\delta^{11}B$ values will increase with an increase in the water concentration (Kloppmann et al., 2001). However, in non-marine evaporation environments with a pH less than 7, $\delta^{11}B$ values change oppositely, indicating that the high $\delta^{11}B$ value of the intercrystalline brine is not due to evaporation (Yingkai and Lan, 2001). Another process that occurred in the study area is halite dissolution. According to Qin et al. (2021), B ions would not enter the crystal lattice during halite deposition and without isotopic fractionation; therefore, halite dissolution does not affect $\delta^{11}B$ of brines.

Two reactions can lead to the $\delta^{11}B$ increase, clay absorption, and hydrothermal recharge (Hemming and Hanson, 1992). When clay absorption occurs, the Na^+ and K^+ concentrations decrease in contrast to the hydrochemical analysis, which indicated that no clay absorption occurred in the study area. The hydrothermal process is Ca–Cl-type water with a low $\delta^{11}B$ value. It can react with CO_3^{2-} ions and make $B(OH)_4^-$ ions, enrich with B^{10}, and coprecipitate with $CaCO_3$, and this process will decrease B and Ca^{2+} concentrations and increase the $\delta^{11}B$ value (Xiao et al., 1999). There is no significant correlation between Ca vs. $\delta^{11}B$ and B vs. $\delta^{11}B$, and the *p*-value of these two groups is higher than 0.05, as shown in Figures 8, 9. However, the number of samples was insufficient to reflect the statistical law. However, the fit line showed a downward trend. Compared with Potassium Lake water, the intercrystalline brine has larger $\delta^{11}B$ isotope values and lower Ca^{2+} concentrations. Both of these phenomena can effectively confirm the influence of hydrothermal treatment.

5.4 Origin of the intercrystalline brine

Synthesizing the previous results inferred from multiple chemical and isotopic analyses with geological structures and hydrogeological conditions, a conceptual model for the origin of saline and brine groundwater in shallow aquifers can be inferred. The shallow intercrystalline brine in the Holocene is modern, and the water source is mainly atmospheric precipitation. Atmospheric water with a low TDS value is stored in the formation, which dissolves a large amount of halite and increases the concentration of Na^+ and Cl^- ions in the solution. Simultaneously, the brine in the deep formation of the Pleistocene was affected by the Ca–Cl-type deep hydrothermal water, and polyhalite dissolution and $CaCO_3$ precipitation occurred to form Mg- and K-rich ionic brines. The brine rose along the channel formed by the fracture and was supplied to the shallow intercrystalline brine.

6 Conclusion

The chemical characteristics and isotopic compositions of the intercrystalline brine in Kunteyi display a non-marine origin, and they are influenced by mineral dissolution, geothermal system heat sources, and water recharge sources.

(1) From the perspective of H and O isotopic compositions, the fitting curve of the H and O isotope values of the intercrystalline brine is almost parallel to the local meteoric water line, and there is an apparent O isotope positive drift, indicating that the water source in this area is mainly atmospheric water.
(2) The curves of C_{Na}/C_{Cl} vs. TDS and C_{Na}/C_{Cl} vs. C_{Br}/C_{Cl} show that halite is the main dissolved mineral in the formation and is also the primary source of salinity in the brine. However, the high content of Mg^{2+} and K^+ ions, and the ion cluster analysis showed that polyhalite dissolution is another source of salinity for the brine.
(3) The analyses of the C_{Br}/C_{Cl} ratio and $\delta^{11}B$ show that the study area was affected by the hydrothermal fluid. The hydrothermal fluid first stranded in the Pleistocene dissolved polyhalite and continued to recharge the shallow intercrystalline brine such that K^+ ions in the brine increased to the mining grade.

Data availability statement

The original contributions presented in the study are included in the article/Supplementary Materials; further inquiries can be directed to the corresponding author.

Author contributions

QR: methodology, analysis, visualization, validation, and writing—original draft. BL: sampling, data test, and supervision. YZ: investigation and writing—review and editing. HW: investigation and writing—review and editing.

Funding

This research work is supported by the National Key Laboratory Opening Fund Project of Hydroscience and Engineering—Tsinghua University (No. sklhse-2020-B-04).

Acknowledgments

The authors would like to thank all the workers who assisted with analyzing boron isotope contents. They all acknowledge the Frontier Editorial Team for their professional handling of the manuscript and dedicated referees who provided very constructive and insightful comments to significantly improve the quality of the work.

Conflict of interest

The authors declare that the research was conducted in the absence of any commercial or financial relationships that could be construed as a potential conflict of interest.

Publisher's note

All claims expressed in this article are solely those of the authors and do not necessarily represent those of their affiliated organizations, or those of the publisher, the editors, and the reviewers. Any product that may be evaluated in this article, or claim that may be made by its manufacturer, is not guaranteed or endorsed by the publisher.

References

Bagheri, R., Nadri, A., Raeisi, E., Kazemi, G., Eggenkamp, H., and Montaseri, A. (2014). Origin of brine in the kangan gasfield: Isotopic and hydrogeochemical approaches. *Environ. Earth Sci.* 72 (4), 1055–1072. doi:10.1007/s12665-013-3022-7

Barth, S. (1993). Boron isotope variations in nature: A synthesis. *Geol. Rundsch.* 82 (4), 640–651. doi:10.1007/bf00191491

Basyoni, M. H., and Aref, M. A. (2016). Composition and origin of the sabkha brines, and their environmental impact on infrastructure in Jizan area, Red Sea Coast, Saudi Arabia. *Environ. Earth Sci.* 75 (2), 105–117. doi:10.1007/s12665-015-4913-6

Bershaw, J., Penny, S. M., and Garzione, C. N. (2012). Stable isotopes of modern water across the Himalaya and eastern Tibetan Plateau: Implications for estimates of paleoelevation and paleoclimate. *J. Geophys. Res. Atmos.* 117 (D2), 16132. doi:10.1029/2011JD016132

Boschetti, T., Awadh, S. M., Al-Mimar, H. S., Iacumin, P., Toscani, L., Selmo, E., et al. (2020). Chemical and isotope composition of the oilfield brines from Mishrif Formation (southern Iraq): Diagenesis and geothermometry. *Mar. Petroleum Geol.* 122, 104637. doi:10.1016/j.marpetgeo.2020.104637

Cartwright, I., Weaver, T. R., Fulton, S., Nichol, C., Reid, M., and Cheng, X. (2004). Hydrogeochemical and isotopic constraints on the origins of dryland salinity, Murray Basin, Victoria, Australia. *Appl. Geochem.* 19 (8), 1233–1254. doi:10.1016/j.apgeochem.2003.12.006

Chen, Y. (1983). Sequence of salt separation and regularity of some trace elements distribution during isothermal evaporation (25 °C) of the Huanghai seawater. *Acta Geol. Sin.* 4, 379–390.

Cheng, F., Garzione, C. N., Jolivet, M., Guo, Z., Zhang, D., Zhang, C., et al. (2019). Initial deformation of the northern Tibetan plateau: Insights from deposition of the lulehe formation in the Qaidam Basin. *Tectonics* 38 (2), 741–766. doi:10.1029/2018TC005214

Cheng, F., Jolivet, M., Guo, Z., Wang, L., Zhang, C., and Li, X. (2021). Cenozoic evolution of the Qaidam Basin and implications for the growth of the northern Tibetan plateau: A review. *Earth-Science Rev.* 220, 103730. doi:10.1016/j.earscirev.2021.103730

Clark, I. D., and Fritz, P. (2013). *Environmental isotopes in hydrogeology*. Lewis, Boca Raton: CRC Press.

Cowgill, E. (2007). Impact of riser reconstructions on estimation of secular variation in rates of strike–slip faulting: Revisiting the Cherchen River site along the Altyn Tagh Fault, NW China. *Earth Planet. Sci. Lett.* 254 (3-4), 239–255. doi:10.1016/j.epsl.2006.09.015

Craig, H. (1961). Isotopic variations in meteoric waters. *Science* 133 (3465), 1702–1703. doi:10.1126/science.133.3465.1702

Du, Y., Ma, T., Chen, L., Xiao, C., and Liu, C. (2016). Chlorine isotopic constraint on contrastive Genesis of representative coastal and inland shallow brine in China. *J. Geochem. Explor.* 170, 21–29. doi:10.1016/j.gexplo.2016.07.024

Engle, M. A., and Rowan, E. L. (2013). Interpretation of Na–Cl–Br systematics in sedimentary basin brines: Comparison of concentration, element ratio, and isometric log-ratio approaches. *Math. Geosci.* 45 (1), 87–101. doi:10.1007/s11004-012-9436-z

Fan, Q., Ma, H., Lai, Z., Tan, H., and Li, T. (2010). Origin and evolution of oilfield brines from Tertiary strata in Western Qaidam Basin: Constraints from 87Sr/86Sr, δD, δ18O, δ34S and water chemistry. *Chin. J. Geochem.* 29 (4), 446–454. doi:10.1007/s11631-010-0478-y

Fan, Q., Ma, Y., Cheng, H., Wei, H., Yuan, Q., Qin, Z., et al. (2015). Boron occurrence in halite and boron isotope geochemistry of halite in the Qarhan Salt Lake, Western China. *Sediment. Geol.* 322, 34–42. doi:10.1016/j.sedgeo.2015.03.012

Farber, E., Vengosh, A., Gavrieli, I., Marie, A., Bullen, T. D., Mayer, B., et al. (2007). The geochemistry of groundwater resources in the Jordan valley: The impact of the rift valley brines. *Appl. Geochem.* 22 (3), 494–514. doi:10.1016/j.apgeochem.2006.12.002

Gupta, I., Wilson, A. M., and Rostron, B. J. (2012). Cl/Br compositions as indicators of the origin of brines: Hydrogeologic simulations of the Alberta Basin, Canada. *Bulletin* 124 (1-2), 200–212. doi:10.1130/B30252.1

Han, D., Song, X., Currell, M. J., Yang, J., and Xiao, G. (2014). Chemical and isotopic constraints on evolution of groundwater salinization in the coastal plain aquifer of Laizhou Bay, China. *J. Hydrology* 508, 12–27. doi:10.1016/j.jhydrol.2013.10.040

Han, J., Zhou, X., Jiang, C., Hu, L., Fang, B., and Sun, Q. (2013). Hydrochemical characteristics, origin and evolution of the subsurface brines in western Qaidam Basin. *GEOSCIENCE* 27 (6), 1454–1464.

Hemming, N. G., and Hanson, G. N. (1992). Boron isotopic composition and concentration in modern marine carbonates. *Geochimica Cosmochimica Acta* 56 (1), 537–543. doi:10.1016/0016-7037(92)90151-8

Hussain, S. A., Han, F.-Q., Ma, Z., Hussain, A., Mughal, M. S., Han, J., et al. (2021). Unraveling sources and climate conditions prevailing during the deposition of neoproterozoic evaporites using coupled chemistry and boron isotope compositions (δ11B): The example of the salt range, Punjab, Pakistan. *Minerals* 11 (2), 161. doi:10.3390/min11020161

Jolivet, M., Brunel, M., Seward, D., Xu, Z., Yang, J., Malavieille, J., et al. (2003). Neogene extension and volcanism in the Kunlun fault zone, northern tibet: New constraints on the age of the Kunlun fault. *Tectonics* 22 (5), 1428. doi:10.1029/2002TC001428

Kloppmann, W., Négrel, P., Casanova, J., Klinge, H., Schelkes, K., and Guerrot, C. (2001). Halite dissolution derived brines in the vicinity of a Permian salt dome (N German Basin). Evidence from boron, strontium, oxygen, and hydrogen isotopes. *Geochimica Cosmochimica Acta* 65 (22), 4087–4101. doi:10.1016/S0016-7037(01)00640-8

Li, C., Chen, X., Guo, H., Zhou, X., and Cao, J. (2021). Production of potash and N-Mg compound fertilizer via mineral shoenite from Kunteyi Salt Lake: Phase diagrams of quaternary system (NH4) 2SO4-MgSO4-K2SO4-H2O in the isothermal evaporation and crystallization process. *Acta Geol. Sinica-English Ed.* 95 (3), 1016–1023. doi:10.1111/1755-6724.14409

Li, J., Li, T., Ma, H., and Peng, X. (2013a). Investigation of the chemical characteristics and its geological significance of the Tertiary oilfield brine in the Western Qaidam basin. *HYDROGEOLOGY Eng. Geol.* 40 (6), 28–36.

Li, J., Li, T., Ma, Y., and Chen, F. (2022). Distribution and origin of brine-type Li-Rb mineralization in the Qaidam Basin, NW China. *Sci. China Earth Sci.* 65 (3), 477–489. doi:10.1007/s11430-021-9855-6

Li, M. H., Yan, M. D., Wang, Z. R., Liu, X. M., Fang, X. M., and Li, J. (2015). The origins of the mengye potash deposit in the lanping–simao basin, yunnan province, western China. *OreGeology Rev.* 69, 174–186. doi:10.1016/j.oregeorev.2015.02.003

Li, R., Liu, C., Jiao, P., Liu, W., Tang, D., and Wang, S. (2020). The effect of solvent chemistry on potassium dissolution extraction from low-grade solid potash ore in Qarhan Salt Lake, China. *Appl. Geochem.* 115, 104550. doi:10.1016/j.apgeochem.2020.104550

Li, T., Li, J., Ma, H., and Li, B. (2013b). Boron isotope geochemical study on oil-field brine in western Qaidam Basin. *J. Salt Lake Reserch* 21 (2), 1–9.

Li, Y., Li, J., Fan, Q., Wang, M., and Shan, F. (2019). Origin of deep intercrystalline brines from dayantan mine area in Qaidam Basin. *J. Salt Lake Reserch* 27 (1), 82–88.

Liu, J., Chen, Z., Wang, L., Zhang, Y., Li, Z., Xu, J., et al. (2016). Chemical and isotopic constrains on the origin of brine and saline groundwater in Hetao plain, Inner Mongolia. *Environ. Sci. Pollut. Res.* 23 (15), 15003–15014. doi:10.1007/s11356-016-6617-1

Llewellyn, G. T. (2014). Evidence and mechanisms for Appalachian Basin brine migration into shallow aquifers in NE Pennsylvania, USA. *Hydrogeology J.* 22 (5), 1055–1066. doi:10.1007/s10040-014-1125-1

Lu, H., and Xiong, S. (2009). Magnetostratigraphy of the dahonggou section, northern Qaidam Basin and its bearing on cenozoic tectonic evolution of the qilian Shan and Altyn Tagh fault. *Earth Planet. Sci. Lett.* 288 (3-4), 539–550. doi:10.1016/j.epsl.2009.10.016

Lyu, M., Pang, Z., Huang, T., and Yin, L. (2019). Hydrogeochemical evolution and groundwater quality assessment in the dake lake basin, northwest China. *J. Radioanalytical Nucl. Chem.* 320 (3), 865–883. doi:10.1007/s10967-019-06515-8

Qin, X., Ma, H., Zhang, X., Hu, X., Li, G., Jiang, Z., et al. (2021). Origin and evolution of saline spring water in north and Central Laos based on hydrochemistry and stable isotopes (δD, δ18O, δ11B, and δ37Cl). *Water* 13 (24), 3568. doi:10.3390/w13243568

Ren, Q., Du, Y., Gao, D., Lii, B., Zhang, X., Liu, X., et al. (2018). A multi–fluid constrain for the forming of potash deposits in the savannakhet basin: Geochemical evidence from halite. *Acta Geol. Sinica-English Ed.* 92 (2), 755–768. doi:10.1111/1755-6724.13552

Royden, L. H., Burchfiel, B. C., and van der Hilst, R. D. (2008). The geological evolution of the Tibetan Plateau. *Science* 321 (5892), 1054–1058. doi:10.1126/science.1155371

Sun, D., Li, B., Ma, Y., and Liu, Q. (2002). An investigation on evaporating experiments for Qinghai Lake water, China. *J. Salt Lake Res.* 10 (4), 1–12. doi:10.3969/j.issn.1008-858X.2002.04.001

Tan, H., Rao, W., Ma, H., Chen, J., and Li, T. (2011). Hydrogen, oxygen, helium and strontium isotopic constraints on the formation of oilfield waters in the Western Qaidam Basin, China. *J. Asian Earth Sci.* 40 (2), 651–660. doi:10.1016/j.jseaes.2010.10.018

Tapponnier, P., Zhiqin, X., Roger, F., Meyer, B., Arnaud, N., Wittlinger, G., et al. (2001). Oblique stepwise rise and growth of the Tibet Plateau. *Science* 294 (5547), 1671–1677. doi:10.1126/science.105978

Vengosh, A., Chivas, A., Starinsky, A., Kolodny, Y., Baozhen, Z., and Pengxi, Z. (1995). Chemical and boron isotope compositions of non-marine brines from the Qaidam Basin, Qinghai, China. *Chem. Geol.* 120 (1-2), 135–154. doi:10.1016/0009-2541(94)00118-R

Xia, W., Zhang, N., Yuan, X., Fan, L., and Zhang, B. (2001). Cenozoic Qaidam Basin, China: A stronger tectonic inversed, extensional rifted basin. *AAPG Bull.* 85 (4), 715–736. doi:10.1306/8626c98d-173b-11d7-8645000102c1865d

Xiao, Y., Liu, W., Wang, W., and Jin, L. (1999). Boron isotope geochemistry of salt lakes in Qaidam Basin, Qinghai. *Adv. Nat. Sci.* 9 (7), 616–618.

Ye, C., Zheng, M., Wang, Z., Hao, W., Wang, J., Lin, X., et al. (2015). Hydrochemical characteristics and sources of brines in the Gasikule salt lake, Northwest Qaidam Basin, China. *Geochem. J.* 49 (5), 481–494. doi:10.2343/geochemj.2.0372

Yin, A., and Harrison, T. M. (2000). Geologic evolution of the Himalayan-Tibetan orogen. *Annu. Rev. Earth Planet. Sci.* 28 (1), 211–280. doi:10.1146/annurev.earth.28.1.211

Yingkai, X., and Lan, W. (2001). The effect of pH and temperature on the isotopic fractionation of boron between saline brine and sediments. *Chem. Geol.* 171 (3-4), 253–261. doi:10.1016/S0009-2541(00)00251-5

Yu, J., Gao, C., Cheng, A., Liu, Y., Zhang, L., and He, X. (2013). Geomorphic, hydroclimatic and hydrothermal controls on the formation of lithium brine deposits in the Qaidam Basin, northern Tibetan Plateau, China. *Ore Geol. Rev.* 50, 171–183. doi:10.1016/j.oregeorev.2012.11.001

Yuan, X., Meng, F., Zhang, X., Sheng, J., Galamay, A., Cheng, H., et al. (2021). Ore-forming fluid evolution of shallow polyhalite deposits in the Kunteyi playa in the north Qaidam Basin. *Front. Earth Sci.* 727, 698347. doi:10.3389/feart.2021.698347

frontiers | Frontiers in Environmental Science

TYPE Original Research
PUBLISHED 27 March 2023
DOI 10.3389/fenvs.2023.1139237

OPEN ACCESS

EDITED BY
Xiaoning Zhao,
Nanjing University of Information Science and Technology, China

REVIEWED BY
Jing Zhao,
Xiamen University, China
Min Jin,
State Oceanic Administration, China

*CORRESPONDENCE
Rixin Wang,
wrx_zjou@163.com

SPECIALTY SECTION
This article was submitted to Freshwater Science, a section of the journal Frontiers in Environmental Science

RECEIVED 06 January 2023
ACCEPTED 07 February 2023
PUBLISHED 27 March 2023

CITATION
Wang J, Tian C, Wu D and Wang R (2023), Dissolved oxygen shapes the archaeal communities in the seawater of Changjiang Estuary.
Front. Environ. Sci. 11:1139237.
doi: 10.3389/fenvs.2023.1139237

Dissolved oxygen shapes the archaeal communities in the seawater of Changjiang Estuary

Jianxin Wang[1], Chunmiao Tian[2], Dongmei Wu[3] and Rixin Wang[1]*

[1]School of Marine Sciences, Ningbo University, Ningbo, Zhejiang, China, [2]University of Pisa Marine Graduate School, Zhejiang Ocean University, Zhoushan, Zhejiang, China, [3]Leibniz Institute DSMZ-German Collection of Microorganisms and Cell Cultures, Braunschweig, German

Archaea play a significant role in regulating the biogeochemical processes of marine ecosystems. In this study, the high-throughput sequencing was used to explore the archaeal communities in the seawater from the hypoxic and non-hypoxic zones of the Changjiang Estuary. Thaumarchaeota dominated the archaeal communities in the hypoxic zones (bottom water), and Euryarchaeota were mainly distributed in the non-hypoxic zones (surface water). However, the diversity and richness of the archaeal communities showed no obvious difference in the hypoxic and non-hypoxic zones. Moreover, Thaumarchaeota and Nitrosopumilales were positively correlated with salinity, but negatively correlated with dissolved oxygen (DO) and temperature. Temperature, phosphorus, and dissolved oxygen had significant correlations with archaeal richness, while ammonia nitrogen was correlated with archaeal diversity. The networks of archaeal communities possessed a high proportion of positive interspecific interaction and revealed that the Marine Group II species may play distinct roles in both hypoxic and non-hypoxic zones. The current work assessed the influence of dissolved oxygen on the archaeal community patterns and network interaction, thereby illumining the community structure shift of archaea caused by the hypoxia phenomenon in the Changjiang Estuary, which laid a foundation for the future studies on the ecological functions of archaea in estuary ecosystems.

KEYWORDS

archaeal community, Changjiang Estuary, 16S rRNA, dissolved oxygen, network

1 Introduction

Archaea have been confirmed to be abundant in extreme environments and marine ecosystems (Wishner et al., 1995; Massana et al., 2000; Madrid et al., 2001), including the seawater, estuaries, and sediments. Previous studies have reported that archaea could play a key role in cycling nitrogen, sulfur, and carbon (Cornelia et al., 2006; Jingxu et al., 2015). Thaumarchaeota [formerly Marine Group (MG) I] and MG II are the most abundant archaeal groups in the marine ecosystem (Ken et al., 2004; Zhang, 2012), and members of Thaumarchaeota play an important role in aerobic ammonia oxidation (Martin et al., 2005).

The Changjiang Estuary is a complex and dynamic region that interfaces the terrestrial and marine environments. The mixture of freshwater and Taiwan Current makes this area a complex and an ideal region for conducting studies on the microorganism distribution. Hypoxia often occurs near the bottom waters of the Changjiang Estuary and is a common phenomenon observed in many estuaries (Li et al., 2002; Orita et al., 2015). The hypoxia in this region might be caused by the water stratification and the decomposition of organic matter that comes from the upstream sediments and dissolved organic compounds (Huabing et al., 2012). Previous studies

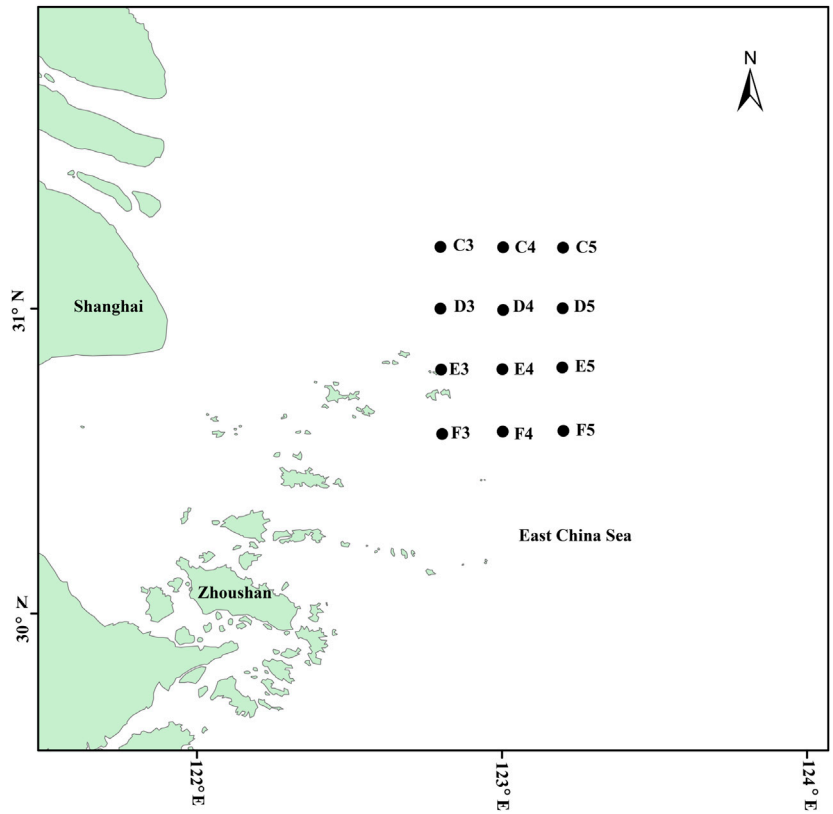

FIGURE 1
Map of the sampling sites in the Changjiang Estuary.

have reported that hypoxia is the most important factor that shapes the bacterial communities (Heike and Osvaldo, 2010; Huabing et al., 2012). However, the response of these archaeal communities to this changing environment remains unclear.

Several studies on the archaeal communities have been conducted in the Changjiang Estuary. Liu et al. (2011) studied the archaeal community in the seawater of the hypoxic zone in Changjiang Estuary, which demonstrated that Euryarchaeota and Crenarchaeota were the predominant phyla and salinity was the major environmental factor that shaped the archaeal community (Liu et al., 2011). Zeng et al. (2007) found that MG I and II were the most abundant groups in the East China Sea (Zeng et al., 2007). A previous study revealed that the ammonia-oxidizing archaea (AOA) community was significantly correlated with nitrite in the Changjiang Estuary (Hui et al., 2014). However, extensive information on the archaeal community in the Changjiang Estuary is lacking, as the relationships between archaeal richness, diversity, and environmental factors remain to be uncovered.

In this study, high-throughput sequencing was used to explore the archaeal community structure and to reveal the influence of dissolved oxygen (DO) on the archaeal community pattern and network interaction in the seawater of Changjiang Estuary. The findings of this study could enhance our understanding of the hypoxia impact on the archaeal community shift in the seawater of the Changjiang Estuary.

2 Materials and methods

2.1 Sampling and locations

In July 2016, water samples were collected using the SBE 32 sampler (Sea-Bird Electronics, United States) from twelve sites of the Changjiang Estuary including hypoxic and non-hypoxic zones (Figure 1). Samples from each site were collected from the surface layers (10 m depth) and bottom layers (40–55 m depth), and six duplicate samples were collected for each depth. Samples were collected for DNA isolation using a vacuum pump suction filter under 20 kPa. One liter of seawater per sample was successively filtered by using the 3- and 0.22-μm pore size polycarbonate nucleopore membranes (Merck Millipore Ltd., United States), and then the membranes were stored in 5-ml sterile cryopreservation tubes at −20°C during the cruise and at −80°C after returning to the laboratory.

2.2 DNA extraction, PCR amplification, and sequencing

The genomic DNA from each water sample was exacted using the FastPrep®-24 rapid nucleic acid extraction kit (MP Biomedicals, United States) according to the manufacturer's instructions. The concentration of purified DNA was measured using Nanodrop 2000

(Thermo, United States). The DNA solution from each duplicate sample was pooled together to avoid the extraction bias. The 16S rRNA genes were amplified using the archaeal primers 515F (5′-GTGCCAGCMGCCGCGG-3′) and 907R (5′-CCGTCAATTCMTTTRAGTTT-3′) (Muyzer et al., 1993). The PCR products were detected by the 1.2% agarose gel electrophoresis and were purified by using the MiniBEST Agarose Gel DNA Extraction Kit Version 4.0 (TaKaRa, Japan) following the manufacturer's instructions. The purity and concentration of the PCR products were determined by Nanodrop 2000 (Thermo, United States). The PCR products were sent to Shanghai Majorbio Bio-pharm Technology Co., Ltd., (China) for the high-throughput sequencing using the Miseq platform (Illumina, United States).

2.3 Measurement of environmental parameters

The environmental parameters, including pH, salinity, DO, temperature, chemical oxygen demand (COD), and concentration of chlorophyll a (Chl a) in the seawater were determined by using an SBE2 sampler (Washington Seabird, United States) *in situ*. The concentrations of nitrite ($N\text{-}NO_2$), nitrate ($N\text{-}NO_3$), and ammonia nitrogen ($N\text{-}NH_4$) in the seawater samples were determined by using the ultraviolet spectrophotometry method (Qin et al., 2022). The concentration of phosphate ($P\text{-}PO_4$) in the samples was measured by using a QuAAtro continuous flow analyzer (SEAL Analytical, Germany) (Wu et al., 2019). The silicate concentration in the seawater were determined by using the method of ion exclusion chromatography with conductivity detection (Li and Chen, 2000).

2.4 Data analysis

The DNA sequences were processed using QIIME, USEARCH, and FLASH software. First, the paired-end reads were combined with FLASH (Hawley et al., 2014). Then, the adapters were trimmed and the low-quality sequences were discarded using QIIME. Chimera sequences were assessed and filtered with USEARCH. Finally, the clean sequences were aligned against the SILVA 132 database and were clustered into operational taxonomic units (OTUs) with 97% sequence identity. In order to assess the archaeal richness and diversity, the Chao1, ACE, Shannon, and Simpson indexes were calculated after normalizing the sequences to 30,125 reads by using QIIME. Principal coordinate analysis (PCoA), clustering analysis, redundancy analysis (RDA), and Mantel test were conducted by using R packages of ape, ggtree, vegan, and linkET, respectively. Variation partition analysis (VPA) was analyzed by using R package of vegan. Networks of archaeal communities were constructed using the Molecular Ecological Network Analyses (MENA) Pipeline with a St value of 0.850 (http://129.15.40.240/mena/) (Deng, 2012). The OTUs with Zi values ≥ 2.5 or Pi values ≥ 0.62 were identified as the keystone taxa (Olesen et al., 2007). The networks were visualized by using Cytoscape (https://cytoscape.org/).

3 Results

3.1 Statistical information of the environmental properties

The environmental factors changed vertically between the hypoxic and non-hypoxic zones (Figure 2). $N\text{-}NO_3$, $N\text{-}NO_2$, $N\text{-}NH_4$, and temperature were significantly higher in the non-hypoxic zones (Student's *t*-test, $p < 0.05$). In contrast, $P\text{-}PO_4$ and salinity were significantly lower in the non-hypoxic zones (Student's *t*-test, $p < 0.05$). The DO was significantly lower in the hypoxic zones (Student's *t*-test, $p < 0.05$). Silicate was not significantly different between the two zones.

3.2 Richness and diversity of archaeal communities

The 24 samples yielded a total of 1,050,783 raw reads. A total of 921,221 clean reads were retained for the downstream analysis. All normalized sequences were grouped into 1,375 OTUs. Samples in hypoxic zones were comprised of 128–241 OTUs, while samples in non-hypoxic zones were comprised of 141–238 OTUs. A total of 234 OTUs were shared between the hypoxic and non-hypoxic zones (Figure 3A). Additionally, 124 OTUs were significantly different between the two zones. Compared to the non-hypoxic zone, 55 OTUs were enriched and 69 OTUs were depleted in the hypoxic zone (Figure 3B). No significant differences were detected in the richness and diversity indexes between the hypoxic and non-hypoxic zones (Student's *t*-test, $p > 0.05$), except for the chao1 index (Student's *t*-test, $p < 0.05$) (Figure 4).

3.3 Archaeal community composition

The results of PCoA and clustering analysis revealed that the samples formed two groups based on the hypoxic and non-hypoxic zones (Figure 5; Supplementary Figure S1A). Hypoxic samples were clearly separated from non-hypoxic samples, indicating that there was a distinct archaeal structure between the two zones. Moreover, archaeal communities were dissimilar between the hypoxic and non-hypoxic zones ($R = 0.993$, $p = 0.001$), where the archaeal communities in the hypoxic zone had a higher similarity composition (Supplementary Figure S1B).

Euryarchaeota was abundant in the non-hypoxic zones, while Thaumarchaeota was prevalent in the hypoxic zones (Figure 6A). Moreover, the two major classes exhibited opposing trends, with MG II and Nitrosopumilales dominating the non-hypoxic and hypoxic zones, respectively (Figure 6B). Further analysis at the phylum and order levels showed that the abundance of the archaeal community was significantly different between the two zones (Supplementary Table S1).

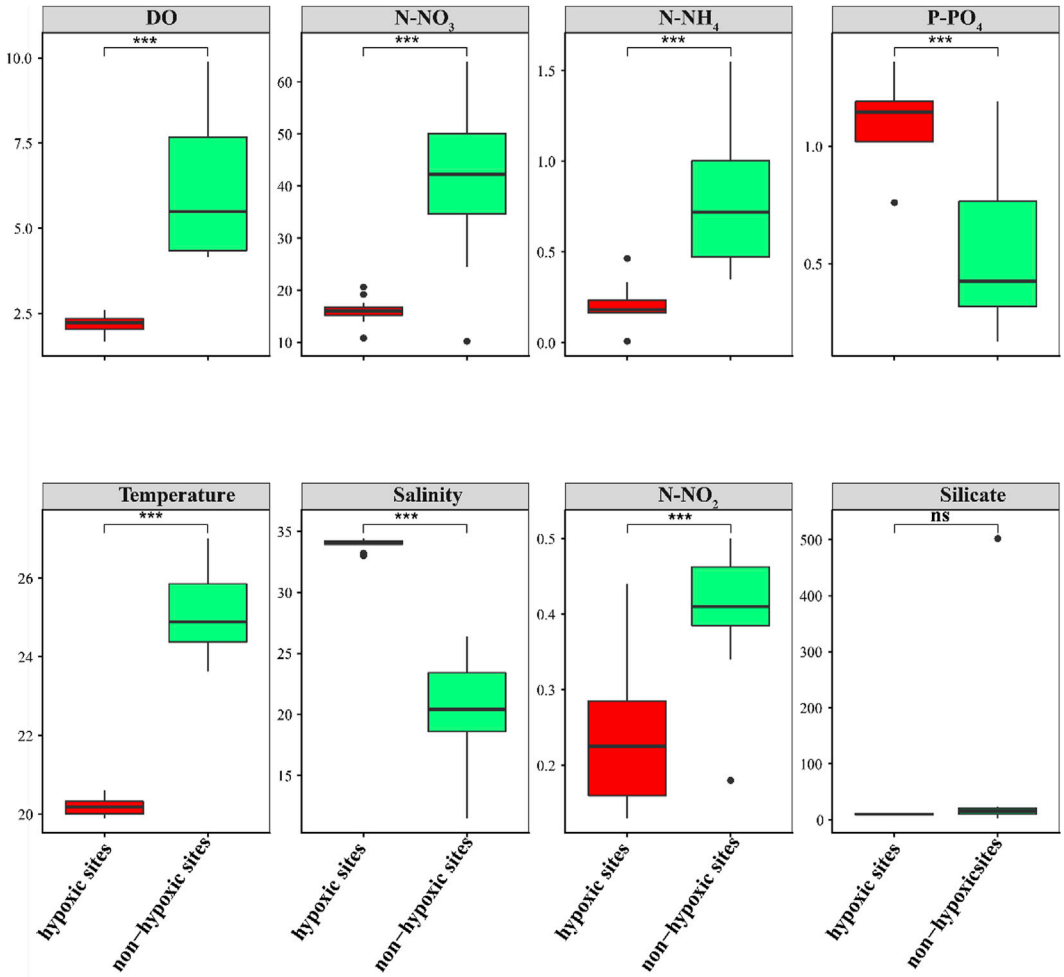

FIGURE 2
Box plots of the environmental factors between the hypoxic and non-hypoxic zones.

3.4 Relationship between local environmental factors and archaeal communities

The archaeal richness was significantly and negatively correlated with DO ($p < 0.05$) and temperature, but was positively correlated with P-PO_4 (Supplementary Figure S2). N-NH_4 and N-NO_3 were positively correlated with the archaeal Simpson indexes, while salinity was negatively correlated with the Simpson indexes. The archaeal Shannon indexes were negatively correlated with N-NH_4 (Supplementary Figure S2). The Mantel test revealed that the environmental factors except silicate significantly influenced the archaeal communities ($p < 0.05$; Figure 7). The RDA result showed that DO ($p = 0.001$), N-NO_3 ($p = 0.001$), N-NH_4 ($p = 0.001$), P-PO4 ($p = 0.001$), temperature ($p = 0.001$), N-NO_2 ($p = 0.001$), and salinity ($p = 0.001$) significantly influenced the archaeal communities (Figure 8A; Table 1). The VPA result indicated that the salinity and temperature accounted for the most archaeal variation in the hypoxic and non-hypoxic zones (Figure 8B). In the hypoxic zone, DO ($p = 0.026$) was the most important factor that shaped the archaeal composition (Supplementary Figure S3; Supplementary Table S2). DO and temperature were negatively correlated with Thaumarchaeota and Nitrosopumilales, but was positively correlated with Euryarchaeota and MG II. Salinity was positively correlated with Thaumarchaeota, Nitrosopumilales, and MG III, but was negatively correlated with MG II and Euryarchaeota. N-NH_4, N-NO_3, and N-NO_2 were positively correlated with Euryarchaeota and MG II, but was negatively correlated with Thaumarchaeota, MG III, and Nitrosopumilales (Supplementary Figure S4).

3.5 Archaeal community networks in the hypoxic and non-hypoxic zones

The archaeal community networks in the hypoxic zones had 108 nodes and 486 edges, while those in the non-hypoxic zones had 105 nodes and 462 edges (Figure 9; Supplementary Table S3). The modularity values of the archaeal networks in hypoxic and non-hypoxic zones were 0.35 and 0.42, respectively (Figure 9; Supplementary Table S3). Both the hypoxic (84%) and non-hypoxic (86%) networks possessed a high proportion of positive correlation for the interspecific interaction of the archaeal

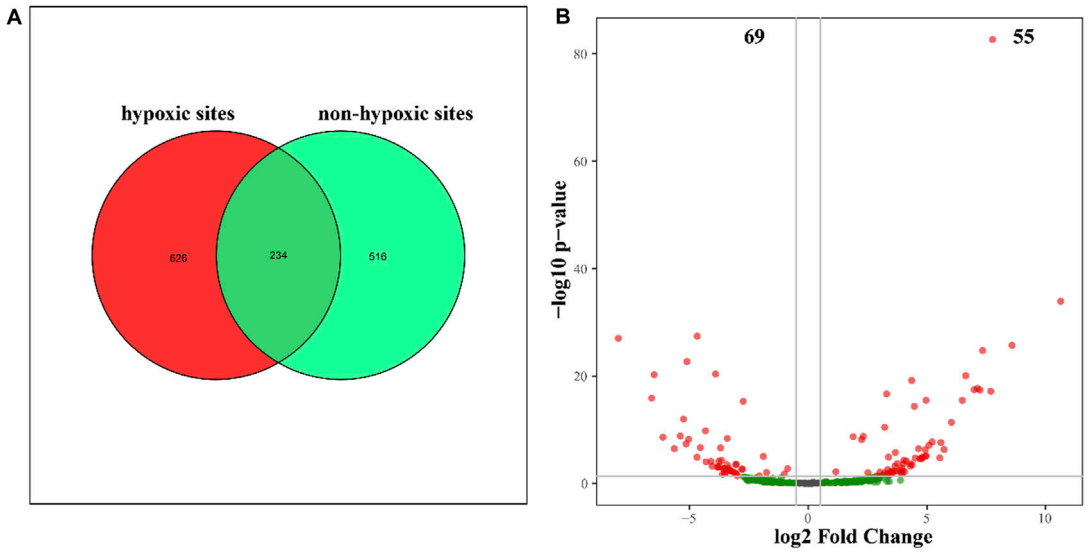

FIGURE 3
Unique and shared OTUs between the hypoxic and non-hypoxic zones. **(A)** Venn diagram showing the OTUs unique to the hypoxic (red) and non-hypoxic (green) zones and the shared OTUs (dark green). **(B)** Volcano plot showing the significant differences between enriched (red) and depleted (green) hypoxic OTUs.

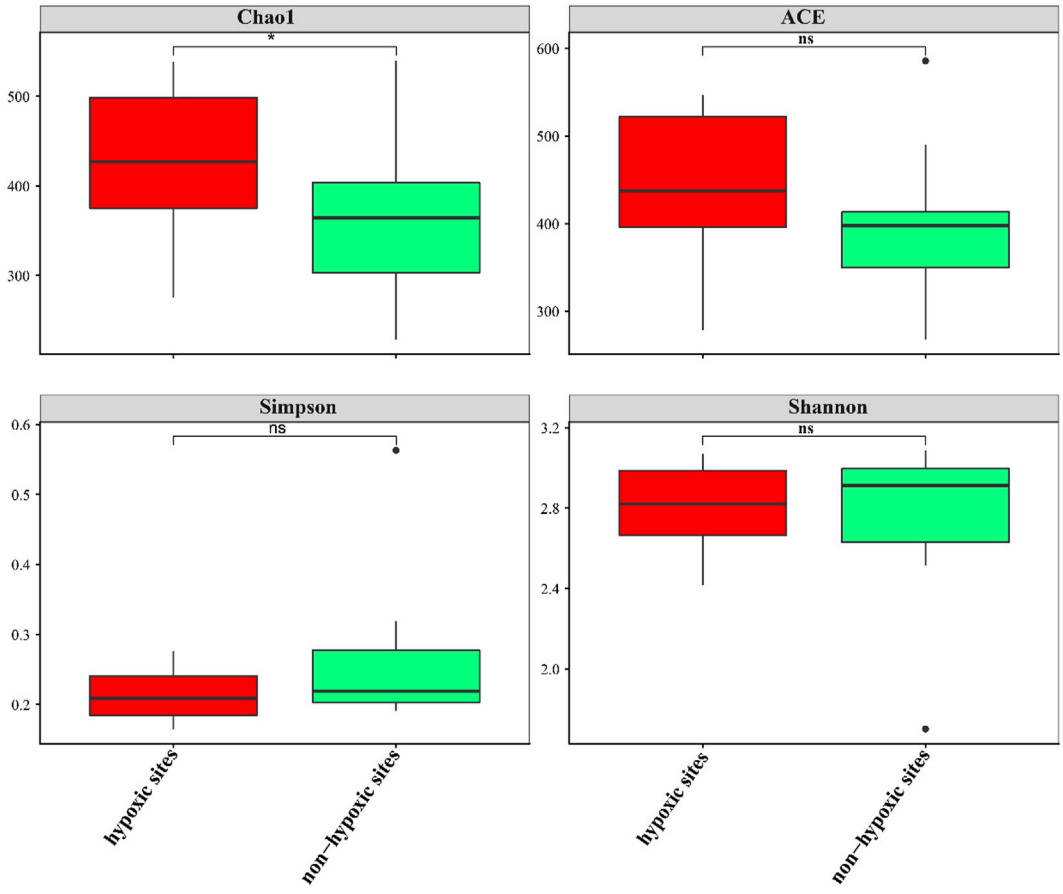

FIGURE 4
Box plots of the alpha diversity of the archaeal communities between the hypoxic and non-hypoxic zones.

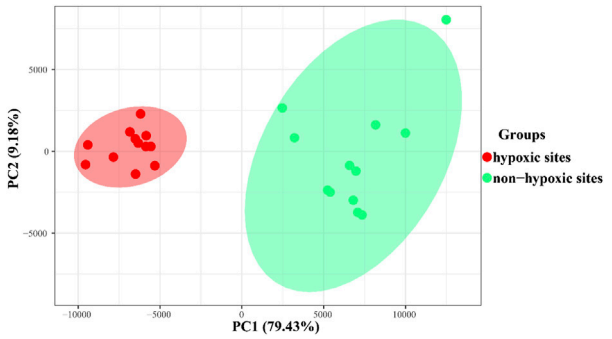

FIGURE 5
PCoA plot showing the archaeal similarities within the hypoxic and non-hypoxic zones and dissimilarities between zones based on Bray-Curtis distances.

communities. The Zi-Pi plot revealed that four module hubs were identified between the two networks (Supplementary Figure S5). No keystone taxa were identified in the archaeal networks from the non-hypoxic samples, and MGII was identified as the keystone taxa in the archaeal networks from the hypoxic samples.

4 Discussion

4.1 Archaeal community richness and diversity in the Changjiang Estuary

Archaeal community richness and diversity in the estuary were previously investigated (Gordon et al., 2015; Jiwen et al., 2015; Liu et al., 2018). Gordon et al. (2015) found that archaeal richness and diversity decreased with the depth (Gordon et al., 2015). However, Jiwen et al. (2015) found that archaeal richness and diversity were not significantly different between the surface and bottom water samples (Jiwen et al., 2015). A separate study on the archaea in the global estuaries found that the archaeal richness and diversity varied with latitude (Liu et al., 2018). Previous studies have investigated archaeal richness and diversity in the Changjiang Estuary (Zeng et al., 2007; Liu et al., 2011; Hui et al., 2014). However, there is limited knowledge on the environmental factors that influence archaeal richness and diversity in the Changjiang Estuary to date. In this study, high-throughput sequencing was used to compare the archaeal communities of the hypoxic and non-hypoxic zones. Compared to a previous study (Zeng et al., 2007), the Shannon and Simpson indexes of the archaea in this study were considerably higher, which may be due to the different sequencing methods. Zeng et al. (2007) used PCR-restriction fragment length polymorphism to examine the archaeal community pattern in the Changjiang Estuary. However, high-throughput sequencing, as used in this study, can detect more phyla than traditional tools. Additionally, the archaeal richness in the hypoxic zone was slightly higher than that in the non-hypoxic zone. In our previous study, the bacterial richness was significantly higher in the hypoxic zone than in the non-hypoxic zone (Wu et al., 2019). Clearly, both bacterial and archaeal richness were higher in the hypoxic zone. Furthermore, archaeal richness was not significantly different between the hypoxic and non-hypoxic

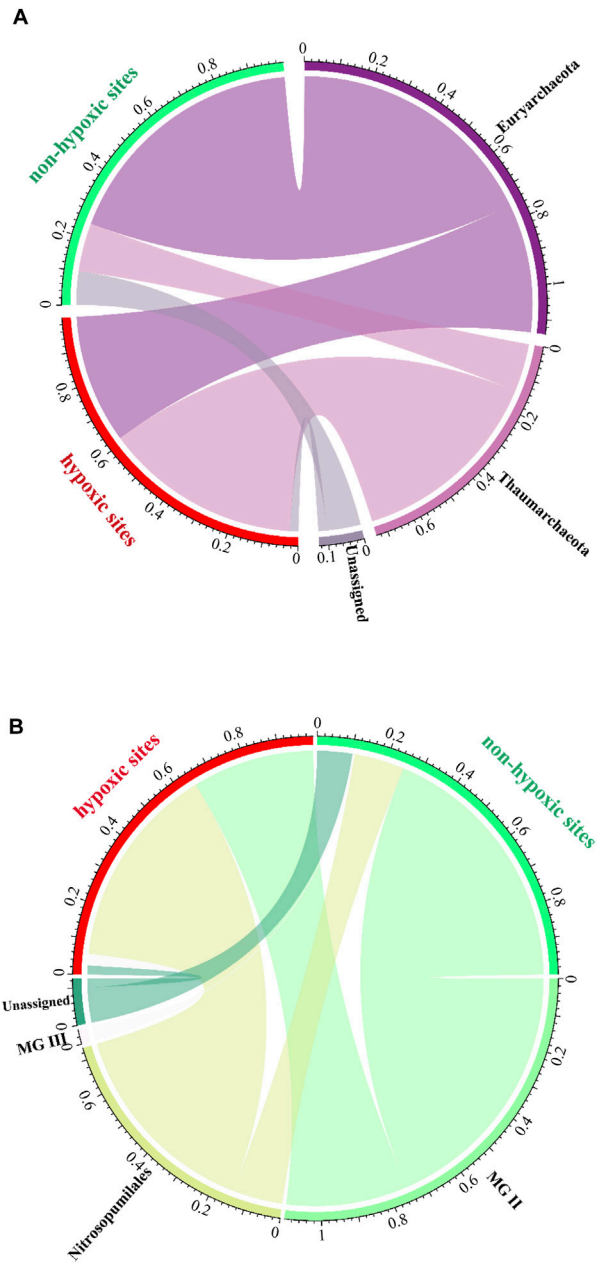

FIGURE 6
Archaeal community composition of the hypoxic and non-hypoxic zones at the phylum **(A)** and order **(B)** levels.

zones (Student's *t*-test, $p > 0.05$). This is in agreement with the findings of a previous study (Gillies et al., 2015). The Spearman correlation analysis indicated that archaeal richness exhibited a positive correlation with $P\text{-}PO_4$, but was significantly and negatively correlated with DO. This suggests that the archaeal richness in the Changjiang Estuary was greatly impacted by DO. Furthermore, the Simpson index was positively correlated with $N\text{-}NH_4$ and $N\text{-}NO_3$, while the Shannon index was negatively correlated with $N\text{-}NH_4$, indicating that nutrient concentrations may be important factors that influenced archaeal diversity in the Changjiang Estuary.

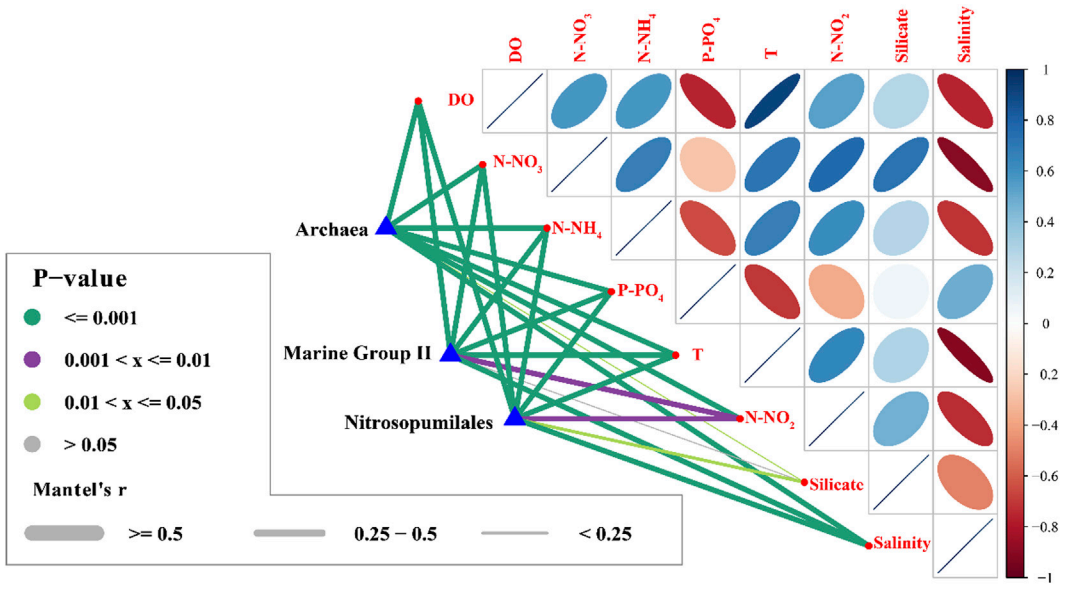

FIGURE 7
Mantel test showing the relationship between environmental factors and major archaea.

4.2 Archaeal community structure in the Changjiang Estuary

The temporal and spatial changes of the archaeal community structure in many marine ecosystems and lakes have been well-documented (Massana et al., 2000; Church et al., 2003; Jiang et al., 2009; Meyerhof, 2011; Yan et al., 2015). The PCoA and clustering analysis revealed that the archaeal community between the hypoxic and non-hypoxic zones was different. Furthermore, samples from the hypoxic zone possessed a similar archaeal community structure. Liu et al. (2015) studied shifts in archaea plankton community structure in the Pearl Estuary and found that the archaeal community in the hypoxic and non-hypoxic sites grouped together (Jiwen et al., 2015). A separate study found that the archaeal community structure in hypoxic samples was distinct from non-hypoxic samples (Gillies et al., 2015). A remarkable difference in bacterial community structure between the hypoxic and non-hypoxic zones has also been observed (Wu et al., 2019), indicating that specific bacterial and archaeal community structures exist in the hypoxic and non-hypoxic zones of the Changjiang Estuary.

Currently, the relationship between the archaeal community structure and environmental factors is not well understood. A previous study indicated that temperature, nutrients, and DO may have an effect on archaeal communities in the seawater. In this study, the RDA and Mantel test revealed that salinity, DO, and nutrient content significantly influenced the archaeal community in the Changjiang Estuary. VPA indicated that temperature and salinity were the major environmental factors that shaped the archaeal community, which is consistent with a previous study that found that salinity had a significant effect on the archaeal community in the Changjiang Estuary (Liu et al., 2011). Hongyue et al., 2008 also reported that AOA significantly correlated with salinity in the sediments of the Changjiang Estuary. Liu et al. (2011) pointed out that this may be caused by the freshwater of the Changjiang River. Furthermore, DO was the most influential environmental factor that shaped the archaeal community in the hypoxic zone ($p = 0.024$). In contrast, Liu et al. (2011) found that DO had no significant influence on the archaeal community in the Changjiang Estuary, and samples from the hypoxic area did not group together. Therefore, we speculated that the different sampling sites and time may result in different findings.

In this study, Euryarchaeota (57.0%) and Thaumarchaeota (36.6%) dominated both the hypoxic and non-hypoxic zones. This is consistent with the findings of previous studies, which indicated that Thaumarchaeota and Euryarchaeota were the two major phyla in the estuaries (Liu et al., 2011; Yan et al., 2015) and marine system (Liu et al., 2011). In this study, Euryarchaeota abundance was significantly higher in the non-hypoxic zones, while Thaumarchaeota dominated the hypoxic zone samples. At the order level, Nitrosopumilales (36.6%) and MG II (55%) were the predominant groups, which is in agreement with previous studies (Zeng et al., 2007; Liu et al., 2011). In this study, MG III was also detected with a low proportion (2%). MG III was reported to be distantly related to Thermoplasmales (López-Garcı´;A et al., 2001). Quaiser et al. (2013) pointed out that MG III is usually detected in deep waters. This is in agreement with our study that MGIII was found with significantly higher abundance in bottom waters (Student's t-test, $p < 0.05$).

Only a small proportion of OTUs was shared between the archaeal communities in the hypoxic and non-hypoxic zones, and 55 OTUs were significantly enriched in the hypoxic zones. These results further confirmed that the hypoxic and non-hypoxic habitats differed remarkably in terms of their archaeal community structure. However, the knowledge on how environmental factors influence phyla in these zones is still limited.

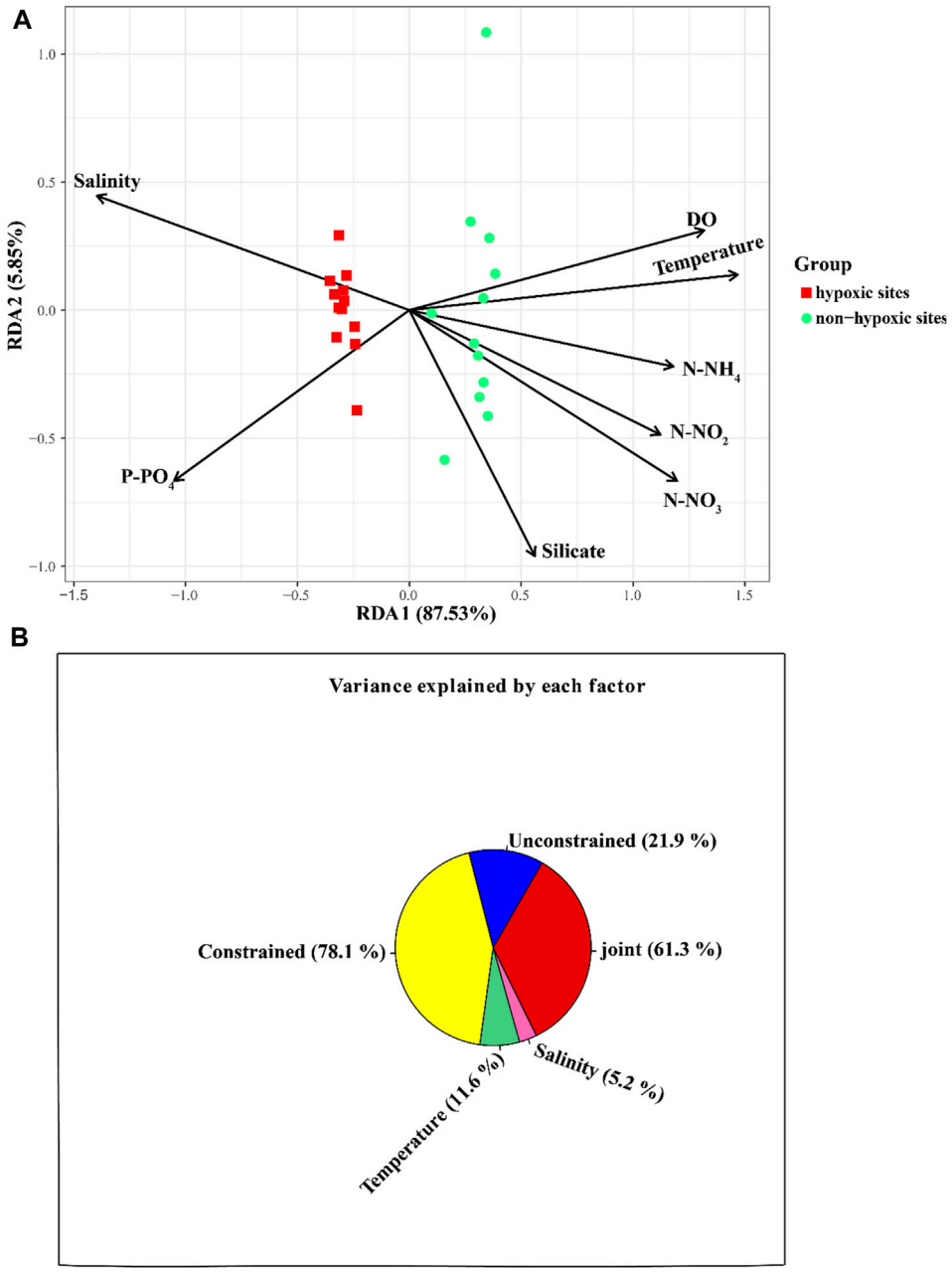

FIGURE 8
Relationship between environmental factors and archaeal community at the OTU level. **(A)** RDA showing the relationship between environmental variables and archaeal community in the Changjiang Estuary. **(B)** VPA analysis for contribution of environmental factors to archaeal composition.

In this study, spearman correlation analysis indicated that Euryarchaeota positively correlated with DO, $N\text{-}NO_2$, $N\text{-}NO_3$, and $N\text{-}NH_4$ but negatively correlated with $P\text{-}PO_4$ and salinity. Thaumarchaeota was positively correlated with $P\text{-}PO_4$ and salinity, but was negatively correlated with $N\text{-}NO_2$, $N\text{-}NO_3$, $N\text{-}NH_4$, and DO. Gillies et al. (2015) also found that Thaumarchaeota was negatively correlated with DO (R = −0.061) but was positively correlated with $P\text{-}PO_4$ (R = 0.75). These findings are logical, considering previous studies have reported that Thaumarchaeota plays a key role in the nitrogen cycle (Schleper and Nicol, 2010; Walker et al., 2010).

Nitrosopumilales was an isolated culture of AOA (Kirchman et al., 2005). In this study, Nitrosopumilales was abundant in the Changjiang Estuary and was abundant in the hypoxic zone. Thus, we speculated that the high proportions of Thaumarchaeota and Nitrosopumilales may play important roles in the nitrification process of the hypoxic zone in the Changjiang Estuary. However, this hypothesis requires further investigation by analyzing the abundance of AOA or amoA genes in the area.

MG II was significantly abundant in the non-hypoxic zone (surface water). This mathed the findings of previous studies that found that MG II was prevalent in surface waters (Rinke et al.;

TABLE 1 RDA results for the Changjiang Estuary.

Environmental factor	RDA1	RDA2	r^2	*p*-value
DO	0.98269	0.18525	0.7769	0.001**
$N\text{-}NO_3$	−0.87730	−0.45358	0.7996	0.001**
$N\text{-}NO_2$	0.92814	−0.37224	0.6417	0.001***
$P\text{-}PO_4$	−0.87730	−0.47994	0.6315	0.001***
$N\text{-}NH_4$	0.98313	−0.18289	0.6219	0.001***
Temperature	0.99807	0.06203	0.9309	0.001***
Salinity	−0.95716	0.28957	0.9257	0.002***
Silicate	0.55943	−0.82888	0.4965	0.001***

Number of permutations: 999. The symbol "***" means the *p* values ≤ 0.01.

deep waters (Liu et al., 2017). In this study, MG II was positively correlated with DO and nutrient levels, but was negatively correlated with salinity. Additionally, the spearman correlation analysis indicated that DO, nutrient levels, and salinity may be the key environmental factors that shaped the archaeal community in the Changjiang Estuary, which was also supported by the RDA results.

4.3 Network analysis in the hypoxic zones and non-hypoxic zones

In this study, the archaeal community networks in the hypoxic and non-hypoxic zones were similar in size, and the higher positive correlation in the networks indicated that there was less competition among the archaeal species from the hypoxic and non-hypoxic

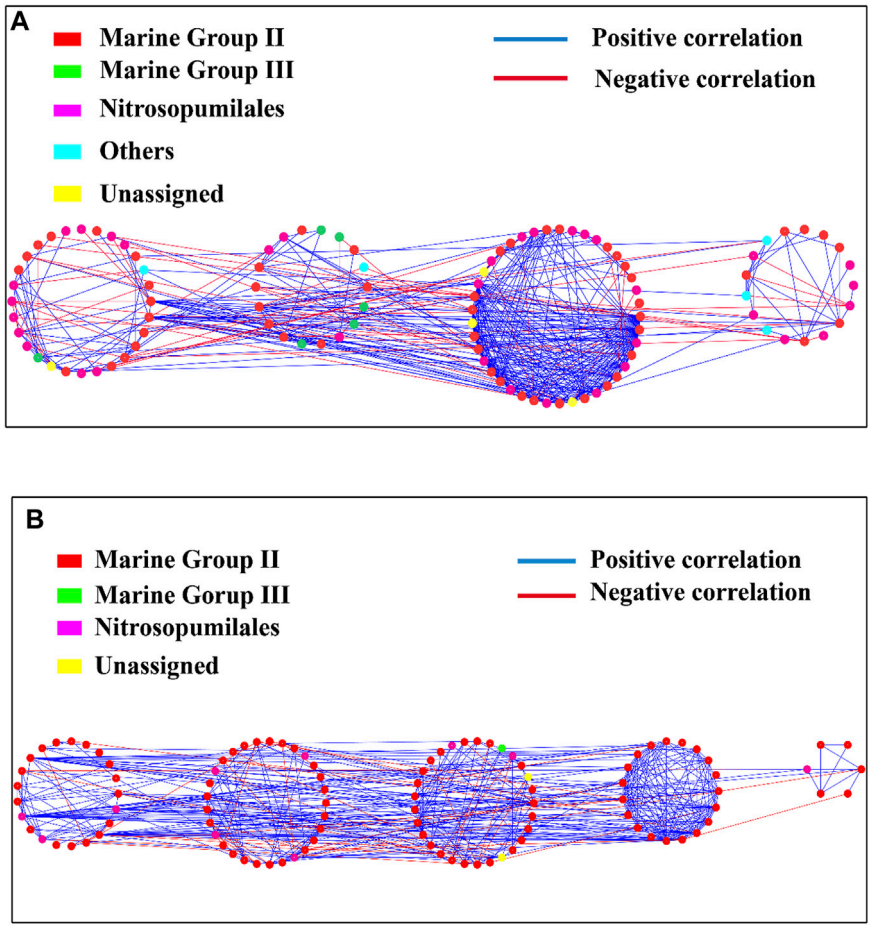

FIGURE 9
Network of archaeal communities in the hypoxic **(A)** and non-hypoxic zones **(B)**.

Massana et al., 2000; Jiwen et al., 2015). Tseng et al. (2015) also found that MG II was predominant in the surface waters of the South China Sea (Tseng et al., 2015). Moreover, a previous study reported that MG II had the ability to degrade protein and lipids (Jia et al., 2012). Liu et al. (2017) also observed that MG II dominated surface waters, while Thaumarchaeota was mainly distributed in zones. In our previous study, bacteria in the hypoxic zone experienced more competition than in the non-hypoxic zone (Wu et al., 2019). Clearly, archaea and bacteria respond differently to hypoxia.

The community networks are considered modular when the modularity values are >0.4 (Newman, 2006). The modularity value

of the archaeal community network in the non-hypoxic zone was 0.42, which revealed that the non-hypoxic network was modular. Additionally, the number of modules, clustering coefficient, and network centralization values were 4, 0.346, and 0.229 in the hypoxic network and 5, 0.380, and 0.237 in the non-hypoxic network, respectively. Zi and Pi were described previously (Olesen et al., 2007) and were used to describe a node that connects to other nodes or modules. Thus, Zi and Pi divided the OTUs into four categories: module hubs, peripherals, network hubs, and connectors, which was important for microorganisms (Chen et al., 2018). In ecology, generalists play key roles in promoting the exchange of energy and nutrients, as well as in maintaining the balance of microbial communities (Chen et al., 2018). In this study, both the hypoxic and non-hypoxic networks had no network hubs, indicating that there was no node with many links within its modules and other modules. Only five generalists were found in the hypoxic zone, while thirteen generalists were found in the non-hypoxic zone. Therefore, we speculated that the archaeal community in the non-hypoxic zone was more stable and ordered than that in the hypoxic zone.

Interestingly, OTU 41 was a generalist in the hypoxic network, but a specialist in the non-hypoxic network. Moreover, the generalists OTUs (OTU 406 and OTU 1173) in the non-hypoxic network were specialists in the hypoxic network. OTU 406 and OTU 1173 belonged to MG II. As generalist in the non-hypoxic network, MG II played key roles in connecting other archaea and forming a stable ecological system in the non-hypoxic zone. However, as specialist in the hypoxic network, MG II was rarely connected other archaea. These results suggest these OTUs exhibit role-shifts. A previous study also reported that the same bacteria could serve different functions under two different environments (Chen et al., 2018). Most generalists in the hypoxic and non-hypoxic networks belonged to MG II, indicating that MG II plays a significant role in exchanging energy, metabolites, and nutrients, as well as maintaining the balance of the microbial community in the Changjiang Estuary.

5 Conclusion

There was a distinct archaeal communities' pattern between the hypoxic and non-hypoxic zones in the seawater of the Changjiang Estuary. RDA results showed that temperature and salinity were the major environmental factors that shaped the archaeal communities in the seawater of the Changjiang Estuary. The archaeal richness was significantly influenced by DO, while archaeal diversity was influenced by nutrient levels, and MG II displayed different functions in the hypoxic and non-hypoxic zones. All of these can enhance our understanding of archaeal communities in the seawater of the Changjiang Estuary.

Data availability statement

The datasets presented in this study can be found in online repositories. The names of the repository/repositories and accession number(s) can be found in the article/Supplementary Material.

Author contributions

RW designed this work. CT, DW, and RW revised the manuscript; JW collected the samples, performed the experiments, and wrote this paper.

Funding

This work was supported by National Key R&D Program of China (2019YFD0901305) and the Fundamental Research Fund for the Provincial Universities of Zhejiang (2021JD003).

Conflict of interest

The authors declare that the research was conducted in the absence of any commercial or financial relationships that could be construed as a potential conflict of interest.

Publisher's note

Supplementary material

The Supplementary Material for this article can be found online at: https://www.frontiersin.org/articles/10.3389/fenvs.2023.1139237/full#supplementary-material

References

Chen, S., Qi, G., Luo, T., Zhang, H., Jiang, Q., Wang, R., et al. (2018). Continuous-cropping tobacco caused variance of chemical properties and structure of bacterial network in soils. *Land Degrad. Dev.* 29 (11), 4106–4120. doi:10.1002/ldr.3167

Church, M. J., DeLong, E. F., Ducklow, H. W., Karner, M. B., Preston, C. M., Karl, D., et al. (2003). Abundance and distribution of planktonic archaea and bacteria in the waters west of the Antarctic Peninsula. *Limnol. Oceanogr.* 48 (5), 1893–1902. doi:10.4319/lo.2003.48.5.1893

Cornelia, W., Ben, A., Coolen, M. J. L., Lydie, H., Judith, V. B., Peer, T., et al. (2006). Archaeal nitrification in the ocean. *Proc. Natl. Acad. Sci.* 103 (33), 12317–12322. doi:10.1073/pnas.0600756103

Deng, Y., Jiang, Y. H., Yang, Y., He, Z., Luo, F., and Zhou, J. (2012). Molecular ecological network analyses. *BMC Bioinforma.* 13 (1), 113. doi:10.1186/1471-2105-13-113

Gillies, L. E., Thrash, J. C., Derada, S., Rabalais, N. N., and Mason, O. (2015). Archaeal enrichment in the hypoxic zone in the northern Gulf of Mexico. *Environ. Microbiol.* 17 (10), 3847–3856. doi:10.1111/1462-2920.12853

Gordon, W., O'Sullivan, L. A., Yiyu, M., Williams, A. S., Sass, A. M., Watkins, A. J., et al. (2015). Archaeal community diversity and abundance changes along a natural salinity gradient in estuarine sediments. *FEMS Microbiol. Ecol.* 91 (2), 1–18. doi:10.1093/femsec/fiu025

Hawley, E. R., Malfatti, S. A., Pagani, I., Huntemann, M., Chen, A., Foster, B., et al. (2014). Metagenomes from two microbial consortia associated with Santa Barbara seep oil. *Mar. Genomics* 18, 97–99. doi:10.1016/j.margen.2014.06.003

Heike, S., and Osvaldo, U. (2010). Bacterial diversity in the oxygen minimum zone of the eastern tropical South Pacific. *Environ. Microbiol.* 10 (5), 1244–1259. doi:10.1111/j.1462-2920.2007.01539.x

Hongyue, D., Xiaoxia, Z., Jin, S., Tiegang, L., Zhinan, Z., and Guanpin, Y. J. M. (2008). Diversity and spatial distribution of sediment ammonia-oxidizing crenarchaeota in response to estuarine and environmental gradients in the Changjiang Estuary and East China Sea. *Microbiology* 154 (7), 2084–2095. doi:10.1099/mic.0.2007/013581-0

Huabing, L., Peng, X., and Wu, Q. L. (2012). Characterization of the bacterial community composition in a hypoxic zone induced by Microcystis blooms in Lake Taihu, China. *FEMS Microbiol. Ecol.* 79 (3), 773–784. doi:10.1111/j.1574-6941.2011.01262.x

Hui, H., Yu, Z., Mi, T., and Yu, Z. (2014). Community composition and abundance of ammonia-oxidizing archaea in sediments from the Changjiang Estuary and its adjacent area in the East China Sea. *Geomicrobiol. J.* 33 (5), 416–425. doi:10.1080/01490451.2014.986695

Jia, G., Zhang, J., Chen, J., Peng, P. A., and Zhang, L. (2012). Archaeal tetraether lipids record subsurface water temperature in the South China Sea. *Org. Geochem.* 50 (50), 68–77. doi:10.1016/j.orggeochem.2012.07.002

Jiang, H., Dong, H., Deng, S., Yu, B., Huang, Q., and Wu, Q. (2009). Response of archaeal community structure to environmental changes in lakes on the Tibetan Plateau, Northwestern China. *Geomicrobiol. J.* 26 (4), 289–297. doi:10.1080/01490450902892662

Jingxu, Z., Yuyin, Y., Lei, Z., Yuzhao, L., Shuguang, X., Yong, L., et al. (2015). Distribution of sediment bacterial and archaeal communities in plateau freshwater lakes. *Appl. Microbiol. Biotechnol.* 99 (7), 3291–3302. doi:10.1007/s00253-014-6262-x

Jiwen, L., Shaolan, Y., Meixun, Z., Biyan, H., and Xiao-Hua, Z. (2015). Shifts in archaeaplankton community structure along ecological gradients of Pearl Estuary. *FEMS Microbiol. Ecol.* 90 (2), 424–435. doi:10.1111/1574-6941.12404

Ken, T., Hanako, O., Yohey, S., Hisako, H., Satoshi, N., Takuro, N., et al. (2004). Spatial distribution of marine crenarchaeota group I in the vicinity of deep-sea hydrothermal systems. *Appl. Environ. Microbiol.* 70 (4), 2404–2413. doi:10.1128/aem.70.4.2404-2413.2004

Kirchman, D., Dittel, A., Malmstrom, R. R., and Cottrell, M. T. (2005). Biogeography of major bacterial groups in the Delaware Estuary. *Limnol. Oceanogr.* 50, 1697–1706. doi:10.4319/lo.2005.50.5.1697

Li, D., Zhang, J., Huang, D., Wu, Y., and Liang, J. (2002). Oxygen depletion off the Changjiang (yangtze river) estuary. *Sci. China Ser. D Earth Sci.* 45 (12), 1137–1146. doi:10.1360/02yd9110

Li, H. B., and Chen, F. (2000). Determination of silicate in water by ion exclusion chromatography with conductivity detection. *J. Chromatogr. A* 874 (1), 143–147. doi:10.1016/s0021-9673(00)00078-9

Liu, H., Zhang, C. L., Yang, C., Chen, S., Cao, Z., Zhang, Z., et al. (2017). Marine group II dominates planktonic archaea in water column of the Northeastern South China Sea. *Front. Microbiol.* 8, 1098. doi:10.3389/fmicb.2017.01098

Liu, M., Xiao, T., Wu, Y., Zhou, F., and Zhang, W. (2011). Temporal distribution of the archaeal community in the Changjiang Estuary hypoxia area and the adjacent East China Sea as determined by denaturing gradient gel electrophoresis and multivariate analysis. *Can. J. Microbiol.* 57 (6), 504–513. doi:10.1139/w11-037

Liu, X., Pan, J., Liu, Y., Li, M., and Gu, J. (2018). Diversity and distribution of Archaea in global estuarine ecosystems. *Sci. Total Environ.* 637, 349–358. doi:10.1016/j.scitotenv.2018.05.016

López-Garcı´A, P., López-López, A., Moreira, D., and Rodrı´Guez-Valera, F. (2001). Diversity of free-living prokaryotes from a deep-sea site at the Antarctic Polar Front. *FEMS Microbiol. Ecol.* 36 (2), 193–202. doi:10.1016/s0168-6496(01)00133-7

Madrid, V. M., Taylor, G. T., Scranton, M. I., and Chistoserdov, A. Y. (2001). Phylogenetic diversity of bacterial and archaeal communities in the anoxic zone of the Cariaco Basin. *Appl. Environ. Microbiol.* 67 (4), 1663–1674. doi:10.1128/aem.67.4.1663-1674.2001

Martin, K. N., Bernhard, A. E., Torre, J. R., de la Torre, J. R., Walker, C. B., Waterbury, J. B., et al. (2005). Isolation of an autotrophic ammonia-oxidizing marine archaeon. *Nature* 437 (7058), 543–546. doi:10.1038/nature03911

Massana, R., Delong, E. F., and Pedrós-Alió, C. (2000). A few cosmopolitan phylotypes dominate planktonic archaeal assemblages in widely different oceanic provinces. *Appl. Environ. Microbiol.* 66 (5), 1777–1787. doi:10.1128/aem.66.5.1777-1787.2000

Meyerhof, M. (2011) ProQuest ID: 2011_mmeyerhof. Diversity and distribution of archaea and bacteria in marine lakes, palauMerced, CA, USA: UC Merced.

Muyzer, G., de Waal, E. C., and Uitterlinden, A. G. (1993). Profiling of complex microbial populations by denaturing gradient gel electrophoresis analysis of polymerase chain reaction-amplified genes coding for 16S rRNA. *Appl. Environ. Microbiol.* 59 (3), 695–700. doi:10.1128/aem.59.3.695-700.1993

Newman, M. (2006). Modularity and community structure in networks. *Proc. Natl. Acad. Sci.* 103 (23), 8577–8582. doi:10.1073/pnas.0601602103

Olesen, J. M., Jordi, B., Dupont, Y. L., and Pedro, J. (2007). The modularity of pollination networks. *Proc. Natl. Acad. Sci.* 104 (50), 19891–19896. doi:10.1073/pnas.0706375104

Orita, R., Umehara, A., Komorita, T., Choi, J. W., Montani, S., Komatsu, T., et al. (2015). Contribution of the development of the stratification of water to the expansion of dead zone: A sedimentological approach. *Estuar. Coast. Shelf Sci.* 164 (2), 204–213. doi:10.1016/j.ecss.2015.07.028

Qin, J., Wu, K., Chen, L., Wang, X., Zhao, Q., Liu, B., et al. (2022). Achieving high selectivity for nitrate electrochemical reduction to ammonia over MOF-supported Ru_xO_y clusters. *J. Mater. Chem. A* 10 (8), 3963–3969. doi:10.1039/d1ta09441f

Quaiser, A., Zivanovic, Y., Moreira, D., and López-García, P. (2013). Comparative metagenomics of bathypelagic plankton and bottom sediment from the sea of Marmara. *ISME J.* 5 (2), 285–304. doi:10.1038/ismej.2010.113

Rinke, C., Rubino, F., Messer, L. F., Youssef, N., Parks, D. H., Chuvochina, M., et al. (2019). A phylogenomic and ecological analysis of the globally abundant Marine Group II archaea (Ca. Poseidoniales ord. nov.). *ISME J.* 13 (3), 663–675. doi:10.1038/s41396-018-0282-y

Schleper, C., and Nicol, G. (2010). Ammonia-oxidising archaea-physiology, ecology and evolution. *Adv. Microb. Physiology* 57, 1–41. doi:10.1016/B978-0-12-381045-8.00001-1

Tseng, C. H., Chiang, P. W., Lai, H. C., Shiah, F. K., Hsu, T. C., Chen, Y. L., et al. (2015). Prokaryotic assemblages and metagenomes in pelagic zones of the South China Sea. *BMC Genomics* 16 (1), 1–16. doi:10.1186/s12864-015-1434-3

Walker, C. B., de la Torre, J. R., Klotz, M. G., Urakawa, H., Pinel, N., Arp, D. J., et al. (2010). Nitrosopumilus maritimus genome reveals unique mechanisms for nitrification and autotrophy in globally distributed marine crenarchaea. *Proc. Natl. Acad. Sci.* 107 (19), 8818–8823. doi:10.1073/pnas.0913533107

Wishner, K. F., Ashjian, C. J., Gelfman, C., Gowing, M. M., Kann, L., Levin, L. A., et al. (1995). Pelagic and benthic ecology of the lower interface of the Eastern Tropical Pacific oxygen minimum zone. *Deep Sea Res. Part I Oceanogr. Res. Pap.* 42 (1), 93–115. doi:10.1016/0967-0637(94)00021-j

Wu, D. M., Dai, Q. P., Liu, X. Z., Fan, Y. P., and Wang, J. X. (2019). Comparison of bacterial community structure and potential functions in hypoxic and non-hypoxic zones of the Changjiang Estuary. *PloS one* 14 (6), e0217431. doi:10.1371/journal.pone.0217431

Yan, L., Liu, Q., Li, C., Yi, D., Zhang, W., Zhang, W., et al. (2015). Bacterial and archaeal community structures in the Arctic deep-sea sediment. *Acta Oceanol. Sin.* 34 (2), 93–113. doi:10.1007/s13131-015-0624-9

Zeng, Y., Li, H., and Jiao, N. (2007). Phylogenetic diversity of planktonic archaea in the estuarine region of East China Sea. *Microbiol. Res.* 162 (1), 26–36. doi:10.1016/j.micres.2006.03.007

Zhang, L., and He, J. (2012). A novel archaeal phylum: Thaumarchaeota-A review. *Acta Microbiol. Sin.* 52 (4), 411–421. doi:10.13343/j.cnki.wsxb.2012.04.015

frontiers | Frontiers in Environmental Science

TYPE Original Research
PUBLISHED 03 October 2023
DOI 10.3389/fenvs.2023.1230778

OPEN ACCESS

EDITED BY
Biyun Guo,
Zhejiang Ocean University, China

REVIEWED BY
Shaohua Lei,
Nanjing Hydraulic Research Institute, China
Donghui Zhang,
China Academy of Space Technology (CAST), China

*CORRESPONDENCE
Qi Lang,
langqi1988@163.com

†These authors share first authorship

RECEIVED 29 May 2023
ACCEPTED 21 September 2023
PUBLISHED 03 October 2023

CITATION
Shi K, Lang Q, Wang P, Yang W, Chen G, Yin H, Zhang Q, Li W and Wang H (2023), Dissolved oxygen concentration inversion based on Himawari-8 data and deep learning: a case study of lake Taihu. *Front. Environ. Sci.* 11:1230778. doi: 10.3389/fenvs.2023.1230778

Dissolved oxygen concentration inversion based on Himawari-8 data and deep learning: a case study of lake Taihu

Kaifang Shi[1†], Qi Lang[2*], Peng Wang[3], Wenhao Yang[4], Guoxin Chen[1], Hang Yin[3], Qian Zhang[3], Wei Li[5] and Haozhi Wang[3]

[1]State Key Laboratory of Plateau Ecology and Agriculture, Qinghai University, Xining, China, [2]Chinese Research Academy of Environmental Sciences, Beijing, China, [3]College of Water Conservancy and Civil Engineering, Shandong Agricultural University, Taian, China, [4]School of Computer and Cyberspace Security, Hebei Normal University, Shijiazhuang, China, [5]Government Service Center of Beijing Municipal Water Bureau, Beijing, China

Dissolved Oxygen (DO) concentration is an essential water quality parameter widely used in water environments and pollution assessments, which indirectly reflects the pollution level and the occurrence of blue-green algae. With the advancement of satellite technology, the use of remote sensing techniques to estimate DO concentration has become a crucial means of water quality monitoring. In this study, we propose a novel model for DO concentration estimation in water bodies, termed Dissolved Oxygen Multimodal Deep Neural Network (DO-MDNN), which utilizes synchronous satellite remote sensing data for real-time DO concentration inversion. Using Lake Taihu as a case study, we validate the DO-MDNN model using Himawari-8 (H8) satellite imagery as input data and actual DO concentration in Lake Taihu as output data. The research results demonstrate that the DO-MDNN model exhibits high accuracy and stability in DO concentration inversion. For Lake Taihu, the performance metrics including adj_R^2, RMSE, Pbias, and SMAPE are 0.77, 0.66 mg/L, −0.44%, and 5.36%, respectively. Compared to the average performance of other machine learning models, the adj_R^2 shows an improvement of 6.40%, RMSE is reduced by 8.27%, and SMAPE is decreased by 12.1%. These findings highlight the operational feasibility of real-time DO concentration inversion using synchronous satellite data, providing a more efficient, economical, and accurate approach for real-time DO monitoring. This method holds significant practical value in enhancing the efficiency and precision of water environment monitoring.

KEYWORDS

inversion for water quality, remote sensing model, multi-modal deep neural network, synchronous satellite, dissolved oxygen

1 Introduction

In recent years, the rapid growth of population, accelerated industrialization, and excessive use of fertilizers and pesticides have resulted in numerous adverse effects on the water quality of lakes. As a consequence, local lake environments are facing serious deterioration in water quality and eutrophication issues (e.g., Liu et al., 2019; Liang et al., 2021). Therefore, enhancing the capability of water quality monitoring and timely understanding the changes in lake water environments are of great significance for lake

protection and pollution control (e.g., Lyu et al., 2015; Batur and Maktav, 2018; Chen et al., 2021). Dissolved Oxygen (DO) concentration is a commonly used water quality indicator in water environments and pollution studies. Monitoring the spatio-temporal variations of DO has become crucial in assessing water environments. DO, primarily originated from atmospheric diffusion, biological photosynthesis, and runoff, is influenced by factors such as radiation flux density, precipitation, and water nutrient concentrations. If the water body becomes eutrophic, it can lead to abnormal proliferation of cyanobacteria, and the decomposition of microorganisms and organic matter can significantly deplete DO concentrations (e.g., Ma et al., 2013). The decrease in DO concentration has various adverse effects on the ecological diversity of the region. It leads to the death of other organisms in the water and results in discoloration and foul odor (e.g., Guo et al., 2021). Therefore, DO concentration can indirectly describe the degree of water pollution and reflect the ecological and pollution status of the water body.

Traditional water quality monitoring methods rely on manual sampling or station monitoring, which can provide certain monitoring data (e.g., Zhang et al., 2022). However, these methods are costly for deploying monitoring buoys, and have a limited effective monitoring range, which makes it difficult to observe the dynamic changes of pollution on a macro scale (e.g., Sagan et al., 2020). With the continuous improvement in the spatial and temporal resolution of satellite remote sensing data, the use of satellite remote sensing data for water quality inversion has gradually become an important approach for monitoring surface water quality (e.g., Batur and Maktav, 2018). In current research, DO is primarily inferred indirectly through optically active constituents (OACs) or directly through remote sensing reflectance (Rrs). In terms of indirect inference using OACs, Guo et al. (2021) used Landsat and MODIS satellite data and employed a Support Vector Regression (SVR) model with strong generalization capability to estimate the measured DO concentration in four lakes. The study successfully reproduced the spatial distribution and monthly variation of DO in Lake Huron from 1984 to 2000. Peterson et al. (2020) utilized the relationship between OACs and NOACs to apply deep learning methods for anomaly detection of DO. Their approach successfully identified water quality anomalies. Kim et al. (2020) established a multiple regression analysis model based on the correlation between DO, water temperature, and Chlorophyll-a (Chl-a), demonstrating the potential monitoring capability of satellite remote sensing in high spatio-temporal resolution DO concentration. Regarding direct estimation using Rrs, Karakaya and Evrendilek. (2011) proposed a simple approach based on optimal fit multiple linear regression to estimate DO concentrations using Landsat 7 data. Sharaf, et al. (2017) developed a backpropagation neural network to estimate DO using Landsat 8 data and mapped the spatial distribution of DO concentrations in the Saint John River in Canada. Batur and Maktav. (2018) estimated DO concentrations in Lake Gala (Turkey) using data fusion and mining techniques, such as principal component analysis (PCA), with the assistance of Landsat 8 and Sentinel-2A. These studies demonstrate the potential of remote sensing satellites in monitoring DO concentrations at high spatial and temporal resolutions. For learning features from a single modal (such as text, audio, or video), Artificial Neural Network (ANN) is the most direct learning approach in general. However, different modalities exhibit a complementary yet imbalanced relationship. Inspired by the way humans perceive and process complex information through multiple senses (e.g., vision, hearing), Ngiam, et al. (2018) from Stanford University proposed Multimodal Deep Learning (MDL). In contrast to a single modal, one of the ideas behind multimodal learning is to employ multiple independent sub neural networks (sNNs) to learn features from different modalities. The learned results are then fused and inputted into a new sNN for prediction, enabling the fusion of information from various modalities and facilitating the exchange of information between them. During the training process, a single modal often fails to encompass all the necessary information for producing accurate outputs. By incorporating information from multiple modalities, the multimodal network training process achieves information supplementation, expands the coverage of information contained in the input data, enhances model accuracy, and improves model robustness.

However, previous studies often used polar-orbiting remote sensing satellites, which have low revisit rates for the same location (e.g., Sentinel-2 (e.g., Peterson et al., 2020; Wang et al., 2022) with a revisit period of 5 days, and Landsat-8 (e.g., Chen and Quan, 2012) with even longer intervals of 16 days), often requiring several years of data accumulation to establish effective inversion models.

The new generation geostationary satellite, Himawari-8 (H8) possesses high temporal resolution (e.g., Wang et al., 2017; Wang et al., 2020; Ning et al., 2021). Compared to commonly used polar-orbiting satellites for water quality remote sensing, it offers a higher revisit rate, which allows for repeated sampling of the same location every 10 min. This makes it suitable for monitoring continuous changes in water quality and provides important data support for environmental monitoring. Some researchers have already conducted effective monitoring studies using H8 satellite remote sensing data. Wang et al. (2017) utilized H8 satellite remote sensing data for dynamic monitoring of cyanobacterial blooms in lake Taihu. Chen. (2019), with the support of H8 satellite remote sensing data, effectively monitored floating algae, achieved better monitoring results than the Geostationary Ocean Color Imager (GOCI) satellite (with a revisit period of 1 h). These research findings demonstrate that the high revisit rate characteristic of the H8 satellite can capture more frequent water quality changes, thereby detecting phenomena that may be missed by existing satellites (such as the GOCI satellite) and providing robust data support for the continuous and dynamic monitoring of lake water quality (e.g., Yang et al., 2021). Currently, there is no existing research on DO concentration inversion using H8 satellite remote sensing data. This study aims to establish a correlation model between H8 satellite remote sensing data and DO concentration through machine learning or deep learning algorithms to achieve real-time monitoring of DO concentration.

This study takes Lake Taihu as an example to construct a high-precision deep learning model based on H8 satellite remote sensing data for estimating DO concentration. The main objective is to provide an efficient inversion method for monitoring DO indicators in Lake Taihu and other inland lakes, aiming to reduce monitoring time delays and improve inversion accuracy. This research plays a crucial role in strengthening the management of organic pollution in

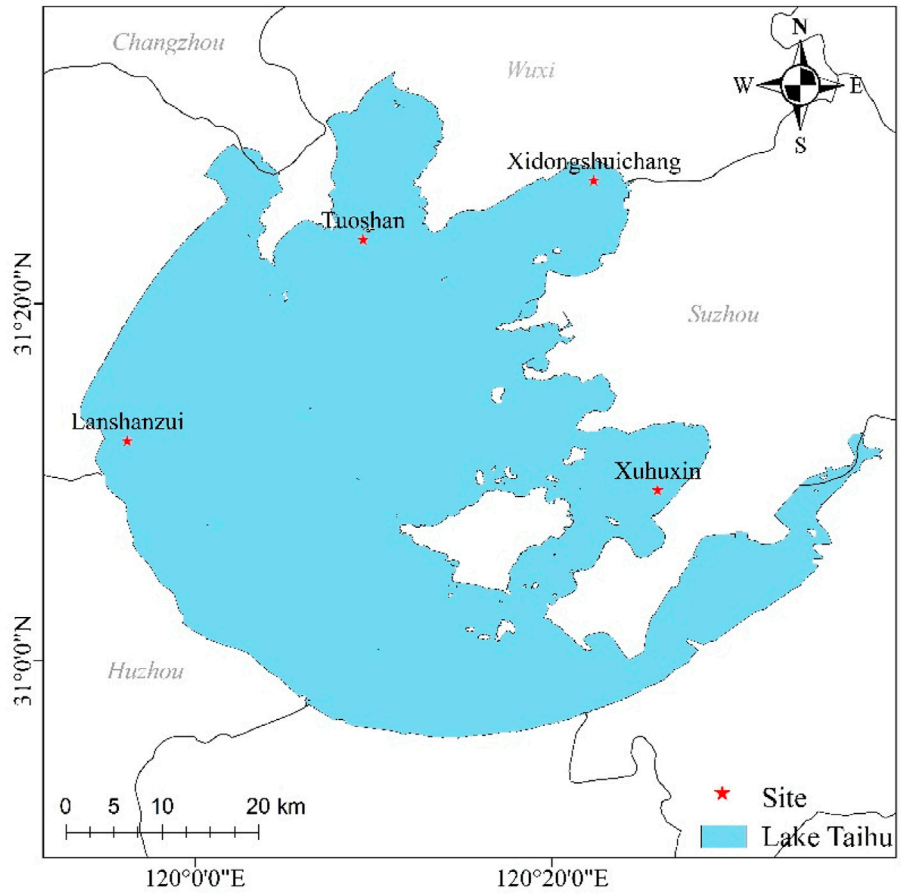

FIGURE 1
Map of Lake Taihu's Scope and Distribution of Monitoring Sections.

lakes, supporting water environment pollution prevention and control, pollutant source tracing, and water quality monitoring and early warning. It is expected to serve as a valuable supplement to water quality remote sensing inversion and estimation methods.

2 Materials and methods

2.1 Research area overview

Lake Taihu, as shown in Figure 1, is the third largest freshwater lake in China. It is located in the southern part of Jiangsu Province, between 119°52′32″E to 120°36′10″E and 30°55′40″N to 31°32′58″N. The lake is situated in the economic core area of the Yangtze River Delta and provides daily water supply for irrigation, domestic use, transportation, and other purposes for the surrounding residents. Lake Taihu has a surface area of 2,427.8 km^2, a water area of 2,338.11 km^2, a shoreline length of 393.2 km, an average depth of 1.9 m, a maximum depth of 2.6 m, and a total storage capacity of approximately 5 billion m^3 (e.g., Lyu et al., 2015).

The surrounding areas of lake Taihu suffer from significant pollution, frequent algal blooms, and widespread accumulation of cyanobacteria, which keep the lake in a state of mild eutrophication (e.g., Ma et al., 2008; Zhang et al., 2010; Zhu et al., 2021). The Ecological Environment Reports of Wuxi City, Suzhou City, and Changzhou City in 2021 (e.g., Changzhou Ecological Environment Bureau, 2021; Suzhou Ecological Environment Bureau, 2021; Wuxi Ecological Environment Bureau, 2021) indicated that, according to the "Surface Water Environmental Quality Standards" (GB3838-2002), the overall water quality of lake Taihu during the year was classified as Class IV. The comprehensive nutrient status index ranged from 53.3 to 59.5, indicating a mild eutrophication status.

2.2 Data and preprocessing

2.2.1 DO data

The DO measured data used in this study were obtained from the Comprehensive Business Portal of the Ministry of Ecology and Environment, which provides real-time data from the national automatic monitoring system for surface water quality during the "13th Five-Year Plan" period. The selected data includes DO (mg/L) and water temperature (°C) indicators from four monitoring sections within the Lake Taihu Basin, covering the period from January 1, 2019, to December 31, 2021 (Table 1). The data collection frequency is 1 h per measurement, and it adheres to the technical

TABLE 1 Latitude and Longitude information of monitoring sections in lake Taihu.

Monitoring sections	Longitude	Latitude
Xuhuxin	120°25′54″E	31°9′33″N
Xidongshuichang	120°22′20″E	31°26′54″N
Lanshanzui	119°56′13″E	31°12′19″N
Tuoshan	120°9′25″E	31°23′36″N

specifications for automatic monitoring of surface water (HJ 915-2017).

Due to the potential influence of environmental changes or instrument malfunctions during data collection at water quality automatic monitoring stations, it is necessary to address missing and abnormal data to ensure the accuracy of data used for model fitting. Missing values in the obtained DO data were excluded, and the 3σ principle was applied. Concentration data falling within the range of $[DO_{mean} - 3 \times DO_{std}, DO_{mean} - 3 \times DO_{std}]$ were retained as the measured DO data for the model, while data outside this range were considered abnormal and removed. Here, DO_{mean} represents the average DO concentration for the current monitoring section, and DO_{std} is the standard deviation of DO concentration for the same section.

2.2.2 Synchronous satellite data

H8 satellite carries an advanced optical sensor, namely, Advanced Himawari Imager (AHI), which includes 3 visible light bands, 3 near-infrared bands, and 10 infrared bands. It captures full-disc images of the Earth every 10 min. These images provide high-frequency coverage of the entire Asia-Pacific region, which includes Asia, Oceania, and part of the Pacific Ocean. The specific coverage area is approximately half of the Earth, equivalent to about 3.9 million square miles. It possesses characteristics of high spatial coverage and high temporal resolution. The H8 satellite remote sensing data used in this study is obtained from the Himawari Monitoring System P-free (https://www.eorc.jaxa.jp/ptree/), accessed on 15 July 2022, which provides full-disc satellite images with a spatial resolution of 2 km. Data from the H8 satellite were selected from January 1, 2019, to December 31, 2021, with hourly sampling to match the temporal resolution of the DO measured data. In total, 26258 images were acquired. Channels 1 to 16 were used for DO inversion, where channels 1–6 were mainly used to obtain visible light and infrared images for monitoring cloud cover, atmospheric details, and temperature, as well as studying weather patterns and cloud formation; Channels 7–16 were primarily used for infrared temperature detection and high-resolution infrared images to detect atmospheric temperature, water vapor distribution, cloud characteristics and properties, as well as observe cloud and surface temperature distribution. The H8 satellite data used are L1-level data, the data file format is Network Common Data Form (NetCDF), the spatial resolution is 2 km × 2 km, the temporal resolution is 10 min/times, and the wavelength ranges and uses of each channel of data are shown in the Table 2.

The H8 satellite has unique advantages over other satellites in lake water quality monitoring. Firstly, H8 is a geostationary orbit satellite, whose position is stabilized at a specific location over the Earth, providing high-resolution images continuously every 10 min/time, enabling us to obtain long time series data and to observe changes in the water bodies of lakes more frequently. Secondly, H8 is

TABLE 2 Information parameters by band.

Band		Center wavelength/um	Spatial resolution/km	Use
Visible light	1	0.46	1	Vegetation, Aerosol Observation, Color Image Synthesis
	2	0.51	1	Vegetation, Aerosol Observation, Color Image Synthesis
	3	0.64	0.5	Lower Cloud (Fog) Observation, Color Image Synthesis
Near-infrared	4	0.86	1	Vegetation, Aerosol Observation
	5	1.6	2	Identification of Various Cloud Phases
	6	2.3	2	Observation of Cloud Droplet Effective Radius
Infrared	7	3.9	2	Observation of Lower Clouds (Fog), Natural Disasters
	8	6.2	2	Observation of Upper- and Middle-Level Water Vapor Content
	9	7.0	2	Observation of Middle-Level Water Vapor Content
	10	7.3	2	Observation of Middle- and Lower-Level Water Vapor Content
	11	8.6	2	Cloud Phase Identification and SO2 Monitoring
	12	9.6	2	Measurement of Total Ozone Amount
	13	10.4	2	Observation of Cloud Images and Cloud Top Conditions
	14	11.2	2	Observation of Cloud Images and Sea Surface Temperature
	15	12.3	2	Observation of Cloud Images and Sea Surface Temperature
	16	13.3	2	Measurement of Cloud Layer Height

equipped with an advanced multispectral imaging instrument, which is capable of capturing different wavelengths of light, thus providing more detailed and multilevel information on water quality, and therefore H8 satellite data is selected for this paper.

When using H8 satellite remote sensing data, it is necessary to perform atmospheric correction using an improved version of the 6S model (e.g., Li et al., 2014). The improved 6S model incorporates parameters are from the Copernicus Climate Data Store of European Centre for Medium-Range Weather Forecasts (ECMWF) (e.g., Hersbach et al., 2020). After atmospheric correction, the apparent reflectance is further corrected for water body using the Gordon model. Finally, the corrected radiance data is converted into surface temperature. Eqs 1, 2 are used to convert the atmospherically corrected radiance temperatures into brightness temperatures, and Eq. 3 is used to calculate the surface temperature.

$$T_b = \frac{c_2}{ln\left(1 + \frac{c_1}{L_{sfc}}\right)} \tag{1}$$

$$L_{sfc} = \frac{L}{T_a} \tag{2}$$

$$T_s = \frac{T_b}{1 + \left(\frac{\lambda_1 T_b}{\rho_v}\right) \ln(e)} \tag{3}$$

Where T_b refers to brightness temperature, c_1 and c_2 are constants, L_{sfc} represents land surface radiance temperature, L represents radiance temperature data after atmospheric correction, T_a represents land surface temperature, T_s represents surface temperature, λ_1 represents the proportional constant in the TBB band of H8, ρ_v represents atmospheric water vapor content, and e represents water vapor pressure.

According to the study by Chen et al. (2022), the portion of remote sensing reflectance (Rrs) corresponding to solar zenith angle (SOZ) less than 60° is considered as valid data. A correction is applied to the Rrs of bands 1 to 6 using Eq. 4 to mitigate errors caused by SOZ offset. Based on the threshold proposed by Ning et al. (2021) and Qi et al. (2014), when Rrs of band 1 is less than or equal to 0.25, the obtained reflectance is essentially unaffected by solar flickering, thick aerosols, and heavy cloud cover, and is considered as valid data. No invalid data was found during this process that required filling.

$$R'_{rsi} = \frac{R_{rsi}}{\cos(\alpha \times (1 - 1.3 \times sin(0.05 \times \alpha)))} \tag{4}$$

Where $i = 1 \ldots..6$, R'_{rsi} represents the i-th channel of the corrected reflectance, R_{rsi} represents the Remote Sensing Reflectance of the i-th channel, and α represents SOZ.

2.3 Model construction and evaluation methods

2.3.1 Input data

Reference (e.g., Guo et al., 2022) introduced the use of visible and near-infrared bands of remote sensing reflectance (Rrs) to extract more spectral information. In this chapter, we combine these spectral bands to derive multiple spectral indices for more accurate water quality inversion. The selected spectral bands for the visible range from H8 are 460 nm, 510 nm, and 640 nm, while the near-infrared band is at 860 nm. By combining these bands, several spectral indices can be calculated, such as the Normalized Difference Vegetation Index (NDVI) shown in Eq. 5 and the Normalized Difference Water Index (NDWI) shown in Eq. 6. Additionally, due to the significant negative correlation between DO concentration and temperature, infrared bands (from 7th to 16th band) are included as input features in the model.

$$NDVI = \frac{R'_{rs4} - R'_{rs3}}{R'_{rs4} + R'_{rs3}} \tag{5}$$

$$NDWI = \frac{R'_{rs2} - R'_{rs4}}{R'_{rs2} + R'_{rs4}} \tag{6}$$

Where $NDVI$ is the Normalized Difference Vegetation Index, R'_{rs3} is the 3-band of the corrected Visible light, and R'_{rs4} is the 4-band of the corrected Near-infrared; $NDWI$ is the Normalized Difference Water Index, and $R'_{rs2}$is the 2-band of the corrected Visible light.

The extracted features from the H8 satellite remote sensing data, based on different central wavelengths and spectral indices, are divided into three modes. Mode A includes the visible, near-infrared, and shortwave infrared bands (1st to 6th channels) of Rrs. Mode B consists of various spectral indices. Mode C includes the surface temperature from the infrared bands (7th to 16th channels). Before inputting the features into the model, standardization processing is applied to each feature, as shown in Eq. 7:

$$x'_i = \frac{x_i - x_{min}}{x_{max} - x_{min}} \tag{7}$$

Where x'_i is the normalized variable of the i-th feature in sample x, x_i is the i-th feature in sample x, x_{max} is the maximum value of the feature in the training dataset, and x_{min} is the minimum value of the feature in the training dataset. It is important to note that during the normalization process, the formulas involving the maximum and minimum values of the sample x are limited to the training dataset only.

2.3.2 Output data

To develop a DO inversion model suitable for the entire lake area, this study combines data from four representative monitoring sections in Lake Taihu, resulting in a total of 7429 valid data points ($N = 7429$). The merging of data from multiple monitoring stations increases the sample size and enriches the training data for water quality inversion models, thereby improving the accuracy and precision of the inversion. Different areas within a lake may exhibit varying water quality conditions, and building individual inversion models for each station may not fully consider the spatial heterogeneity within the lake. By merging data from multiple stations, the model gains a better understanding of spatial variations within the lake, enhancing its generalization ability. The model's output data represents the merged DO concentrations from the four selected monitoring sections. The overall data processing process is shown in Figure 2.

2.3.3 Model framework

The paper proposes a DO-MDNN (Dissolved Oxygen Multimodal Deep Neural Network) model, which consists of four single-modal neural networks (sNNs). Here, sNN refers to an

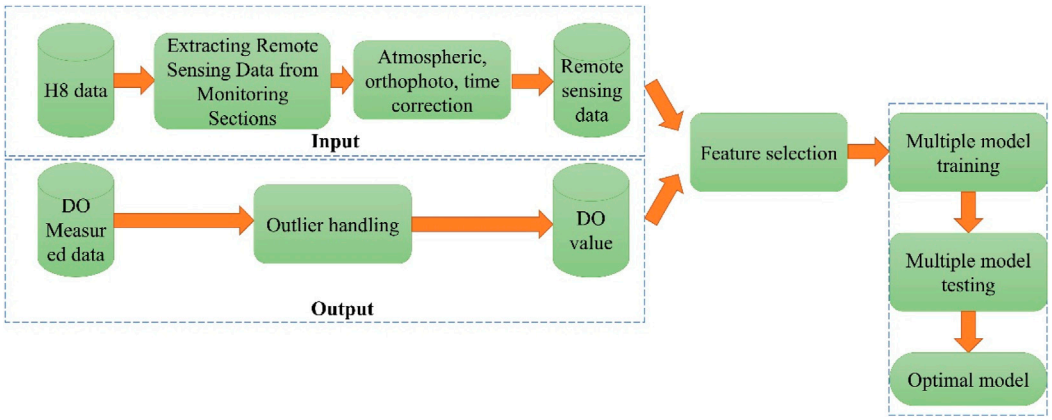

FIGURE 2
Technical Roadmap.

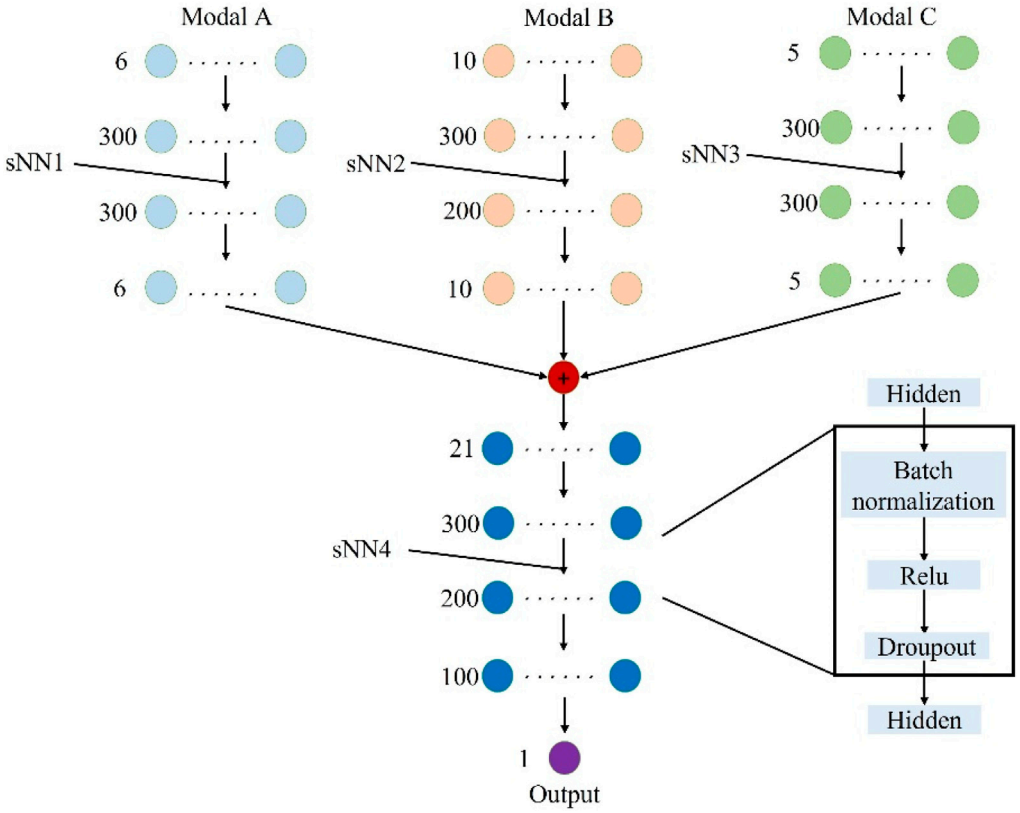

FIGURE 3
The model network structure diagram.

independent neural network corresponding to each perception modal in the multimodal neural network. Each sNN processes its respective input data and extracts useful information from the multimodal data through a fusion or integration mechanism, as illustrated in Figure 3. The model is designed with one sNN for each modal, allowing the model to effectively balance information and noise during the training phase. Modal A, Modal B, and Modal C represent remote sensing data. The outputs of Subnetwork 1 (sNN1), Subnetwork 2 (sNN2), and Subnetwork 3 (sNN3) are non-linearly mapped through a weighted sum in the hidden layer to obtain the input features, which are then connected to Subnetwork 4 (sNN4) for DO inversion. The number of neurons in each layer of the network is labeled in Figure 3 to illustrate the model structure.

2.3.4 Structure and parameter determination

In Figure 3, sNN1, sNN2, and sNN3 are all set as neural networks with three hidden layers, while sNN4 is set as a neural network with four hidden layers. The number of neurons in the input layer of sNN1, sNN2, and sNN3 depends on the features number in each modal, while the number of neurons in the output layer is determined based on the model's performance.

To prevent overfitting, a Batch Normalization (BN) layer, a Rectified Linear Unit (ReLU) activation function, and a dropout layer are added after each hidden layer. The BN layer and dropout layer serve to normalize the features and discard some neurons in the network to improve the generalization ability of the inversion model. During the training process, the three modalities are trained separately in sNN1, sNN2, and sNN3, and their outputs are then concatenated (represented by the red nodes in Figure 3) and fed into sNN4 for further training. In terms of model optimization, Mean Squared Error Loss (MSELoss) is used as the optimization parameter (Eq. 8), and the Adaptive Moment Estimation (Adam) optimizer is employed for gradient descent.

$$\boldsymbol{MSELoss} = \frac{\mathbf{1}}{\boldsymbol{n}}\sum_{i=1}^{n}\left(\boldsymbol{y_i} - \boldsymbol{\hat{y}_i}\right)^2 \tag{8}$$

Where y_i and $\hat{y}_i$ represent the observed and inverted DO concentrations, respectively, and n denotes the number of samples.

2.3.5 Comparison with other models

In this study, 80% of the data was randomly allocated for training the model (N = 5940), and the remaining 20% of the data was used as the test set for model evaluation (N = 1489).

In this study, six machine learning algorithms, namely, ElasticNet, K-Nearest Neighbors (KNN), Support Vector Regression (SVR) (e.g., Guo et al., 2021), Random Forest (RF) (e.g., Cao et al., 2020), Extreme Gradient Boosting (XGBoost) (e.g., Bui et al., 2020), and Light Gradient Boosting Machine (LightGBM), were used as comparative models. The same data partitioning method was applied to all algorithms, and a Genetic Algorithm (GA) was used to search for the optimal hyperparameters relative to each model.

2.3.6 Model evaluation

To quantitatively describe the inversion capability of the DO inversion model, this chapter utilizes multiple indicators to evaluate its performance. These indicators include adj_R^2, Root Mean Square Error (RMSE), Percent bias (Pbias) (e.g., Bui et al., 2020) and Symmetric Mean Absolute Percentage Error (SMAPE) (e.g., Zaini et al., 2021a). The calculation formulas, value ranges, and optimal values for these evaluation indicators are presented in Table 3.

Where R^2 is the coefficient of determination between the simulated values and the measured values, y_i represents the i-th variable of the measured DO, $\bar{y}$ is the average value of the measured DO, $\hat{y}_i$ represents the i-th variable of the simulated DO, n is the number of samples, and p is the number of features.

TABLE 3 Calculation formula, value range, and optimal value of evaluation indicators.

Index	Formula	Value range	Best value
adj_R^2	$adj\_R^2 = (1 - \frac{(1-R^2)(n-1)}{(n-p-1)})$	[0,1]	1
R^2	$R^2 = (1 - \frac{\sum_{i=1}^{n}(y_i-\hat{y}_i)^2}{\sum_{i=1}^{n}(y_i-\bar{y})^2})$	[0,1]	1
$RMSE$	$RMSE = \sqrt{\frac{1}{n}\sum_{i=1}^{n}(y_i - \hat{y}_i)^2}$	[0,+∞)	0
$Pbias$	$Pbias = \frac{\sum_{i=1}^{n}(y_i-\hat{y}_i)}{\sum_{i=1}^{n}y_i}$	(-∞,+∞)	0
$SMAPE$	$SMAPE = \sum_{i=1}^{n}\frac{\lvert\hat{y}_i-y_i\rvert \times 2}{(\lvert\hat{y}_i\rvert+\lvert y_i\rvert) \times n}$	[0,+∞)	0

3 Result

3.1 Statistical analysis of measured DO

Figure 4 displays the monthly average DO concentrations from 2019 to 2021. The original DO concentrations in the monitoring sections of Lake Taihu exhibit evident seasonal variations. The MK trend test reveals a significant decreasing trend in DO concentrations during spring (March to May) ($p < 0.01$) and a significant increasing trend during autumn (September to November) ($p < 0.01$). DO concentrations in summer (June to August) are lower than in winter (December to February of the following year), with varying trends across different years, indicating substantial inter-seasonal variations. The range of DO concentrations throughout the year is 6–14 mg/L, with the lowest average values observed in summer and the highest average values occurring during the colder winter months, suggesting uneven seasonal distribution of DO concentrations in the monitored sections of Lake Taihu, likely influenced by temperature. Pearson correlation analysis indicates a significant negative correlation between DO concentrations and water temperature in the monitoring sections, with a Pearson coefficient of −0.81 and p-value <0.01.

Regarding spatial heterogeneity, the Tuoshan monitoring section shows higher overall DO concentrations, with an average DO concentration of 9.99 mg/L from January 2019 to December 2021. On the other hand, the Xidongshuichang monitoring section exhibits lower overall DO concentrations, with an average DO concentration of 9.10 mg/L during the same period. In general, DO concentrations in the western part of Lake Taihu are slightly higher than in the eastern part, especially during winter, where Tuoshan and Lanshanzui sections have relatively higher DO concentrations. These findings indicate the presence of spatial heterogeneity among the four monitoring sections in Lake Taihu.

3.2 Feature selection

After merging the DO concentrations from the four monitoring sections, the correlation between all remote sensing features and DO concentrations was examined using the Pearson correlation analysis method. Table 4 displays pearson correlation coefficient between DO and various characteristics, indicating the feasibility of using remote sensing information such as visible, near-infrared, and

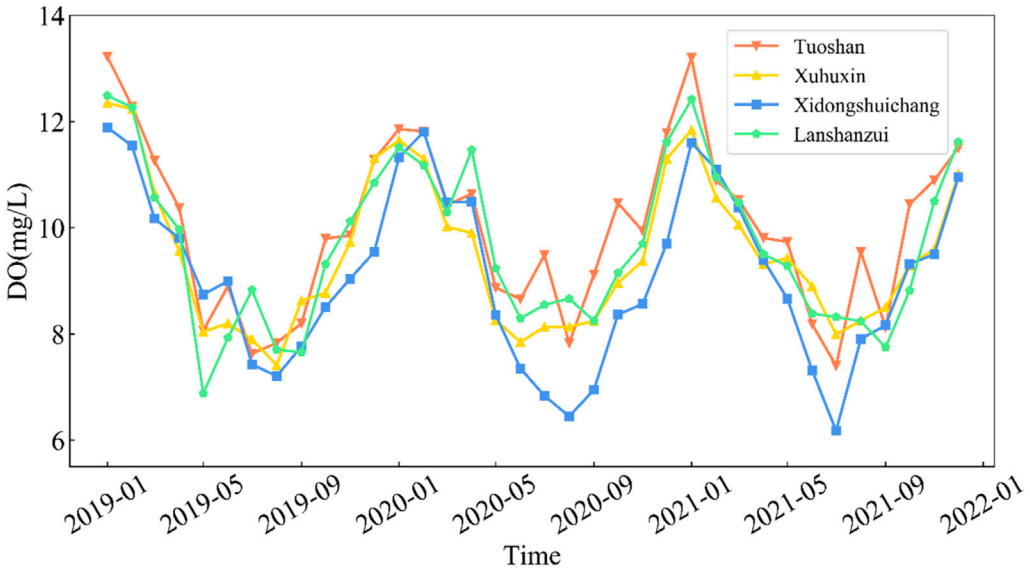

FIGURE 4
Monthly Average Trends of DO Concentration from 2019 to 2021.

TABLE 4 Pearson correlation coefficient between DO and various characteristics.

Modal	Features	Pearson	Modal	Features	Pearson
A	Rrs_01	0.15**	B	Tbb_12	−0.70**
	Rrs_02	0.14**		Tbb_13	−0.64**
	Rrs_03	0.09**		Tbb_14	−0.57**
	Rrs_04	−0.30**		Tbb_15	−0.47**
	Rrs_05	−0.30**		Tbb_16	−0.50**
	Rrs_06	−0.21**	C	NDVI	−0.41**
B	Tbb_07	−0.79**		NDWI	0.40**
	Tbb_08	0.02**		MNDWI	0.36**
	Tbb_09	0.01**		FAI	−0.40**
	Tbb_10	−0.09**		ρ_{Chl}	0.05**
	Tbb_11	−0.66**			

** Indicates a significant correlation at the 0.01 level (two-tailed) based on Pearson correlation analysis.

shortwave infrared bands of Rrs, spectral indices, and surface temperature in the infrared band for DO concentration inversion.

3.3 Model performance

The evaluation results on the test set were chosen to represent the model's performance in practical applications. Firstly, six machine learning models were used to compare the effectiveness of the DO-MDNN method. As shown in Figure 5, the LightGBM model demonstrated the best performance among the six models, with adj_R^2, RMSE, SMAPE, and Pbias values of 74.18%, 0.70 mg/L, 5.94%, and −0.007% respectively. On the other hand, the ElasticNet model showed the poorest performance, with adj_R^2, RMSE, SMAPE, and Pbias values of 69.73%, 0.76 mg/L, 6.61%, and −0.003% respectively. Using the same dataset, we trained and validated the DO-MDNN model developed in this study to further investigate its advantages. As illustrated in Figure 6, the DO-MDNN model developed in this study provided more accurate DO concentration estimations (adj_R^2, RMSE, SMAPE, and Pbias values of 77.11%, 0.66 mg/L, 5.36%, and −0.44% respectively), as expected. The evaluation results indicated that the DO-MDNN model outperformed all other models. Compared to the average performance of the other baseline models, DO-MDNN showed a 6.40% increase in adj_R^2, an 8.27% reduction in RMSE, and a 12.1% decrease in SMAPE. The density plot shown in Figure 6

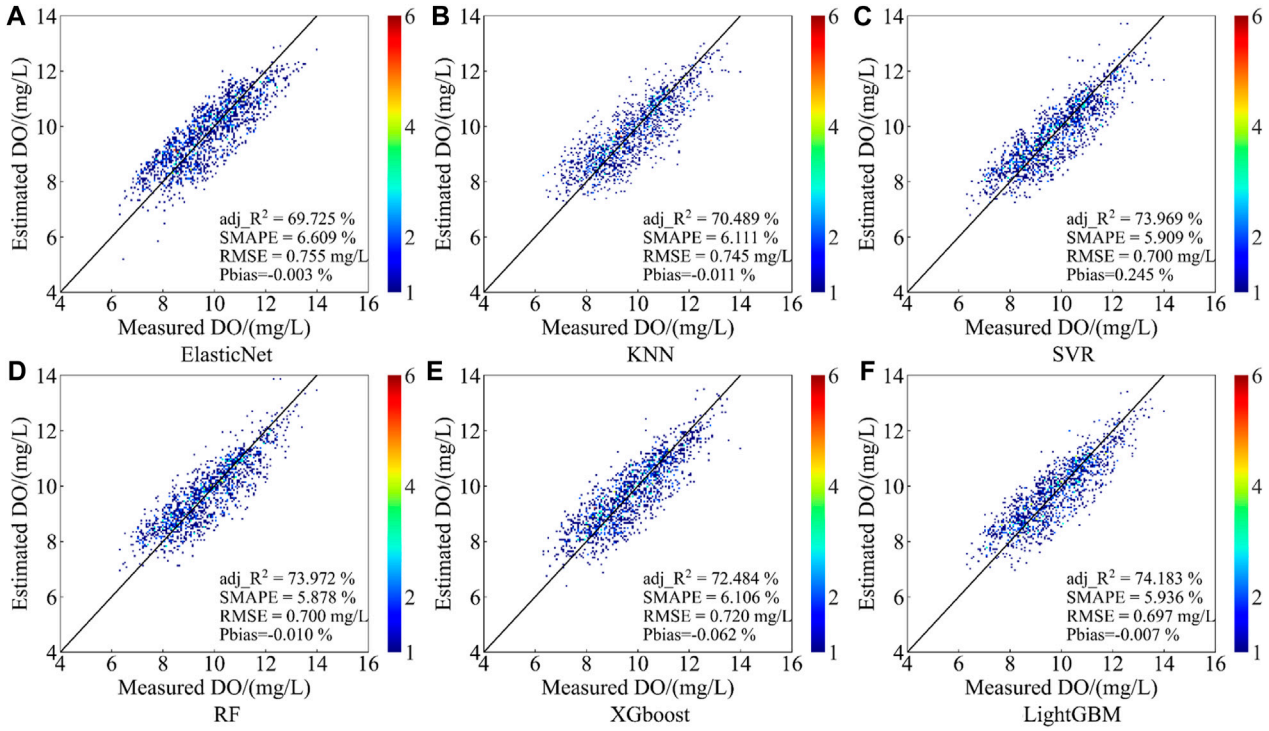

FIGURE 5
Fitting Plots of Six Machine Learning Models.

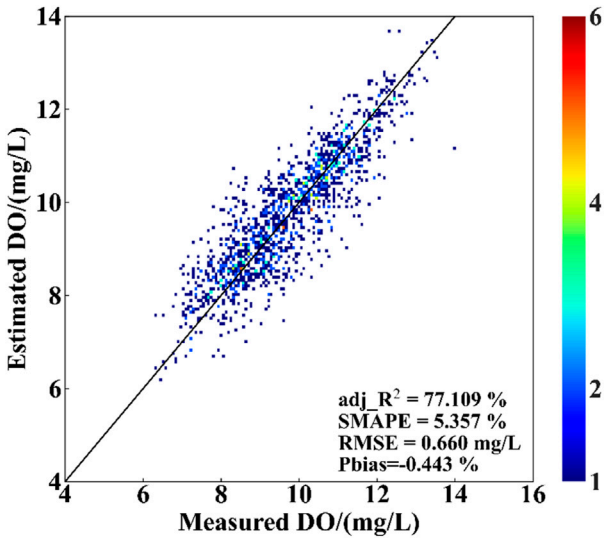

FIGURE 6
Fitting Plot of the DO-MDNN Model.

visually demonstrates the performance of the DO-MDNN model's DO estimations compared to the actual measurements on the test set, effectively avoiding data stacking issues.

Therefore, the DO -MDNN model developed in this study has been demonstrated to successfully invert DO concentration using H8 satellite data and can be used for high-frequency dynamic monitoring of DO.

In order to verify the application of the DO-MDNN model in the whole Lake Taihu region, we selected the H8 data from 08:00-13:00 on May 16, 2022, and mapped the DO concentration in the Lake Taihu region on a time-by-time basis, and the results are shown in Figure 7. DO concentration varied from 8.5 to 11.5 mg/L from 8:00 to 13:00, with an overall increase and then a decrease in DO concentration values, with an overall increase in DO concentration values from 8:00 to 10:00, and a beginning of a decrease in DO concentration values from 11:00 to 13:00, especially in littoral areas such as the southwestern and northeastern parts of the country. The southwestern part of Lake Taihu is mostly the river inlet, with vigorous vegetation and shallow water nearby leading to strong photosynthesis and higher DO concentrations. The northeastern part of Lake Taihu is mainly an economically developed urban area with a large population density, which is affected by anthropogenic factors all year round, and the littoral areas of the lake are in a state of nutrient fertilization all year round, resulting in a higher DO concentration. The above results show that the DO-MDNN model has some applicability in the Taihu Lake region.

4 Discussion

4.1 Model advantages and limitations

4.1.1 Model advantages

(1) The DO-MDNN model constructed in this study validates the feasibility of using geostationary satellite remote sensing data for the inversion of non-optical active parameter, DO concentration. The model demonstrates high accuracy and

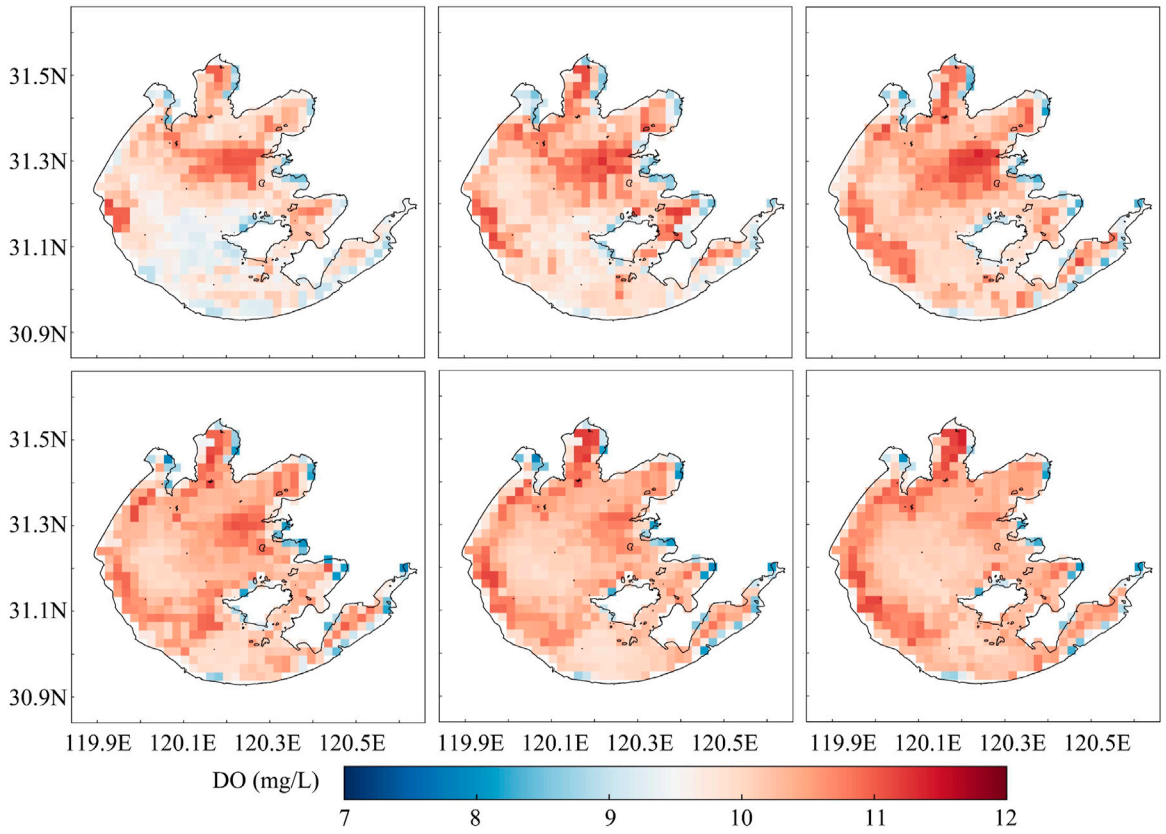

FIGURE 7
Remote sensing mapping of DO concentrations in the Lake Taihu region from 08:00 to 13:00 (order is from top left to bottom right).

provides reliable data support for lake water quality inversion using geostationary satellite data, which complements the limitations of traditional water quality monitoring and estimation. It offers advantages such as wide coverage, rapid monitoring, and addresses the low revisit rate of polar-orbiting satellites, thereby enhancing the current level of water environment protection and management.

(2) Firstly, this model divides the input features into three modalities, enabling the model to capture multimodal information. Each modality can focus on extracting and learning specific types of features, thus reflecting the influencing factors of DO more comprehensively. Secondly, the adoption of multimodal neural networks allows for the full utilization of the expressive capabilities of each modality. Through hierarchical feature extraction and combination, the model enhances its ability to represent the input features and better learn the complex relationship between DO and these features. Finally, different modalities of features may possess distinct scales, distributions, and correlations. By handling them separately, the model can reduce interference during the learning process. Moreover, multimodal neural networks can effectively learn correlations between different modalities through appropriate weight sharing and joint training, thereby improving the model's generalization ability.

(3) The H8 satellite data inversion model not only shows technical advantages in DO monitoring, but also has the potential to be extended to other water quality indicators, such as total phosphorus and total nitrogen. Specific spectral channels may capture optical features associated with total phosphorus and total nitrogen concentrations, such as particulate matter concentrations, the presence of nitrogen compounds, and the color of the water column. In addition, changes in temperature distribution and biological activity may also be affected by total nitrogen. Through in-depth research and model development, we can further explore how to effectively utilize H8 data as well as deep learning models to enable remote monitoring and estimation of key water quality indicators such as total phosphorus and total nitrogen, which can provide important support for water resource management and ecosystem monitoring.

4.1.2 Model limitations

The discrepancy between the model's output and the true values can be attributed to several factors. Firstly, the water quality parameters are collected from fixed monitoring points, while the spatial resolution of the satellite data used in this study is relatively low (2 km). As a result, the presence of other interfering factors within the same remote sensing pixel adds complexity and makes it challenging to achieve a perfect match. Secondly, the DO concentrations outputted by the proposed DO inversion model represent average values within the remote sensing pixel and may not directly correspond to the measured concentrations at automatic

monitoring stations. The proximity to the land adjacency effect (e.g., Sun et al. 2022) negatively impacts the inversion results, with poorer performance observed in areas closer to the lake shore (e.g., Zhao et al. 2021). Additionally, the measurements taken at automatic monitoring stations may be affected by unexpected events such as changes in sensor environment, network failures, or the presence of boats and fish. Furthermore, remote sensing satellites are unable to monitor the vertical profiles of water bodies, and different water bodies exhibit significant individual variations in their optical properties. All of these factors can contribute to certain errors in water quality inversion and prediction.

4.2 Reasons for the uneven distribution of DO over time

Based on the analysis of DO measured data over time, it is evident that the DO concentration in Lake Taihu exhibits an uneven temporal distribution, with higher levels observed in summer and autumn compared to spring and winter. This phenomenon is likely attributed to several factors. During the summer and autumn, local water temperature rises, and there is abundant sunlight, leading to significant reproduction of aquatic organisms. Additionally, increased rainfall in summer results in a higher influx of pollution loads into Lake Taihu, leading to eutrophication and increased DO consumption, thereby causing higher-than-normal occurrences of cyanobacterial blooms and a gradual decline in water quality (e.g., Dai et al., 2020). In the winter, the Lake Taihu ecosystem enters a dormant state, although some aquatic organisms remain active due to the subtropical monsoon climate of the region (e.g., Lyu et al., 2015). Cyanobacterial frequency decreases during this period, resulting in gradually higher DO content in the water. As a result, the correlation between DO concentration and cyanobacterial blooms becomes weaker during non-blooming periods, while during cyanobacterial bloom outbreaks, there is a negative correlation between DO concentration and the frequency of bloom events. Rapid increases in cyanobacterial populations lead to a large amount of photosynthesis, depleting DO levels in the water. Moreover, after cyanobacteria die, they also consume oxygen, further reducing the DO concentration in the water. Hence, cyanobacterial bloom periods are often associated with lower DO concentrations in the water. These combined factors result in the uneven temporal distribution of DO concentrations in Lake Taihu during different seasons. Analyzing the spatiotemporal distribution changes of non-optical active parameters in different research areas is crucial for improving the precision of remote sensing inversion of non-optical active parameters.

4.3 Comparison of models based on time series decomposition

In typical situations, during the training of a machine learning model, the high correlation between the input and output data may be due to both exhibiting simultaneous upward or downward trends in time, rather than a true fit. This phenomenon is particularly evident in time series data. If the trend component (a persistent upward or downward movement or state that develops over a long period) and the seasonal component (regular variations in the level of development caused by seasonal changes) cannot be eliminated, it becomes challenging to accurately map features in residual analysis. This is also referred to as the "spurious regression" phenomenon (e.g., Tian, 2014).

This study takes the "Xuhuxin" section as an example. Due to the longer data sequence of this site, it was chosen as the research object. The measured DO data can be treated as a time series $Y(t)$, and the Seasonal and Trend decomposition using Loess (STL) algorithm (e.g., Rojo et al., 2017) is used to decompose it.

$$\boldsymbol{Y(t) = S(t) + T(t) + R(t)} \tag{9}$$

Where $Y(t)$ represents the DO concentration at time t, $S(t)$ represents the periodic component at time t, $T(t)$ represents the trend component at time t, and $R(t)$ represents the residual component at time t. The time series $Y(t)$ exhibit a fixed "annual cycle" $S_{year}(t)$ over the course of a year and a fixed "daily cycle" $S_{day}(t)$ within a day. The parameters for the annual cycle are set as $n_{p-year} = 365$ days, and for the daily cycle as $n_{p-day} = 24$ h. Since a single STL decomposition can only extract one type of periodic component, the first step is to remove the annual cycle component $S_{year}(t)$ from $Y(t)$ to obtain a new time series $X_1(t)$ without the annual cycle. Then, the daily cycle component $S_{day}(t)$ is removed from $X_1(t)$ to obtain the combined trend and residual components of the DO measured data in the series $X_2(t)$.

The Augmented Dickey-Fuller (ADF) test (e.g., Zaini et al., 2021b) is applied to the merged component $X_2(t)$ to check for stationarity. If $X_2(t)$ is not stationary, differencing will be performed. If $X_2(t)$ is stationary, a white noise test will be conducted. If $X_2(t)$ is a white noise sequence, it indicates that the data is invalid and the experiment should be stopped. If $X_2(t)$ is a stationary non-white noise sequence, it implies that the output data has eliminated periodic variations, and $X_2(t)$ can be used as the output for model construction in the next section.

The evaluation results on the test set were chosen to represent the model's performance in practical applications. Firstly, six machine learning models were used to compare the effectiveness of the STL method. The merged component $X_2(t)$ obtained from the second STL decomposition of DO concentration was used as the model output, and the performance of the models before and after STL decomposition was compared. As shown in Figure 8 and Table 5, the comparison models after STL processing exhibited significant improvements compared to the models without STL decomposition. The average adj_R^2 of the six machine learning models increased by 0.26, RMSE decreased by 0.24 mg/L, and SMAPE decreased by 2.2% after STL processing. Among them, the ElasticNet model showed the largest improvement in the comparison before and after STL decomposition, with a difference of 0.19 in adj_R^2, 0.23 mg/L in RMSE, and 1.56% in SMAPE, indicating a significant enhancement in its performance. Meanwhile, the DO-MDNN model showed an increase of 0.14 in adj_R^2, a decrease of 0.23 mg/L in RMSE, and a decrease of 2.1% in SMAPE after STL decomposition. The above results demonstrate that STL decomposition helps remove noise and trend components from the DO concentration time series, thereby improving the accuracy of DO inversion.

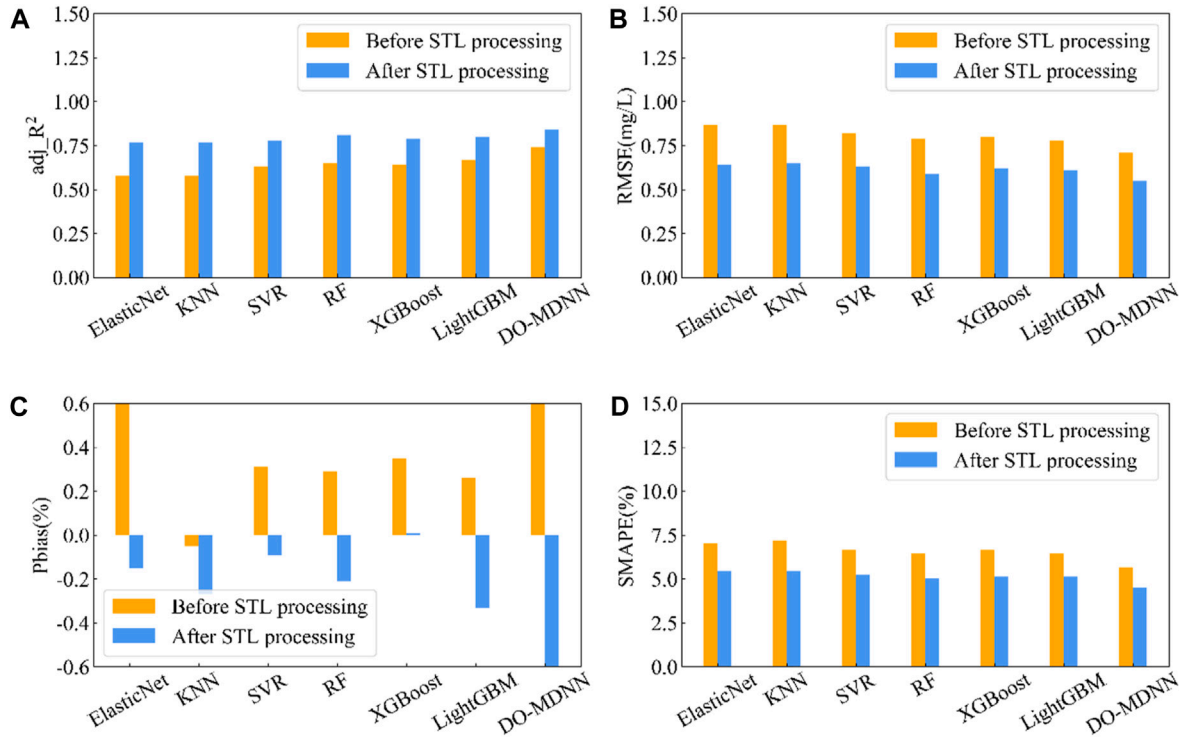

FIGURE 8
Comparison plots of each model before and after STL processing.

TABLE 5 Comparison of each model before and after STL processing.

Model	adj_R^2	RMSE(mg/L)	Pbias(%)	SMAPE(%)
ElasticNet	0.58	0.87	0.60	7.01
KNN	0.58	0.87	−0.05	7.21
SVR	0.63	0.82	0.31	6.68
RF	0.65	0.79	0.29	6.44
XGBoost	0.64	0.80	0.35	6.67
LightGBM	0.67	0.78	0.26	6.45
DO-MDNN	0.74	0.71	1.41	5.67
STL-ElasticNet	0.77	0.64	−0.15	5.45
STL-KNN	0.77	0.65	−0.27	5.47
STL-SVR	0.78	0.63	−0.09	5.26
STL-RF	0.81	0.59	−0.21	5.02
STL-XGBoost	0.79	0.62	0.01	5.15
STL-LightGBM	0.80	0.61	−0.33	5.14
STL-DO-MDNN	0.84	0.55	−0.79	4.50

The model constructed in this section is specifically designed for the single observation station "Xuhuxin" and does not have the feasibility to be applied to other areas within Lake Taihu or other water bodies outside of Lake Taihu. In this study, only the time series of the "Xuhuxin" site were relatively complete for the four sites, while the time series of the other three sites were not complete enough. Therefore, the accuracy of the removed periodic terms in the overall time series decomposition cannot be determined. Therefore, this study only used the "Xuhuxin" site. In practical applications, it is necessary to increase the number of DO observation stations and establish a unified model that fits all DO observation stations. Only then can we consider the model to be applicable to the water bodies represented by these DO observation stations.

4.4 Optical basis for remote sensing inversion methods

In the field of water ecology and bio-optics, the optical mechanism and bio-optical processes of DO are of great significance for monitoring and analyzing ecosystems, and the H8 satellite plays a key role in this regard. DO, as the dissolved state of oxygen in water, is essential for sustaining aquatic organisms. Optical analysis methods, such as oxygen sensors, utilize the H8 satellite's high-resolution optical sensors to achieve accurate measurements of DO concentration through the interaction of fluorescence or absorption properties with oxygen molecules. At the same time, the H8 satellite monitored the refraction and reflection of light on the surface of water bodies, providing important data for processes such as photosynthesis and oxygen dissolution. In addition, the H8 satellite was able to capture the temperature distribution of the water body, helping us to understand the effect of light on the interrelationship between

temperature and oxygen solubility. In summary, the optical mechanism and bio-optical processes of DO are integrated with the H8 satellite observation data, which will help to explore the dynamics of aquatic ecosystems in depth and provide scientific support for ecological protection and sustainable management.

Among them, Tbb_07, Tbb_08, Tbb_10, Tbb_12 as infrared bands are mainly used to invert the water temperature (e.g., Yamamoto et al., 2018), and the correlation between the water temperature and DO is high (e.g., Rajwa-Kuligiewicz et al., 2015), so Tbb_07, Tbb_08, Tbb_10, and Tbb_12 have strong correlation to DO in this study; MNDWI (e.g., Guha and Govil, 2022), ρ_{Chl} (e.g., Feng et al., 2022) and others as spectral indices are assess the vegetation growth condition by calculating the ratio between the reflectance of red, near-infrared and blue light bands, so it can indirectly reflect the concentration of DO; Wang, et al. (2013) pointed out that DO was negatively correlated with the remote sensing reflectance with the center wavelength in the range of 400-900 nm, and the highest correlation was found at 686 nm, and the center wavelength of Rrs_03 was 640 nm, and the correlation to the DO The center wavelength of Rrs_03 is 640 nm, and the correlation of Rrs_03 to DO is stronger, which is consistent with the conclusion of its research; Rrs_06 and Rrs_05 mainly invert environmental parameters such as vegetation index (e.g., Wang et al., 2022b), soil moisture, surface temperature, etc., which are indirectly related to DO, and therefore the correlation of Rrs_06 and Rrs_05 to DO is also higher.

5 Conclusion

With the rapid development of artificial intelligence and remote sensing technology, the application of machine learning or deep learning models in the inversion and prediction of lake water quality has become a hot topic in the interdisciplinary field of artificial intelligence and environment. The process of obtaining traditional water quality indicators is time-consuming and labor-intensive, often requiring on-site collection of water samples, appropriate storage, and transportation to laboratories for testing. Even data generated by automatic monitoring stations may have some defects. To address the shortcomings of traditional water quality monitoring, this study combines a large amount of historical monitoring water quality data with satellite remote sensing data and uses the DO-MDNN model to achieve more frequent and macroscopic monitoring activities. This approach has the advantages of wide coverage and fast monitoring, providing an effective reference for improving the level of water environment monitoring and holding significant importance for protecting lake water quality. The conclusions of this research are as follows:

(1) Based on H8 data and DO measured data, a deep learning method was employed to propose a DO inversion model called DO-MDNN. The results showed that the average performance of the DO-MDNN model was adj_R^2 of 0.77, RMSE of 0.66 mg/L, Pbias of −0.44%, and SMAPE of 5.36%. Compared to other baseline models, DO-MDNN exhibited better average performance, with a 6.40% increase in adj_R^2, an 8.27% decrease in RMSE, and a 12.1% decrease in SMAPE.

(2) The comparison models after STL processing exhibited significant improvement compared to the models without STL decomposition. The six machine learning models showed an average increase of 0.26 in adj_R^2, a decrease of 0.24 mg/L in RMSE, and a decrease of 2.2% in SMAPE. Among them, the ElasticNet model showed the largest difference in the before and after STL decomposition comparison, with a 0.19 difference in adj_R^2, a 0.23 mg/L difference in RMSE, and a 1.56% difference in SMAPE, showing a significantly improved performance. Additionally, the DO-MDNN model had an increase of 0.14 in adj_R^2, a decrease of 0.23 mg/L in RMSE, and a decrease of 2.1% in SMAPE compared to before STL decomposition. The above results indicate that STL decomposition helps remove noise and trend components from the DO concentration time series, thereby enhancing the accuracy of DO inversion.

(3) Based on the H8 data, DO measurements, and the DO-MDNN model, it is possible to achieve hourly monitoring of DO concentration. This capability meets the demand for high-frequency and dynamic monitoring of DO concentration, providing strong support for marine environmental management and conservation efforts.

Data availability statement

Publicly available datasets were analyzed in this study. This data can be found here: Himawari-8 data from https://www.eorc.jaxa.jp/ptree/ Water quality data from Chinese Research Academy of Environmental Sciences.

Author contributions

KS and QL designed the research. WY and PW conducted experiments and developed models. KS and WY analyzed the result and wrote the manuscript. QL reviewed and edited the manuscript. All authors contributed to the article and approved the submitted version.

Funding

This work was supported by the Key Research Project of Qinghai Province (2021-SF-A7-1), the National Key Research and Development Program (2021YFC310170504) and the Research Project on Machine Learning-based Satellite Remote Sensing for Multi-index Water Quality Inversion, Monitoring, and Early Warning Technology of the State Key Laboratory of Ecological and Agricultural on the Qinghai-Tibet Plateau (2023-ZZ-09).

Conflict of interest

The authors declare that the research was conducted in the absence of any commercial or financial relationships that could be construed as a potential conflict of interest.

Publisher's note

References

Batur, E., and Maktav, D. (2018). Assessment of surface water quality by using satellite images fusion based on PCA method in the Lake Gala, Turkey. *IEEE Trans. Geoscience Remote Sens.* 57 (5), 2983–2989. doi:10.1109/TGRS.2018.2879024

Bui, D. T., Khosravi, K., Tiefenbacher, J., Nguyen, H., and Kazakis, N. (2020). Improving prediction of water quality indices using novel hybrid machine-learning algorithms. *Sci. Total Environ.* 721, 137612. doi:10.1016/j.scitotenv.2020.137612

Cao, Z. G., Ma, R. H., Duan, H. T., Pahlevan, N., Melack, J., Shen, M., et al. (2020). A machine learning approach to estimate chlorophyll-a from Landsat-8 measurements in inland lakes. *Remote Sens. Environ.* 248, 111974. doi:10.1016/j.rse.2020.111974

Changzhou Ecological Environment Bureau, (2021). *Suzhou ecological environment status bulletin*. Changzhou, China: Changzhou Ecological Environment Bureau.

Chen, J., and Quan, W. T. (2012). Using landsat/TM imagery to estimate nitrogen and phosphorus concentration in Taihu Lake, China. *IEEE J. Sel. Top. Appl. Earth Observations Remote Sens.* 5 (1), 273–280. doi:10.1109/jstars.2011.2174339

Chen, J., Zheng, W., Wu, S., Liu, C., and Yan, H. (2022). Fire monitoring algorithm and its application on the geo-kompsat-2A geostationary meteorological satellite. *Remote Sens.* 14 (11), 2655. doi:10.3390/RS14112655

Chen, N. W., Yu, Y. Q., Chen, J. X., Chen, L. B., and Zhang, D. Z. (2021). Artificial neural network models for water quality early warning: A review. *Acta Sci. Circumstantiae* 41 (12), 4771–4782. doi:10.13671/j.hjkxxb.2021.0343

Chen, X. R. (2019). *High-frequency observation of floating algae bloom from AHI on himawari-8*. Xiamen, China: Xiamen University.

Dai, Q. Z., Zhang, K., and Xu, B. (2020). The trend of water quality variation and analysis of meiliang bay and dongtaihu bay in Taihu Lake from 2014 to 2018. *China Rural Water Hydropower* (7), 82–84.

Feng, T. S., Pang, Z. G., and Jiang, W. (2022). Remote sensing retrieval of chlorophyll-a concentration in Lake chaohu based on zhuhai-1 hyperspectral satellite. *Spectrosc. Spectr. Analysis* 42 (8), 2642–2648. doi:10.3964/j.issn.1000-0593(2022)08-2642-07

Guha, S., and Govil, H. (2022). Annual assessment on the relationship between land surface temperature and six remote sensing indices using landsat data from 1988 to 2019. *Geocarto Int.* 37 (15), 4292–4311. doi:10.1080/10106049.2021.1886339

Guo, H. W., Tian, S., Huang, J. .H. J. .N., Zhu, X. T., Wang, B., and Zhang, Z. J. (2022). Performance of deep learning in mapping water quality of Lake Simcoe with long-term Landsat archive. *ISPRS J. Photogrammetry Remote Sens.* 183, 451–469. doi:10.1016/j.isprsjprs.2021.11.023

Guo, H. W., Huang, J. J., Zhu, X. T., Wang, B., Tian, S., Xu, W., et al. (2021). A generalized machine learning approach for dissolved oxygen estimation at multiple spatiotemporal scales using remote sensing. *Environ. Pollut.* 288, 117734. doi:10.1016/J.ENVPOL.2021.117734

Hersbach, H., Bell, B., Berrisford, P., Hirahara, S., Horanyi, A., Munoz-Sabater, J., et al. (2020). The ERA5 global reanalysis. *Q. J. R. Meteorological Soc.* 146 (730), 1999–2049. doi:10.1002/qj.3803

Karakaya, N., and Evrendilek, F. (2011). Monitoring and validating spatio-temporal dynamics of biogeochemical properties in Mersin Bay (Turkey) using Landsat ETM+. *Environ. Monit. Assess.* 181, 457–464. doi:10.1007/s10661-010-1841-5

Kim, Y. H., Son, S., Kim, H. C., Kim, B., Park, Y. G., Nam, J., et al. (2020). Application of satellite remote sensing in monitoring dissolved oxygen variabilities: A case study for coastal waters in korea. *Environ. Int.* 134, 105301. doi:10.1016/j.envint.2019.105301

Li, Y., Li, Y. M., Wang, Q., Zhu, L., and Guo, Y. L. (2014). An observing system simulation experiments framework based on the ensemble square root kalman filter for evaluating the concentration of chlorophyll a by multi-source data: A case study in Taihu Lake. *Aquatic Ecosyst. Health & Manag.* 17 (3), 233–241. doi:10.1080/14634988.2014.940799

Liang, Y. C., Yin, F., Zhao, Y. F., and Liu, L. (2021). Remote sensing inversion of biochemical oxygen demand in Taihu Lake based on Landsat 8 images. *Ecol. Environ. Sci.* 30 (7), 1492–1502. doi:10.16258/j.cnki.1674-5906.2021.07.018

Liu, P., Wang, J., Sangaiah, A. K., Xie, Y., and Yin, X. C. (2019). Analysis and prediction of water quality using LSTM deep neural networks in IoT environment. *Sustainability* 11 (7), 2058. doi:10.3390/su11072058

Lyu, H., Zhang, J., Zha, G. H., Wang, Q., and Li, Y. M. (2015). Developing a two-step retrieval method for estimating total suspended solid concentration in Chinese turbid inland lakes using Geostationary Ocean Colour Imager (GOCI) imagery. *Int. J. Remote Sens.* 36 (5), 1385–1405. doi:10.1080/01431161.2015.1009654

Ma, R. H., Duan, H. T., Gu, X. H., and Zhang, S. X. (2008). Detecting aquatic vegetation changes in Taihu Lake, China using multi-temporal satellite imagery. *Sensors* 8 (6), 3988–4005. doi:10.3390/s8063988

Ma, Z. M., Niu, Y., Xie, P., Chen, J., Tao, M., and Deng, X. W. (2013). Off-flavor compounds from decaying cyanobacterial blooms of Lake Taihu. *J. Environ. Sci.* 25 (3), 495–501. doi:10.1016/S1001-0742(12)60101-6

Ngiam, J., Khosla, A., Kim, M., Nam, J., Lee, H., and Ng, A. Y. (June 2018). Multimodal deep learning. Proceedings of the international conference on machine learning, Bellevue Washington USA,

Ning, H. T., Jiang, P., and Wu, Y. L. (2021). Research on aerosol optical depth retrieval of himawari-8 data based on deep neural networks. *Adm. Tech. Environ. Monit.* 33 (1), 8–12. doi:10.19501/j.cnki.1006-2009.2021.01.003

Peterson, K. T., Sagan, V., and Sloan, J. J. (2020). Deep learning-based water quality estimation and anomaly detection using Landsat-8/Sentinel-2 virtual constellation and cloud computing. *GIScience Remote Sens.* 57 (4), 510–525. doi:10.1080/15481603.2020.1738061

Qi, L., Hu, C. M., Duan, H. T., Cannizzaro, j., and Ma, R. H. (2014). A novel MERIS algorithm to derive cyanobacterial phycocyanin pigment concentrations in a eutrophic lake: Theoretical basis and practical considerations. *Remote Sens. Environ.* 154, 298–317. doi:10.1016/j.rse.2014.08.026

Rajwa-Kuligiewicz, A., Bialik, R. J., and Rowinski, P. M. (2015). Dissolved oxygen and water temperature dynamics in lowland rivers over various timescales. *J. HYDROLOGY HYDROMECHANICS* 63 (4), 353–363. doi:10.1515/johh-2015-0041

Rojo, J., Rivero, R., Romero-Morte, J., Fernandez-Gonzalez, F., and Perez-Badia, R. (2017). Modeling pollen time series using seasonal-trend decomposition procedure based on LOESS smoothing. *Int. J. Biometeorol.* 61 (2), 335–348. doi:10.1007/s00484-016-1215-y

Sagan, V., Peterson, K. T., Maimaitijiang, M., Sidike, P., Sloan, J., Greeling, B. A., et al. (2020). Monitoring inland water quality using remote sensing: Potential and limitations of spectral indices, bio-optical simulations, machine learning, and cloud computing. *Earth-Science Rev.* 205, 103187. doi:10.1016/j.earscirev.2020.103187

Sharaf, El. D. E., Zhang, Y., and Suliman, A. (2017). Mapping concentrations of surface water quality parameters using a novel remote sensing and artificial intelligence framework. *Int. J. Remote Sens.* 38 (4), 1023–1042. doi:10.1080/01431161.2016.1275056

Sun, X., Zhang, Y. L., Shi, K., Zhang, Y. B., Li, N., Wang, W. J., et al. (2022). Monitoring water quality using proximal remote sensing technology. *Sci. Total Environ.* 803, 149805. doi:10.1016/J.SCITOTENV.2021.149805

Suzhou Ecological Environment Bureau, (2021). *Suzhou ecological environment status bulletin*. Suzhou, China: Suzhou Ecological Environment Bureau.

Tian, L. F. (2014). Analysis of the "pseudo regression" of non stationary data. *Statistics Decis. Mak.* 39 (3), 17–21. doi:10.13546/j.cnki.tjyjc.000004

Wang, B., An, H. J., and Lv, C. W. (2013). Inversion modeling of dissolved oxygen in Hulun Lake of Northeast China based on multisource remote sensing. *Chin. J. Ecol.* 32 (4), 993–998. doi:10.13292/j.1000-4890.2013.0174

Wang, G., Wang, D. Y., and Wu, R. (2020). Application study of Himawari-8/AHI ionfrared spectral data on precipitation signal recognition and retrieval. *J.Infrared Millim. Waves.* 39 (02), 251–262. doi:10.11972/j.issn.1001-9014.2020.02.013

Wang, M., Zheng, W., and Liu, C. (2017). Application of Himawari-8 data with high-frequency observation for Cyanobacteria bloom dynamically monitoring in Lake Taihu. *J. Lake Sci.* 29 (05), 1043–1053. doi:10.18307/2017.0502

Wang, X. X., Lu, X. P., and Li, G. Q. (2022b). Extracting urban vegetation information by combining the red edge near red vegetation index with DEM. *Spectrosc. Spectr. Analysis* 42 (7), 2284–2289. doi:10.3964/J.ISSN.1000-0593(2022)07-2284-06

Wang, Z. C., Wang, J., Yan, S. J., Cui, Y. H., and Wang, H. H. (2022a). Annual dynamic remote sensing monitoring of phycocyanin concentration in Lake Chaohu based on Sentinel-3 OLCI images. *J. Lake Sci.* 34 (2), 391–403. doi:10.18307/2022.0203

Wuxi Ecological Environment Bureau, (2021). *Suzhou ecological environment status bulletin*. Wuxi, City: Wuxi Ecological Environment Bureau.

Yamamoto, Y., Ishikawa, H., Oku, Y., and Hu, Z. (2018). An algorithm for land surface temperature retrieval using three thermal infrared bands of himawari-8. *J. METEOROLOGICAL Soc. Jpn.* 96 (B), 59–76. doi:10.2151/jmsj.2018-005

Yang, J. Y., Zhang, S., Bai, Y., Huang, A. Q., and Zhang, J. H. (2021). SPEI simulation for monitoring drought based machine learning integrating multi-source remote

sensing data in shandong. *Chin. J. Agrometeorology* 42 (3), 230–242. doi:10.3969/j.issn.1000-6362.2021.03.007

Zaini, N., Ean, L. W., Ahmed, A. N., and Malek, M. A. (2021a). A systematic literature review of deep learning neural network for time series air quality forecasting. *Environ. Sci. Pollut. Res.* 29 (4), 4958–4990. doi:10.1007/S11356-021-17442-1

Zaini, N., Ean, L. W., Ahmed, A. N., and Malek, M. A. (2021b). A systematic literature review of deep learning neural network for time series air quality forecasting. *Environ. Sci. Pollut. Res.* 29 (4), 4958–4990. doi:10.1007/s11356-021-17442-1

Zhang, H. J., Wang, B., Zhou, J., Yu, Y., Ke, S., and Huang, F. K. (2022). Remote sensing retrieval of inland river water quality based on BP neural network. *J. Central China Normal Univ. Sci.* 56 (02), 333–341. doi:10.19603/j.cnki.1000-1190.2022.02.017

Zhang, Y. C., Lin, S., Liu, J. P., Qian, X., and Ge, Y. (2010). Time-series MODIS image-based retrieval and distribution analysis of total suspended matter concentrations in Lake Taihu (China). *Int. J. Environ. Res. Public Health* 7 (9), 3545–3560. doi:10.3390/IJERPH7093545

Zhao, X. L., Xu, H. L., Ding, Z. B., Wang, D. Q., Deng, Z. D., Wang, Y., et al. (2021). Comparing deep learning with several typical methods in prediction of assessing chlorophyll-a by remote sensing: A case study in Taihu Lake, China. *Water Supply* 21 (7), 3710–3724. doi:10.2166/WS.2021.137

Zhu, W., Cheng, L., Xue, Z. P., Feng, G. Y., Wang, R. C., Zhang, Y., et al. (2021). Changes of water exchange cycle in Lake Taihu(1986-2018) and its effect on the spatial pattern of water quality. *J. Lake Sci.* 33 (04), 1087–1099. doi:10.18307/2021.0411

Frontiers in
Environmental Science

Explores the anthropogenic impact on our natural world

An innovative journal that advances knowledge of the natural world and its intersections with human society. It supports the formulation of policies that lead to a more inhabitable and sustainable world.

Discover the latest Research Topics

See more →

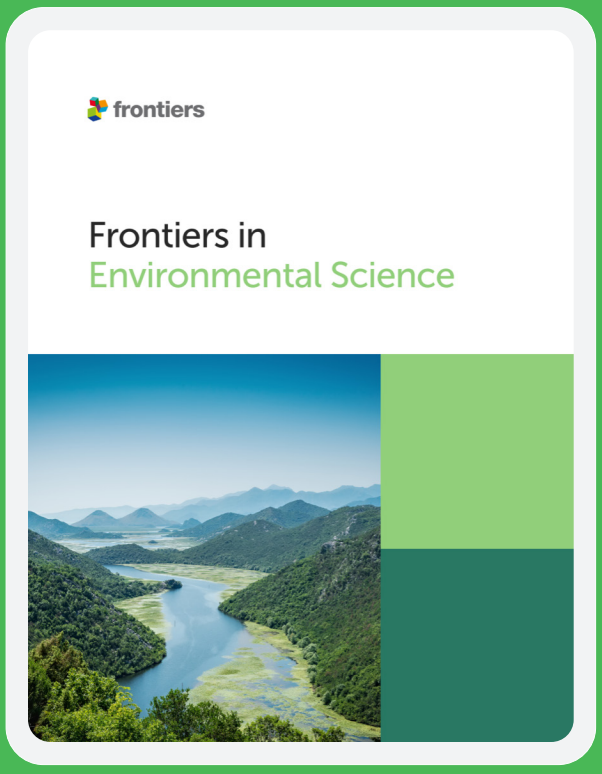

Frontiers

Avenue du Tribunal-Fédéral 34
1005 Lausanne, Switzerland
frontiersin.org

Contact us

+41 (0)21 510 17 00
frontiersin.org/about/contact